

Development Of a Nanobody-Conjugate Platform for Targeted Drug Delivery in Airway Hypersecretory Diseases

Thesis submitted to the University of Nottingham for the degree of Doctor of Philosophy

January 2025

Lola Marie Louise Cusin

20120289

Supervisors: Professor Patrick J. Tighe and Dr Nicholas Mitchel

School of Life Sciences, Faculty of Medicine and Health Sciences

University of Nottingham

Table of Contents

Abstract VIII

Acknowledgments X

List of abbreviations XII

List of figures XV

List of Tables XXI

Chapter 1 General Introduction and Literature Review 1

1.1 Airway Hypersecretory Diseases 1

1.1.1 The Airway Epithelium 1

1.1.2 Pathophysiology and Incidence of Airway Hypersecretory Diseases 4

1.1.3 The Problem of Mucus Hypersecretion 8

1.2 Current Treatments for Airway Hypersecretory Diseases 9

1.2.1 Commonly Used Treatments for Airway Hypersecretory Diseases 9

1.2.2 Biologics 15

1.2.3 Technologies 17

1.3 A Nanobody-Conjugate Platform for the Treatment of Airway Hypersecretory Diseases 31

1.3.1 Targeting the Mucin Pathway 31

1.3.2 Platform Mechanism 36

1.4 Conclusion 37

1.5 Aims and Objectives 37

Chapter 2 Constructing a Semi-Synthetic Nanobody Library 38

2.1 Introduction 38

2.1.1 The Nanobody Scaffold in the Wild 38

2.1.2 Molecular Display Platforms for Nanobody Libraries 41

2.1.3 Constructing a Nanobody Library 45

2.1.4 Aims and Objectives 47

2.2 Materials and Methods 48

2.2.1 Microbiology Techniques 48

2.2.2 *In vitro* Synthesis of Variable DNA Fragments and Cloning into the Phagemid pSEX81 51

2.2.3 Construction of a vNAR Phage Display Library 56

2.2.4 PpSEX81_5A7 ELISA Binding Assay 58

2.2.5 Reagents 59

2.3 Results and Discussion 62

2.3.1 Pilot Experiment 62

2.3.2 Library Construction 70

2.3.3 Assessing Final Library Diversity 86

2.4 Conclusion 90

Chapter 3 Identification of Targets 91

3.1 Introduction 91

3.1.1 The Role of Goblet Cells in Airway Hypersecretion 91

3.1.2 Airway Epithelium Models 91

3.1.3 Fluorescence Activated Cell Sorting and Goblet Cell Isolation 93

3.1.4 Biopanning 94

3.1.5 Aim and Objectives 99

3.2 Materials and Methods 100

3.2.1 Human Bronchial Epithelial Primary Cell Culture 100

3.2.2 MucilAir™ 101

3.2.3 IL-13 Stimulation 102

3.2.4 Flow Cytometry 102

3.2.5 Shark Nanobody Library Biopanning 103

3.2.6 Western Blotting 107

3.2.7 Sequencing 108

3.2.8 Estimation of Protein Hydrophobicity 111

3.2.9 Reagents 111

3.3 Results and Discussion 113

3.3.1 Cell Culture 113

3.3.2 Analytical Flow Cytometry 115

3.3.3 Fluorescence Activated Cell Sorting (FACS) 124

3.3.4 Biopanning 128

3.3.5 Investigation of Potential Binders 130

3.4 Conclusion 141

Chapter 4 Functionalisation of Target-Specific Nanobodies 142

4.1 Introduction 142

4.1.1 Protein Expression and Purification 142

4.1.2 Bioconjugation Methods 143

4.1.3 Sortase A Conjugation 144

4.1.4 Solid Phase Peptide Synthesis 145

4.1.5 Aim and Objectives 146

4.2 Materials and Methods 147

4.2.1 Peptide Synthesis 147

4.2.2 Conjugation of Cy5.5 to Lysine Residues 149

4.2.3 High-Performance Liquid Chromatography 149

4.2.4 Mass Spectrometry 151

4.2.5 Protein Expression and Purification 151

4.3 Results and Discussion 160

4.3.1 Peptide Synthesis 160

4.3.2 Sortase A Expression and Purification 170

4.3.3 Nanobody Expression and Purification 177

4.4 Conclusion 192

Chapter 5 General Discussion 193

5.1 Introduction 193

5.2 Interpretation of Key Findings 194

5.2.1 Development of a Diverse Nanobody Library 194

5.2.2 Establishing an Airway Epithelium Model 197

5.2.3 Whole Cell Biopanning 199

5.2.4 Chemical Synthesis of a Fluorescent Label for the Functionalisation of Nanobodies by Sortase A Conjugation 203

5.2.5 Expression and Purification of the vNAR 5A7 203

5.3 Future Directions 205

5.4 Conclusion 207

Chapter 6 Contribution to the COVID-19 Research Effort 208

6.1 Introduction 208

6.1.1 Coronaviruses 208

6.1.2 Emergence and Characteristics of SARS-CoV-2 210

6.1.3 Clinical Manifestations and Transmission 214

6.1.4 Academic Contribution to the COVID19 Research Effort: The PANTHER Study 214

6.2 Aim, Objectives and Acknowledgements 215

6.3 Materials and Methods 216

6.3.1 Sample Collection and Processing 216

6.3.2 Enzyme-Linked Immunosorbent Assays 216

6.3.3 Data Analysis 217

6.4 Results and Discussion 218

6.4.1 Longitudinal Assessment of Symptoms and Risk of SARS-CoV-2 Infection in Healthcare Workers across 5 Hospitals to Understand Ethnic Differences in Infection Risk 220

6.4.2 HLA-DR Polymorphism in SARS-CoV-2 Infection and Susceptibility to Symptomatic COVID-19. 222

6.4.3 Two Doses of the SARS-CoV-2 BNT162b2 Vaccine Enhance Antibody Responses to Variants in Individuals with Prior SARS-CoV-2 Infection 223

6.5 Conclusion 225

References 226

Appendix 1 Maps of Plasmids XX

Appendix 2 Agar Plates XXIV

First Library Construction XXIV

Second Library Construction XXV

Biopanning Rounds XXVI

Appendix 3 Flow Cytometry Complementary Data XXVII

Single Colour Controls XXVII

Fluorescence Minus One (FMO) Controls XXXIV

Second Repeat XXXIX

Cell Sorting (Third Repeat) XL

Appendix 4 PIPS Reflective Statement XLII

Note To Examiners XLII

Statement XLII

Abstract

Airway Hypersecretory Diseases (AHDs) are conditions in which the main pathophysiology is mucus hypersecretion. The incidence of AHDs is high (over 500 million affected worldwide) and comes with a diminished quality of life for patients. Very few treatment protocols focus on mucus hypersecretion. We propose a nanobody-conjugate platform for the targeted treatment of AHDs based on nanobody targeting of goblet cell surface antigens and a site-directed conjugation method to allow therapeutics to be attached to the nanobodies.

A diverse synthetic nanobody library based on the shark vNAR 5A7 scaffold and expressed as N-terminal pIII fusion proteins within the phagemid pSEX81 was developed to create a naïve nanobody library displayed on M13-based bacteriophage particles, for screening. NGS analysis confirmed a diversity of 2.56×10^9, comparable to libraries described in the literature.

Human bronchial epithelial cells (HBEpc) were cultured at the air- liquid interface as a model for the human airway epithelium, and IL-13 stimulation was used to simulate the hypersecretory phenotype observed in AHDs. Flow cytometry analysis validated IL-13 driven airway remodelling, and goblet cells metaplasia. Increases in the percentage of goblet cells in culture were observed, similar to the effects reported in the literature (from 3.77% to 17.92% post IL-13 stimulation, N=3). A whole cell biopanning protocol was designed for phage display selection of potential binders to stimulated epithelial cells and yielded 8 clones. Sequencing of these clones revealed highly disturbed origin of replication and nanobody regions, and no binders could be identified.

Functionalisation of nanobodies by site-specific bioconjugation of a fluorescent tag was investigated. Sortase A catalysed coupling was selected as it allowed for the conjugation of the fluorescent label selectively at the C-terminus, preventing the labelling of the binding sites of nanobodies. A Cy5.5 label was synthesised by solid-phase peptide synthesis and amide coupling. The label encoded

the oligoglycine recognition site of Sortase A enzyme, and the cyanine fluorophore was coupled to the side chain of a lysine. The original vNAR 5A7 was engineered to express the LPXTG recognition sequence of Sortase A alongside a poly-histidine tag for purification by immobilized metal affinity chromatography. Despite several optimisations of the expression protocol, the Hen egg white lysozyme specific vNAR 5A7 was not expressed in E. coli, and further work will be needed to produce the protein. The challenges of whole cell biopanning and nanobody expression and purification are discussed.

Acknowledgments

I would like to express my deepest gratitude to my supervisors, Professor Paddy Tighe and Dr Nicholas Mitchell, for their guidance, encouragement, and patience throughout this journey. Their expertise and support have been instrumental in shaping this thesis.

I would like to thank my university colleagues across departments, your camaraderie and encouragements have been an integral part of this journey. A special mention goes to the university technicians Tyler Harvey-Cowlishaw and Matthew Kokolski, and to the flow cytometry staff Dr David Onion and Nicola Croxall, whose expertise, patience, and tireless efforts ensured that experiments ran smoothly, and equipment remained functional.

I would also like to extend my heartfelt thanks to my lab and office colleagues, who have made this experience truly memorable. Thank you for the stimulating discussions, collaborative spirit, and countless moments of laughter that made even the most challenging days enjoyable.

I am profoundly grateful to the PANTHER research team for inviting me to join them in their participation to the COVID19 research effort, and especially Professor Ana Valdes and Professor Ben Ollivere. Working alongside such a talented and driven group during these unprecedented times has been both a privilege and a learning experience.

This work was supported by the Biotechnology and Biological Sciences Research Council Doctoral Training Partnership, and I would like to thank the Nottingham BBSRC DTP team for their running of this program, training sessions and in-school events. Your hard work has enriched my academic experience and provided me with a wide range of skills to support my career.

To my parents, Laurence and Pierre-Yves, I owe everything. Your unconditional love, belief in me, and constant encouragement have been my source of strength, and have kept me going through all these years at university.

To my sister Suzy, thank you for being my sounding board, game partner and cheerleader.

To Katie, Holly, Emma and Amélia, thank you for your unwavering friendship and for always being there to lift my spirits.

To my partner Jonathan, I could not have done this without you. Your love and faith in me have carried me through this process.

I dedicate this thesis to the memory of my grandad, Louis, who sadly passed away during the course of this work. I hope you would be proud. I carry your wisdom, warmth and love with me every day.

Finally, a special thanks to my dog Echo, who has been an unlimited source of joy, even when stealing socks or barking at delivery drivers during online meetings. Your wagging tail and endless enthusiasm kept a smile on my face through the hardest times. You truly are the goodest of good dogs.

To all of you, thank you from the bottom of my heart.

List of abbreviations

Abbreviation	Meaning
ADCC	Antibody-Dependent Cell-mediated Cytotoxicity
ADC	Antibody Drug Conjugate
AHDs	Airway Hypersecretory Diseases
ALI	Air-Liquid Interface
AMP	Adenosine Monophosphate
AP	Activator Protein
ATCC	American Type Culture Collection
ATP	Adenosine Triphosphate
AUC	Area Under Curve
BCA	Bicinchoninic Acid
Boc	tert-butyloxycarbonyl
BSA	Bovine Serum Albumin
Bzl	benzyl
CDR	Complementarity Determining Region
CEACAM6	Carcinoembryonic antigen-related cell adhesion molecule 6
CF	Cystic Fibrosis
CFTR	Cystic fibrosis transmembrane conductance regulator
CFU	Colony Forming Unit
CH	Conserved heavy chain domain
CL	Conserved light chain domain
CMC	Complement mediated cytotoxicity
COPD	Chronic Obstructive Pulmonary Disease
COVID-19	Coronavirus disease 2019
DCM	Dichloromethane
dF	Degree of Freedom
DIC	Diisopropylcarbodiimide
DIPEA	Diisopropylethylamine
DMF	Dimethylformamide
DMSO	Dimethyl sulfoxide
DNA	Deoxyribonucleic acid
DTT	Dithiothreitol
EDTA	Ethylenediaminetetraacetic acid
EGFR	Epidermal growth factor receptor
ELISA	Enzyme Linked Immunosorbent Assay
ER	Endoplasmic Reticulum
ESI	Electrospray Ionisation
F_{ab}	Fragment antigen-binding
FACS	Fluorescence-Activated Cell Sorting
FBS	Fœtal Bovine Serum
F_c	Fragment crystallisable
FDA	Food and Drug Administration

FMO	Fluorescence Minus One
Fmoc	Fluorenyl methoxycarbonyl
FOXA2	Forkhead box protein A2
FPLC	Fast Protein Liquid Chromatography
FSC	Forward Scatter
GFP	Green Fluorescent Protein
HBTU	Hexafluorophosphate Benzotriazole Tetramethyl Uronium
HEL	Hen Egg white Lysozyme
HEPES	2-[4-(2-hydroxyethyl)piperazin-1-yl]ethanesulfonic acid
HF	High Fidelity or Hydrofluoric Acid
HIBAG	HLA Genotype Imputation with Attribute Bagging
HLA	Human Leukocyte Antigen
HPLC	High-Performance Liquid Chromatography
HRP	Horseradish Peroxidase
HV	Hyper Variable
ID	Identity
Ig	Immunoglobulin
IgNAR	Immunoglobulin new antigen receptors
IL	Interleukin
IMD	Index of Multiple Deprivation
IPTG	Isopropyl β-D-1-thiogalactopyranoside
JAK/STAT	Janus kinase/signal transducer and activator of transcription
LB	Lysogeny Broth
LPS	Lipopolysaccharide
MAPK	Mitogen-Activated Protein Kinase
MAPK13	p38 MAP kinase
MARCKS	Myristoylated Alanine Rich C-Kinase Substrate
MERS	Middle East Respiratory Syndrome
MMAE	Monomethyl auristatin E
MS	Mass Spectrometry
MUC	Mucin
NF-κB	Nuclear factor kappa-B
NGFR	Nerve Growth Factor Receptor
NGS	Next Generation Sequencing
NHS	N-Hydroxy succinimide
NIBSC	National Institute for Biological Standards and Control
NMP	N-Methyl-2-pyrrolidone
NS	Non-Significant
Oxyma	Ethyl cyanohydroxyiminoacetate
PANTHER study	PANdemic Tracking of Healthcare woRkers study
PBA	Staining Buffer
PBS/PBST	Phosphate Buffered Saline/Phosphate Buffered Saline with Tween 20
PCR	Polymerase Chain Reaction
PDB	Protein Databank
PDE	Phosphodiesterase

PEG	Polyethylene glycol
PMSF	Phenylmethylsulfonyl fluoride
RBD	Receptor Binding Domain
RBS	Ribosome Binding Site
RER	Rough Endoplasmic Reticulum
RFP	Red Fluorescent Protein
RIPA	Radioimmunoprecipitation assay
RNA	Ribonucleic acid
RP-HPLC	Reverse Phase High-Performance Liquid Chromatography
SARS	Severe Acute Respiratory Syndrome
SD	Standard Deviation
SDS	Sodium dodecyl sulfate
SDS-PAGE	Sodium dodecyl sulfate polyacrylamide gel electrophoresis
SE	Standard Error
SNARE	SNAP REceptors
SOC	Super Optimal Broth with Catabolite Repression
SPDEF	SAM Pointed Domain Containing ETS Transcription Factor
SPPS	Solid Phase Peptide Synthesis
SSC	Side Scatter
TBE	Tris-borate-EDTA
TBS/TBST	Tris-buffered saline/Tris-buffered saline with Tween 20
TFA	Trifluoroacetic acid
TIS	Triisopropylsilane
TLR	Toll-Like Receptor
TNF	Tumour Necrosis Factor
TSPAN8	Tetraspanin 8
TY	Tryptone Yeast extract
TY-GA	Tryptone Yeast extract with Glucose and Ampicillin
UCSF	University of California, San Francisco
UV	Ultraviolet
v/v	Volume for volume
VAMP	Vesicle-Associated Membrane Protein
VH	Variable heavy chain domain
VL	Variable light chain domain
vNAR	Variable New Antigen Receptor
w/v	Weight for volume
WCP	Whole Cell Panning
WHO	World Health Organisation

List of figures

Figure 1.1 Schematic representation of the airway epithelium and the mechanism of mucus secretion and mucociliary clearance. 3

Figure 1.2 Schematic representation of airways and alveoli in both healthy patients and patients suffering from AHDs focusing on main symptom presentation. 5

Figure 1.3 Compared structures of human, camelids, and shark antibodies, alongside a single domain nanobody..... 23

Figure 1.4 Mechanisms of various bioconjugation methods..... 28

Figure 1.5 Schematic structures of proteins MUC5AC and MUC5B domains and glycan side chains..... 32

Figure 1.6 Schematic representation illustrating the regulatory mechanisms governing the expression and secretion of mucins MUC5AC and MUC5B in the lungs. 34

Figure 2.1 Schematic representation of the two-step splicing by overlap extension PCR introducing genetic diversity into the CDR3 of 5A7 vNAR..... 46

Figure 2.2 2% agarose gel of PCR-amplified vNAR_5A7 fragment. 62

Figure 2.3 1.5% Diagnostic digest of pSEX81_5A7..... 63

Figure 2.4 ELISA of PpSEX81_5A7 against serial dilutions of HEL. 65

Figure 2.5 ELISA of PpSEX81_5A7 against serial dilutions of HEL. 65

Figure 2.6 ELISA of PpSEX81_5A7 against serial dilutions of HEL. 66

Figure 2.7 ELISA of PpSEX81_5A7 against serial dilutions of HEL. 68

Figure 2.8 ELISA of serial dilutions of PpSEX81_5A7 against HEL and 3% BSA as a control. 68

Figure 2.9 ELISA of serial dilutions of PpSEX81_5A7 against HEL and 3% BSA as a control. 69

Figure 2.10 1% agarose gel of PCR-amplified vNAR_5A7 fragment and the 6 variants. 71

Figure 2.11 Colony PCR of the pSEX81: fragment 3 ligation at various molecular ratios. 73

Figure 2.12 Colony PCR of the pSEX81: fragment 1 and pSEX81: fragment 6 ligations at various molecular ratios. 73

Figure 2.13 Selected results of FastQC analysis of library 1 NGS. 75

Figure 2.14 Alignments of NGS library 1 with the native 5A7 fragments, as well as the various randomised fragments. 78

Figure 2.15 Alignment of the translated consensus resulting from the NGS data processing. 79

Figure 2.16 Selected results of FastQC analysis of library 2 NGSs. 81

Figure 2.17 GC content distribution of library 2 analysed by NGS twice..... 82

Figure 2.18 Sequence length distribution of library 2 analysed by NGS twice. 82

Figure 2.19 Alignments of NGS library 2 with the native 5A7 fragments, as well as the various randomised fragments. 84

Figure 2.20 Alignment of the translated consensus resulting from the NGS data processing. 86

Figure 3.1 Schematic representation of the biopanning process in nanobody phage display. 97

Figure 3.2 Schematic representation of each biopanning protocol developed to isolate goblet cell-specific nanobodies. 105

Figure 3.3 Confocal microscopy of HBEpc culture. 114

Figure 3.4 Flow cytometry gating strategy for isolating a single, viable cell population of HBEpc cultured at ALI with (IL-13+) or without (IL-13-) interleukin 13 treatment. 117

Figure 3.5 Flow cytometry analysis of IL-13- and IL-13+ cell populations stained with a multicolour panel for cell type identification. 120

Figure 3.6 Histograms of cell counts for each of the 4 markers, in unstimulated (in blue) and IL-13 stimulated samples (in red). 121

Figure 3.7 Percentage of total cells identified as either basal, ciliated, secretory or goblet cells by flow cytometry. 124

Figure 3.8 Flow cytometry gating strategy for sorting HBEpc cultured at ALI with (IL-13+) or without (IL-13-) interleukin 13 treatment into specific cell subpopulation. 126

Figure 3.9 Fluorescence activated cell sorting of IL-13- and IL-13+ cell populations stained with a multicolour panel for cell type identification. 127

Figure 3.10 Phage titre as CFU of each experiment of biopanning. 130

Figure 3.11 Western blot of IL-13+ (column 1), IL-13- (column 2) lysates, and HEL (column 3, final membrane only). 131

Figure 3.12 Western blot of IL-13+ (column 1), IL-13- (column 2) lysates, and HEL (column 3, final membrane only). 133

Figure 3.13 Molecular surface representation of vNAR 5A7 bound to HEL highlighting hydrophobicity. 134

Figure 3.14 Alignment of plasmid assembly against pSEX81_5A7. 138

Figure 3.15 GC Content Across the ColE1 Origin Sequence in pSEX81 as plasmid replication origin. 139

Figure 4.1 Functionalisation of a nanobody with a Cy5.5 fluorophore catalysed by Sortase A..... 145

Figure 4.2 Predicted sequence to be expressed by BL21-AI as a result of a Gibson assembly between plasmid pET52b(+) and 5A7 nanobody in pSEX81..... 153

Figure 4.3 Synthetic gene sequence used for the Gibson assembly of the 5A7 alongside relevant linker and tag into pET101 154

Figure 4.4 Mechanism of Fmoc Solid Phase Peptide Synthesis (Fmoc SPPS). 162

Figure 4.5 Chemical structure of the Fmoc-GGGK peptide following cleavage from rink amide resin in order to check for proper synthesis prior to Cy5.5 coupling. 163

Figure 4.6 Mass Spectra confirming the synthesised Fmoc-GGGK peptide. 163

Figure 4.7 Chemical structure of the Fmoc-GGGKGGG peptide following cleavage from rink amide resin in order to check for proper synthesis prior to Cy5.5 coupling. 164

Figure 4.8 Mass Spectra confirming the synthesised Fmoc-GGGKGGG peptide. 164

Figure 4.9 Chemical structure of the GGGK(Cy5.5)GGG peptide following cleavage from rink amide resin. 166

Figure 4.10 Mass Spectra confirming the synthesised GGGK(Cy5.5)GGG-NH_2 peptide. 166

Figure 4.11 Stepwise synthesis of GGGK(Cy5.5)GGG following Fmoc-based solid-phase peptide synthesis (SPPS), followed by dye conjugation through amide coupling to a lysine residue..... 167

Figure 4.12 HPLC chromatogram depicting the separation of GGGK(Cy5.5)GGG alongside corresponding MS spectra showing the m/z values of the detected ions..... 170

Figure 4.13 Representative chromatogram of Sortase A protein purification using an ÄKTA FPLC system..... 171

Figure 4.14 SDS-PAGE analysis of fractions collected from the Sortase A protein purification process, stained with Coomassie Brilliant Blue..... 172

Figure 4.15 SDS-PAGE analysis of fractions collected from the Sortase A protein with various concentrations of DTT to reduce the protein dimer, stained with Coomassie Brilliant Blue..... 173

Figure 4.16 Representative chromatogram of Sortase A protein purification using an ÄKTA FPLC system..... 175

Figure 4.17 SDS-PAGE analysis of fractions collected from the Sortase A protein second purification process, stained with Coomassie Brilliant Blue. 176

Figure 4.18 Determination of Sortase A protein concentration by Pierce BCA Protein Assay..... 177

Figure 4.19 1% agarose gel of PCR-amplified Gibson fragment from pSEX81_5A7. 178

Figure 4.20 1% agarose gel of PCR-linearised vector pet52b(+)..... 179

Figure 4.21 SDS-PAGE analysis of 5A7 pilot protein expression from BL21 carrying pET52b_5A7, stained with Coomassie Brilliant Blue. 181

Figure 4.22 Representative chromatogram of 5A7 from pET52b(+) protein purification using an ÄKTA FPLC system. 182

Figure 4.23 SDS-PAGE analysis of 5A7 pilot protein expression from BL21 carrying pET101_5A7, stained with Coomassie Brilliant Blue. 184

Figure 4.24 Representative chromatogram of 5A7 from pET101_5A7 protein purification using an ÄKTA FPLC system. 185

Figure 4.25 SDS-PAGE analysis of fractions collected from the 5A7 from pET101_5A7 protein purification process, stained with Coomassie Brilliant Blue. 187

Figure 4.26 Representative chromatogram of 5A7 from pET101_5A7 protein purification with urea treatment using an ÄKTA FPLC system. 189

Figure 4.27 SDS-PAGE analysis of fractions collected from the 5A7 from pET101_5A7 protein purification process with urea treatment, stained with Coomassie Brilliant Blue..... 190

Figure 4.28 Western blot analysis of 5A7 expression. 191

Figure 5.1 3D structure of a vNAR showing the four hypervariable loops. . 197

Figure 6.1 Schematic representation of SARS-CoV-2's genome, showing the two ORFs alongside the 4 genes encoding the structural proteins S, E, M and N. A schematic virion structure is also shown. 211

Figure 6.2 SARS-CoV-2 infection and replication mechanism. 213

Figure 6.3 PANTHER team study objectives as part of the SARS-CoV-2 COVID19 research effort. 215

Figure 6.4 Representative data showing weekly samples for a single participant. 219

List of Tables

Table 1.1 Side effects of the main drugs used in the treatment of AHDs classed by commonality..... 13

Table 1.2 Reported side effects of newly approved biologics for the treatment of asthma. 17

Table 1.3 Potential targets and inhibitors of mucus synthesis and secretion as described by Ha and Rogers (2016). 35

Table 2.1 Antibody gene library sizes per platform technology. From Valldorf *et al.* (2022). published in Biological Chemistry. © 2022, licensed under CC BY. 43

Table 2.2 List of primers used for isolating the vNAR_5A7 fragment and introducing genetic diversity in the vNAR_5A7 fragment. 51

Table 2.3 Q5® High-Fidelity DNA PCR reaction conditions 52

Table 2.4 Q5® High-Fidelity DNA PCR thermocycling conditions 52

Table 2.5 OneTaq® Quick-Load® DNA PCR reaction conditions 53

Table 2.6 OneTaq® Quick-Load® DNA PCR thermocycling conditions..... 53

Table 2.7 List of primers used for Sanger sequencing. 55

Table 2.8 List of primers used for next-generation sequencing. 56

Table 2.9 Table of antibiotics used, along with the relevant solvent and working concentration. 59

Table 2.10 Table of buffers with compositions..... 59

Table 2.11 Number of possible sequences per fragment size. 87

Table 2.12 Values obtained from libraries used to calculate diversity..... 88

Table 2.13 Selected examples of phage-display antibody fragment library. 89

Table 3.1 List of stains and antibodies used for flow cytometry analysis and cell sorting. 103

Table 3.2 Phusion® High-Fidelity DNA PCR reaction conditions 109

Table 3.3 Phusion® High-Fidelity DNA PCR thermocycling conditions 109

Table 3.4 List of primers used for Sanger sequencing. 110

Table 3.5 List of primers used for next-generation sequencing. 111

Table 3.6 Table of antibiotics used, along with the relevant solvent and working concentration. 111

Table 3.7 Table of buffers with compositions. Buffer pH is measured at room temperature (20° C). 112

Table 4.1 Reagent abbreviations and full names. 147

Table 4.2 Automated FMOC SPPS parameters 149

Table 4.3 List of primers used for the Gibson assembly of nanobodies into pET52(b)+ and subsequent analysis 152

Table 4.4 Reaction conditions for Gibson assembly using the Gibson Assembly® Master Mix (New-England Biolab) 152

Table 4.5 List of primers used for the Gibson assembly of the 5A7 synthetic gene into pET101. 155

Table 4.6 Composition of buffers for protein purification by FPLC. 157

Chapter 1 General Introduction and Literature Review

Airway hypersecretory diseases are characterised by a build-up of mucus in the airways, resulting in respiratory problems (Ha and Rogers, 2016). These conditions have a high incidence, and some of them also present high mortality rates. Moreover, the quality of life for patients suffering from AHDs is greatly diminished (Ståhl *et al.*, 2005). Treatments are available, but not always very effective. They can also be costly and present with many side effects. In the last two decades, new biotechnologies have appeared and have been applied therapeutically to many diseases, but those applications did not target AHDs.

In this review, an overview of airway hypersecretory diseases and current treatments is presented, followed by a presentation of new technologies, mechanisms, and current applications. Finally, the combined use of nanobodies and various bio-conjugate technologies for the treatment of AHDs is discussed and prospective research is investigated.

1.1 Airway Hypersecretory Diseases

1.1.1 The Airway Epithelium

The human airway epithelium serves as a protective physical barrier against pathogens, toxins, and pollutants, preventing them from entering the body through the respiratory system. It houses various immune cells such as dendritic cells, macrophages, and intraepithelial lymphocytes, and produces antimicrobial peptides and proteins antimicrobial peptides and proteins, including defensins, cathelicidins, and lysozyme, that directly target and neutralize microbes (Nicod, 2005; Schleimer *et al.*, 2007). The airway epithelium main role is gas exchange, which occurs across the epithelial lining of the respiratory tract. Oxygen molecules diffuse across the thin epithelial barrier of the alveoli and into the bloodstream, while carbon dioxide molecules produced by cellular metabolism diffuse across the airway epithelium from

the bloodstream into the alveolar spaces, where it can be exhaled (Davis and Wypych, 2021).

The airway epithelium consists of a layer of specialised cells that vary in structure and function along different regions of the respiratory tract, from the nasal passages down to the smaller airways of the lungs. In the larger airways, such as the trachea and bronchi, the epithelium appears pseudostratified, where all cells are attached to the basal membrane, but might not all reach the apical surface. In the smaller airways, such as the bronchioles, the epithelium transitions to a simple columnar or cuboidal arrangement. This type of epithelium is thinner and composed of a single layer of cells (Knight and Holgate, 2003).

The human airway epithelium is composed of various cell types, most commonly ciliated cells, goblet cells, basal cells, and club (secretory) cells (formerly Clara cells). Other less common cell types include neuroendocrine cells, surface serous cells and brush cells (Proud, 2008).

Ciliated cells are characterised by the presence of cilia on their apical surface. Those structures play a critical role in moving mucus and trapped particles out of the airways through mucociliary clearance (Yaghi and Dolovich, 2016). Secretory (or club) cells (formerly known as Clara cells) are non-ciliated, secretory cells found primarily in the bronchioles of the respiratory tract. They secrete proteins and lipids and contribute to the regeneration of the epithelial lining following injury. Goblet cells are specialised secretory cells that produce and secrete mucus, which helps to trap and eliminate inhaled particles, pathogens, and pollutants. Basal cells are located at the base of the epithelial layer and contribute to the maintenance and repair of the airway epithelium by differentiating into other cell types, such as ciliated cells and goblet cells, in response to injury or damage (Rogers, 1994).

Neuroendocrine cells are scattered throughout the airway epithelium and play a role in regulating airway function and homoeostasis by secreting neurotransmitters and neuropeptides that modulate processes such as airway smooth muscle contraction, mucus secretion, and inflammation in response to various stimuli (Thakur *et al.*, 2024). Serous cells are secretory cells most commonly

found in the submucosal glands but can be sporadically observed in the small bronchi and bronchioles. Finally, brush cells are rare, columnar-shaped cells with microvilli on their surface. They are found predominantly in the trachea and larger airways and are thought to be involved in chemical sensing and immune surveillance (Joo *et al.*, 2004).

Overall, the human airway epithelium is a dynamic tissue that plays a crucial role in maintaining the integrity and function of the respiratory tract, while also protecting it from harmful external agents. A schematic representation of the airway epithelium can be seen in Figure 1.1.

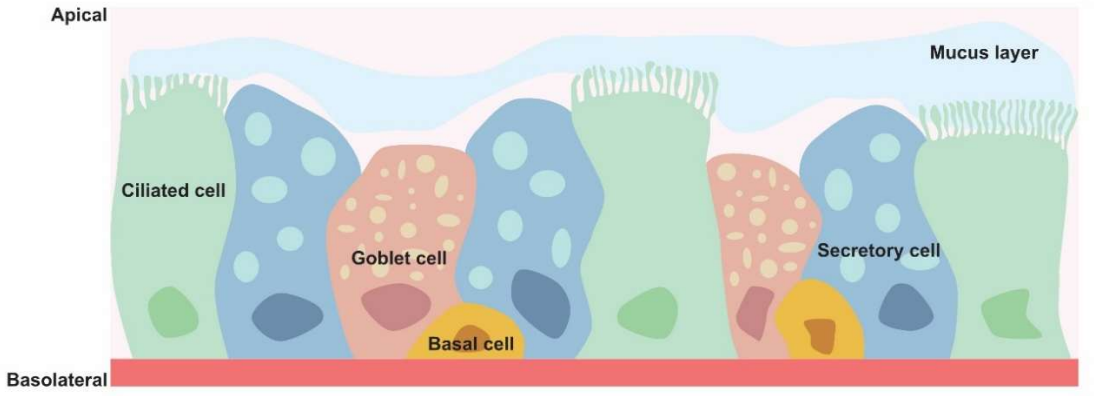


Figure 1.1 Schematic representation of the airway epithelium and the mechanism of mucus secretion and mucociliary clearance.

Ciliated cells (in green) are equipped with cilia that beat in a coordinated manner to move mucus towards the epithelium, aiding in its clearance. Goblet cells (in pink) are responsible for mucus production and secretion, which traps inhaled particles and pathogens. Basal (progenitor) cells (in yellow) help regenerate and repair the epithelium, maintaining its integrity. Secretory cells (in blue) secrete proteins and lipids and contribute to the regeneration of the epithelial lining following injury. This schematic emphasises the collaborative roles of these cells in respiratory health. Figure created using Affinity Designer 2.6.2 (available at affinity.serif.com).

1.1.2 Pathophysiology and Incidence of Airway Hypersecretory Diseases

Four main conditions can be categorised as AHDs: Chronic obstructive pulmonary disease (COPD); Asthma; Cystic fibrosis (CF) and bronchiectasis. All present different pathophysiology, but all include mucus hypersecretion as a main symptom. Those pathologies also have various causes and incidence and mortality rates (Hill *et al.*, 2022). In this section, those pathologies are detailed, and their various characteristics are listed. A schematic representation of affected airways can be seen in Figure 1.2.

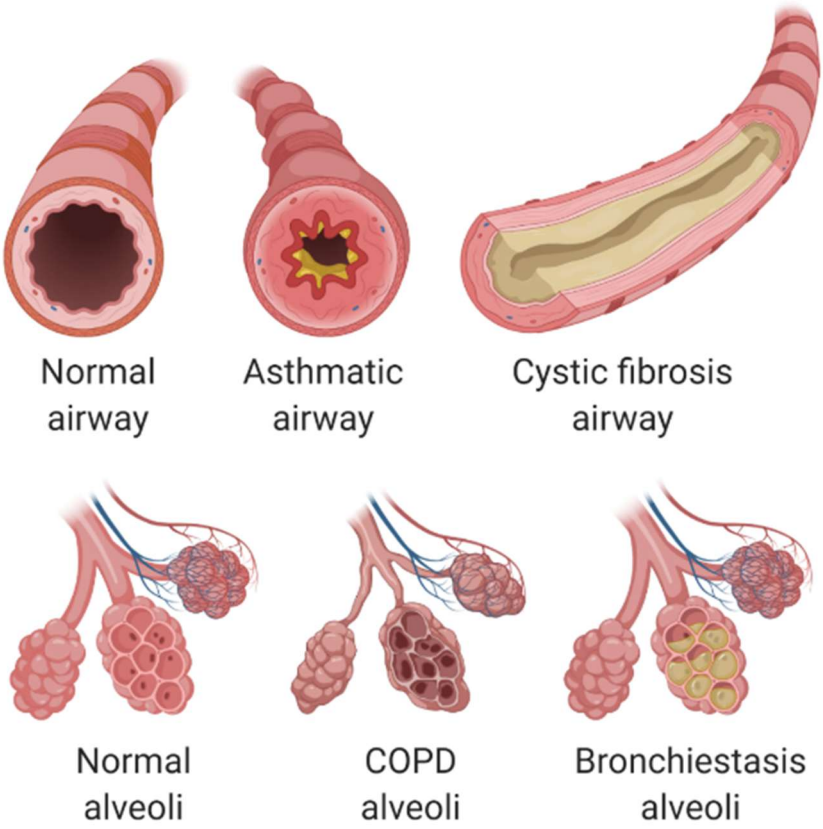


Figure 1.2 Schematic representation of airways and alveoli in both healthy patients and patients suffering from AHDs focusing on main symptom presentation.

Asthma: narrowing of the airway; CF: mucus oversecretion; COPD: damaged air sacs; Bronchiectasis: extended air sacs and mucus oversecretion. Figure created in BioRender (available at biorender.com).

1.1.2.1 Chronic Obstructive Pulmonary Disease

Chronic obstructive pulmonary disease, or COPD, is a common lung disease characterised by inflamed respiratory tissues and damaged alveoli, along with mucus hypersecretion. Key aspects of COPD pathophysiology include chronic inflammation triggered by exposure to noxious particles, leading to the recruitment of inflammatory cells and the release of pro-inflammatory mediators. This chronic inflammation causes structural changes in the airways, such as thickening of airway walls and mucus hypersecretion, contributing to airflow limitation and increased airway resistance (Bourdin *et al.*, 2009). Additionally, parenchymal destruction, primarily emphysema, leads to loss of lung tissue elasticity and impaired gas exchange. Oxidative stress from environmental pollutants exacerbates inflammation and promotes airway remodelling and emphysema. Dysregulated immune responses compromise host defence mechanisms, increasing susceptibility to respiratory infections and exacerbations. Overall, the complex interplay of inflammation, structural changes, oxidative stress, and altered immune responses contributes to the characteristic symptoms of COPD, including dyspnoea, cough, sputum production, and exercise intolerance (World Health Organisation, 2020a).

Previously categorised into chronic bronchitis and emphysema, it is now recognised as one condition with several stages, starting from simple tissue irritation to unrepairable tissue damage. It is mainly caused by smoking, although other environmental factors such as air pollution and industrial triggers have been isolated (Schikowski *et al.*, 2014). Moreover, in rare cases, non-smokers who lack a protein called alpha-1 antitrypsin can develop a form of COPD. COPD is the third leading cause of death worldwide (Chen *et al.*, 2023), cases increased to 384 million in 2010, with a global prevalence of 11.7% (8.4%–15.0%) (Adeloye *et al.*, 2015), and those numbers are predicted to increase, especially in developed countries (Mathers and

Loncar, 2006). In 2015, over 3.17 million people died of COPD worldwide (World Health Organisation, 2020a).

1.1.2.2 Asthma

Asthma is a chronic disease of the air passages of the lungs, characterised by inflamed and narrowed airways, which results in sporadic breathing difficulties. Cause by a combination of genetic and environmental factors, it is often first observed in childhood but affects people of all ages. Pathophysiology involves a complex interplay of factors, including inflammation, airway hyper-responsiveness, bronchoconstriction, mucus hypersecretion, and airway remodelling (see Figure 1.2). Triggers like allergens or pollutants lead to inflammation, recruiting inflammatory cells that release mediators causing bronchoconstriction. Airway hyper-responsiveness exacerbates symptoms, leading to wheezing, coughing, and chest tightness (Rogers, 2004). Bronchoconstriction narrows airways, while mucus hypersecretion worsens obstruction. Chronic inflammation and recurrent bronchoconstriction can cause structural changes, contributing to persistent airflow limitation. Overall, asthma pathophysiology involves a dynamic interplay of these factors, resulting in the characteristic symptoms experienced by individuals with asthma. There is currently no definitive cure, but symptom management protocols have been developed, and low mortality is now being observed in developed countries (World Health Organisation, 2020b). While in many locations, asthma is underdiagnosed, 272.7 million cases were estimated in 2017 (Ellwood *et al.*, 2017; James *et al.*, 2018).

1.1.2.3 Cystic Fibrosis

In 1938, Doctor Dorothy Hansine Andersen, an American pathologist, first described cystic fibrosis as a distinct clinical entity in the American Journal of Diseases of Children, after observing pancreatic fibrosis and cyst formation during the autopsies of malnourished children (Andersen, 1938). Cystic fibrosis (CF) is a chronic, progressive genetic condition that affects the respiratory, digestive, and reproductive systems of 1 in 2000–3000 newborns (Cystic Fibrosis Worldwide, 2020). A long term often fatal condition, CF patients have a reduced life expectancy of 48.4 years

(Marshall *et al.*, 2018). Over 150,000 people worldwide are estimated to be living with CF in 2022 (Guo *et al.*, 2022). It is caused by a mutation of the cystic fibrosis transmembrane conductance regulator (CFTR) gene, and results in an abnormally thick mucus layer along the epithelia (Wang *et al.*, 2014). The CFTR gene encodes an ATP-binding cassette transporter that functions as a ligand-gated chlorine ion channel and is tightly regulated by an intrinsically disordered protein segment distinguished by multiple consensus phosphorylation sites (Riordan *et al.*, 1989).

Abnormal functioning of CFTR results in mucus hypersecretion in narrowed airways, which causes persistent coughing, at times with phlegm, wheezing or shortness of breath. It can also lead to fatal lung infections due to the normal cleaning mechanism of mucus being compromised. This abnormally thick mucus also creates digestive issues, as nutrient uptake is limited by the thickening of mucus in the gastrointestinal system, resulting in excessive appetite but poor weight gain, and greasy bulky stools. Over a thousand different mutations of the CFTR gene have been identified (Fanen *et al.*, 2014).

1.1.2.4 Bronchiectasis

Bronchiectasis is a chronic and progressive respiratory disease characterised by an abnormal widening of the airways. Dilation of the bronchi and bronchioles disrupt mucociliary clearance of the airway, leading to an accumulation of mucus. This initial airway damage and mucus accumulation leads to chronic inflammation driven by recurrent infections, injuring the airway and leading to further structural damages and dilation. Thickening of bronchial walls exacerbates airflow limitation, and obstruction by mucus and debris further impairs gas exchange. This creates a vicious cycle of mucus accumulation, inflammation, and structural damages, perpetuating bronchiectasis and causing progressive lung deterioration and respiratory symptoms such as cough and dyspnoea. Again, symptoms such as wheezing, coughing and shortness of breath are common (Bush and Floto, 2019; Chalmers, 2018; Chalmers *et al.*, 2018).

Bronchiectasis can be caused by a wide variety of factors. Post-infectious damage resulting from prior conditions such as tuberculosis, pertussis or pneumonia

can trigger the initial airway damage; the risk can also be heightened by the presence of immunodeficiency or autoimmune disorders. Environmental factors such as air pollution have also been shown to trigger bronchiectasis (Carbajal and Teneback, 2022). Finally, genetic conditions such as cystic fibrosis or primary ciliary dyskinesia are linked to the development of bronchiectasis due to their impact on mucus production and clearance (Morillas *et al.*, 2007).

It is estimated that around 700 people per 100,000 are affected, with a mortality rate of 5 to 20% depending on age (Chalmers, 2018; Quint *et al.*, 2016).

1.1.3 The Problem of Mucus Hypersecretion

Mucus is a necessary component of the respiratory system. It acts as a trap for foreign molecules, more specifically pathogens and particles such as dust and pollen. The mucus is then moved through the airway by the cilia. Cilia are situated on the apical surface of ciliated cells and move the mucus away from the peripheral airways and towards the pharynx, where the mucus can then be coughed out or swallowed. This clearing defensive mechanism prevents pathogens from infecting the cells of pulmonary tissues. The particles trapped within the mucus are then destroyed by the digestive system. Mucus consists of a thin layer of viscous gel. Its main components include water, lipids, proteins, and mucus glycoproteins called mucins. Mucus is produced by the goblet cells and the submucosal glands through a complex production and secretion pathway (Fahy *et al.*, 2010).

Mucus hypersecretion occurs when the mucus synthesis or secretion mechanism is upregulated. This can be caused by genetic, environmental, or infectious factors. Mucus hypersecretion can lead to airway obstruction and subsequently diminished lung function. It also increases the risk of infection, as the cilia cannot clear all the mucus and foreign particles. The process of mucus production and secretion is discussed in more details in section 1.3.1, page 31.

1.2 Current Treatments for Airway Hypersecretory Diseases

1.2.1 Commonly Used Treatments for Airway Hypersecretory Diseases

Respiratory diseases are primarily treated by bronchodilators (either beta2-adrenergic receptor agonist or anticholinergic), anti-inflammatory drugs (such as corticosteroids, phosphodiesterase-4 inhibitors, or leukotriene modifiers), and mucolytic agents (such as cysteine derivatives) (Spina, 2014).

Selective beta2-adrenergic receptor agonists stimulate the binding of the receptor to epinephrine to induce smooth muscle relaxation through calcium channel interaction. This, in turn, relaxes the smooth muscle of the airway, widening bronchi and increasing airflow through the lungs (Ito *et al.*, 2002). They exist either as short- or long-acting treatments. Anticholinergics block muscarinic acetylcholine receptors, preventing acetylcholine from binding and generating an action potential at the neuromuscular junction. This inhibition stops calcium release through the cell membrane responsible for muscle contraction. As a result, the contractility of the smooth muscles decreases. Again, this leads to relaxation of the smooth muscles, widening of the bronchi and increasing airflow through the respiratory system. The main side effects of bronchodilators are results of the muscular relaxation process: muscle cramps, vasodilatation, headaches and arrhythmias are commonly observed in patients (Spina, 2014).

Glucocorticoids attenuate the immune response by inhibiting the inflammatory process, and therefore the inflammation of the lung tissue, which can help decrease mucus synthesis and secretions (Van Der Velden, 1998). Glucocorticoids bind the cytoplasmic glucocorticoid receptor, inducing a conformational change and a hyper-phosphorylation. This leads the receptor to dissociate from the multi-protein complex and translocate into the nucleus, where it regulates gene expression through the glucocorticoid receptor (Ramamoorthy and Cidlowski, 2016). The glucocorticoid receptor normally resides in the cytoplasm,

bound to a large multi-protein complex. When glucocorticoids are present, the glucocorticoid receptor is translocated to the nucleus, where it binds to glucocorticoid response elements and stimulates gene expression or is recruited to chromatin with the transcriptional activation of NF-κB (a major transcription factor for both the innate and adaptive immune response) and activator protein-1 (AP-1, a regulator of cytokine expression). While glucocorticoids have been used since the early 1950s, they cannot definitively treat AHDs, but only mitigate the symptoms (Benedek, 2011). Moreover, due to their wide range of actions and untargeted nature of the treatment, those drugs come with many side effects (see Table 1.1). Glucocorticoid-associated side effects may involve most major organ systems, and interfere with musculoskeletal, gastrointestinal, cardiovascular, endocrine, neuropsychiatric, dermatological, ocular, and immunologic processes. Proper use and careful monitoring can mitigate some of the risks and minimise side effects (Oray *et al.*, 2016). Finally, resistance to corticosteroids has been observed in severe asthma, reducing the treatment options for this condition (Hakim *et al.*, 2012).

Phosphodiesterase-4 (or PDE-4) inhibitors inhibit the activity of phosphodiesterase type-4 and subsequently the degradation of cyclic adenosine monophosphate (cAMP) to 5'adenosine monophosphate (5'-AMP). This leads to increased levels of cAMP, which results in suppression of pro-inflammatory mediator synthesis and promotes anti-inflammatory mediators, relaxing smooth muscles and inhibiting inflammation and fibrosis (Mulhall *et al.*, 2015). Leukotrienes are a group of inflammatory mediators produced in leukocytes through the oxidation of arachidonic acid (released from cell membrane phospholipids mainly by phospholipase A2) and the essential fatty acid eicosapentaenoic acid and catalysed by the enzyme arachidonate 5-lipoxygenase. Leukotrienes promote inflammation, mucus secretion, bronchoconstriction, and microvascular permeability in AHDs. 5-LO inhibitors (Zileuton) prevent the catalytic activity of arachidonate 5-lipoxygenase, preventing the synthesis of leukotrienes, while cysteinyl leukotriene receptor antagonist (such as montelukast and zafirlukast) prevent the binding of leukotrienes to CysLT1 and 2 receptors, blocking the leukotriene pathways. While corticosteroids might also impact the leukotriene pathway by inhibiting phospholipase A2 and

subsequent synthesis of eicosanoid inflammatory mediators, the more targeted action of leukotriene modifiers leads to fewer side effects and treatment resistance in patients (Montuschi and Peters-Golden, 2010; Paggiaro and Bacci, 2011; Scott and Peters-Golden, 2013).

Mucolytic agents, especially cysteine derivatives such as carbocysteine, N-acetylcysteine and N-acystelyn (lysine salt of n-acetylcysteine), have also been used to target mucus production in AHDs. Cysteine derivatives demonstrate radical scavenging activities and can counteract the decrease in antioxidant enzyme activity by activating the NF-κB signalling pathway, resulting in the transcription of inflammatory mediators such as interleukin 6 (IL-6) and tumour necrosis factor α (TNFα). Cysteine derivatives have also been shown to hydrolyse the disulphide bonds of mucus protein, which decreases mucus viscosity, as well as increases chloride secretion (Aldini *et al.*, 2018).

Several other molecules have been developed to treat AHDs. Theophylline has historically been used in the treatment of asthma and remains the primary line of defence in undeveloped countries. First introduced as a clinical treatment in 1922, theophylline is a dimethylxanthine that functions as a phosphodiesterase inhibitor, an adenosine receptor blocker, and a histone deacetylase activator. It also acts as a diuretic, smooth muscle relaxant, bronchial dilator, cardiac and central nervous system stimulant, and has been used as an oral therapy to alleviate the symptoms of asthma (Barnes, 2013; Ito *et al.*, 2002; Jenne *et al.*, 1972).

While numerous therapeutic options exist, serious and common side effects have been reported (see Table 1.1). Within the last decade, several new treatment options have been explored for AHDs in an attempt to find therapeutic options with less severe impacts on patients. For example, mucus hydration therapies have been trialled in cystic fibrosis patients, with promising results (Tildy and Rogers, 2015). Mucus hydration therapy works by increasing the water content of mucus within the airway, thus thinning the viscous layer, and facilitating its evacuation through coughing. Mucus hydration can be induced by administering hypertonic saline through inhalation, creating an osmotic gradient. It can also be achieved

pharmaceutically by targeting ion channels on epithelial cells (Bennett *et al.*, 2016). However, this treatment would not be efficient for other AHDs where no mucus dehydration is observed, such as asthma or COPD. New gene therapies are also being developed for cystic fibrosis, with the aim of re-introducing a functional CFTR gene into airway epithelial cells. Using retroviral or cationic liposome/DNA complexes, the CFTR gene is targeted. These promising techniques are not yet approved but show promising results for the treatment of cystic fibrosis (Cooney *et al.*, 2018). New small molecules have also been developed to specifically target the CFTR gene. For example, Ivacaftor is a CFTR potentiator. By binding to the defective CFTR, it restores the flow of chloride ions through the cell membrane, preventing mucus build up and progressively increasing lung function. It can be used in combination with CFTR correctors, such as lumacaftor and tezacaftor, which bind to CFTR to facilitate its translocation to the cell surface, where it can perform its function of regulating chloride ion transport. Together, these drugs can correct the effect of the G551D and F508del mutations, which impact the acting and folding domain of CFTR (respectively). Other therapeutic options, including antimicrobials, beta blockers and oxygen therapy, have been used to mitigate the symptoms and associated risks of AHDs but still do not offer a real cure for those diseases (Rosenwasser *et al.*, 2022).

Table 1.1 Side effects of the main drugs used in the treatment of AHDs classed by commonality.

As reported by the National Institute for Health and Care Excellence as part of the British National Formulary (Joint Formulary Committee, 2024).

	Common or very common	Uncommon	Rare or very rare
MAIN DRUG GROUPS			
Beta-2-adrenoceptor agonists	Arrhythmias; headache; palpitations; tremor.	Hyperglycaemia.	Bronchospasm paradoxical (sometimes severe).
Anticholinergic	Arrhythmias; constipation; cough; dizziness; dry mouth; headache; nausea.	Dysphonia; glaucoma; palpitations; skin reactions; stomatitis; urinary disorders; vision blurred.	
Corticosteroids	Anxiety; behaviour abnormal; cataract subcapsular; cognitive impairment; Cushing's syndrome; electrolyte imbalance; fatigue; fluid retention; gastrointestinal discomfort; headache; healing impaired; hirsutism; hypertension; increased risk of infection; menstrual cycle irregularities; mood altered; nausea; osteoporosis; peptic ulcer; psychotic disorder; skin reactions; sleep disorders; weight increased.	Adrenal suppression; alkalosis hypokalaemic; appetite increased; bone fractures; diabetic control impaired; eye disorders; glaucoma; haemorrhage; heart failure; hyperhidrosis; leucocytosis; myopathy; osteonecrosis; pancreatitis; papilloedema; seizure; thromboembolism; tuberculosis reactivation; vertigo; vision blurred.	Malaise; tendon rupture.
PDE-4 inhibitors	Appetite decreased; back pain; cough; depression; diarrhoea; fatigue; gastrointestinal discomfort; gastrointestinal disorders; headaches;	Gastrointestinal haemorrhage; suicidal behaviours; anxiety; asthenia; back pain; dizziness; malaise; muscle complaints; muscle weakness; palpitations; skin	Angioedema; constipation; gynaecomastia; haematochezia; respiratory tract infection; taste altered

	increased risk of infection; insomnia; nausea; vomiting; weight decreased	reactions; tremor; vertigo	
Leukotriene modifiers	Diarrhoea; fever; gastrointestinal discomfort; headache; nausea; skin reactions; upper respiratory tract infection; vomiting.	Akathisia; anxiety; arthralgia; asthenia; behaviour abnormal; depression; dizziness; drowsiness; dry mouth; haemorrhage; irritability; malaise; muscle complaints; oedema; seizure; sensation abnormal; sleep disorders.	Angioedema; concentration impaired; disorientation; eosinophilic granulomatosis with polyangiitis; erythema nodosum; hallucination; hepatic disorders; memory loss; palpitations; psychiatric disorders; pulmonary eosinophilia; speech disorder; suicidal behaviours; tremor.
N-acetylcysteine	Diarrhoea; fever; gastrointestinal discomfort; headache; hypotension; nausea; stomatitis; tinnitus; vomiting, acidosis; anaphylactoid reaction; angioedema; anxiety; arrhythmias; cardiac arrest; chest discomfort; cough; cyanosis; eye pain; eye swelling; generalised seizure; hyperhidrosis; hypertension; hypotension; joint disorders; malaise; nausea; pain facial; respiratory disorders; skin reactions; syncope; thrombocytopenia; vasodilation; vision blurred.		Haemorrhage.

OTHER NOTABLE TREATMENTS	
Theophylline	**Frequency unknown**
	Anxiety; arrhythmias; diarrhoea; dizziness; gastrointestinal discomfort; gastroesophageal reflux disease; headache; hyperuricaemia; nausea; palpitations; seizure; skin reactions; sleep disorders; tremor; urinary disorders; vomiting.

1.2.2 Biologics

The field of biologics started developing in 1982 when the Food and Drug Administration (FDA) first approved recombinant human insulin for clinical use. It encompasses a class of medications derived from living organisms, such as humans, animals, or microorganisms, through biotechnological processes. Biologics can include monoclonal antibodies, cytokines, growth factors, enzymes, and vaccines. They are designed to target specific molecules or pathways involved in diseases, offering highly targeted treatment approaches. Biologics are used to treat a wide range of conditions, including autoimmune diseases, cancer, and inflammatory disorders (Morrow and Felcone, 2004).

Recently, several biologics have been approved for the treatment of severe eosinophilic asthma and cystic fibrosis. In 2003, omalizumab was approved by the FDA for the treatment of asthma. Omalizumab is a monoclonal antibody that targets the mediator of allergic response immunoglobulin E (IgE). By binding to the antigen-specific region of IgE, omalizumab prevents its interaction with the high-affinity IgE receptors (FcεRI) on mast cells and basophils. This inhibits the release of inflammation mediators and reduces the symptoms associated with asthma, leading to improved control of symptoms and reduced frequency of exacerbations (Schulman, 2001). Following the success of omalizumab, mepolizumab and reslizumab were developed and approved (2015 and 2016, respectively). These monoclonal antibodies bind to interleukin 5 (IL-5), therefore preventing the IL-5 mediated production and maturation of eosinophils. This leads to decreased eosinophilic inflammation in the airways and lungs, alleviating the symptoms associated with eosinophilic asthma (Ridolo *et al.*, 2020). Last in date, benralizumab was approved in 2017. Similarly to mepolizumab and reslizumab, it targets the IL-5

pathway by binding the IL5 receptor α, blocking IL5 binding and inducing antibody-dependent cell-mediated cytotoxicity (ADCC), which further reduces eosinophil levels by triggering the destruction of eosinophils by natural killer cells (Pelaia *et al.*, 2018).

These examples highlight the relevance of biologics in the treatment of AHDs. They also offer the advantage of low production costs, and a lower number of reported side effects (see Table 1.2). While the lower amount of reported side effects could be due to the more recent launch of these drugs, the more targeted mechanism of action of biologics often results is a lower overall impact due to their specificity, reduced systemic exposure or enhanced therapeutic index.

Table 1.2 Reported side effects of newly approved biologics for the treatment of asthma. *As reported by the National Institute for Health and Care Excellence as part of the British National Formulary (Joint Formulary Committee, 2024).*

Drug	Common or very common	Uncommon	Rare, very rare or frequency not known
Benralizumab	**Fever; headache; hypersensitivity (may be delayed); increased risk of infection; skin reactions**		**Anaphylactic reaction**
Mepolizumab	**Abdominal pain upper; administration-related reaction; back pain; eczema; fever; headache; hypersensitivity; increased risk of infection; nasal congestion**		
Omalizumab	**Headache; skin reactions**	**Cough; diarrhoea; dizziness; drowsiness; dyspepsia; fatigue; flushing; increased risk of infection; influenza-like illness; limb swelling; nausea; paraesthesia; photosensitivity reaction; postural hypotension; respiratory disorders; syncope; weight increased**	**Angioedema; hypersensitivity; systemic lupus erythematosus (SLE), alopecia; eosinophilic granulomatosis with polyangiitis; immune thrombocytopenic purpura; joint disorders; lymphadenopathy; myalgia**
Reslizumab		**Anaphylactic reaction; myalgia**	**Secondary malignancy**

1.2.3 Technologies

In recent years, new mechanisms for cell targeting and the delivery of biological compounds to specific cell types have been developed. Those new tools allow for the development of several new treatments and diagnostic tools. Here,

nanobodies and bioconjugates are presented and explored as new tools in biomedical science.

1.2.3.1 Nanobodies

1.2.3.1.1 The Origins of Immunotherapy

Immunoglobulins, colloquially referred to as antibodies, are large protein molecules that bind to a small molecule or specific region of a macromolecule (called an epitope or antigenic determinants) with very high specificity. Antibodies contribute to immunity through neutralisation, where they bind to antigens, preventing them from binding cellular receptors; the triggering of complement activation, where antibodies recruit complement components to induce cell lysis; and opsonisation, where antibodies facilitate phagocytosis of the pathogen.

Antibodies are composed of four polypeptide chains organised in a Y-shaped structure (see Figure 1.3). The fragment antigen binding (F_{ab}) region encompasses both the light and heavy chain above the antibody hinge and is composed of conserved and variable domains. The F_{ab} region is responsible for antigen binding variability, which greatly varies amongst different immunoglobulins. The heavy chain part of the F_{ab} is composed of a conserved (C_H) and variable (V_H) domain. The light chains also contain a conserved (C_L) and a variable (V_L) domain. The fragment crystallisable (F_c) region encompasses the bottom part of the two longer heavy (H) chains of immunoglobulins, below the hinge, and provide stability to the molecule through multiple conserved (C_H) domains. They encode either a C-terminal hydrophobic transmembrane region for membrane-bound antibodies, which are anchored on the surface of B lymphocytes and combine with other membrane proteins to trigger B lymphocytes proliferation, differentiation and immunoglobulin production, or a hydrophilic tail for secreted antibodies. The conserved domain anchors the light chain to the heavy chain by disulphide bonds, while the variable domain is responsible for antigen binding (Vidarsson *et al.*, 2014).

Human antibodies are classified into five main isotypes: IgG, IgA, IgM, IgD, and IgE, each defined by the structure of their heavy chains (γ, α, μ, δ, and ε, respectively). Each isotypes plays a different function in immune responses. IgG has a monomeric

structure and is primarily found in serum. IgG is further subdivided into four subclasses (IgG1, IgG2, IgG3, and IgG4) based on variations in the C_H domains. IgG covers a number of functions, including pathogens and toxins neutralisation, opsonisation of microbes and activation of the complement system (IgG1 and IgG3). Therapeutic monoclonal antibodies are primarily produced using the IgG scaffold due to its stability, long serum half-life, and ease of production (Castelli *et al.*, 2019; Ryman and Meibohm, 2017). IgA is primarily found in mucosal tissues (where it presents as a dimer and has the ability to resist to proteases in secretions) and acts as a first line of defence by preventing microbial adhesion and invasion. IgM is primarily found in serum and is the first type of antibody produced in a primary immune response and a strong activator of the classical complement pathway. Its pentameric forms makes it particularly efficient at agglutination, contributing to pathogen immobilisation and enhancing phagocytosis. IgM has been investigated as a scaffold for therapeutic antibodies due to its high avidity and potential for rapid pathogen neutralization but poses challenges in recombinant expression systems (Keyt *et al.*, 2020). IgD is a monomeric immunoglobulin found on the surface of immature and naïve B cells and primarily functions as a receptor, triggering cell activation and transition to IgM or IgG producing cells. Finally, IgE plays a key role in mediating allergic reactions by triggering the degranulation of mast cells and basophils upon allergen binding, releasing mediators such as histamine (Sun *et al.*, 2020).

While differences in heavy chains results in difference isotypes, immunoglobulins can also possess either kappa (κ) or lambda (λ) light chains, both of which contribute to antigen binding specificity. During B cell development, the κ genes attempt rearrangement, if the recombination of the fragments fails, the cell initiates λ chain gene rearrangement, leading to only one type of light chain being expressed in any given B cell. In the human B cell repertoire, the kappa-to-lambda ratio is approximately 2 to 1 in healthy individuals (Abe *et al.*, 2001; Heilmann and Barington, 1989). The kappa-to-lambda ratio can be used to diagnose B-cell disorders such as myeloma or light chain amyloidosis. No major biophysical differences can be observed between λ and κ antibodies, with both displaying similar levels of antigen

binding. κ antibodies are generally considered more developable than λ antibodies, with lower risks of aggregation, but both κ and λ light chains have been successfully employed in FDA-approved monoclonal antibodies, such as adalimumab (IgG1-κ) and trastuzumab (IgG1-λ) (Boekhout *et al.*, 2011; Raybould *et al.*, 2024; Scheinfeld, 2003).

The development of the hybridoma technology by the fusion of B cells and myeloma cells in 1975, allowing for the mass production of targeted monoclonal antibodies, accelerated the development and use of therapeutic antibodies (Köhler and Milstein, 1975). Antibodies can be used to elicit immunogenicity in patients, disturb the normal function of their target cell, evoke antibody-dependent cellular cytotoxicity (ADCC) and complement mediated cytotoxicity (CMC), and regulate the immune response. They possess multiple applications as diagnostic tools, and can, for example, be engineered to detect tumours through molecular imaging (Mishani and Hagooly, 2009; Zhao *et al.*, 2008). Antibodies can also be engineered to carry various loads, the resulting molecule being termed an Antibody Drug Conjugate (ADC), such as cytotoxic drugs, nanomedicines or other nanoparticles (Fay and Scott, 2011). Their applications are diverse, from fighting infectious diseases to cancers, to vaccines, or to help regulate autoimmune diseases (Alley *et al.*, 2010). But if antibodies are versatile, they are also big molecules (150 kDa and above). Their large size can lead to suboptimal dispersal and limited tissue penetration, which can diminish their efficacy (Minchinton and Tannock, 2006). They also require significant engineering to improve stability and reduce micro-heterogeneity to produce defined products. Unstable or poorly engineered antibodies lead to reduce target binding, hindering their efficacy. To remedy this, novel types of modified antibodies have been developed.

The binding capacity of antibodies is contained within the light and heavy variable domains of the molecule (V_L & V_H) present on the tip of the antigen binding fragment (F_{ab}). Therefore, antibody fragments have been developed using only this F_{ab} binding motif. This also allowed for the development of bispecific antibodies ($F_{ab}2$) by conjugating two F_{ab} together (Nisonoff and Rivers, 1961). In 1994, minibodies were developed. Minibodies are composed of one light and one heavy variable domain (V_L and V_H), linked via CH3 domains, which are both attached through

heterodimerization to a conserved light and heavy chain (respectively) linked by disulphide bonds. Minibodies are smaller but conserve the bivalency of full-size antibodies and the concomitant avidity effect. Despite successful isolation, low expression, and poor solubility remained challenging.

Synthetic scaffolds have also been developed. Non-immunoglobulin protein fragments of around 100 amino acids have been developed based on the scaffold of naturally occurring proteins and can be engineered to target specific epitopes. Their sequence can be altered to adjust their specificity and affinity to the target. Those synthetic scaffolds can then present the same targeting properties as immunoglobulin-based antibodies, while being more customisable and applicable to a wider range of uses. For example, affibodies, developed in 1997, utilise a three-helical subdomain of a natural receptor as a scaffold for the development of target-binding molecules (Nord *et al.*, 1997). By creating a library of affibodies with random amino acid sequences for two of the three helices and then isolating binding molecules using a variety of display methods, specific affibodies can be isolated. The binding molecule can then be engineered to fit specific requirements (Beck *et al.*, 2010; Goulet and Atkins, 2020; Richards, 2018).

Heavy-chain only antibodies were discovered in the camel (*Camelus dromedarius*) in 1993 (Hamers-Casterman *et al.*, 1993), followed closely by the discovery of similar structures in nurse sharks (*Ginglymostoma cirratum*) (Greenberg *et al.*, 1995). In camelids, the absence of light chains led to the V region being termed V_HH. Whereas the homodimeric heavy-chain complex, which also naturally lacks light chains, was discovered in the serum of the nurse shark and named immunoglobulin isotype novel antigen receptor (IgNAR). Camelid and shark antibodies can be isolated, like other species antibodies, by hyper-immunisation of animals, and affinity purification.

Those heavy-chain only antibodies possess a unique paratope architecture composed of single variable heavy domains involved in antigen recognition, and a heavy chain conserved domain, with no light chain. The molecules, however, do still form as dimers of the same heavy chain protein. Consequently, the variable domain

can easily be isolated and engineered, creating a molecule termed a nanobody, composed of only one variable heavy chain domain (V_HH), conserving all targeting properties of full-length antibodies with a much smaller size (generally below 15 kDa, compared to up to 160 kDa for full-size IgG antibodies). Nanobodies are monomeric and show no tendency to aggregate, with a favourable solubility: normally, residues that form the interaction with the light chain in the V region are highly hydrophobic, but in heavy chain only antibodies, these residues are substituted for more hydrophilic amino acids, since the region is solvent exposed (Desmyter *et al.*, 1996; Muyldermans *et al.*, 1994). These properties mean that they can diffuse into tissues relatively easily compared to full-size antibodies. While the physical size of nanobodies can vary depending on factors such as the amino acid sequence, post-translational modifications, and specific structural features, they usually have a diameter of around 2.5 nm and a height of around 4 nm, which means they can penetrate cell membranes if required (Revets *et al.*, 2005). Their small size also means nanobodies fall below the renal threshold and can therefore be easily cleared by the kidneys. They can possess high affinity, selectivity, and specificity. Moreover, they present with low toxicity and low immunogenicity, meaning they can bind with their target without eliciting an immune response (Tanha *et al.*, 2002). This is due to their lack of conserved domains, which are involved in complement activation. The ability of nanobodies to bind to specific target without triggering the immune cascade allows for a wider range of applications, they can for example be used for imaging, or in immunocompromised patients. They were also shown to be robust molecules, relatively resistant to high temperatures, and show an ability to refold (Dumoulin *et al.*, 2009). They possess a longer Complementarity-Determining Region 3 (CDR3) than humans and mice, and non-canonical cysteine-cysteine disulphide bonds between CDR1 and CDR3 that have evolved to stabilise the biophysical properties of the domain (Mendoza *et al.*, 2020; Muyldermans *et al.*, 1994). These unique features enable the isolation of antigen-binding fragments with high affinity in the nanomolar range, which are also stable at elevated temperatures like 37° C (Arbabi Ghahroudi *et al.*, 1997). Similar to minibodies, nanobodies can be produced in a multivalent format to regain bivalency if needed. Other multivalent formats have also been explored successfully. For example, the company Ablynx developed a trimeric

Nanobody that binds the antigenic site II of human respiratory syncytial virus F protein with subnanomolar affinity (Detalle *et al.*, 2016; Steeland *et al.*, 2016).

Different variations of nanobodies have also been developed to facilitate intracellular activity. Intrabodies, for example, are nanobodies intracellularly expressed and bind directly to intracellular proteins (Kontermann, 2004). Transbodies are fused to cell-penetrating moieties and are therefore capable of crossing the cell membrane, and have, for example, been used to treat human lung adenocarcinoma by using cell-penetrating nanobodies to bind the EGFR tyrosine kinase domain in order to inhibit intracellular signaling and supress the growth and migration of EGFR-overexpressing cancer cells (Tabtimmai *et al.*, 2019). Finally, advancements in phage display technology allowed for easy construction and screening of scF_v (single-chain F_v) and dsF_v (dual-specificity F_v) antibody fragments libraries (Hoogenboom *et al.*, 1998; Winter *et al.*, 1994).

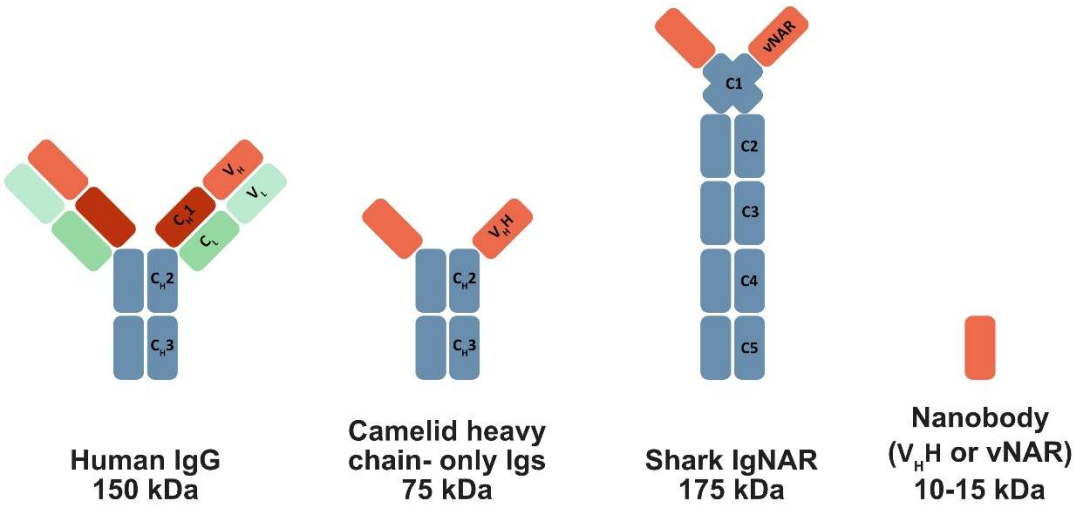


Figure 1.3 Compared structures of human, camelids, and shark antibodies, alongside a single domain nanobody.

The F_c region is shown in blue. The F_{ab} region is shown either in orange (heavy chain) or green (light chain). Figure created using Affinity Designer 2.6.2 (available at affinity.serif.com).

1.2.3.1.2 Limitations of Nanobodies

If nanobodies present a wide range of interesting characteristics, they also present some inconveniences. If their small size guarantees good diffusion and cell

penetration, it also means that nanobodies are very quickly cleared through kidney glomerular filtration. This is advantageous for nanobodies used in in-vivo imaging but is a problem for therapeutic approaches and, more specifically, cell targeting and penetration (Gainkam *et al.*, 2008). This can be addressed by creating multivalent nanobodies, which include a nanobody cross-reacting with serum albumin, which has a half-life of 19 days (Roovers *et al.*, 2011; Tijink *et al.*, 2008). PEGylation can also be used to improve the penetration of nanobodies across biological barriers and has been successfully used to facilitate the accumulation of anticancer drugs in Epidermal Growth Factor Receptor (EGFR)-positive tumour cells (Wu *et al.*, 2018).

Another issue of nanobodies is that they are incapable of triggering antibody-dependent cellular cytotoxicity and complement-dependent cytotoxicity. In canonical full-length antibodies, the F_c region is responsible for those events. As nanobodies do not include this F_c region, they cannot trigger those events. Including the F_c region into the design of nanobodies could fix this issue, and allow, for example, tumour eradication by the activation of cell lysis. However, the small size advantages of nanobodies would be lost, as well as their low immunogenicity (Bell *et al.*, 2010; Richard *et al.*, 2013).

1.2.3.1.3 Applications

Nanobodies have already been applied to various diseases. Firstly, nanobodies are being extensively researched and used in cancer treatment, as a new form of immunotherapy (Roovers *et al.*, 2011). More specifically, the targeting of EGFR with nanobodies has been extensively researched and successfully used in *in vivo* labelling and tumour growth inhibition (Gainkam *et al.*, 2008; Huang *et al.*, 2008; Mishani and Hagooly, 2009; Schmitz *et al.*, 2013). Nanobodies have also been used in infectious diseases, for example in the treatment of Rotavirus-Induced Diarrhoea (Pant *et al.*, 2006; van der Vaart *et al.*, 2006). Lactobodies, or nanobodies produced by genetically engineered probiotic *Lactobacilli*, were developed for this purpose. They can also be used as prophylactics or therapeutics. A large number of nanobodies are currently being developed and tested for a wide range of conditions, from

influenza viruses to parasitic infections, all the way from cancers to autoimmune disorders .

1.2.3.1.4 Nanobody Libraries

One main advantage of nanobodies is that they can easily be selected and produced from synthetic libraries. This removes the need for *in vivo* production, and allows for fast, easy and cheap production of specific nanobodies (Harmsen and De Haard, 2007). Various molecular display platforms have been developed for efficient screening of peptide or protein libraries. Yeast display systems utilise *Saccharomyces cerevisiae* to present recombinant proteins on the cell surface, offering advantages of fast growth and relatively large library sizes, although lower throughput due to lower transformation efficiency (Benatuil *et al.*, 2010; Rosowski *et al.*, 2018). Mammalian cell systems are suitable for producing full-length immunoglobulin molecules with proper folding and post-translational modifications, despite limitations in throughput and speed (Parthiban *et al.*, 2019; Waldmeier *et al.*, 2016). Bacterial cell display offers fast and inexpensive culture conditions but lacks endoplasmic reticulum-specific processing, potentially affecting nanobody folding and activity (Bessette *et al.*, 2004). Ribosome display systems enable high diversity and affinity through a cell-free process without transformation limitations (Lipovsek and Plückthun, 2004; Plückthun, 2012). Phage display, the most extensively employed platform, involves genetic fusion of proteins to bacteriophage coat proteins, allowing selection of specific binders via simple biopanning methods but may face challenges in elution and binder loss during selection (Schwimmer *et al.*, 2013; Tiller *et al.*, 2013). Phage display is discussed in more detail in section 2.1.2 (page 41).

1.2.3.2 Bioconjugation and Bioconjugates

Bioconjugation is a technique that attaches two molecules together, usually through a covalent bond, to create a complex consisting of both molecules linked together (Hermanson, 2013). The resulting complex possesses the combined properties of its individual components.

The idea of bioconjugates can be linked to Paul Ehrlich's concept of the 'magic bullet', a targeted therapeutic agent. He envisioned compounds that could selectively target pathogens without harming the host, laying the groundwork for the idea of conjugating drugs to targeting moieties (Ehrlich, 1910; Zipfel and Skerka, 2022).

1.2.3.2.1 Bioconjugation Techniques

Several techniques of bioconjugation have been developed and are routinely used. The most common is amide coupling. Amide coupling can be used on a wide range of proteins or peptide molecules, as well as other types of macromolecules. Two types of reactions result in amide coupling: acylation or alkylation, creating either stable amide or secondary amid bonds between the two molecules. A very common type of amide coupling is N-hydroxy-succinimide (NHS) ester coupling (see Figure 1.4, A). This acylation reaction was first introduced in 1975 and is now extensively used in the production of amine-reactive crosslinking or modification reagents (Bragg and Hou, 1975).

The second most common type of crosslinking reaction are thiol reactions. This links a sulphydryl containing molecules to an amine-reactive group, either by alkylation or disulphide interchange, to create thioether or disulphide bonds. A common example of thiol bioconjugation are maleic acid imides, or maleimides, reactions (see Figure 1.4, B). Maleimides undergo an alkylation reaction with sulphydryl groups to form stable thioether bonds (Smyth *et al.*, 1964).

More recently, copper catalysed azide-alkyne cycloaddition (CuAAC, or 'click chemistry') methodologies have been developed and awarded the Nobel Prize in Chemistry in 2022 (Rostovtsev *et al.*, 2002; Tornøe *et al.*, 2002). In CuAAC, the copper catalyst first activates and binds the alkyne, forming a copper-acetylide intermediate (see Figure 1.4, C). The azide then attacks the copper-activated alkyne, leading to the formation of a triazole ring, resulting in a 1,4-disubstituted 1, 2, 3-triazole.

Other types of bioconjugation reactions include those involving carboxylate, hydroxyl, aldehydes and ketones, active hydrogen, photochemical and cycloaddition reactions. Different types of bioconjugates will be more suited to certain types of

bioconjugation reactions. The first successful cancer drug developed using bioconjugation was Adcetris (brentuximab vedotin). Adcetris is an antibody-drug conjugate (ADC) that consists of the cAC10 anti-CD30 monoclonal antibody (brentuximab) linked by a maleimide reaction to a highly potent antimicrotubule agent called monomethyl auristatin E (MMAE). The antibody targets the CD30 protein, which is expressed on the surface of certain cancer cells, including Hodgkin lymphoma and systemic anaplastic large cell lymphoma. Upon binding, the ADC is internalised, and MMAE is released inside the cells, where it disrupts the microtubule network, leading to cell cycle arrest and apoptosis (Van De Donk and Dhimolea, 2012). For nanobodies, various methods have been explored. Labelling at solvent-exposed lysine residues by NHS ester has been used to attach fluorophores to nanobodies (Ries *et al.*, 2012). Maleimides functional groups have also been used to label cysteine residues of nanobodies (Kim *et al.*, 2008; Massa *et al.*, 2014).

Finally, chemoenzymatic labelling has also been used. Sortase A conjugation allows for the site-specific labelling of nanobodies (see Figure 1.4, D). Sortase A is a transpeptidase enzyme derived from *Staphylococcus aureus* and can covalently attach various molecules to a protein of interest by targeting a specific amino acid sequence. Sortase A labelling is particularly relevant to the functionalisation of antibodies and antibody fragment, as labelling is confined to the C-terminus, preventing unwanted interactions between the tag and the CDRs (David Row *et al.*, 2015; Guimaraes *et al.*, 2013; Massa *et al.*, 2016; Rashidian *et al.*, 2016).

The mechanisms of the main bioconjugation techniques can be seen in Figure 1.4.

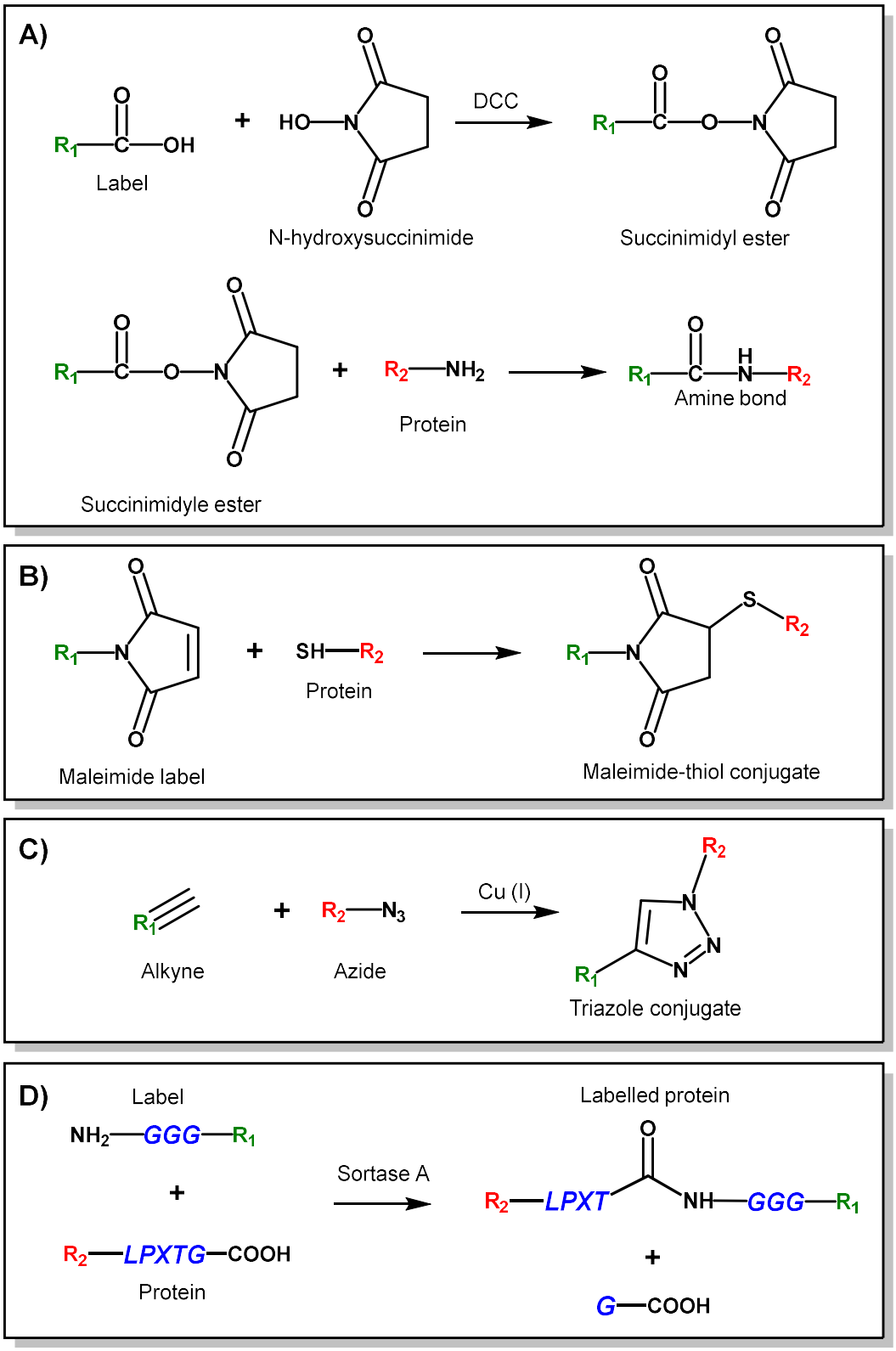


Figure 1.4 Mechanisms of various bioconjugation methods.

A) N-hydroxy-succinimide (NHS) ester coupling; B) Maleimides, reactions; C) Click chemistry D) Sortase A conjugation, amino acids are shown in blue. Figure created using ChemDraw 23.1.2 (available at revvitysignals.co).

1.2.3.2.2 Bioconjugates and Chemical Functionalisation of Nanobodies

The definition of bioconjugates encapsulates every functional molecule bound to a biologic. Therefore, theoretically, any molecule could be used as a bioconjugate. However, a certain number of molecules have been developed specifically for the functionalisation of antibodies or nanobodies. Those can be categorised into two groups.

Firstly, bioconjugates consisting of directly active compounds such as enzymes, toxins, fluorescent proteins, markers, or photosensitisers (molecules that trigger the production of reactive oxygen species when exposed to light at a specific wavelength, thus resulting in the destruction of the targeted cell). Chromobodies, for example, are nanobodies conjugated to fluorescent protein, such as Green Fluorescent Protein (GFP) or Red Fluorescent Protein (RFP) and have been used in cellular imaging (de Beer and Giepmans, 2020). Immunocytokines are composed of nanobodies bound to nontoxic cytokines and are used to activate the cytokine cascade (Lode *et al.*, 1998). Finally, photoimmunotherapy uses nanobodies bound to photosensitisers to induce cell death in tumours (Mohiuddin *et al.*, 2023).

Secondly, bioconjugates can also consist of vesicles that act as vessels for the active compound. Bionanocapsules were developed using the scaffold of the hepatitis B virus (Higuchi *et al.*, 1997). Micelles, monolayer aggregates of surfactant molecules, allow for the delivery of hydrophobic compounds to the site of interest. Spherical protein shells containing gas, known as microbubbles or nanobubbles, depending on size, have been used as contrast agents for ultrasound imaging.

One of those vessels is the liposome, they were first described in 1964 by Dr Alec D. Bangham. They consist of a microscopic spherical membrane-enclosed vesicle or sac (20–30 nm in diameter), with a lipid bilayer structure. A hydrophobic head group made of phosphate and other organic molecules is attached to a glycerol backbone and a hydrophobic tail made of fatty acids. Their properties, such as size, charge, lamellarity and membrane fluidity, can be easily altered to fit a wide range of applications. Six types of naturally occurring phospholipids (phosphatidylcholine, phosphatidylethanolamine, phosphatidylserine, phosphatidylinositol,

phosphatidylglycerol, and phosphatidic acid) can be used to form liposomes, but synthetic phospholipids can also be engineered (Grimaldi *et al.*, 2016). Lipid composition can affect the stability of the liposome and other physiochemical properties. For example, archaeal lipids can be used for increased immunogenicity. Thanks to their hydrophilic core, liposomes can be used to carry extra molecules, such as hydrophilic drugs, DNA or RNA for gene therapy. On the other hand, hydrophobic molecules can be inserted in the membrane leaflet. And finally, targeting molecules such as peptides, antibodies and nanobodies can easily be bound to the surface for site-directed application. Liposomes have been engineered and used to treat a variety of conditions in a variety of form (Daraee *et al.*, 2016). Various vaccines for both viral and bacterial diseases have been developed using liposomes (Drulis-Kawa and Dorotkiewicz-Jach, 2010; Gould-Fogerite *et al.*, 1998; Kende *et al.*, 1985; Wong *et al.*, 2003). A notable example is the used of the liposome technology in the formulation of the Pfizer/BioNTech SARS-Cov-2 vaccine. Most importantly, liposomes have been extensively researched and used in relation to cancer, for both detection of cancerous cells and for the development of new treatments (Olusanya *et al.*, 2018; Park, 2002).

1.3 A Nanobody-Conjugate Platform for the Treatment of Airway Hypersecretory Diseases

As previously stated, nanobody-conjugate platforms have already been developed and used to treat a variety of conditions. But no such platform has been developed for the treatment of AHDs. This gap in research could be explained by the lack of exposure received by AHDs, despite their high incidence.

1.3.1 Targeting the Mucin Pathway

The mucus production and secretion pathways are complex multi-step processes regulated by a large number of proteins. Twenty different mucin genes (MUC) have been identified. Those can be divided between secreted and membrane-tethered mucins. MUC5AC and MUC5B are two major secreted gel-forming mucins in the respiratory tract. They exist as overlapping sequences on chromosome 11 in the region p15.5 and are crucial for maintaining the viscoelastic properties of mucus, and this is reflected in their structure. Starting at the N-terminal, each protein encodes specific D domains, followed by alternating cysteine-rich and PTS (proline/threonine/serine) domains. A central multi-domain structure containing O-glycosylated variable numbers of tandem repeats intercalated with unique sequences and cysteine-rich domains. O-glycosylation initiates within the Golgi apparatus, where an enzyme called N-acetyl galactosaminyl peptidyl transferase attaches N-acetyl galactosamine to serine or threonine residues on the mucin polypeptide chain. Subsequently, specific glycosyltransferases catalyse the stepwise addition of additional glycan components, including galactose, N-acetylglucosamine, fucose, and sialic acid, resulting in the formation of the complete glycan side chain. At the C-terminal, domains D, B, C and CK conclude the structure (Figure 1.5) (Lillehoj *et al.*, 2013; Moniaux, 2001). These unique domains confer mucins their gel-forming properties: the formation of disulphide bonds between the structures creates long linear polymers, creating a viscous mucus layer in the airway.

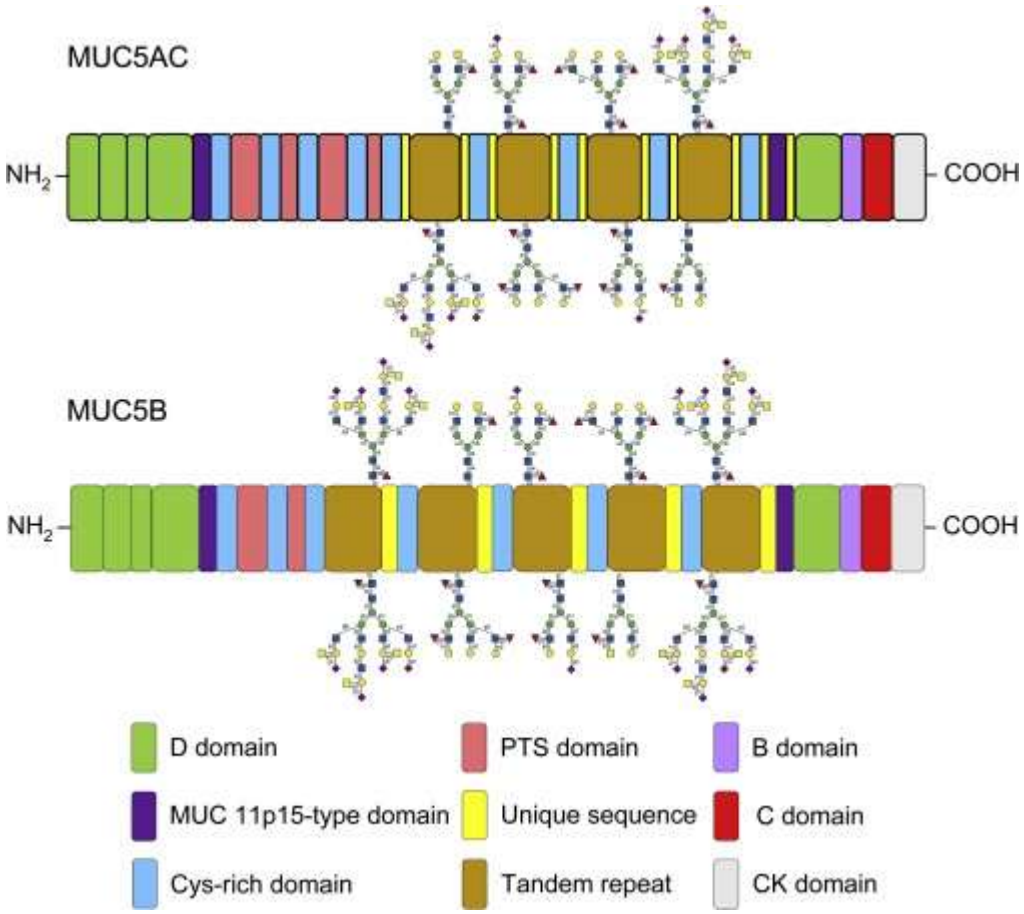


Figure 1.5 Schematic structures of proteins MUC5AC and MUC5B domains and glycan side chains.

D domains flank the N terminus of MUC5AC and MUC5B, preceding the MUC 11p15 type domain. Subsequently, repeated PTS and cysteine rich domains precede tandem repeats of O-glycosylated elements, intercalated with unique sequences and cysteine-rich domains. At the C-terminus, the mucin specific domains MUC 11p15, D B, C and CK conclude the protein. Reproduced with permission from Lillehoj et al. (2013) Elsevier. © 2013. Licensed for use in this thesis through the Copyright Clearance Center.

The mucin pathway can be divided into two distinct processes: mucin expression and mucin secretion (depicted in Figure 1.6).

The expression of mucin genes MUC5AC and MUC5B is regulated at the transcriptional level by various transcription factors and signalling pathways. Most notably, cytokines such as IL-4 and IL-13 can trigger the JAK/STAT (Janus kinase (JAK)-signal transducer and activator of transcription (STAT)) pathway, which triggers the transcription factor SPDEF (SAM Pointed Domain Containing ETS Transcription

Factor) and blocks FOXA2 (Forkhead box protein A2), leading to MUC5AC gene expression as a response to exposure to pulmonary allergens (Krishn *et al.*, 2018; Turner and Jones, 2009). Toll-like receptor 4 (TLR4) activation by bacterial lipopolysaccharide (LPS) leads to NF-κB (Nuclear Factor κB) activation, which in turn triggers the expression of mucin genes as a response to infection (Chen *et al.*, 2009). Nearby cell signalling can also lead to mucin gene expression: Epidermal Growth Factor (EGFR) ligands bind to EGFR, resulting in EGFR tyrosine phosphorylation, which induces the Ras–Raf–MEK1/2–ERK1/2-Sp1 pathway, leading to MUC5AC and MUC5B transcription (Nadel, 2001).

Following mucin gene expression, the peptide backbone of mucins is synthesised in the ribosomes attached to the rough endoplasmic reticulum (RER) and secreted into the RER lumen. These apomucins then undergo post-translational modifications leading to the formation of the glycan side chains described above. Mucins then travel to the Golgi apparatus, where they are packaged into carrier vesicles. Those mucin granules are transported towards the plasma membrane through cytoskeletal interactions regulated by Myristoylated Alanine-Rich C-Kinase Substrate (MARCKS) protein (Adler *et al.*, 2013). There, they become tethered to the membrane by Rab and Munc13 proteins, and undergo exocytosis mediated by the Synaptosomal-Associated Protein Receptors (SNARE) and Vesicle-Associated Membrane Protein (VAMP) proteins (Jaramillo *et al.*, 2018).

Finally, mucus production can also be triggered by increased goblet cell differentiation, as an increased proportion of goblet cells within the airway epithelium results in increased mucus in the airway. The Wnt/β-catenin signal transduction pathway was shown to play a critical role in the differentiation of the respiratory epithelium (Mucenski *et al.*, 2005). The Notch pathway was implicated in the silencing of ciliated cell differentiation, leading the cells to further expand and further differentiate into secretory phenotypes (Guseh *et al.*, 2009; Tsao *et al.*, 2009). As well as triggering mucin gene expression, IL-13 activation of signal transducer and activator of transcription 6 (STAT6) also triggers the p38 mitogen-activated protein kinase (p38-MAPK) and extracellular signal-regulated kinase (ERK), leading to goblet

cell metaplasia (Fujisawa *et al.*, 2008). Similarly, the EGFR pathway has also been implicated in goblet cells metaplasia (Nadel, 2001).

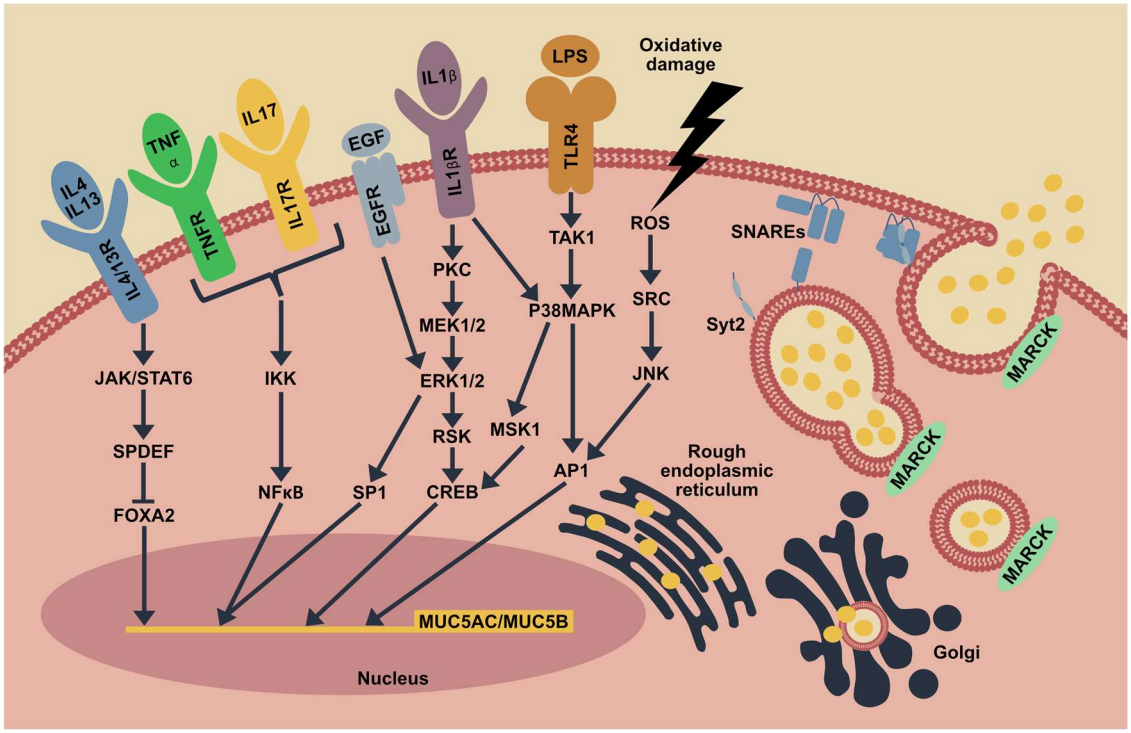


Figure 1.6 Schematic representation illustrating the regulatory mechanisms governing the expression and secretion of mucins MUC5AC and MUC5B in the lungs.

Upon stimulation by diverse signalling pathways, gene expression of MUC5AC and MUC5B is initiated. The transcribed mRNA molecules traverse to the endoplasmic reticulum, where they undergo translation to synthesise apomucins. Subsequently, these apomucins are processed and glycosylated within the ER and Golgi apparatus. The mature mucins are then encapsulated into secretory vesicles within the Golgi network. Finally, these vesicles fuse with the cell membrane, enabling the release of mucins into the airway lumen. This depiction elucidates the sequential events underlying the finely orchestrated process of mucin synthesis and secretion in the respiratory epithelium. Figure created using Affinity Designer 2.6.2 (available at affinity.serif.com).

In asthma, COPD, CF and bronchiectasis, mucus hypersecretion is a major issue. But no currently available treatment currently focuses on this specific aspect

of the conditions. Several inhibitors have been isolated, which focus on either mucin synthesis within the goblet cells and submucosal glands, or on mucin secretion into the airway. As of April 2020, the company Biomarck Pharmaceuticals has reached clinical trial phase 2A with their compound BIO-11006. This peptide inhibits the phosphorylation of the MARCKS protein, which blocks mucin secretion into the airway. More compounds are in the developmental stages or in clinical trial phase 1, but none has reached the market as of time of this thesis (Table 1.3). The main inconvenience of inhibitor-only compounds is the number of side effects they could generate. Moreover, the limited size of molecules means a fast clearance rate through glomerular filtration and therefore increases the dosage and the overall cost of treatments: this is an important issue when looking at long-term conditions such as AHDs. Using some of these inhibitors but combining them with nanobodies for a targeted approach could solve these problems. Nanobody-conjugate platforms could allow for site-directed drug delivery, longer *in vivo* half-life, and reduced treatment costs. As of now, nanobody-conjugate platforms have not been applied to AHDs.

Table 1.3 Potential targets and inhibitors of mucus synthesis and secretion as described by Ha and Rogers (2016).

Reproduced with permission from Ha and Rogers (2016) Elsevier. © 2016. Licensed for use in this thesis through the Copyright Clearance Center.

	Targets	**Inhibitor(s)**
Mucin synthesis	CCR3	Anti-CCR3 monoclonal antibodies
	EGFR tyrosine kinase	BIBW 2948, BIBX1382, BIBX1522, cetuximab, gefitinib
	GABA-A receptors	$GABA_A$ receptor antagonists
	hCLCA1	Niflumic acid
	HIF-1	YC-1
	Hyperplasia (goblet cells)	Ellagic acid, statins
	MUC5AC expression	Macrolides, statins
Mucin secretion	HSP-70	MAL3-101
	MARCKS	Bio-11006, MANS peptide
	Munc proteins	Munc-18 inhibitors
	P2Y2 receptors	P2Y2 receptor agonists (mucus hydration) and antagonists
	SNARE proteins	Modified bacterial neurotoxins of Clostridium botulinum

1.3.2 Platform Mechanism

This thesis proposes a new platform to include a nanobody specific to extra- or intracellular targets of goblet cells. As the compound is administered, it will travel through the body and only bind with those specific targets. The conjugate portion of the platform, be it the inhibitor itself or an inhibitor-containing vessel, will then be able to interact with its target. In the case of an extracellular nanobody target, a vessel presenting a phospholipid bilayer envelope would be able to fuse with the cell and release the inhibitor intracellularly. The inhibitor will then be able to bind to its intracellular target and inactivate one or multiple mucus-related mechanisms. In the case of an intracellular nanobody target, then a smaller compound would be needed to penetrate the cellular envelope and reach the intracellular target directly, where the inhibitor will be able to take effect. Various routes of administration could be considered. In the past, nanobody-conjugates have been administered orally, intravenously or directly into airways via inhalation (Detalle *et al.*, 2016; Tokuhara *et al.*, 2013).

Several advantages of such a platform in the treatment of mucus hypersecretion in AHDS can be cited. Firstly, a targeted approach, achieved through the isolation of nanobodies specific to cell types or receptors of the lung epithelium, helps maximise delivery efficiency, all while limiting side effects, and notably on the digestive system, which is often impacted by the current treatment protocols of AHDs. The dose required would also be lowered, and thus treatment impact of the patient's quality of life, and costs would be reduced. Secondly, the small size of nanobody-conjugates limits the amount of bio-disruption and increases cell penetration, which would be ideal for intracellular approach. This also means that the complex could easily be cleared through glomerular filtration, increasing, or decreasing the size of the compound would allow for a tailored *in vivo* half-life.

1.4 Conclusion

In conclusion, AHDs are highly prevalent diseases with a high impact on patients' quality of life. New discoveries in biotechnology have revealed a range of technologies that could be suited for the treatment of such conditions. A nanobody-conjugate platform could target elements of the mucin pathway and deliver a specific mucus synthesis or mucus secretion inhibitor, therefore reducing mucus secretion, which is a major pathophysiology in AHDs. Such platform could come at a lower cost for patients and the healthcare system, be easily administered by a variety of routes, and target specifically goblet cells to limit side effects. This could lead to an improvement in patients' quality of life.

1.5 Aims and Objectives

This PhD consists of three objectives, reflected in the three chapters. Firstly, the generation of a diverse nanobody library based on the IgNAR scaffold. Secondly, the isolation of goblet cells as targets for nanobody enrichment, and the biopanning of the phage-displayed nanobody library. Finally, the functionalisation of goblet cell-specific nanobodies with a fluorescent label, using a specific Sortase A-catalysed methodology. The overall aim of this thesis is to present a targeted drug delivery platform utilising goblet cell-specific nanobodies to deliver therapeutic molecules to the site of mucus secretion.

Chapter 2 Constructing a Semi-Synthetic Nanobody Library

2.1 Introduction

This introduction will cover the characteristics and structure of the nanobody scaffold in the wild, the various molecular display platforms available for the construction of nanobody libraries and provide background for the method used throughout this project.

2.1.1 The Nanobody Scaffold in the Wild

As previously stated, nanobodies are naturally occurring in sharks and camelids. Sharks are a group of elasmobranch fish from the class Chondrichthyes or Cartilaginous fish. As cartilaginous fishes, sharks lack bone marrow and instead rely on a specialised epigeal organ to perform lymphopoiesis. They possess three immunoglobulin isotypes: pentameric IgM, long and short form IgW, and IgNAR (Barelle and Porter, 2015; Rumfelt *et al.*, 2004; Zhang *et al.*, 2013). IgNAR, or immunoglobulin isotype novel antigen receptor, has been isolated in the serum of the nurse shark *Ginglymostoma cirratum* (Greenberg *et al.*, 1995). The IgNAR is secreted by splenocytes and does not associate with immunoglobulin light chains; instead, they are composed of two identical heavy chains containing three to five conserved domains and one variable domain each (Greenberg *et al.*, 1995; Roux *et al.*, 1998).

IgNAR are not derived from conventional antibody gene locus, but instead a specific cluster encoding a specific set of V (Variable), D (Diversity), and J (Joining) gene segments, and a constant (C) region. A rearrangement occurs within a single cluster, involving the recombination of a V gene with two or more D gens and one J gene. The resulting variable domain (VNAR) is capable of binding antigen independently, without a light chain (Zielonka *et al.*, 2015). By contrast, camelids use a conventional immunoglobulin heavy chain locus, similar to other mammals.

Specialised V gene segments have evolved to function without a light chain rearrange with D and J segments through the same recombination process seen in conventional antibodies: they possess unique amino acid changes that allows for enhanced solubility and stability despite the lack of light chain. Additional diversity is acquired through random nucleotide additions at the J (joining) sites and through somatic hypermutation, particularly affecting the CDR3 region (Muyldermans *et al.*, 2009).

Since the IgNAR lacks a light chain, its variable region does not dimerise but instead each variable domain (vNAR) acts as a bivalent antigen binding site. The hydrophobic residues responsible for domain interaction, which are typically conserved, show poor conservation in these regions (Roux *et al.*, 1998). It remains unclear whether the single-domain function of IgNAR is a leftover trait from an ancestral antigen receptor that predates the evolution of homodimeric antigen receptors or if it has evolved to withstand the harsh physiological conditions they encounter.

Despite as low as 25% sequence identity with other mammalian V_H regions, the immunoglobulin fold remains well preserved in the IgNAR variable region (Mashoof and Criscitiello, 2016). Initial sequence analysis categorised IgNAR variable domains into two closely related classes. A notable feature of IgNAR V regions in both classes is the deletion of a substantial portion of the Fr2 (framework 2) Complementarity-Determining region 2 (CDR2), resulting in a comparatively small domain size (~12 kDa). Type IV regions contain conserved cysteine residues in Fr2 and Fr4, with additional cysteine pairs within CDR3. Two structural models have been proposed for the type IV region: one suggests that the extra CDR3 cysteine pairs form disulphide bridges within the CDR, similar to bovine V_H domains with long CDR3s encoding multiple cysteine residues; the second proposes disulphide bonds between certain CDR3 cysteine residues and the Fr2/Fr4 encoded cysteine residues, with remaining cysteine residues forming intra-CDR3 disulphide bonds (Cabanillas-Bernal *et al.*, 2019; Roux *et al.*, 1998).

Type II IgNAR V regions resemble type I in overall structure but have additional cysteine residues situated in CDR1 and CDR3. These cysteine residues are

thought to form a domain-constraining disulphide bond, akin to camel V_HH (Muyldermans *et al.*, 1994; Roux *et al.*, 1998). The primary repertoire of IgNAR V regions arises from four recombination events, leading to a diverse CDR3 repertoire in terms of sequence and length. Upon encountering an antigen, this repertoire undergoes rapid expansion through extensive somatic hypermutations with a clustering of mutations in CDRs (Diaz *et al.*, 1998). Recent findings suggest that the position of disulphide bridges in the two variable region types differentially influences the selection of replacement mutations in CDR1 and CDR3. Thus, mutations tend to accumulate in CDR1 of type II clones and in CDR3 of type I clones, indicating an impact on domain structure (Diaz *et al.*, 2002).

As a result, the IgNAR V domain can be envisioned as a constrained two-loop library displayed on a stable V region framework. Similar to camelid V_HH, the IgNAR domain retains the original antigen-binding site of its parent molecule, implying an anticipated response to antigens with high specificity and affinity. Previous research by Nuttall *et al.* (2001) demonstrated the feasibility of selecting antigen-binding clones from a semisynthetic library of IgNAR variable regions. This library was founded on the IgNAR variable region sequence from the wobbegong shark (*Orectolobus maculates*), a member of the shark family Orectolobidae, similar to the nurse shark. The library was designed to incorporate a randomised, synthetic CDR3 of either 16 or 18 amino acids. Selection against several proteinaceous antigens yielded anti-Kgp protease clones, exhibiting specific and high-affinity binding (Nuttall *et al.*, 2002, 2001).

In 2003, a study led by Helen Dooley's research group at the University of Maryland focused on IgNAR (Dooley *et al.*, 2003). This study described the successful immunisation of nurse sharks (*Ginglymostoma cirratum*) with the proteinaceous antigen HEL (Hen Egg-white Lysozyme), followed by the creation of a phage-displayed single-domain library based on the IgNAR V region repertoire of these sharks. This approach facilitated the extraction of intact antigen-specific binders that matured *in vivo*. Selection from this library yielded clones with remarkable specificity for the antigen, demonstrating nanomolar affinity and notable resilience against irreversible thermal denaturation. This study was later used as the basis for Zadeh *et al.* method

papers describing the efficient construction of a nanobody library based on this isolated scaffold (Zadeh *et al.*, 2019).

2.1.2 Molecular Display Platforms for Nanobody Libraries

Construct screening of libraries requires an efficient molecular display platform that can successfully express all the genetic variants, be utilised for biopanning and variant screening and provides endoplasmic reticulum-specific post-translational processing for efficient folding and activity.

Various molecular display platforms have been developed for the presentation and efficient screening of peptide or protein libraries. Yeast display platforms can display recombinant proteins on the surface of *Saccharomyces cerevisiae* by C-terminal fusion to the Aga2p mating adhesion receptor (Boder and Wittrup, 1997; Cherf and Cochran, 2015). Yeasts are fast and cheap to grow, and the observed library size is usually around 10^9 (Benatuil *et al.*, 2010; Rosowski *et al.*, 2018). The lower transformation efficiency of yeast cells can limit the size of the libraries.

Mammalian cell expression systems are particularly well suited to the production of human full-length immunoglobulin molecules, as they provide the proper folding, glycosylation and post-translational modifications, thus most commercially available antibody therapeutics are produced in mammalian cells (Birch and Racher, 2006). Mammalian cell display libraries have been developed using various cell lines and genetic fusion of the C-terminus of V_HH to various transmembrane domains. New tools, such as CRISPR/Cas9 and transposon technologies can also be used to increase the genetic diversity of the library (Bowers *et al.*, 2014; Parthiban *et al.*, 2019). However, mammalian cell lines are not ideal as molecular display platforms for V_HH domains. If biopanning can be achieved easily through fluorescence-activated cell sorting (FACS), transiently transfected cells require the plasmid to be recovered after each round of biopanning, which considerably limits the throughput and fastness of the molecular display platform.

Bacterial cell display was first developed in 1997. Bacteria are a good option for surface molecular display, as they offer fast and inexpensive culture conditions, as well as high transformation efficiency. However, surface secreted bacterial protein lacks the appropriate folding offered by reticulum-specific post-translational modification, which can impact the folding and activity of nanobodies. However, if the nanobody displays a sensitive and specific antigen binding capacity, the lack of similarities between the eukaryotic and prokaryotic-produced molecules is not necessarily problematic. Thus, bacterial molecular display libraries have been used to isolate engineered, full-length antibodies (Mazor *et al.*, 2007; Ward *et al.*, 1989). Molecular display platforms require fluorescence-activated cell sorting and fluorescently labelled antigen for biopanning, which can complicate the process.

Cell-free or ribosome display technologies fuse the library candidate to its corresponding mRNA to form mRNA-ribosome-polypeptide complexes (Hanes *et al.*, 2000; Hanes and Plückthun, 1997; Mattheakis *et al.*, 1994). The main advantage of ribosome display is that a cell-free system requires no transformation, and therefore transformation efficiency of the host does not limit the library size (Lipovsek and Plückthun, 2004; Plückthun, 2012). Moreover, diversity can be increased throughout the selection process by gene shuffling or error-prone PCR amplification, increasing the potential affinity of binders (Hanes *et al.*, 2000).

Phage display, which was awarded the Nobel Prize in 1985, stands as the most extensively employed molecular platform for peptides and antibodies (Barderas and Benito-Peña, 2019; Smith, 1985; Smith and Petrenko, 1997). This technique combines the benefits of bacterial display technologies with a simpler biopanning process, as phage particles can be secreted and used for panning against various antigens. Phage display involves the genetic fusion of a protein of interest to a coat protein of a bacteriophage, typically the minor coat protein pIII of the filamentous phage M13. This fusion results in the presentation of the protein of interest on the surface of the phage, enabling the selection and isolation of phages that bind to specific targets. Selections can be conducted using antigen-coupled magnetic beads or antigen-coated microtitre plates. To enhance the isolation of high-affinity binders, stringent conditions can be applied, such as reducing antigen concentration and intensifying

washes during subsequent selection rounds. The strength of binding between the binders and their antigens can impact elution difficulty, potentially leading to the loss of the best binders during the selection process.

Various molecular display technologies yield different library sizes. Table 2.1 presents the reported size of antibody gene libraries constructed for various display technologies.

Table 2.1 Antibody gene library sizes per platform technology. From Valldorf et al. (2022). published in Biological Chemistry. © 2022, licensed under CC BY.

Display technology	Library size (unique clones)	References
Mammalian display	10^7 to 10^9	Waldmeier *et al.*, (2016); Parthiban *et al. (*2019)
Yeast surface display	10^9	Benatuil *et al.* (2010; Rosowski *et al.* (2018)
Bacterial display	10^{11}	Bessette, Rice and Daugherty (2004)
Phage display	10^{11} to 10^{12}	Schwimmer *et al.* (2013); Tiller *et al. (*2013)
Ribosome display	10^{12} to 10^{15}	Lipovsek and Plückthun (2004); Plückthun (2012)

In order to construct a phage display library, a collection of genes encoding different protein variants (here IgNAR nanobodies) and representing a diverse array of potential binding partners is cloned into a phagemid and fused to a coat protein gene of a bacteriophage (most often the minor coat protein pIII of the M13 filamentous phage). This allows for the library to be introduced into bacteria, which are subsequently infected with helper phages supplying the essential components to phage production. The phage-bound library can then be amplified and propagated, resulting in the display of the protein variants on the phage surface.

Next, the phage library is exposed to the target of interest, such as an antigen or protein, and phages binding specifically to the target are retained while unbound phages are washed away. The binding to the target immobilised on a solid phase depends on multiple factors, such as molecular affinity, surface characteristics, number of attachment points (avidity effects), and hydrodynamic conditions. Bound phages can then be eluted from the target, usually by increasing pH or by using cleaver enzymes such as trypsin and be used to reinfect bacteria for further amplification. This enrichment process, also referred to as biopanning, selects for

phages with the desired binding properties. Multiple rounds of biopanning with increasingly more stringent conditions are usually required to isolate the best binders.

Finally, individual clones can be sequenced, or the enriched library can be analysed through next-generation sequencing, resulting in a consensus sequence. Binding capabilities can then be further assessed by Enzyme Linked Immunosorbent Assay (ELISA), surface plasmon resonance, or other protein-protein interaction assays.

This system can be improved upon using specialised helper phages like Hyperphage. Hyperphages do not carry a functional version of the pIII gene, necessary for the infectivity and stability of filamentous phages. Instead, they rely on the *Escherichia coli* (*E. coli*) host to provide a functional copy of pIII. When the bacterium also contains a phagemid encoding for a pIII protein linked to an antibody fragment, this phagemid is used by the Hyperphage for packaging, resulting in all pIII copies displaying the antibody fragment. This highly increases the number of antibody fragments displayed by the phage, enabling the display of multiple copies of the target molecule and facilitating selections based on increased number of attachment points, also referred to as avidity (Rondot *et al.*, 2001; Soltes *et al.*, 2003).

2.1.3 Constructing a Nanobody Library

2.1.3.1 Introduction of Genetic Diversity in the Nanobody Scaffold

To create a nanobody library, a high number of random variants needs to be produced. In the case of the vNAR nanobody, the sequence diversity is confined to the Complementary-Determining Region 3, or CDR3 (Dooley *et al.*, 2003). The CDR3 encodes different combinations of non-canonical cysteines, thought to be providing structural stability to the vNAR through disulphide bonds (Roux *et al.*, 1998). A method developed by Zadeh *et al.* (2019) utilised randomised primers to introduce genetic diversity into the CDR3 through a two-step splicing by overlap extension polymerase chain reaction: the first step inserting genetic diversity within the CDR3, and the second adding enzymatic restriction site for ease of cloning (see Figure 2.1). Each primer was designed around the two conserved cysteine residues, and with variable length to increase the structural diversity within the library. The 5A7 domain isolated by Helen Dooley was used as a template (Dooley *et al.*, 2003).

An established issue with randomised codons is the appearance of stop codon with a probability of above 50% after 10 random codons. To remedy this issue, degenerated NNK codons were used where N has an equal chance of standing for adenine (A), cytosine (C), guanine (G), and thymine (T), and K has an equal chance of standing for thymine (T) or guanine (G) (Jacobs *et al.*, 2015). This means that the NNK codons can code for the 20 amino acids, and one stop codon (TAG) or amber codon. SupE *E. coli* strains (like TG1) can translate the amber codon into glutamine (Bossi, 1983). This means that NNK primers allow for the production of a high number of genetic variants without the introduction of stop codons within the sequence, which increases the diversity of the library produces.

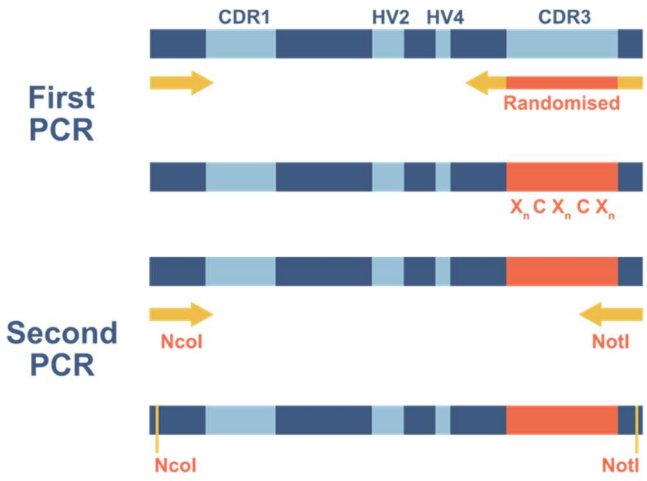


Figure 2.1 Schematic representation of the two-step splicing by overlap extension PCR introducing genetic diversity into the CDR3 of 5A7 vNAR.

CDR = complementarity-determining region; HV2 and HV4 = hypervariable regions 2 and 4; C = cysteine-encoding codon; X = NNK codon. Figure created using Affinity Designer 2.6.2 (available at affinity.serif.com).

2.1.3.2 Phage Display

To produce and select binding variants, the diversified 5A7 domains were fused to the pIII protein – a coliphage protein responsible for the infection of bacteria through binding of the F pili – to create a phage display library. A phagemid expressing a single chain variable antibody fragment (scFv) fused to pIII was obtained commercially (pSEX81, Progen). The pSEX81 cassette vector was engineered to facilitate the easy incorporation of coding regions for heavy and light chain variable domains. It was designed specifically for generating single-chain Fv antibody-pIII fusion proteins that are functional and can be displayed on the surface of M13 bacteriophages (Breitling *et al.*, 1991). Subsequently, the scFv can be separated from the pIII protein by trypsinisation. The gene fragments that have been amplified and encode the variable domain of either the heavy or light chain are inserted in a sequential manner, aligning them with the signal peptide sequence of bacterial pectate lyase (pelB). This positioning ensures the fusion protein's secretion into the periplasmic space.

The V_H and V_L genes were connected using a DNA fragment that encodes a flexible linker spanning eighteen amino acids. This linker includes the initial six amino acids from the CH1 constant region domain and the hydrophilic peptide sequence EEGEFSEAR from the pig brain alpha tubulin. Additionally, the vector backbone features essential components, such as a robust promoter (inducible by IPTG), the T7 terminator, the ColE1 origin of replication, the intergenic region of phage F1, and an ampicillin resistance marker for the purpose of selection.

This system can be modified to suit the expression of pIII-fused nanobodies, by removing the coding regions for heavy and light chain variable domains as well as the flexible linker using a simple restriction digest. Subsequently the digested plasmid can be used for ligation of prepared randomised nanobody fragment.

2.1.4 Aims and Objectives

This chapter will focus on the construction of a genetically diverse nanobody library. The library will be constructed by randomisation of the vNAR 5A7 CDR3. The library quality and diversity will be assessed by next-generation sequencing. The binding capability of vNAR 5A7 against its original target hen egg-white lysozyme will also be tested.

2.2 Materials and Methods

2.2.1 Microbiology Techniques

2.2.1.1 Agar Plates

LB agar plates were prepared using 25 mL of LB broth (Lennox) per plate (Lysogeny Broth Lennox, 0.5% (w/v) tryptone, 0.5% (w/v) yeast extract, 1% (w/v) Sodium chloride, pH at 20° C 7.0 ± 0.2, Sigma Aldrich, L3022), autoclaved with 1.5 % (w/v) agar powder. After cooling down, antibiotics were added if required. Under sterile conditions, plates were poured and left to solidify, before being used, or dried at 37° C for 30 to 60 minutes for storage. Stored plates were reheated in the 37° C incubator for 15 to 30 minutes before being used.

2X TY agar plates were prepared using 25 mL of 2X TY (1.6% (w/v) tryptone, 1% (w/v) yeast extract, 0.5% (w/v) NaCl, pH at 20° C 7.0 ± 0.2, Sigma Aldrich, Y2377), autoclaved with 1.5 % (w/v) agar powder. After cooling down, antibiotics were added if required. Under sterile conditions, plates were poured and left to solidify, before being used, or dried in a 37° C incubator for 30 to 60 minutes for storage. Stored plates were reheated in the 37° C incubator before being used.

2X TY-GA agar plates were prepared using 25 mL of 2X TY (1.6% (w/v) tryptone, 1% (w/v) yeast extract, 0.5% (w/v) NaCl), pH at 20° C 7.0 ± 0.22), autoclaved with 1.5 % (w/v) agar powder. After cooling down, 100 mg/mL ampicillin and 100 mM sterile glucose were added. Under sterile conditions, plates were poured and left to solidify, before being used, or dried in a 37° C oven for 30 to 60 minutes for storage. Stored plates were reheated in the 37° C incubator for 15 to 30 minutes before being used.

2.2.1.2 Transformation Protocols

2.2.1.2.1 Chemically Competent Cells

Chemically competent DH5α cells were obtained from New-England Biolab (C2987H). Prior to transformation, 100 µL of competent cells were thawed and plated on antibiotic-free agar plates to measure the cells' competency. 10 ng of plasmid DNA

(pUC19 vector, New-England Biolab, N3041) were used per 100 µL of competent cells. Plasmid DNA was added to the cell stock and mixed gently, before being incubated on ice for 30 minutes. Cells were heat shocked at 42° C for 90 seconds and left to recover for 5 minutes on ice. 900 µL of SOC medium (2% (w/v) Vegetable Peptone, 0.5% (w/v) Yeast Extract, 10 mM NaCl, 2.5 mM KCl, 10 mM MgCl2, 10 mM MgSO4, New-England Biolab, B9020S) was added to the cells, and the reaction was incubated at 37° C for 1 h. Cells were then diluted to the appropriate concentration in LB, and 100 µL was spread per plate containing the selecting antibiotic, using a sterile spreader.

2.2.1.2.2 Electrocompetent Cells

Electrocompetent TG1 cells were obtained from Agilent (200123). Prior to transformation, 100 µL of competent cells were thawed and plated on antibiotic-free agar plates to measure the cells' competency. 10 ng of plasmid DNA (pUC19 vector, New-England Biolab, N3041) were used per 100 µL of competent cells. Plasmid DNA was added to the cell stock and mixed gently, before being incubated on ice for 30 minutes. The cells were transferred to pre-chilled 1 mm (40 µL) or 2 mm (100 µL) electroporation cuvettes and shocked using an electroporator (1 mm: 1.7 kV, 100 Ω, and 25 µF; 2 mm: 2.5 kV, 100 Ω, and 25 µF). Cells were immediately resuspended in 900 µL of SOC media pre-warmed (37° C) and incubated for 1 hour with shaking (37° C, 250 rpm). Cells were then diluted to the appropriate concentration in LB, and 100 µL was spread per plate containing the selecting antibiotic, using a sterile spreader.

2.2.1.3 Overnight Cultures

Overnight cultures were set up in sterile test tubes in LB containing the relevant antibiotics. Under sterile conditions, one single colony was picked and used to inoculate the medium. Tubes were then incubated at 37° C for 14 to 18 hours with spinning or shaking.

2.2.1.4 Glycerol Stocks

The desired cell strain was transformed (if required) and grown on LB agar plates containing the appropriate antibiotic. An overnight culture was then set up. When cells reached the stationary phase (OD_{600}> 3.0), 80% (v/v) glycerol was added at a 1:4 ratio (final glycerol concentration 20% (v/v)). The culture was then transferred into cryo-tubes and fast frozen on dry ice, before being stored at -80° C. Cells were retrieved by scrapping the top of the material in the cryo-tube using a sterile loop and spread onto an agar plate containing the relevant antibiotic(s).

2.2.1.5 Preparation of Competent Cells

2.2.1.5.1 Chemically Competent Cells

Chemically competent cells were prepared from 5 mL LB overnight cultures. After sufficient growth, fresh LB was inoculated at a 1:100 ratio, and cells were grown with shaking (37° C, 250 rpm) until OD_{600} reached 0.6. Cultures were transferred to pre-chilled centrifuge bottles and spun down (10 minutes, 2000 x g, 4° C) and resuspended in ice-cold sterile 0.1M calcium chloride. After 4 hours incubation on ice, cells were spun down again (10 minutes, 2000 x g, 4° C) and resuspended in ice-cold sterile 0.1M calcium chloride and 30% (v/v) glycerol. Cells were then aliquoted and immediately used for transformation, or flash-frozen on dry ice for storage at -80° C.

2.2.1.5.2 Electrocompetent Cells

Electrocompetent cells were prepared from 5 mL LB overnight cultures. After sufficient growth, fresh 2x TY media was inoculated at a 1:100 ratio, and cells were grown with shaking (37° C, 250 rpm) until OD_{600} reached 0.45. Cultures were transferred to pre-chilled centrifuge bottles and incubated on ice for 30 minutes. The cells were then spun down (10 minutes, 2000 x g, 4° C) and resuspended in ice-cold sterile HEPES buffer (25 mM 4-(2-hydroxyethyl)-1-piperazineethanesulfonic acid, pH 7.0 at 20° C). This step was repeated once again. Finally, the cells were spun and resuspended in ice-cold sterile 10% (v/v) Glycerol-HEPES solution (pH 7.0 at 20° C) twice, and immediately used for transformation, or flash-frozen on dry ice for storage at -80 °C.

2.2.2 *In vitro* Synthesis of Variable DNA Fragments and Cloning into the Phagemid pSEX81

2.2.2.1 Source Material

The pSEX81 plasmid was obtained commercially from Progen (PR3005). The pHEN2 plasmid encoding the vNAR_5A7 fragment was obtained from Helen Dooley's lab (Dooley *et al.*, 2003). Representative plasmid maps can be seen in Appendix 1 (Figure A. 1 and Figure A. 2).

2.2.2.2 Polymerase Chain Reactions

Primer sequences were either obtained from Zadeh *et al.* (2019) and a list of the primers used is visible in Table 2.2. Each primer was designed by introducing randomised codon within the two cysteine loops. The number of randomised codons within each loop varied for each primer, in order to increase the diversity of the library (for each primer, either 12, 13, 16, 18, 20 or randomised codon were introduced).

Table 2.2 List of primers used for isolating the vNAR_5A7 fragment and introducing genetic diversity in the vNAR_5A7 fragment.

N: any base; A: Adenine; G: Guanine; C: Cytosine; T: Thymine; M means a 50% mix each of amino (A or C) nucleotides in reverse primers (Zadeh et al., 2019).

Name	Sequence 5' – > 3'	Size	Description
ForFR1_NcoI	GCATGACCATGGCTCGAGTGGACCAAACACCG	32	Forward primer with restriction site NcoI.
RevFR4_NotI	GCATGAGCGGCCGCTTTATTCACAGTCACGGC AGTGCCAT	40	Reverse primer with restriction site NotI.
For_pSex	GTATGTTGTGTGGAATTGTG	20	Forward primer for phagemid pSEX81.
Rev_pSex	GTTTTGTCGTCTTTCCAG	18	Reverse primer for phagemid pSEX81.
RevRan_12	CGGCAGTGCCATCTCCGCAMNNMNNMNNGC AMNNMNNACAMNNMNNMNNMNNMNNG AGACCGCAACGATACGTGCCAC	78	Reverse primer randomised number 12.
RevRan_13	CGGCAGTGCCATCTCCGCAMNNMNNMNNM NNMNNMNNGCAMNNACAMNNMNNMNN MNNGAGACCGCAACGATACGTGCCAC	81	Reverse primer randomised number 13.
RevRan_16	CGGCAGTGCCATCTCCGCAMNNMNNMNNM NNMNNMNNGCAMNNMNNMNNACAMNN	90	Reverse primer randomised number 16.

	MNNMNNMNNMNNGAGACCGCAACGATAC GTGCCAC		
RevRan_18	CGGCAGTGCCATCTCCGCAMNNMNNMNNM NNMNNMNNGCAMNNMNNMNNMNNACA MNNMNNMNNMNNMNNMNNGAGACCGCA ACGATACGTGCCAC	96	Reverse primer randomised number 18.
RevRan_20	CGGCAGTGCCATCTCCGCAMNNMNNMNNM NNMNNGCAMNNMNNMNNMNNMNNACA MNNMNNMNNMNNMNNMNNMNNMNNG AGACCGCAACGATACGTGCCAC	102	Reverse primer randomised number 20.
RevRan_23	CGGCAGTGCCATCTCCGCAMNNMNNMNNM NNMNNMNNGCAMNNMNNMNNMNNMNN ACAMNNMNNMNNMNNMNNMNNMNNMN NMNNMNNGAGACCGCAACGATACGTGCCAC	111	Reverse primer randomised number 23.

PCRs requiring high-fidelity output were set up using Q5® High-Fidelity DNA Polymerase (New-England Biolab, M0491S). Reaction conditions are detailed in Table 2.3, and thermocycling conditions are detailed in Table 2.4.

Table 2.3 Q5® High-Fidelity DNA PCR reaction conditions

Component	**Final concentration**
5x Q5 reaction buffer	1x
10 mM dNTPs (New-England Biolab, N0447S)	200 µM
10 µM forward primer	0.5 µM
10 µM reverse primer	0.5 µM
Template DNA	<1,000 ng
Q5 high-fidelity DNA polymerase	0.02 u/µL
5x Q5 high GC enhancer (optional)	(1x)
Nuclease-free water	

Table 2.4 Q5® High-Fidelity DNA PCR thermocycling conditions

Step	**Temperature (°C)**	**Time (s)**	**Cycles**
Initial denaturation	98	30	x1
Denaturation	98	10	X25-35
Annealing	50–72*	30	
Extension	72	**	
Final extension	72	120	x1
*Annealing temperature was determined for each primer set using the New-England Biolab Tm Calculator v1.12.0. ** Extension time was calculated as 30 seconds/kb.			

PCRs requiring high throughput, such as colony PCRs, were set up using OneTaq® Quick-Load® 2X Master Mix (New-England Biolab, M0486S). Reaction conditions are detailed in Table 2.5, and thermocycling conditions are detailed in Table 2.6.

Table 2.5 OneTaq® Quick-Load® DNA PCR reaction conditions

Component	Final concentration
10 µM forward primer	0.2 µM
10 µM reverse primer	0.2 µM
Template DNA	<1,000 ng
OneTaq® quick load® 2x master mix with standard buffer	1x
Nuclease-free water	

Table 2.6 OneTaq® Quick-Load® DNA PCR thermocycling conditions

Step	Temperature (°C)	Time (s)	Cycles
Initial denaturation	94	30	x1
Denaturation	94	30	X30
Annealing	45–68*	60	
Extension	68	**	
Final extension	68	300	x1
*Annealing temperature was determined for each primer set using the New-England Biolab Tm Calculator v1.12.0. ** Extension time was calculated as 1 minute/kb.			

PCR samples were cleaned by either by QIAquick Gel Extraction Kit (QIAGEN, 28704) or QIAquick PCR Purification Kit (QIAGEN, 28104) depending on fragment size and possible contamination. For QIAquick PCR purification, samples were supplemented with 5X PB buffer and applied to a QIAquick column before being centrifuged (60 seconds, 17 900 x g). The column was then washed with PE buffer (10 mM Tris-HCl (pH 7.5 at 20° C), 80% ethanol) twice, and the DNA sample was eluted in 42° C nuclease-free water or EB buffer (10 mM Tris, 0.1 mM EDTA, pH 8.5 at 20° C). For QIAquick Gel Extraction, samples were run on a 1% (w/v) agarose gel, and the correct bands were excised. Three volumes of QG buffer (5.5 M guanidine thiocyanate, 20 mM Tris-HCl, pH 6.6 at 20° C) were added per one volume of gel, and the samples were heated up at 50° C for 10 minutes. One gel volume of isopropanol was added, and the sample was applied to a QIAquick column before being centrifuged (60 seconds, 17 900 x g). The column was then washed with PE buffer twice, and the DNA sample was eluted in 42° C nuclease-free water or EB buffer.

2.2.2.3 Restriction Digests and Ligations

All restriction enzymes were obtained from New-England Biolab. Restriction digests were set up in nuclease-free water with 250 ng to 500 ng of DNA, 1X buffer (either rCutSmart™ Buffer (50 mM Potassium Acetate, 20 mM Tris-acetate, 10 mM Magnesium Acetate, 100 µg/mL Recombinant Albumin, pH 7.9 at 20° C, New-England

Biolab, B6004S) or NEBuffer™ r3.1 (100 mM NaCl, 50 mM Tris-HCl, 10 mM MgCl2, 100 µg/mL Recombinant Albumin, pH 7.9 at 20° C, New-England Biolab, B6003S) depending on the enzyme used) and 1 unit of each enzyme per µg of DNA. Sample, buffer, and enzymes were kept on ice prior to mixing, and the reaction was incubated following supplier's recommendation for each enzyme.

Plasmids were ligated using the appropriate vector to insert ratio determined by ligating a small amount of plasmid at ratios varying from 1:0.5 to 1:2, transforming into *E. coli* and performing colony PCR to confirm fragment insertion. Reactions were set up with 1 µg of plasmid DNA, 4 u/ng of T4 DNA ligase (New-England Biolab, M0202S) and 1X T4 DNA ligase reaction buffer (50 mM Tris-HCl, 10 mM MgCl2, 1 mM ATP, 10 mM DTT, pH 7.5 at 20° C, New-England Biolab, B0202S) in nuclease-free water, and the reaction was incubated at 20° C for 1 hour.

2.2.2.4 Minipreps

To purify high-copy plasmid DNA, samples were minipreped using the QIAprep Spin Miniprep Kit (QIAGEN, 27104). 5 mL of overnight cultures in LB were pelleted (60 seconds, 17,900 x g) and resuspended in buffer P1 (50 mM Tris-HCl (pH 8.0 at 20° C), 10 mM EDTA, 100 µg/mL RNaseA). Buffer P2 (200 mM sodium hydroxide, 1% (v/v) SDS) and N3 (4.2 M guanidinium chloride, 0.9 M potassium acetate, pH 4.8 at 20° C) were added consecutively to lyse and neutralise the sample before centrifugation (60 seconds, 17,900 x g). The supernatant was applied to the QIAprep spin column, and spun down (60 seconds, 17,900 x g). Samples were washed using buffer PE, and DNA was eluted in EB buffer. DNA was quantified using a NanoDrop Microvolume Spectrophotometer (Thermo Fisher Scientific).

2.2.2.5 DNA Gel Electrophoresis

Agarose gels were prepared in 1X TBE (Tris-HCl/Borate/EDTA (ethylenediaminetetraacetic acid)) using 0.2 µg/mL ethidium bromide and 1–3% (w/v) agarose. DNA samples were loaded in 1X purple gel loading dye (New-England Biolab, B7024S) alongside the appropriate DNA ladder (1 kb DNA Ladder (N3232S), 1 kb plus DNA ladder (N3200S) or 100 bp DNA ladder (N3231S), all from New-England

Biolab). Gels were run in 1X TBE buffer (0.13 M Tris (pH 7.6 at 20° C), 45 mM boric acid, 2.5 mM EDTA) at 120 V for 90 minutes.

2.2.2.6 Sequencing

Samples were sent to Eurofins Genomics (Germany) alongside appropriate primers for Sanger sequencing. The primers used are listed in Table 2.7. Results were analysed using SnapGene software 6.1 (from Insightful Science; available at snapgene.com). Primer sequences were either obtained from Zadeh *et al.* (2019) and a list of the primers used is visible in Table 2.7.

Table 2.7 List of primers used for Sanger sequencing.

These primers were used to validate the correct insertion of fragments into the pSEX81 plasmid (Zadeh et al., 2019).

Name	Sequence 5' – > 3'	Size	Description
For_pSex	GTA TGT TGT GTG GAA TTG TG	20	Forward primer for phagemid pSEX81.
Rev_pSex	GTT TTG TCG TCT TTC CAG	18	Reverse primer for phagemid pSEX81.

Library diversity was evaluated by Next-Generation Sequencing (NGS). Primers were designed to specifically amplify the target gene/region using using SnapGene software 6.1 (from Insightful Science; available at snapgene.com). Key parameters considered included melting temperature (Tm) between 55–65 °C, GC content of 40–60%, and minimal secondary structure or self-complementarity to avoid primer-dimer formation; and included the Illumina TruSeq adapters required for sequencing. The NGSelect Amplicons on MiSeq service was used (Eurofins). PCR samples were prepared using universal (TruSeq) adapters (see Table 2.8) and Phusion DNA polymerase (New-England Biolab). Indexing and sequencing of all samples on MiSeq with 2 × 300 bp run mode was then performed by Eurofins. Results were collected and analysed using SnapGene 6.1 (from Insightful Science; available at www.snapgene.com) and Geneious Prime 2024.0.5 (from GraphPad software; available at www.geneious.com).

Table 2.8 List of primers used for next-generation sequencing.

Illumina TruSeq adapters are highlighted in red. These primers were used to validate the diversity of the nanobody library.

Name	Sequence 5' – > 3'	Size	Description
NGS3_for	ACA CTC TTT CCC TAC ACG ACG CTC TTC CGA TCT AAA GAG GAG AAA TTA ACC ATG AAA	57	Forward primer for next generation sequencing amplification, including NGS adapters.
NGS3_rev	GAC TGG AGT TCA GAC GTG TGC TCT TCC GAT CTG AAT TTT CTG TAT GGG ATT TTGC	55	Reverse primer for next generation sequencing amplification, including NGS adapters.

2.2.3 Construction of a vNAR Phage Display Library

2.2.3.1 Transformation of pSEX81_vNAR into Electrocompetent TG1

For each fragment, 15 µL of ligation mixture was transformed into 300 µL of competent *E. coli* TG1 cells by electroporation (see section 2.2.1.2.2, page 49) and incubated in 25 mL of SOC with shaking (1 h, 37° C, 250 rpm). A negative control was set up using 50 µL of competent cells and no DNA, and a positive control was set up using 50 µL of cells and 1 µL of highly pure pSEX81, and incubated in 2 mL of SOC (1 h, 37° C, 250 rpm). Following incubation, the library was pooled and 100 µL of 10^{-2} to 10^{-5} dilutions of the library, 10^{-1} and 10^{-2} dilutions of the positive control and 100 µL of the undiluted negative control were plated on 2X TY-GA plates. The rest of the library was centrifuged (10 minutes, 3500 x g, 4° C), resuspended in 10 mL of SOC medium, and plated on a 20 cm × 20 cm 2X TY-GA plate. Plates were incubated overnight, and the transformation titre was calculated using the following formula:

$$\frac{number\ of\ colonies * volume\ of\ recovery\ medium\ culture}{volume\ plated * dilution\ fold}$$

After overnight incubation (37° C), 10 mL of LB medium was added to the 20 cm × 20 cm agar plate and bacterial colonies were scraped using a flame-sterilised glass spreader. Sterile glycerol was added to a final concentration of 10%, and the library was aliquoted (500 µL aliquots) and stored at -80° C.

2.2.3.2 Phage Preparation and Selection of vNARs against Antigen by Phage Display

A nanobody aliquot was thawed on ice and used to inoculate 500 mL of 2X TY-GA medium. The culture was grown with shaking (37° C, 250 rpm) until OD_{600} reached 0.5. 1×10^{12} Hyperphage M13KO7 ΔpIII (Progen, PRHYPE) were added to the culture and incubated at 37 ° C without shaking for 15 minutes following 30 minutes vigorous shaking. The culture was then spun (320 x g, 15 minutes, room temperature) and the supernatant was discarded. The pellet was resuspended in 500 mL of fresh 2X TY-GA medium and grown overnight (28° C, 250 rpm). The culture was centrifuged (20 minutes, 5500 x g, 4° C) and 125 mL of PEG salt solution (20% (v/v) polyethylene glycol, 2.5 M NaCl) was added to the supernatant to precipitate the phage binder. The supernatant was incubated on ice for 4 h, before being centrifuged again (60 minutes, 5500 x g, 4° C) to pellet the phage binders. The phage pellet was resuspended in 1 mL of PBS (Phosphate Buffered Saline, 137 mM NaCl, 2.7 mM KCl, 8 mM Na_2HPO_4 and 2 mM KH_2PO_4) before being centrifuged at least three times to remove bacterial debris. Following centrifugation, 250 µL of PEG salt solution was added to precipitate the phages, and the solution was incubated on ice for 30 minutes, and centrifuged (10 minutes, 17,900 x g, room temperature). The supernatant was discarded, and the phage pellet was centrifuged again (2 minutes, 17,900 x g, room temperature) to remove the final traces of PEG salt solution. The phage pellet was finally resuspended in 500 µL of PBS and stored at 4° C in preparation for the following round of biopanning.

2.2.3.3 Transformation Titre

An overnight culture of TG1 was set up from a single colony grown on M9 minimal agar plates and used to infect 5 mL of fresh 2x TY-G media (1:5 dilution). The culture was grown to OD_{600} = 0.6. 10 µL of phage solution at various concentrations were used to infect 90 µL of bacterial culture, and incubated at 37° C, 250 rpm for 45 minutes, serial dilutions were then plated on 2x TY-GA plates (0.6% (w/v) tryptone, 1% (w/v) yeast extract, 0.5% (w/v) NaCl, 100 mg/mL ampicillin, 100 mM glucose, 1.5% (w/v) agar powder). 1 µL of highly pure pSEX81 plasmid was transformed into 50 µL TG1 cells as a positive control, and 50 µL of TG1 cells were plated as a negative

control. Plates were incubated at 37° C overnight, and colonies were counted either manually or using ImageJ the next day.

2.2.3.4 Statistical evaluation of library quality

Library quality was assessed using FastQC (v0.12.0, Andrew, 2010; available at https://www.bioinformatics.babraham.ac.uk/projects/fastqc/). Per-base Phred quality scores were calculated to evaluate sequencing accuracy. The distribution of quality scores across read positions as well as read length was analyzed, including assessment of Gaussian distribution patterns. Data was plotted using GraphPad Prism 10.4.1 (from GraphPad software; available at www.graphpad.com). Sequence cleaning and deduplication, as well as alignments, were performed using Geneious Prime 2024.0.5 (from GraphPad software; available at www.geneious.com).

2.2.4 PpSEX81_5A7 ELISA Binding Assay

A 96-well MaxiSorp™ flat bottom plate (Nunc) was coated with either 100 µL of 10 µg/mL HEL (Lysozyme from chicken egg white, Sigma Aldrich, L6876-1G) or 3% (w/v) BSA (Bovine Serum Albumin) in carbonate-bicarbonate buffer (0.03 M sodium carbonate, 0.07 M sodium bicarbonate, pH 9.6 at 20° C) and incubated overnight at 4° C. The plate was then washed three times with TBST, and blocked with 200 µL of blocking buffer (3% (w/v) BSA, 0.05% (w/v) NaNO3 in TBS (Tris Buffered Saline, 150 mM NaCl, 50 mM Tris-HCl, pH 7.6 at 20° C)) and incubated overnight at 4° C. The plate was washed three times in TBST (Tris Buffered Saline with Tween, 150 mM NaCl, 50 mM Tris-HCl, 0.5% (v/v) Tween 20, pH 7.6 at 20° C) before the assay. PpSEX81_5A7 was diluted in blocking buffer, and 11 two-fold serial dilutions were prepared starting at 10^{10} CFU/mL and incubated for 10 minutes at room temperature. 100 µL of PpSEX81 dilution was applied to each well and incubated with rocking at room temperature for 2 hours. The plate was then washed twelve times with TBST. 100 µL of anti-fd bacteriophage antibody produced in rabbit (Sigma B7786, 1:1000 in TBS) was applied to each well and incubated at room temperature for 1 hour. The plate was washed three times with TBST. 100 µL of swine anti-rabbit IgG-HRP (Dako P0399, 1:4000 in TBS) was applied to each well and incubated at room temperature for 1 hour. The plate was washed three times with TBST. The plate was developed with

100 µL 1-step ultra-TMB (3,3´,5,5´-tetramethylbenzidine, Thermo Fisher Scientific, 34029) per well, and stopped after 20 minutes with 100 µL H_2S0_4. Results were read on a GloMax® Discover Microplate Reader (Promega) at 450 nm.

Non-linear regressions were performed in GraphPad Prism 10.4.1 (from GraphPad software; available at www.graphpad.com) using the log(agonist) vs. response – variable slope (four-parameter) model to fit the binding curves. To compare datasets, an extra sum-of-squares F test was used to determine whether the data were better described by separate curves or a shared curve.

2.2.5 Reagents

2.2.5.1 Antibiotics

For each antibiotic used, a 1000X concentration stock was prepared in the relevant solvent (Table 2.9). Stocks were stored at -20° C.

Table 2.9 Table of antibiotics used, along with the relevant solvent and working concentration.

Antibiotic	Solvent	Working concentration in µg/mL
Ampicillin	dH_2O	100
Kanamycin	dH_2O	50

2.2.5.2 Enzymes, Buffers, and Solutions

Enzymes used were obtained from New-England Biolab and stored at -20 °C and kept on ice before use. Enzymes were used according to the provider's guidelines and with supplied buffers. The composition of buffers can be seen in Table 2.10. The table also shows the composition of various buffers used. If composition is protected, the supplier was provided.

Table 2.10 Table of buffers with compositions.

Buffer pH is measured at room temperature (20° C).

Buffer	Composition (in dH_2O, otherwise specified)	Storage
LB broth (Lennox)	1% (w/v) NaCl 0.5% (w/v) Tryptone 0.5% (w/v) Yeast Extract pH 7.0	Room temperature

2X TY	1.6% (w/v) Tryptone 1% (w/v) Yeast Extract 0.5% (w/v) NaCl pH 7.0	Room temperature
2X TY-GA	1.6% (w/v) Tryptone 1% (w/v) Yeast Extract 0.5% (w/v) NaCl 100 mg/mL ampicillin 100 mM sterile glucose pH 7.0	Room temperature
SOC	2% (w/v) Vegetable Peptone 0.5% (w/v) Yeast Extract 10 mM NaCl 2.5 mM KCl 10 mM MgCl2 10 mM MgSO4	Room temperature
2X TY	1.6% (w/v) Tryptone 1% (w/v) Yeast Extract 0.5% (w/v) NaCl	Room temperature
HEPES buffer	25 mM 4-(2-hydroxyethyl)-1-piperazineethanesulfonic acid pH 7.5	4° C
rCutSmart™ Buffer	50 mM Potassium Acetate 20 mM Tris-acetate 10 mM Magnesium Acetate 100 µg/mL Recombinant Albumin, pH 7.9	-20 °C
NEBuffer™ r3.1	100 mM NaCl 50 mM Tris-HCl 10 mM MgCl2 100 µg/mL Recombinant Albumin pH 7.9	-20 °C
PB buffer	5 M Gu-HCl 30% (v/v) isopropanol	Room temperature
PE buffer	10 mM Tris-HCl (pH 7.5) 80% (v/v) ethanol	Room temperature
EB buffer	10 mM Tris 0.1 mM EDTA pH 8.5	Room temperature
QG buffer	5.5 M guanidine thiocyanate 20 mM Tris-HCl pH 6.6	Room temperature
P1 buffer	50 mM Tris-HCl (pH at 20° C pH 8.0) 10 mM EDTA 100 µg/mL RNaseA	4° C
P2 buffer	200 mM sodium hydroxide 1% (w/v) SDS	Room temperature
N3 buffer	4.2 M guanidinium chloride 0.9 M potassium acetate pH 4.8	Room temperature
T4 Ligase buffer	50 mM Tris-HCl 10 mM magnesium chloride 10 mM dithiothreitol	-20 °C

	1 mM adenosine triphosphate pH 7.5	
Carbonate-bicarbonate buffer	0.03 M sodium carbonate 0.07 M sodium bicarbonate pH 9.6	4° C
Blocking buffer	3% (w/v) BSA (Bovine Serum Albumin) 0.05% $NaNO_3$ in TBS	4° C
10X Phosphate buffered saline (PBS)	1.37 M sodium chloride 27 mM potassium chloride 80 mM sodium phosphate 20 mM potassium phosphate	Room temperature
10X Tris-buffered saline (TBS)	500 mM Tris 1.5 M sodium chloride pH 7.6	Room temperature
PBST	1X PBS 0.5% (v/v) Tween 20 (unless specified otherwise)	4° C
TBST	1X TBS 0.5% (v/v) Tween 20 (unless specified otherwise)	4° C
PEG salt solution	20% (w/v) polyethylene glycol 2.5 M NaCl	4° C

2.3 Results and Discussion

2.3.1 Pilot Experiment

The vNAR_5A7 domain was isolated from the pHEN2 plasmid obtained from the Helen Dooley lab (Dooley *et al.*, 2003) by PCR. Primers ForFR1_NcoI and RevFR4_NotI (Sigma) were used to amplify the fragment and introduce restriction sites for ligation (New-England Biolab Q5 High-fidelity DNA polymerase, 30 cycles, Tm = 72° C, predicted amplicon size = 367 bp) (Zadeh *et al.*, 2019). The resulting sample was run on a 2% agarose gel and a size between 300 and 400 bp was observed, which is consistent with the size of vNAR_5A7 of 367 bp (Figure 2.2).

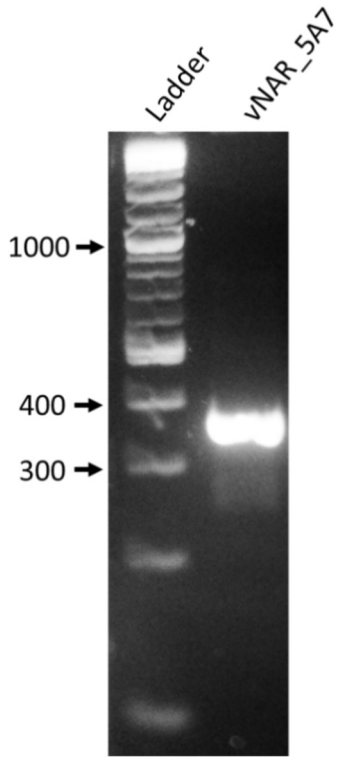


Figure 2.2 2% agarose gel of PCR-amplified vNAR_5A7 fragment.

Lane 1: New-England Biolab 1 kb Plus DNA Ladder. Lane 2: vNAR_5A7 PCR amplicon. The band visible is consistent with the 367 bp size of vNAR_5A7 amplified by PCR from the pHEN2-5A7 plasmid using primers ForFR1_NcoI and RevFR4_NotI.

The amplicon was then digested with restriction enzymes NcoI and NotI (New-England Biolab) and prepared for ligation using QIAquick PCR Purification Kit (QIAGEN). The pSEX81 phagemid was also digested and prepared using QIAquick Gel

Extraction Kit (QIAGEN), and a ligation reaction was set up. Following transformation and miniprep, successful ligation was verified by diagnostic digest with NcoI and NotI. Two bands were observed with sizes consistent with the empty pSEX81 vector (4114 bp) and the vNAR_5A7 fragment (345 bp) (Figure 2.3). The resulting phagemid was named pSEX81_5A7, and confirmed by Sanger sequencing using primers For_pSex and Rev_pSex.

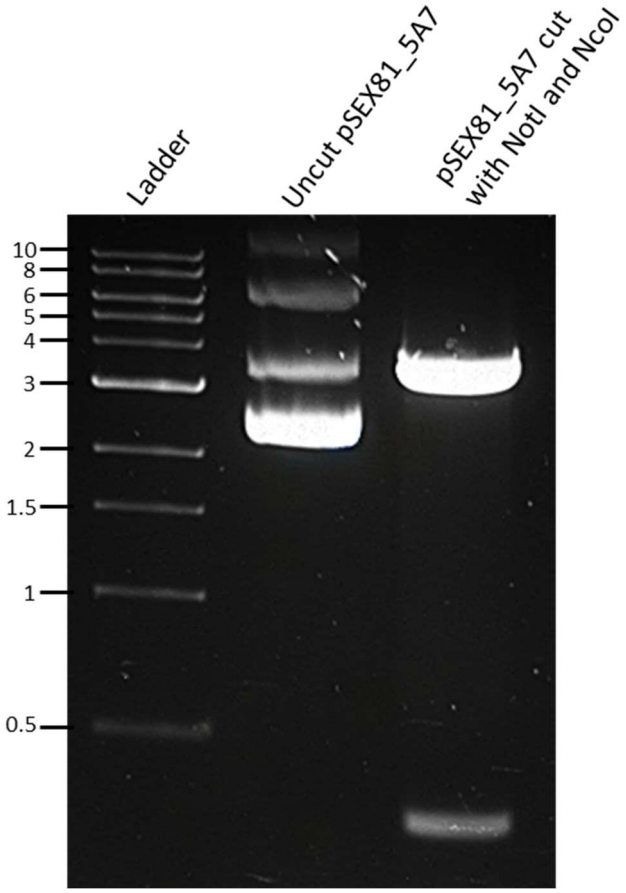


Figure 2.3 1.5% Diagnostic digest of pSEX81_5A7.

Lane 1: 1 kb DNA ladder (New-England Biolab). Lane 2: Uncut pSEX81_5A7 phagemid. The four bands correspond to the nicked, linear, supercoiled and circular single stranded presentations of the plasmid (Garner and Chrambach, 1992). Lane 3: pSEX81_5A7 digested with enzymes NcoI and NotI, showing consistent bands around the 4114 bp (vector) and 345 bp (insert) marks.

The pSEX81_5A7 plasmid was then transformed into *E. coli* TG1 bacteria. The culture was scaled up and infected with M13K07 helper phage (New-England Biolab).

Following phage amplification, phages were precipitated and quantified by bacterial titre. The resulting packaged phagemid was named PpSEX81_5A7.

To develop an ELISA assay that could detect the binding of PpSEX81_5A7 to the antigen HEL, several optimisation experiments were performed. First, a MaxiSorp™ polystyrene ELISA plate (NUNC) was coated with 100 µL of a 2-fold horizontal dilution of HEL starting at 5 µg/mL, and incubated overnight at 4° C. After washing three times with PBST, the plate was blocked with 100 µL of 3% (w/v) milk powder in PBS and left overnight at 4° C. Following another three washes with PBST, PpSEX81_5A7 was diluted in PBS to a concentration of 10^6 phage per well (100 µL of 10^7 CFU/mL). Subsequently, 100 µL of this phage dilution was added to each well and incubated at room temperature for 1 hour. The plate was washed three times with PBST, then incubated with 100 µL of primary anti-fd Bacteriophage antibody in rabbit (Sigma B2661, 1:1000 in PBS) for 1 hour at room temperature. After another three washes with PBST, the plate was incubated with 100 µL of secondary anti-Rabbit IgG peroxidase antibody (Sigma A0545, 1:30, 000 in PBS) for 1 hour at room temperature. Following three more washes with PBST, the plate was developed with 100 µL of 1-step ultraTMB (Thermo Fisher Scientific, 34029), and the reaction was stopped with 100 µL of H2SO4. The results were read at 450 nm and can be seen in Figure 2.4. A non-linear curve was fitted to the data with the following parameters: Hill Slope = 0.6359, EC_{50} = 4.535e-008, R^2 = 0.6888. The delta of signal between the maximum and background value was only 0.3251, which is reflected in a low R^2 value. To improve this combination of a high background and low signal, a different blocking buffer was tested, and the concentration of HEL was increased.

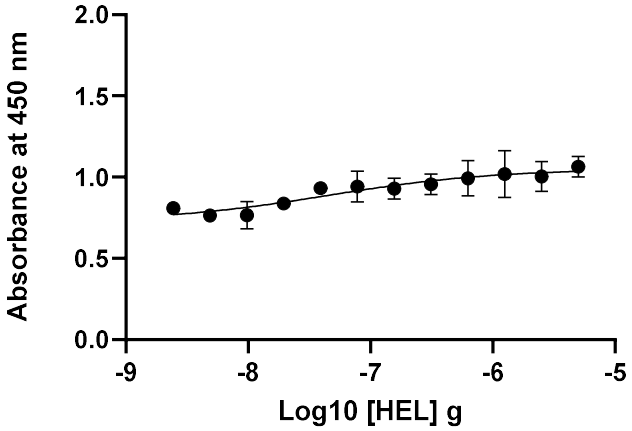


Figure 2.4 ELISA of PpSEX81_5A7 against serial dilutions of HEL.

A non-linear curve was fitted with the following parameters (Hill Slope = 0.6359, EC_{50} = 4.535e-008, R^2 = 0.6888). N=2.

To attempt to reduce background signal, the blocking buffer was changed to 200 µL of 3% whey, 0.25% Tween 20, 0.05% NaN3, 0.1% EDTA and 3% BSA in PBS. This resulted in almost no signal being detected in the assay, as can be seen in Figure 2.5. No curve could be fitted to the data, as the signal was too low. To attempt to increase the signal, a higher concentration of PpSEX81_5A7 was used for the subsequent assays (10^8 phages per well (100 µL of 10^9 CFU/mL)).

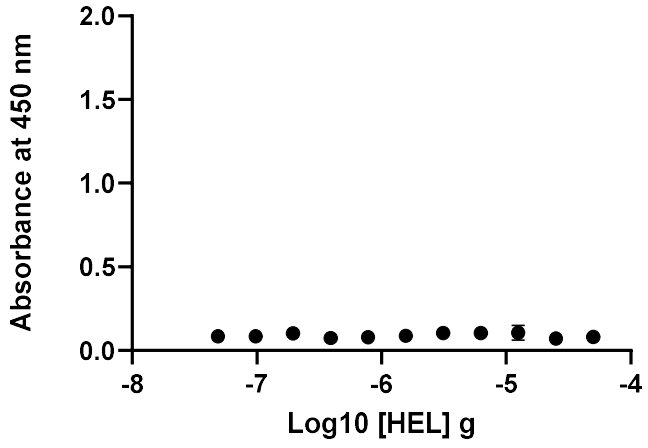


Figure 2.5 ELISA of PpSEX81_5A7 against serial dilutions of HEL.

The low signal resulted in an inconclusive assay. N=2.

The following assay was set up using the increased PpSEX81_5A7 concentration and new blocking buffer. Figure 2.6 showed that the signal still

appeared to be in the lower range for ELISA assays. Moreover, the data revealed the appearance of a hook effect where very high concentrations of an analyte lead to falsely low results due to antibody saturation. This occurs when excess antigen binds to all available antibodies, preventing further binding and resulting in reduced signal detection (Haga, 1995). The hook effect could explain the high signal observed at lower concentration of this assay. Changing the blocking buffer could potentially help mitigate the hook effect in ELISA assays. The choice of blocking buffer influences the binding characteristics of antibodies and can affect their availability for antigen interaction. Using a more suitable blocking agent may reduce non-specific binding and improve the assay's dynamic range, thereby helping to better detect high concentrations of analytes without falling into the hook effect. The antibody concentration could also be increased to limit saturation by abundant antigen.

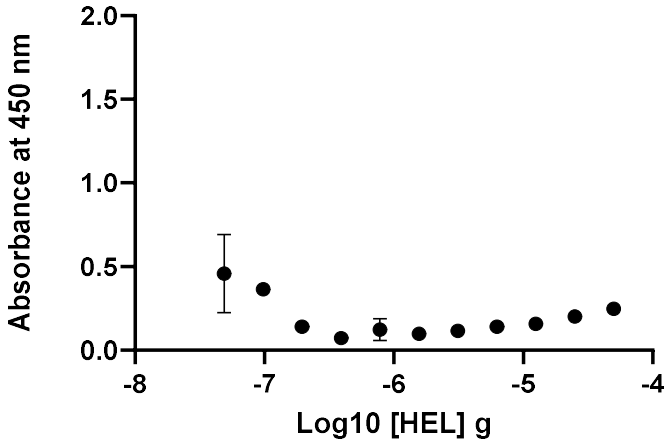


Figure 2.6 ELISA of PpSEX81_5A7 against serial dilutions of HEL.

The appearance of a 'hook effect' where antigen binding is limited by antibody saturation is visible. N=2

For the next assay, the primary antibody dilution was changed from 1:1000 to 1:500. Additionally, a BSA only blocking buffer was used to increase signal while limiting the hook effect observed in the previous assay (3% (w/v) BSA, 0.05% (w/v) NaNO3 in PBS). As can be seen in Figure 2.7, a clear increase in signal can be observed. A non-linear curve could be fitted to the data with the following parameters: Hill Slope = 0.9220, EC50 = 0.02265, R2 = 0.5828. While the signal increase, the high background was still present. This might be due to this specific range of HEL

concentration but might also be a sign of non-specific binding of the phages. Non-specific binding of phages refers to their tendency to attach to surfaces or molecules that do not specifically match its intended target receptors. This type of binding is often due to electrostatic interactions, hydrophobic forces, or non-specific affinities that are not governed by the specific receptor-ligand recognition that phages typically use to infect bacterial cells. In ELISA assays, the non-specific binding of phages can pose challenges, as PpSEX81_5A7 may bind to the assay plate or other assay components in ways that are not dependent on specific antibody or antigen interactions. This non-specific attachment can lead to elevated background signals, reducing assay sensitivity and accuracy by making it difficult to distinguish between specific binding events and irrelevant noise. In this specific assay, using a serial dilution of phage rather than HEL could help lower background noises. The washing buffer was also changed from phosphate-buffered saline with Tween 20 (PBST) to Tris-buffered saline with Tween 20 (TBST). PBS, while effective in maintaining osmolarity and structural integrity, can sometimes increase background staining in complex systems or when high-affinity binding is needed, especially in phage-based systems where non-specific binding is an issue. Therefore, for assays like phage display ELISA, TBS is frequently preferred because it can minimise non-specific binding and improve signal-to-noise ratios, leading to clearer results and reduced false positives. A BSA only control was also included to visualise non-specific binding.

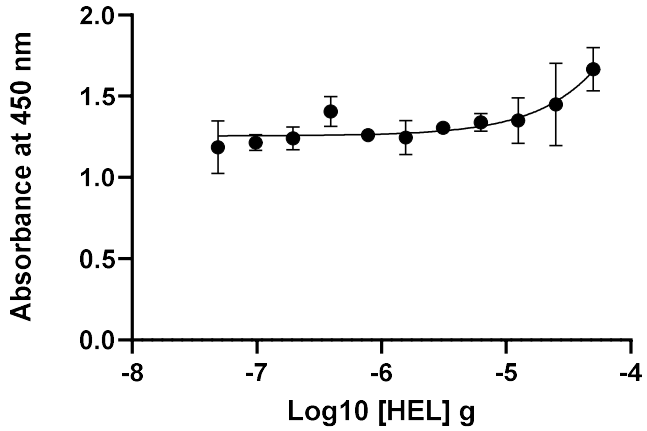


Figure 2.7 ELISA of PpSEX81_5A7 against serial dilutions of HEL.

Hill Slope = 0.9220, EC_{50} = 0.02265, R^2 = 0.5828, N=2.

In the subsequent assay (Figure 2.8), no signal could be observed. As PpSEX81_5A7 was diluted in an uncoated polycarbonate plate before being added to the MaxiSorp™ polystyrene ELISA plate, it was hypothesised that phages remained bound to the dilution plate and therefore were not transferred to the assay plate. To prevent this effect in future assays, dilution plates were blocked with blocking buffer prior to the serial dilutions of PpSEX81_5A7.

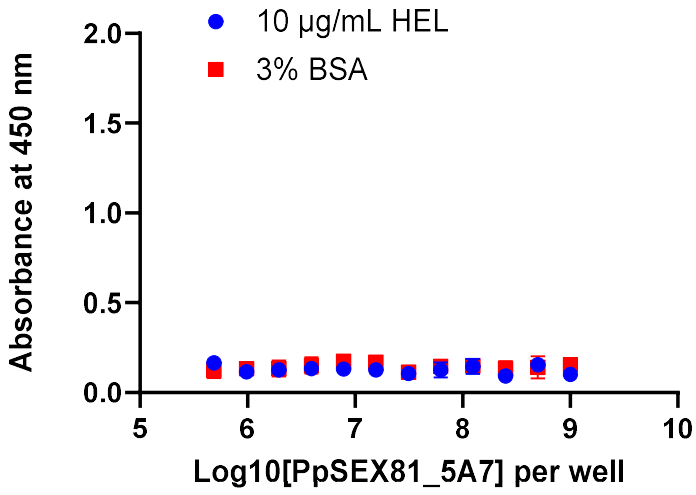


Figure 2.8 ELISA of serial dilutions of PpSEX81_5A7 against HEL and 3% BSA as a control.

No signal could be detected. N=2

The final optimised demonstrated a non-linear binding curve close to sigmoidal curves usually observed in ELISA assays (Figure 2.9). The data revealed a

binding capacity two-fold over control at the higher PpSEX81_5A7 concentrations. This is reflected in the EC_{50} values of 8.92×10^8 and 6.41×10^8 for HEL and BSA, respectively. The fitted curves were of similar Hill slopes (0.8302 and 0.8937, respectively) and displayed a good range of signals with R^2 values of 0.9993 and 0.9961. The lack of plateau can be explained by lower PpSEX81_5A7 concentrations over HEL and could be corrected by increasing the dilution range of phages or by reducing the amount of HEL used for plate coating. To ascertain the specificity of PpSEX81_5A7 to HEL, an extra sum-of-squares F test was performed and revealed a significant difference between the binding curves ($P < 0.0001$, $F = 1611$), indicating that separate fits better describe the data for the HEL and BSA groups than a global model.

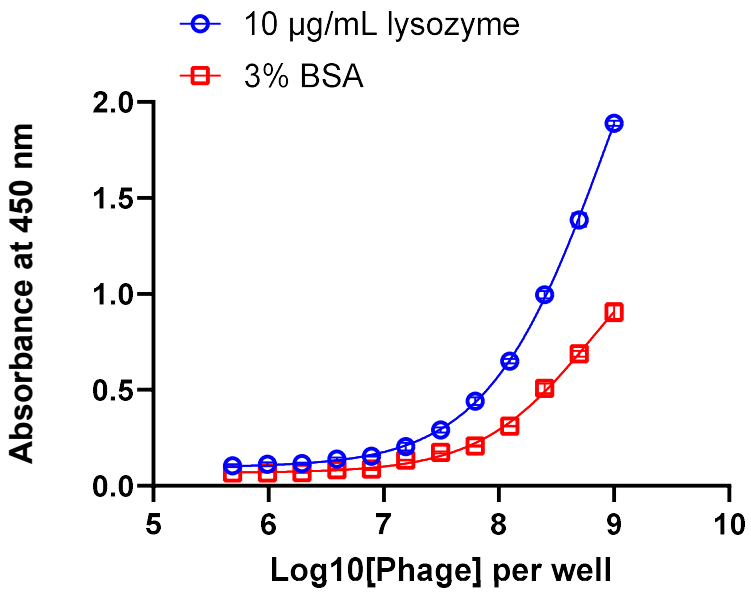


Figure 2.9 ELISA of serial dilutions of PpSEX81_5A7 against HEL and 3% BSA as a control. *Error bars show standard deviation but might not be visible for all data points due to low level of variation across samples. N=3.*

This final assay demonstrates the specificity of the 5A7 nanobody to the antigen egg white HEL and validates its use for targeting of this antigen *in vitro*. This optimised protocol could also be used to validate the binding of varying nanobodies against a range of antigens.

2.3.2 Library Construction

2.3.2.1 Introduction of Genetic Diversity

Genetic diversity was introduced into the vNAR_5A7 fragment by randomised PCR primers, following the procedure developed by Zadeh *et al.* (Q5® High-Fidelity DNA Polymerase, 30 cycles, Tm = 60° C, predicted amplicon size = 321–354 bp) (Zadeh *et al.*, 2019). ForFR1_NcoI was used as a forward primer alongside six different reverse primers, each containing a different number of degenerated NNK codons (N means a 25% mix each of adenine, thymine, cytosine, and guanine nucleotides; K stands for a 50% mix each of thymine and guanine nucleotides). The variants were run on a 1% agarose gel, and all showed a size consistent with the expected size range of 349–382 bp (Figure 2.10). Variants were numbered 1 to 6, reflecting the use of primers RevRan_12, RevRan_13, RevRan_16, RevRan_18, RevRan_20 and RevRan_23 (respectively). Variants were not normalised before the run, and intensity variation between DNA fragments only reflects PCR efficacy. A final PCR was used to introduce the restriction site NotI into all fragments using, once again, primers ForFR1_NcoI and RevFR4_NotI (Q5® High-Fidelity DNA Polymerase, 30 cycles, Tm = 60° C, predicted amplicon size = 349–382 bp). Fragments were digested using restriction enzymes NcoI and NotI (New-England Biolab) and prepared for ligation using QIAquick PCR Purification Kit (QIAGEN).

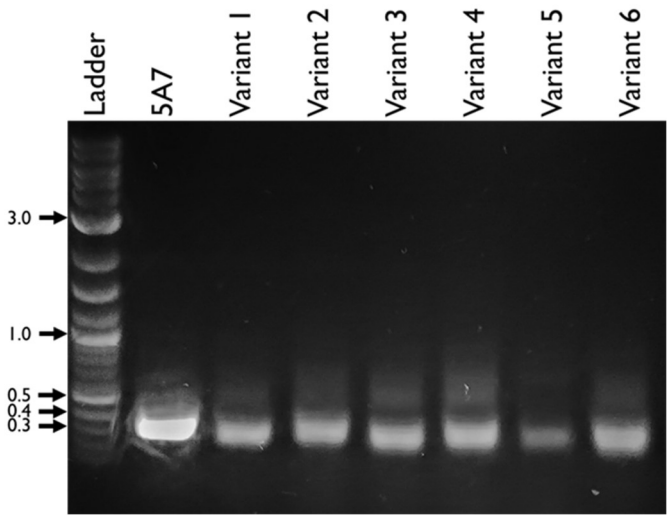


Figure 2.10 1% agarose gel of PCR-amplified vNAR_5A7 fragment and the 6 variants.

Line 1: New-England Biolab 1 kb Plus DNA Ladder. Lane 2: vNAR_5A7 amplified by PCR. Lane 3 to 8: PCR amplified variants introducing genetic diversity into the nanobody sequence.

2.3.2.2 Colony PCR

To optimise the ligation reaction, a pilot experiment was designed. Ligations were set up at three different molar ratios (vector: insert 1:0.5; 1:1; 1:2). Variant 3 was selected as a representative construct, providing a middle ground between the longer variants (5 and 6) and shorter ones (1 and 2). The appropriate amount of inserts was ligated to 100 ng of cut and cleaned pSEX81 vector. Each ligation reaction was then transformed into TG1 cells by electroporation, and the cells were plated on 2X TY-GA agar overnight. For each reaction, eight colonies were picked and prepared for colony PCR (QuickLoad Taq 2X master mix, 30 cycles, Tm = 44° C, predicted amplicon size = 571 bp) using primers For_pSEX and Rev_pSEx (Sigma). Each PCR reaction was then run on a 1% agarose gel. The ligation was considered successful if a 571 bp fragment could be observed. As seen in Figure 2.11, no successful ligation was observed in the negative control, 2 successful ligations were observed for ration 1:0.5, 4 successful ligations were observed for ration 1:1, and 5 successful ligations were observed for ration 1:2. This suggests that the 1:2 molecular ratio is the optimal ration for the pSEX81:variant 3 ligation. To confirm this ratio would be adequate for fragments of different sizes, the pilot experiment was repeated using variants 1 and 6. Contrary to variant 3, variants 1 and 6 showed poor ligations at the 1:2 ratio (Figure 2.12). To mitigate the variations amongst fragments, a molar ratio of 1:1 was used for all variants.

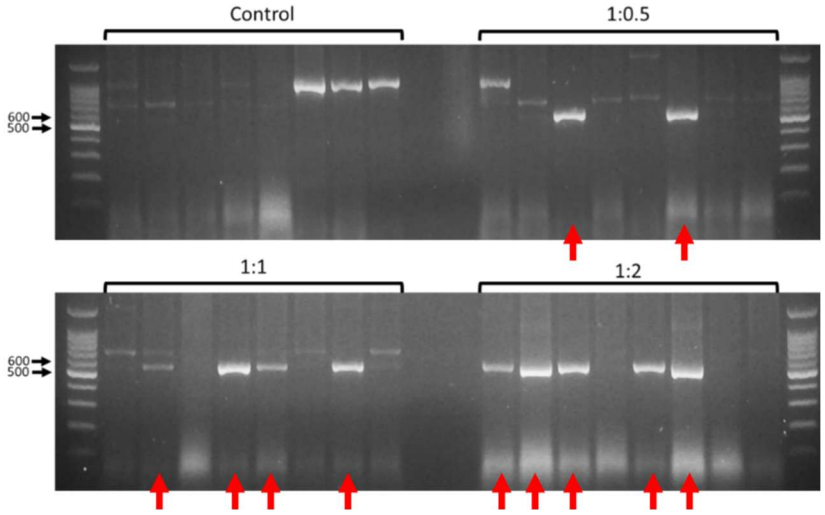


Figure 2.11 Colony PCR of the pSEX81: fragment 3 ligation at various molecular ratios.

Lane 1 for all gels: 1 kb DNA ladder (New-England Biolab). Lane 2 to 9: 8 colonies were picked from each tested ratio for colony PCR. Positive samples are marked with a red arrow.

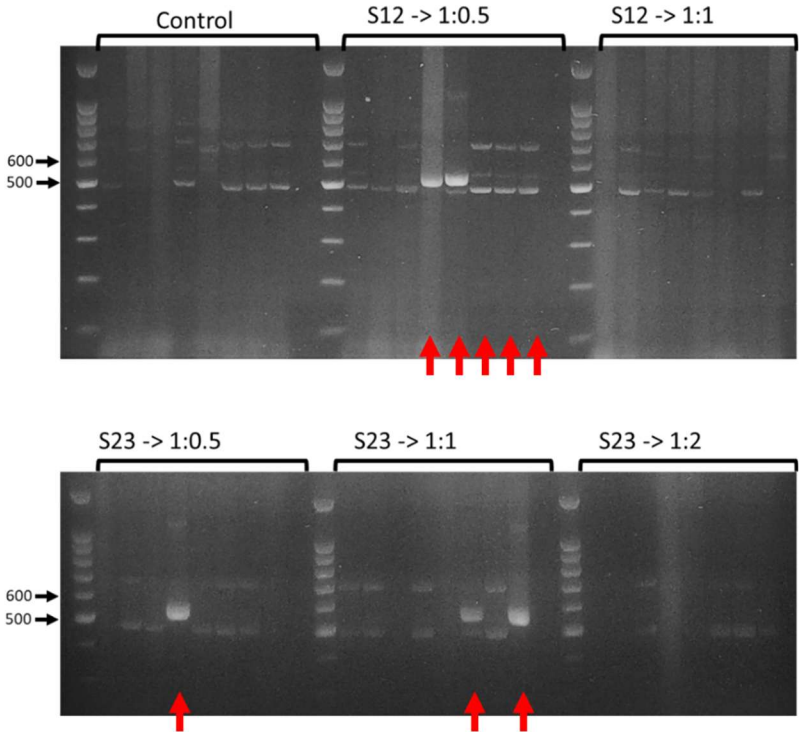


Figure 2.12 Colony PCR of the pSEX81: fragment 1 and pSEX81: fragment 6 ligations at various molecular ratios.

Lane 1 for all gels: 1 kb DNA ladder (New-England Biolab). Lane 2 to 9: For each fragment and ratio, 8 colonies were analysed by PCR. S12 = Variant 1, S23 = Variant 6. Positive samples are marked with a red arrow.

2.3.2.3 First Library Transformation

The ligated plasmids were transformed in TG1 electrocompetent cells by using 1 µg ligated DNA (1 µg linear plasmid ligated with the appropriate amount of DNA based on PCR fragment size, at the 1:1 ratio) and 100 µL of competent cells by electroporation. Following incubation, the library was pooled and 10^{-2} to 10^{-5} dilutions of the library, 10^{-1} and 10^{-2} dilutions of the positive control and 100 µL of the undiluted negative control were plated on 2X TY-GA plates (plates can be viewed in Appendix 2, Figure A. 5). This resulted in a transformation titre of $2.52 \times 10^8 \pm 1.33 \times 10^7$ (SE).

To assess the diversity of the nanobody library, one sample of 50 ng of material was sent to Eurofins for Next-Generation Sequencing (NGS). Low quality reads were trimmed, and sequences were paired, resulting in 222,557 total reads. To assess the quality of the sequencing, FastQC, a quality control tool for high throughput sequence data, was used (Andrew, 2010). As displayed in Figure 2.13 A, FastQC analysed the quality of the reads per base pair using the Phred score. The Phred quality score is used to measure base quality in DNA sequencing. Higher Phred values indicate greater consistency of the sequenced base. A Phred score of 20 signifies that there is a 1 in 100 chance of an incorrect base call, meaning the precision of the base call is 99% (Ewing *et al.*, 1998; Ewing and Green, 1998). The quality of the reads was considered sufficient until past 500 bp. As the run progresses, call quality on most platforms tends to degrade, making it common for base calls to fall into the 'reasonable' quality zone towards the end of a read. Therefore, the quality of the sequencing was considered adequate for further analysis. In Figure 2.13 B, a per sequence quality score report is displayed. It enables the identification of subsets of sequences that consistently exhibit low-quality values (Phred scores) so that they can be removed before subsequent analysis. Figure 2.13 C shows the GC content per percentage sequence. This is usually expected to be normally distributed with a mean corresponding to the average GC genomic content of the organism used. The GC genomic content of *E. coli* is known to be between 50.4% and 50.8% (Mann and Chen, 2010). However, the calculated Gaussian distribution here resulted in a mean of 57.57 ($\mu = 57.57$, $\sigma = 4.376$, dF = 98). This shift in the normal distribution could

indicate some systematic bias that is independent of base position. Finally, in Figure 2.13 D, a graph showing the distribution of fragment sizes reveals that sequences are distributed around the 149 and 429 bp mark. This is unexpected, as all fragments should cluster around the 429 bp size (average size of amplicon following library preparation). Overall, this library was considered sufficient quality for further analysis, but the unexpected sequence length might mean some discrepancy in the alignments and should be kept in mind.

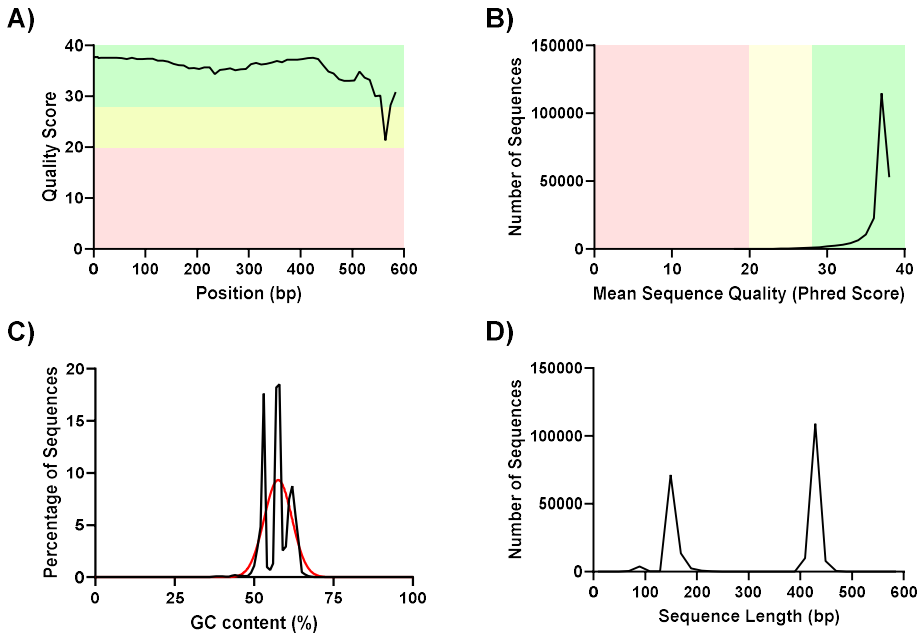


Figure 2.13 Selected results of FastQC analysis of library 1 NGS.

A: Mean quality value across all bases at a given position in the read. A quality of 28 or above is considered good (in green), a quality between 20 and 28 is considered reasonable (yellow) and a quality below 20 is considered poor (red). B: Per sequence quality score. A quality of 28 or above is considered good (in green), a quality between 20 and 28 is considered reasonable (yellow) and a quality below 20 is considered poor (red). C: GC content distribution observed (in black) and calculated according to a Gaussian distribution (in red). D: Sequence length distribution graph, showing peaks at 149 and 429 bp.

Duplicates were removed, resulting in 46,095 unique sequences. Finally, reads under 100 bp were discarded, leaving the final 45,745 sequences for alignments. The shorter sequences clustering around the 149 bp mark were included to account for potentially incomplete sequencing. Those unique sequences were

aligned to the seven possible outcomes of the NGS preparatory PCR: NGS amplicon encoding native 5A7, NGS amplicon encoding F12 randomised sequence, NGS amplicon encoding F13 randomised sequence, NGS amplicon encoding F16 randomised sequence, NGS amplicon encoding F18 randomised sequence, NGS amplicon encoding F20 randomised sequence and NGS amplicon encoding F23 randomised sequence. This operation sorted the sequences by percentage identity to each of the various possible amplicons. It revealed that no sequences mapped to the empty pSEX81 vector, and 20,522 sequences (44.86%) closely resembled the native 5A7, meaning that only the remaining 25,183 sequences (55.05%) were potentially novel nanobodies. In Figure 2.14 A, the number of sequences that aligned to each template was plotted, and revealed that the shorter fragments, and particularly F12, ligated and transformed better than longer fragments. This effect might be due to the unique ligation ratio used for all fragments, and optimising this parameter in the future might lead to a more even distribution of the fragment sizes within the library. Figure 2.14 B shows the percentage identity of the sequences aligned with the 5A7 template. While this percentage identity is high throughout the 5A7 domain, single nucleotide changes could still result in binding effects and novel nanobodies. Finally, Figure 2.14 C shows the identity score of alignments of the NGS reads to the various fragments. As expected, sequences show a low identity score in the primer binding region of the sequence, where the genetic diversity was introduced by randomised PCR. Peaks in these regions reflect the conserved cysteines encoded by each of the primers.

Consensus sequences were then generated from these alignments and translated with the appropriate reading frame to ensure accurate representation of the protein-coding regions. The resulting consensus sequences were subjected to multiple sequence alignments (CLUSTAL) to identify conserved motifs and domains, as well as confirm the variability introduced by the randomised PCR. As can be seen in Figure 2.15, the alignment revealed areas of high conservation where the conserved sequences should be, as well as variability within the randomised region. The cysteines were conserved for all fragments apart from F20, where the cysteines seem to have mutated into prolines. Prolines have a cyclic structure that influences

protein folding by creating kinks, whereas cysteines have a thiol group capable of forming disulphide bonds that stabilise the three-dimensional structure of proteins. This amino acid could be problematic in producing quality nanobodies by altering the structure. Proline is encoded by CCU, CCC, CCA, and CCG, while Cysteine is encoded by UGU and UGC, revealing that an error early in the PCR process might have contributed to this change.

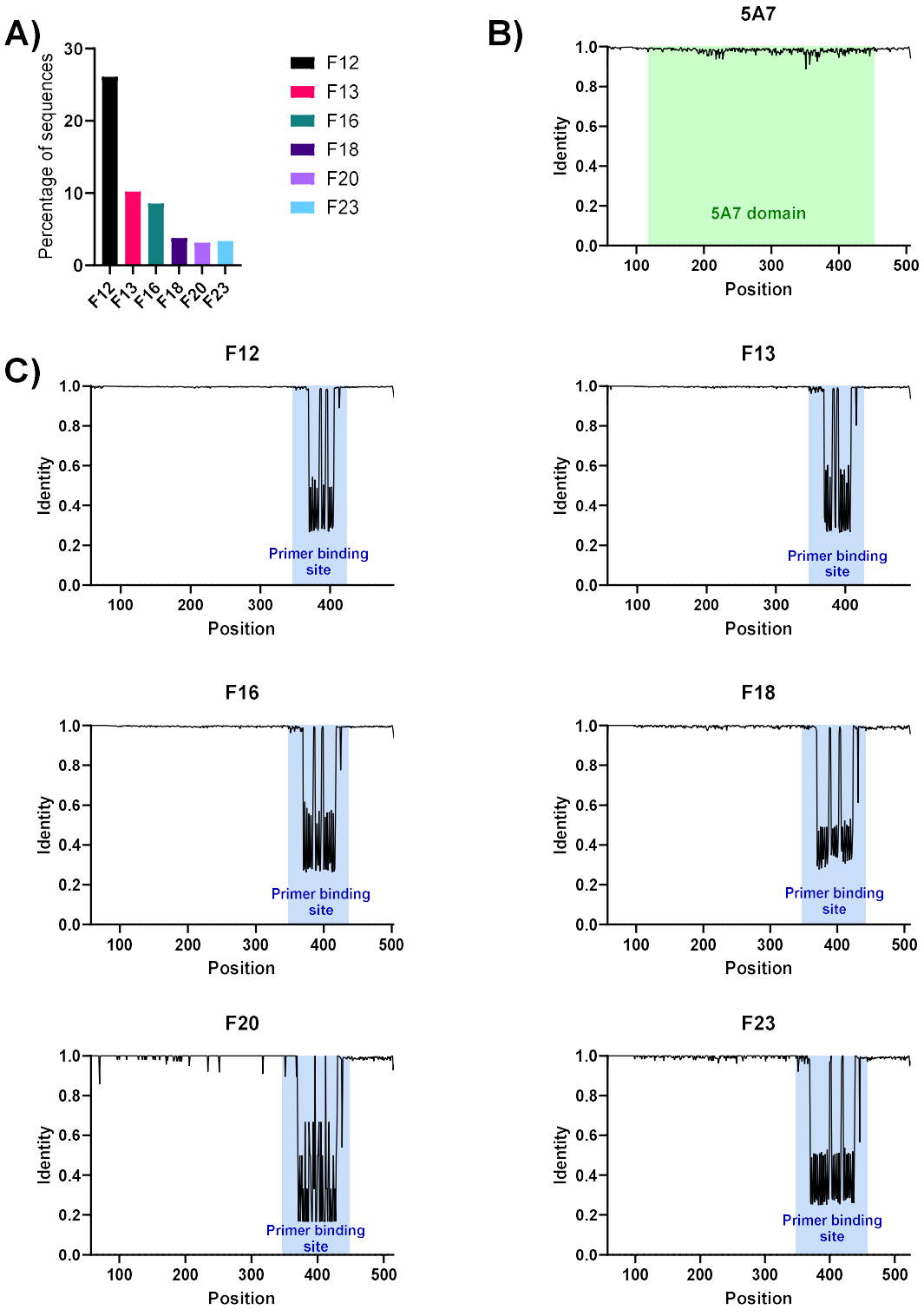


Figure 2.14 Alignments of NGS library 1 with the native 5A7 fragments, as well as the various randomised fragments.

A: Distribution of best fit alignment per fragment, showing that smaller fragments were more successfully transformed and expressed than larger fragments. B: Alignment of sequences with the 5A7 native sequence revealed a high identity level throughout the sequence. C: Alignments with the various randomised fragments revealed a high-level identity throughout apart from the primers binding site, as expected. Peaks of identity through the primer binding domain correspond to the conserved cysteines through the randomised region and confirm proper alignment.

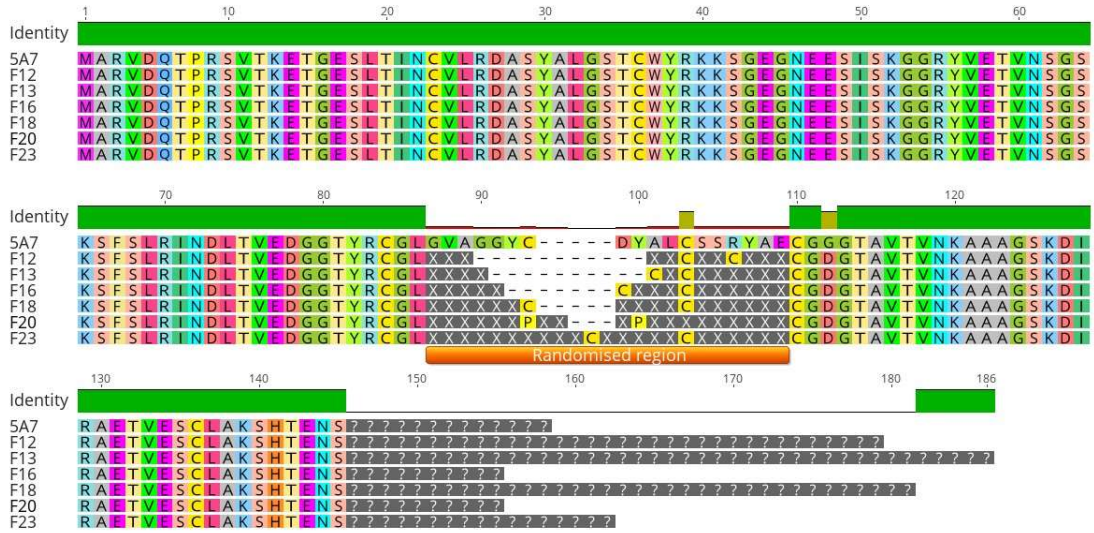


Figure 2.15 Alignment of the translated consensus resulting from the NGS data processing. *Each read was aligned to the best fitting fragment template, and the resulting consensus was translated with the appropriate reading frame, before being aligned to each other using a CLUSTAL multi-sequence alignment algorithm.*

2.3.2.4 Second Library Transformation

To improve the transformation titre, the ligated plasmids were transformed a second time in TG1, by using around 1 µg ligated DNA (1 µg linear plasmid ligated with the appropriate amount of DNA based on PCR fragment size, at the 1:1 ratio) and 300 µL of competent cells (three times more than for the first library) by electroporation. Following incubation, the library was pooled and 10^{-2} to 10^{-5} dilutions of the library, 10^{-1} and 10^{-2} dilutions of the positive control and 100 µL of the undiluted negative control were plated on 2X TY-GA plates (plates can ve viewed in Appendix 2, Figure A. 6). This resulted in a transformation titre of $7.42 \times 10^{9} \pm 1.88 \times 10^{9}$ (SE), which is a fold higher than for the previous library.

To evaluate the diversity of the nanobody library, two 50 ng samples were sent to Eurofins for Next-Generation Sequencing (NGS). After trimming low-quality reads and pairing sequences, the total reads amounted to 64,930 for run 1, and 60,809 for run 2 (125,739 for both runs). The sequencing quality was assessed using FastQC, a quality control tool for high-throughput sequence data (Andrew, 2010). As shown in Figure 2.16 A, FastQC analysed the quality of reads per base pair with the Phred score, which measures base quality in DNA sequencing. Higher Phred values indicate greater consistency of the sequenced base, with a Phred score of 20 indicating a 1 in 100 chance of an incorrect base call, meaning a 99% precision rate (Ewing *et al.*, 1998; Ewing and Green, 1998). The reads maintained good quality up to 500 bp, but call quality typically degrades over the run, causing base calls to fall into the 'reasonable' quality zone towards the end. Once again, the sequencing quality was deemed adequate for further analysis. Figure 2.16 B presents a per sequence quality score report, which helps identify subsets of sequences with consistently low-quality values (Phred scores) that can be removed before further analysis; however, no such sequences were found here.

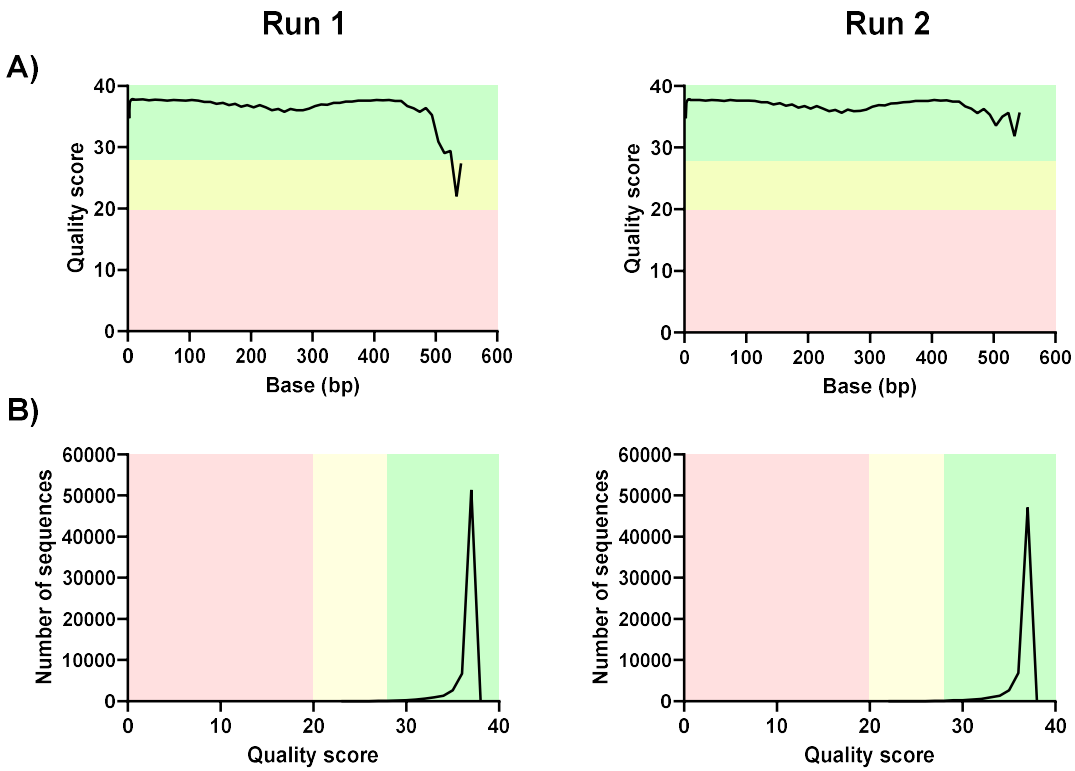


Figure 2.16 Selected results of FastQC analysis of library 2 NGSs.

A: Mean quality value across all bases at a given position in the read. A quality of 28 or above is considered good (in green), a quality between 20 and 28 is considered reasonable (yellow) and a quality below 20 is considered poor (red). B: Per sequence quality score. A quality of 28 or above is considered good (in green), a quality between 20 and 28 is considered reasonable (yellow) and a quality below 20 is considered poor (red).

Figure 2.17 displays the GC content per percentage sequence, which is generally expected to be normally distributed with a mean corresponding to the organism's average genomic GC content. For *E. coli*, this is between 50.4% and 50.8% (Mann and Chen, 2010). Here, the calculated Gaussian showed a mean of 52.31 for each run ($\mu = 52.31$, $\sigma = 0.79330$, dF = 98 for run 1, and $\mu = 52.31$, $\sigma = 0.7893$, dF = 98 for run 2), indicating a potential systematic bias independent of base position, although this is not as pronounced as in library 1, and both runs are within two standard deviations of the average genomic GC content for *E. coli*.

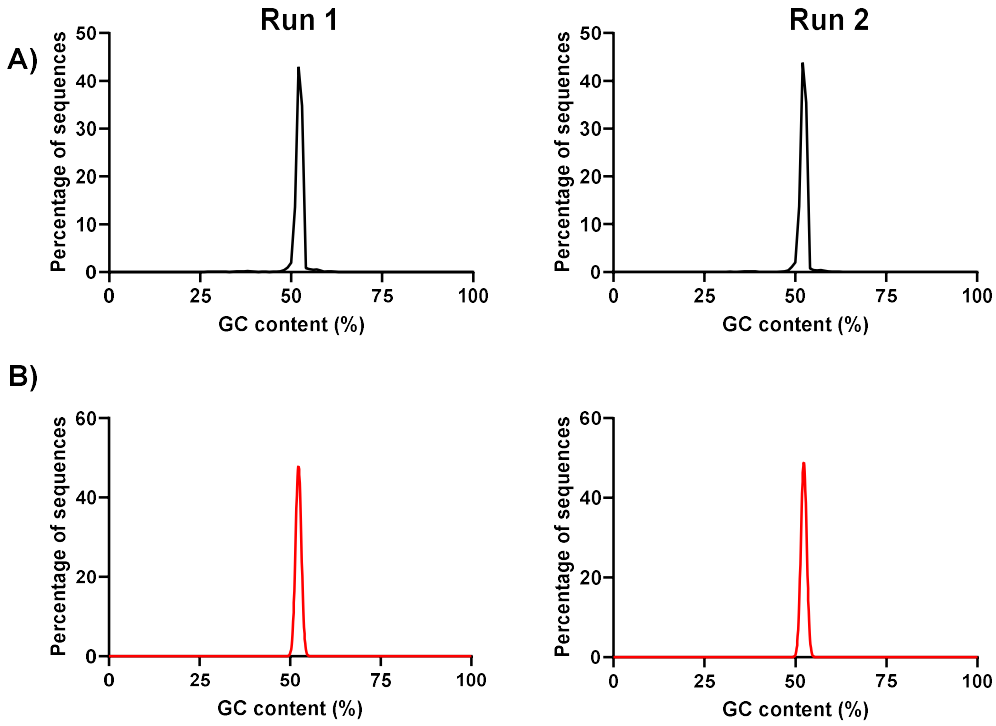


Figure 2.17 GC content distribution of library 2 analysed by NGS twice.

A: GC content distribution observed (in black). B: GC content distribution calculated according to a Gaussian distribution (in red).

Lastly, Figure 2.18 reveals the distribution of fragment sizes, showing sequences clustered around 429 bp for both samples. This is a clear improvement from library 1 and within the expected range.

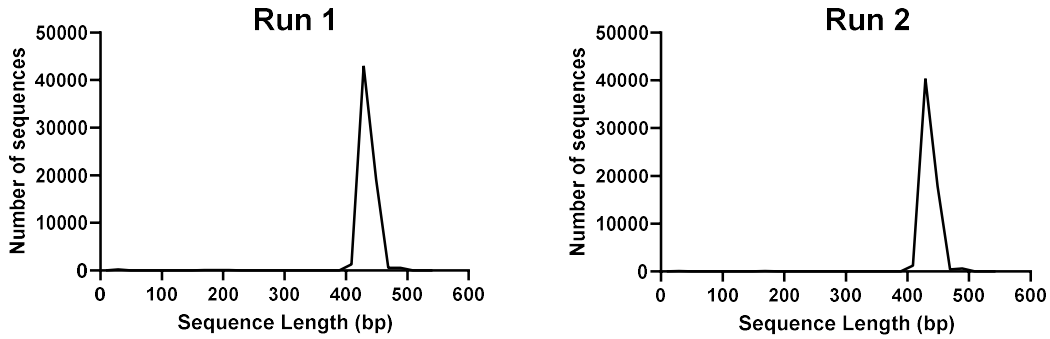


Figure 2.18 Sequence length distribution of library 2 analysed by NGS twice.

A peak at 429 bp is visible for both runs.

Subsequently, sequence lists were merged, and duplicates were removed, resulting in 43,469 unique sequences. Sequences under 100 bp were removed, giving

a final list of 43,403 sequences. Those unique sequences were aligned to the seven possible outcomes of the NGS preparatory PCR: NGS amplicon encoding native 5A7, NGS amplicon encoding F12 randomised sequence, NGS amplicon encoding F13 randomised sequence, NGS amplicon encoding F16 randomised sequence, NGS amplicon encoding F18 randomised sequence, NGS amplicon encoding F20 randomised sequence and NGS amplicon encoding F23 randomised sequence. This operation sorted the sequences by percentage identity to each of the various possible amplicons. The identity per base for each alignment can be seen in Figure 2.19. It revealed that no sequences mapped to the empty pSEX81 vector, and 30,326 sequences (69.87%) closely resembled the native 5A7, meaning that only the remaining 13,075 sequences (30.12%) were novel nanobodies.

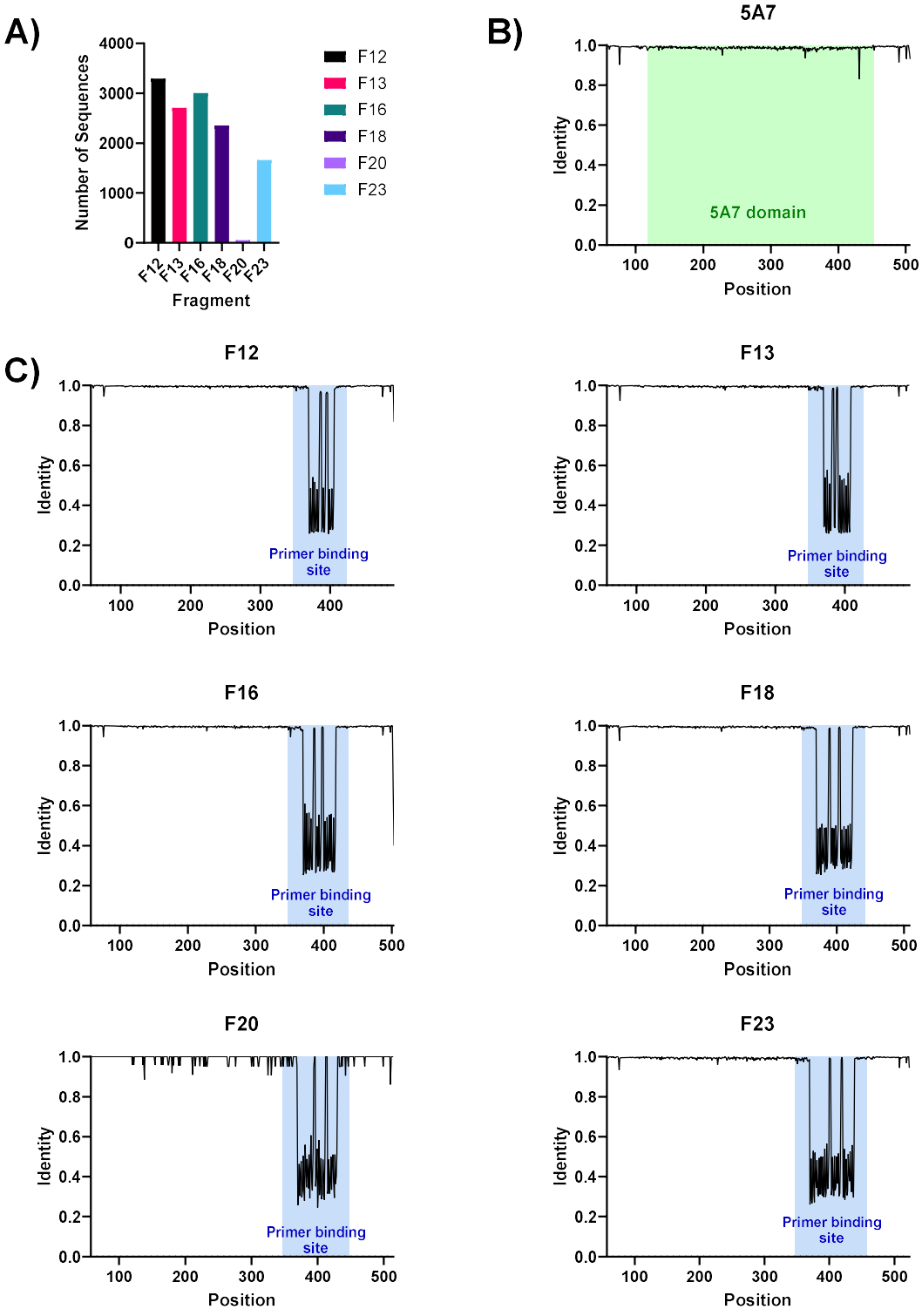


Figure 2.19 Alignments of NGS library 2 with the native 5A7 fragments, as well as the various randomised fragments.

A: Distribution of best fit alignment per fragment, showing that smaller fragments were more successfully transformed and expressed than larger fragments. B: Alignment of sequences with the 5A7 native sequence revealed a high identity level throughout the sequence. C: Alignments with the various randomised fragments revealed a high-level identity throughout apart from the primers binding site, as expected. Peaks of identity through the primer binding domain correspond to the conserved cysteines through the randomised region and confirm proper alignment.

Once again, the F20 fragment posed an issue and showed a very low number of reads aligning. There are several possible explanations for this. Firstly, secondary structures in DNA can pose significant challenges during ligation because they involve intra- or intermolecular interactions that can hinder the accessibility or availability of the ends required for ligation. Hairpin, which occur when sequences within a single strand of DNA are complementary and fold back on themselves to form a double-stranded stem with a loop. Other structures such as cruciforms can form in double double-stranded DNA. Finally, G-quadruplexes are typically stable structures that can form where hydrogen bonds appear between guanines in guanine-rich sequences. These secondary structures can affect ligation and polymerase chain reactions by reducing the accessibility of DNA sequences, creating misalignments of double strands, and impairing enzyme activity, leading to difficulties in digestion and ligation of fragments. Several steps can help reduce the occurrence of secondary structures. Heat treatments or additives such as DMSO or betaine before ligation can help destabilise and reduce secondary structures. Increased reaction time can also increase the successfulness of ligations and PCRs. As mentioned in the above method section, reaction times for fragment PCR and ligations were extended to the maximum recommended by the enzyme manufacturer (New-England Biolab) and DMSO was consistently used. Moreover, the apparition of numerous and frequent secondary structures with F20 only seems unlikely.

Consensus sequences for each alignment were translated and compared to the original vNAR 5A7 using a CLUSTAL multi-sequence alignment algorithm. All obtained consensuses were consistent with the expected synthetic design, validating the construction of the library further (see Figure 2.20).

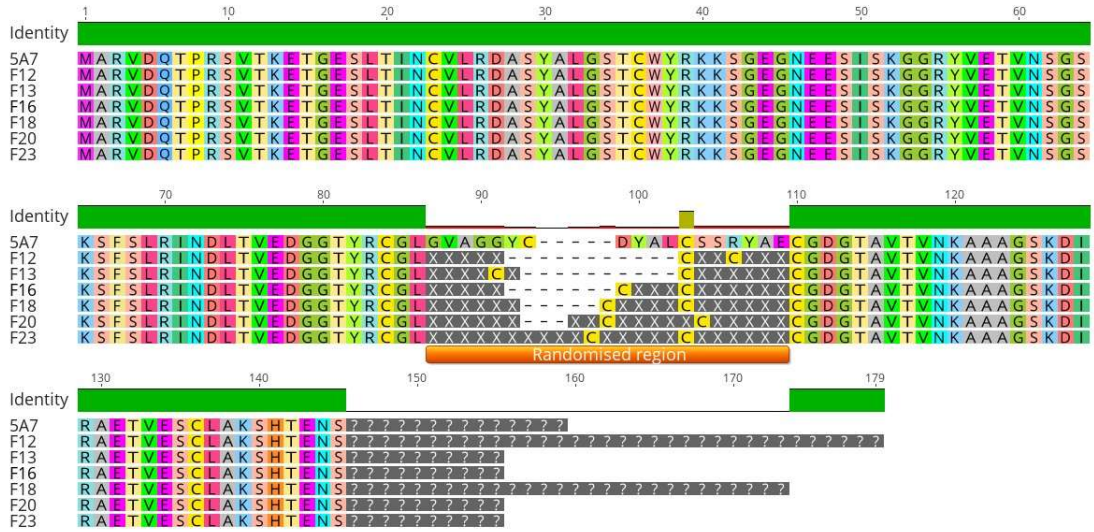


Figure 2.20 Alignment of the translated consensus resulting from the NGS data processing. *Each read was aligned to the best fitting fragment template, and the resulting consensus was translated with the appropriate reading frame, before being aligned to each other using a CLUSTAL multi-sequence alignment algorithm.*

2.3.3 Assessing Final Library Diversity

To determine the number of possible sequences that the given DNA sequence can produce, we need to consider the variability introduced by the ambiguous bases 'N' and 'K'. As mentioned previously, here N stands for any base (A, C, G, or T), meaning there are four possible choices for each N; and K stands for either T or G, meaning there are 2 possible choices for each K. Therefore, NNK codon, there are 20 amino acids possible as well as one stop codon, translated to glutamic acid by the SupE *Escherichia coli* (*E. coli)* strain. So, for each fragment, the number of possible sequences is:

$$Number\ of\ sequences = Number\ of\ NNK\ codons^{20}$$

As an example, for fragment 12, There are 10 NNK codons in the sequence, giving us:

$$Number\ of\ sequences = 10^{20}$$

So, the fragment 12 DNA sequence can produce 10^{20} possible sequences due to the variations introduced by the ambiguous bases N and K. This calculation was

repeated for each fragment, and results can be seen in Table 2.11. This gives us a maximum size for the library based on fragment variability of 2.923×10^{26}.

Table 2.11 Number of possible sequences per fragment size.

Fragment ID	Number of NNK codons	Total Possible Sequences	
F12	10	10000000000000000000	1.000×10^{20}
F13	11	67274999493256000000	6.727×10^{20}
F16	14	83668255425284800000000	8.367×10^{22}
F18	16	1208925819614630000000000	1.209×10^{24}
F20	18	127482362163961000000000000	1.275×10^{25}
F23	21	278218429446952000000000000	2.782×10^{26}
Total for all fragments		292260032488382000000000000	2.923×10^{26}

However, the maximum diversity will be capped by the library construction method. Only a certain number of genes will be synthesised by PCR, and only a certain number of plasmids will transform into a certain number of bacteria. As previously mentioned, the transformation titres of the libraries were $2.52 \times 10^8 \pm 1.33 \times 10^7$ (SE) and $7.42 \times 10^9 \pm 1.88 \times 10^9$ (SE) respectively. When analysed by NGS, only a certain number of sequences were unique and sufficiently long for analysis (above 100 bp). Those represented 20.55% of total sequences for library 1, and 34.52% for library 2. Therefore, the maximum calculated diversity of each library is $5.18 \times 10^7 \pm 2.73 \times 10^6$ (SE) for library 1, and $2.56 \times 10^9 \pm 6.49 \times 10^8$ (SE) for library 2. Those numbers are recapitulated in Table 2.12.

Table 2.12 Values obtained from libraries used to calculate diversity.

The transformation titre was calculated based on the number of colonies in plated dilutions. The total number of sequences was obtained from files provided by Eurofins. Sequences were deduplicated and trimmed using Geneious. The final library diversity was calculated as a percentage of appropriate sequences from the titre.

	Library 1	**Library 2**
Transformation titre	$2.52 \times 10^8 \pm 1.33 \times 10^7$ (SE)	$7.42 \times 10^9 \pm 1.88 \times 10^9$ (SE)
Total sequences (NGS)	222,557	125,739
Deduplicated sequences	46,095	43,469
Length trimmed	45,745	43,403
Percentage of total (%)	20.55428497	34.51832765
Final library diversity	$5.18 \times 10^7 \pm 2.73 \times 10^6$ (SE)	$2.56 \times 10^9 \pm 6.49 \times 10^8$ (SE)

While no other libraries developed using the methodology from Zadeh *et al.* (2019) have been reported in the literature, comparable nanobody libraries constructed using the camelid cAbBCII10 nanobody scaffold have reported similar levels of diversity. 1.65×10^9 CFU/mL with an insertion rate of 100% was reported by Yan *et al.* (2014), but no calculation of bias and/or duplicates was performed. Cabanillas-Bernal *et al.* (2019) reported 1.2 x10^9, 4.0 x10^9 and 3.4 x10^{11} CFU, but only 65% diversity and 86% insertion. In each of these studies, no NGS analyses of nanobodies were performed, meaning that the estimated library size does not take fully into consideration potential duplicates, bias or wild-type sequence contamination. Utilising the NGS technology allows for a more accurate representation of the library size and can help flag biases in the sequences that could result in poor binding efficiency. Tsai *et al.* (2023) constructed a similar nanobody library based on the vNAR 5A7 scaffold and measured their library diversity utilising comparable NGS analysis. They reported a diversity of 1.97×10^9. Commercial libraries tend to report higher diversities, but these are often expressed as colony forming units (CFU) and therefore not a true representation of actual diversity (see Table 2.13).

Table 2.13 Selected examples of phage-display antibody fragment library.

Library size is expressed as colony forming unit (CFU). TU-IB: Technische Universität Braunschweig, Institut für Biochemie, Biotechnologie und Bioinformatik; KNU: Kangwon National University. Adapted from Almagro et al. (2019). Published in Antibodies. © 2019, licensed under CC BY.

Library Name	Company/Laboratory	Repertoire	Display Format	Size
XFab1	Xoma	Naïve	Fab	3.1×10^{11}
XscFv2	Xoma	Naïve	scFv	3.6×10^{11}
HAL9/10	TU-IB	Naïve	scFv	1.5×10^{10}
KNU-Fab	KNU	Naïve	Fab	3.0×10^{10}
pIX V3.0	Janssen Bio	Synthetic	Fab	3.0×10^{10}
HuCAL PLATINUM	MorphoSys	Synthetic	Fab	4.5×10^{10}
Ylanthia	MorphoSys	Synthetic	Fab	1.3×10^{11}
PHILODiamond	ETH Zurich	Synthetic	scFv	4.1×10^{10}
ALTHEA Gold Libraries	GlobalBio/ADL	Semisynthetic	scFv	2.1×10^{10}

2.4 Conclusion

The binding of vNAR 5A7 against HEL was assessed and revealed a strongly significant difference in phage binding capacity between HEL and BSA control (t = 16, 58, dF =11, p<0.0001). A semi-synthetic library was constructed based on previously published methodology, and NGS analysis confirmed a library diversity of $2.56 \times 10^9 \pm 6.49 \times 10^8$ (SE), consistent with previously published libraries in the literature.

Chapter 3 Identification of Targets

3.1 Introduction

3.1.1 The Role of Goblet Cells in Airway Hypersecretion

Goblet cells play a crucial role in airway hypersecretion, a hallmark feature of airway hypersecretory diseases (AHDs). These specialised epithelial cells are abundant in the respiratory tract and are responsible for producing and secreting mucus. In healthy airways, mucus serves as a protective barrier, trapping and removing inhaled particles, pathogens, and irritants, thus maintaining respiratory health. However, in conditions of airway inflammation and hyper-responsiveness, goblet cell activity becomes dysregulated, leading to an excessive production and secretion of mucus. This hypersecretion of mucus can result in mucus plugging, airway obstruction, and impaired lung function, contributing to the characteristic symptoms of increased coughing, wheezing, and shortness of breath. Excess mucus also provides a favourable environment for bacterial growth, further exacerbating airway inflammation and worsening the disease progression. Targeting goblet cell hypersecretion represents a potential therapeutic approach to alleviate airway obstruction and improve respiratory function in patients with airway hypersecretion-related respiratory diseases.

3.1.2 Airway Epithelium Models

3.1.2.1 Immortalised cell lines as airway epithelium models

Calu-3 cells have become invaluable tools in respiratory research due to their relevance as an *in vitro* model for studying airway epithelial function and drug testing. These human bronchial epithelial cells, derived from a lung adenocarcinoma, exhibit characteristics similar to the native respiratory epithelium, including the presence of cilia and mucus-producing goblet cells. Calu-3 genotype is available as part of the American Type Culture Collection (ATCC, Nguyen *et al.*, 2024). Calu-3 cells form

polarised monolayers and retain the ability to secrete and transport ions and molecules across the cell membrane, making them suitable for investigating processes such as mucociliary clearance and ion transport. Their use in respiratory research allows for the exploration of host-pathogen interactions, respiratory virus infections, and the study of drug absorption, metabolism, and toxicity in the context of the lung epithelium. By providing a cost-effective and accessible model, Calu-3 cells continue to play a pivotal role in advancing our understanding of respiratory diseases and aiding the development of novel therapeutic interventions for respiratory disorders. However, as Calu-3 is an immortalised cell line derived from lung adenocarcinoma, it is constituted of only one cell type and does not differentiate in the same way as primary cells, making them an imperfect model for studying the epithelium layer. Moreover, they present an abnormal karyotype and can grow polyps under certain conditions.

BEAS-2B cells have also been used in respiratory research (Sharma *et al.*, 2023). These cells originate from non-tumorigenic human bronchial epithelial cells and were immortalised using Ad12-SV40 virus in 1988 (Ke *et al.*, 1988). While these cells can be an appropriate model for some respiratory research, their inability to generate goblet cells and low mucin production disqualified them for this study (Stewart *et al.*, 2012).

Finally, A549 human alveolar type II-like cells are also commonly used in airway research. While they do produce mucus under stimulation, their alveolar (and not bronchial) origin, where mucus production is normally absent, make them poorly suited to the study of airway hypersecretory diseases (Lagowala *et al.*, 2021).

3.1.2.2 Human Bronchial Epithelium Primary Cells

Primary cells offer a more biologically relevant and representative model of the human respiratory system. These cells are directly derived from human lung tissues, preserving the native cellular characteristics and complex interactions within the lung microenvironment. Compared to immortalised cell lines, primary cells better mimic the *in vivo* physiology and responses of the respiratory epithelium, providing a more biologically relevant understanding of disease mechanisms, host-pathogen

interactions and drug responses (Michi and Proud, 2021; Stewart *et al.*, 2012). Moreover, primary cells offer the advantage of genetic diversity, reflecting individual variations in disease susceptibility and treatment response. Their use enables the investigation of personalised medicine approaches and the development of targeted therapies for respiratory disorders and infections (Lee *et al.*, 2020; Ramalho *et al.*, 2023; Woehlk *et al.*, 2023). However, primary cells are more technically challenging and costly to grow, and they also present a limited lifespan of 16 population doublings, or about four passages, which limits their use in respiratory research (Reeves *et al.*, 2018).

Air-liquid interface (ALI) culture of human bronchial epithelial cells is a specialised technique used to cultivate these cells in a way that closely mimics their natural environment in the human respiratory tract. In this method, bronchial epithelial cells are grown on a semipermeable membrane with their basal surface exposed to a nutrient-rich medium and their apical surface exposed to air. This setup allows the cells to differentiate and form a pseudostratified epithelium, complete with cilia and mucus-producing goblet cells, replicating the cellular architecture and functionality of the bronchial epithelium *in vivo*. ALI cultures are invaluable for studying respiratory biology, disease mechanisms, drug responses, and the effects of environmental exposures on airway epithelium, providing a more physiologically relevant model compared to traditional submerged cultures (Levardon *et al.*, 2018; Silva *et al.*, 2023; Stewart *et al.*, 2012).

The use of ALI cultivated human bronchial epithelium in this research allows for the identification of surface available antigens as target for nanobody binding, by using the cultivated epithelium as a target in lieu of immobilised antigens. This approach replicates physiological conditions more accurately and can result in improved specificity and affinity of the isolated antibody fragments.

3.1.3 Fluorescence Activated Cell Sorting and Goblet Cell Isolation

Flow cytometry allows for the identification of cells through physical and chemical characteristics. Cells in suspension are labelled using fluorescent probes

attached to antibodies and passed through one or more laser beams in single file. This enables rapid and quantitative measurement of cellular characteristics, such as size, granularity and fluorescence, for thousands of cells per second by analysing their scattering and emission signals. By using fluorescently labelled antibodies or other probes, flow cytometry enables the identification and sorting of specific cell subsets and is widely employed in immunology for immunophenotyping, cell cycle analysis, apoptosis detection, and immune response assessment.

Fluorescence-Activated Cell Sorting (FACS) couples the mechanisms of flow cytometry with the ability to sort cell samples into various populations based on predetermined characteristics from heterogenous cell populations. Fluorescently labelled antibodies or probes are used to target specific cell surface or intracellular markers, allowing for precise identification and sorting of distinct cell subsets.

In the context of airway research, this technique can be used to sort ALI cultivated human bronchial epithelium into cell subpopulation, separating the different cell types. In 2021, Bonser *et al.* developed a larger panel of antibodies for the simultaneous analysis of the major subsets of airway epithelial cells, providing a new tool for understanding airway epithelial physiology and pathology (Bonser *et al.*, 2021). Known markers described in the literature, augmented with information from single cell RNA sequencing datasets (such as CDHR3 [cadherin-related family member 3; ciliated] and CEACAM5 [carcinoembryonic antigen-related cell-adhesion molecule 5; secretory]) were used; and antibody panels for flow cytometry to identify, characterise, and isolate the major human airway epithelial subsets were developed (Duclos *et al.*, 2019; Ordovas-Montanes *et al.*, 2018; Plasschaert *et al.*, 2018; Ruiz García *et al.*, 2019).

3.1.4 Biopanning

3.1.4.1 Principle

Antibody biopanning allows for the selection of specific antibodies from large libraries, typically phage display libraries. Advancements in molecular biology and recombinant DNA technology enabled the creation and manipulation of vast libraries

of antibodies. As previously mentioned, the concept of antibody biopanning was significantly advanced by the development of phage display technology by George P. Smith in 1985 (Smith, 1985). Smith demonstrated that peptides could be expressed on the surface of bacteriophages and that phages displaying specific peptides could be isolated from large libraries through affinity selection. In 1990, the technique was further refined when J. McCafferty, A. Griffiths, G. Winter, and D. Chiswell described the display of functional antibody fragments on the surface of bacteriophages, notably utilising the surface protein pIII of M13 bacteriophages (McCafferty *et al.*, 1990). They showed that antibodies could be selected from libraries based on their binding affinity to specific antigens, a process now known as antibody biopanning.

The technique involves several rounds of selection, where a phage library displaying a diverse array of antibody fragments is exposed to an immobilised antigen. Phages that bind to the antigen are retained, while non-binders are washed away. Bound phages are then eluted and amplified in bacteria, enriching the pool of antigen-specific phages. Additionally, depletion round against contaminant antigens (such as plastics and buffers) can be used to remove non-specific binders. Repeated rounds of this selection process progressively enrich the library for high-affinity antibodies. A schematic representation of the biopanning process is presented in Figure 3.1.

Antibody biopanning has since evolved with improvements in library construction, selection methods, and screening technologies. It has become a cornerstone method for generating monoclonal antibodies for research, diagnostic, and therapeutic purposes. The ability to rapidly isolate high-affinity antibodies from vast libraries has revolutionised antibody discovery and development, leading to numerous applications in medicine and biotechnology. Over 70 phage-derived monoclonal antibodies have been entered in clinical studies, and 14 have been approved. For example, Genentech human phage display library was used to screen for recombinants against human PD-L1. The PD-L1/PD-1 axis plays a central role in this suppression by inhibiting T-cell activity and tumour cell killing. Blocking PD-L1 enhances anticancer immunity, particularly in tumours with high PD-L1 expression on immune cells. This led to the development of an anti-PD-L1 antibody, which was

approved for the treatment of non-small cell lung cancer and urothelial carcinoma in 2016 (Alfaleh *et al.*, 2020; Herbst *et al.*, 2014; Irving *et al.*, 2012).

Optimising biopanning in phage display requires careful attention to multiple parameters to maximise the selection of high-affinity binders while minimising off-target interactions. One of the first key points for successful selection of relevant binders relies on ensuring the antigen mimics its native conformation. For this reason, using whole cells as biopanning targets is the most advantageous. Whole cell panning (WCP) removes the need for target protein expression and purification. Large membrane proteins are often insoluble and therefore present many challenges for purification. For example, WCP can be used to identify binders for membrane proteins lacking large soluble extracellular domains, such as ion channels. Secondly, using whole cells or engineered cell lines for displaying the antigen in phage display ensures that the membrane proteins retain their correct conformational structure. This is crucial because membrane proteins often undergo conformational changes or aggregation when isolated in a soluble form. Traditional expression methods often lead to improperly folded proteins due to the lack of appropriate post-translational modifications. Phage display using native cells helps overcome this by ensuring proteins are displayed in their natural, functional state. This can ensure that the isolated binders specifically bind to membrane proteins in their native conformational structure, ensuring that they recognise epitopes that are exposed in a physiological context.

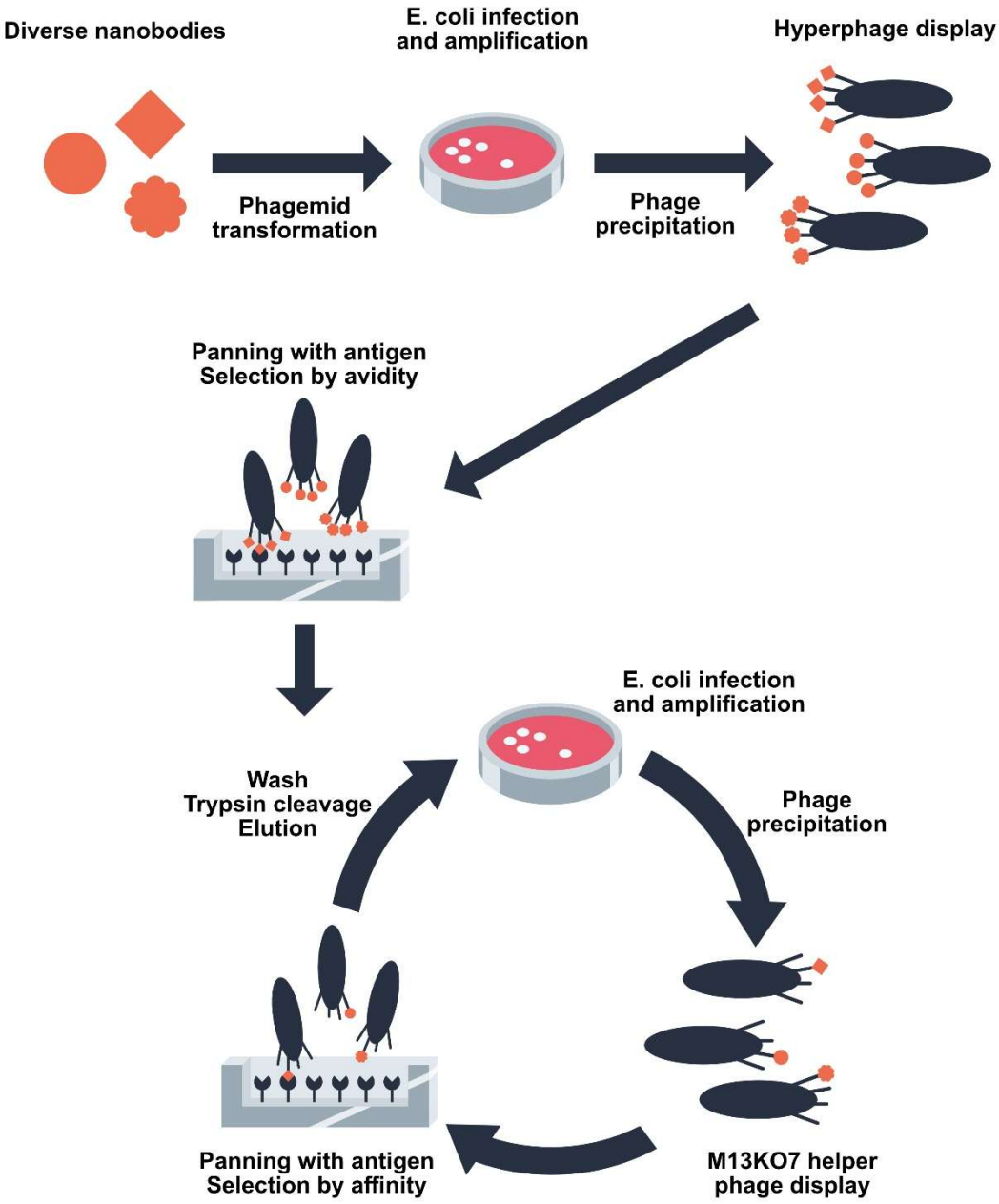


Figure 3.1 Schematic representation of the biopanning process in nanobody phage display. *A diverse nanobody library is transformed into E. coli. The bacteria are infected with Hyperphage and the packaged phagemid is amplified. Phages are precipitated and display a nanobody on each copy of their pIII gene. These phages are used to present their nanobodies to immobilised antigen. The binding phages are eluted and amplified using M13KO7 helper phages. The newly packaged phagemids display a lower number of copies of the nanobodies, leading to selection by affinity rather than avidity. The process is repeated until only the high affinity binders remain. Figure created using Affinity Designer 2.6.2 (available at affinity.serif.com).*

3.1.4.2 Limitations

While phage display is a powerful tool for antibody discovery, it presents notable limitations when compared to the mining of immunised animals' repertoires. The immune system imposes stringent filtration processes, ensuring mammalian-derived antibodies exhibit superior biophysical properties, such as better stability, selectivity, specificity, and reduced developability risks, compared to those generated by phage display. A significant proportion of approved therapeutic antibodies originate from immunised mice, highlighting the advantages of leveraging the natural immune system for antibody selection. Saggy *et al.* (2012) compared the characteristics of antibodies against hapten trinitrophenyl isolated either through the sequencing of V gene cDNAs obtained from total splenocytes of mice immunised with hapten trinitrophenyl, or through the phage display of a scFv library. Antibody genes abundant in immune repertoires and showing strong antigen specificity were poorly displayed on phages and failed to be enriched during phage panning. Additionally, phage display-derived antibodies often present higher self-interaction and poly-reactivity, attributed to a greater proportion of aliphatic residues in their CDRs, which can compromise therapeutic developability. The complex antibody-generation system of mammals leads better biophysical attributes, lower self-interaction and lower poly-reactivity in antibody fragments when compared to phage display methodologies, and additional steps to improve antibody characteristics might be required as a result and this is reflected in the therapeutic landscape (Jain *et al.*, 2017; Kaleli *et al.*, 2019).

3.1.4.3 The pSEX81 System

To facilitate the generation and screening of large and diverse antibody libraries, several molecular tools have been developed. As previously discussed, the pSEX81 system (PROGEN), composed of a phagemid and sets of primers, is one of those tools (see section 2.1.3, page 45).

The previously prepared nanobody library using the pSEX81 scaffold can be infected with M13 helper phage. The precipitated progeny phages can then be used directly for antigen biopanning. Additionally, the M13 Hyperphage (PROGEN) based

on the helper phage technology ('Hyperphage System') developed by Rondot *et al.* (2001) can be used to increase the number of scFv-pIII proteins displayed per phage (up to five versus one for traditional M13 bacteriophage). This allows for improved screening efficiency, requiring smaller amounts of antigens, and a selection by avidity as opposed to affinity. The library can then be further refined by utilising the traditional M13 bacteriophage for more stringent screening conditions.

3.1.5 Aim and Objectives

This chapter will focus on the culture of Air-Liquid Interface Human Bronchial Epithelial Primary Cells (ALI HBEpc) as a target for nanobody phage library biopanning. The successful culture of ALI HBEpc will be described, followed by the optimisation of the biopanning process of the library developed in chapter 2. Finally, the sequences of isolated binders will be analysed and discussed.

3.2 Materials and Methods

3.2.1 Human Bronchial Epithelial Primary Cell Culture

3.2.1.1 Liquid Culture

For liquid culture of Human Bronchial Epithelial primary cells (HBEpc, obtained from PromoCell, C-12640), LHC basal medium (Serum free with glutamine and phenol red, PromoCell, C-21260) was supplemented with 1% Penicillin-Streptomycin 5,000 U/mL (Gibco, 15140122) and 2.46% (v/v) media supplement mix (PromoCell, C-39165). The media was pre-warmed to 37° C and changed every 2 to 3 days, typically on Monday, Wednesday, and Friday. The media volumes used were 15 mL for T75 flasks and 5 mL for T25 flasks. Plastic items were treated with a collagen solution (SAFC, 125-50) at a concentration of 0.1 mL/cm², incubated at 37° C for 2 hours, and then drained. Plasticware, which had been treated with a protective coating, was kept refrigerated at 4° C for as long as six weeks. The coating volumes were 2.5 mL for T75 flasks (75 cm² surface area), 7.5 mL for T25 flasks (25 cm² surface area), 200 µL for large (12-well fit) inserts (1.91 cm² surface area), and 40 µL for small (24-well fit) inserts (0.32 cm² surface area). Cells were passaged upon reaching approximately 80% confluence. Media was removed, and cells were washed three times with 5 mL of pre-warmed PBS (Phosphate Buffer Saline, Gibco, 10010023). Cells were detached when required using 5 mL of TrypLE™ Express Enzyme (Gibco, 12605010) per T75 flask (1.5 mL for T25 flasks) and incubated at 37° C for 10 minutes. An equal volume of growth medium was added, and the cells were centrifuged at 350 x g for 5 minutes before being resuspended in 2 mL of medium. For cell counting and viability assessment, 10 µL of resuspended cells was mixed with 10 µL of Trypan Blue Solution, 0.4% (Gibco, 15250061) and loaded onto a Countess™ 3 Automated Cell Counter (Thermo Fisher Scientific) slide, with concentration and viability (ensuring>70% live cells) recorded. Cells were seeded at minimum densities of 5×10^5 cells for T75 flasks, 1.7×10^5 cells for T25 flasks, 1×10^5 cells for large (12-well fit) inserts, and 0.5×10^5 cells for small (24-well fit) inserts. For freezing, cells were resuspended at a density of 5×10^5 cells in growth media with 10% (v/v) DMSO (Sigma

Aldrich, D8418) and transferred to 2 mL cryotubes. Tubes were transferred into a pre-cooled (4° C) freezing container (Nalgene® Mr. Frosty) and kept at -80 °C overnight before being stored in liquid nitrogen vapour phase (-140 °C).

3.2.1.2 Air-Liquid Interface

Inserts (Corning® Transwell®, 0.4 µm pore size, tissue culture-treated polyethylene terephthalate (Corning, CLS3470-48EA) were seeded and grown at the liquid-liquid interface (growth media in both the apical and basal chamber) for 12 days. The apical media was then removed, and the cells were left to grow at the air-liquid interface. The insert surface was washed once a week with 500 µL pre-warmed PBS to remove potential mucus build up: PBS was applied to the apical surface of the insert before gentle aspiration. Cells were detached when required using 100 µL (apical) and 500 µL (basal) of TrypLE™ Express Enzyme and incubated at 37° C for 10 minutes. An equal volume of growth media was added, and cells were centrifuged at 350 x g for 5 minutes before resuspension in an appropriate buffer.

3.2.2 MucilAir™

MucilAir™ inserts are pre-cultured human upper airway epithelium at the air-liquid interface. Bronchial MucilAir™ from healthy non-smoker patients were obtained from Epithelix (EP01MD) as well as the specialised MucilAir™ culture medium (EP04MM).

Upon reception of the products, the plate was allowed to warm up for 1 hour in an incubator set to 37° C with 99% humidity and 5% CO2. Under a laminar flow hood, a new 24-well plate was prepared by filling each well with 0.7 mL of MucilAir™ culture medium, pre-warmed to 37° C. The cover of the MucilAir™ package was removed, and the plate was taken out of the box and transferred into the laminar flow hood. Using forceps, the inserts were carefully removed from the gel and transferred into the new plate. The plate was then placed into the incubator for normal culturing for up to a month, at 37° C, 99% humidity, and 5% CO2, and the medium was changed every 2 to 3 days.

Cells were detached using 100 µL (apical) and 500 µL (basal) of TrypLE™ Express Enzyme and incubated at 37° C for 10 minutes. An equal volume of growth media was added, and cells were centrifuged at 350 x g for 5 minutes before resuspension in an appropriate buffer.

3.2.3 IL-13 Stimulation

Cells were stimulated using IL-13 (Sigma Aldrich, SRP3274) at a final concentration of 10 ng/mL in the basal chamber for seven days after establishment of the air-liquid interface.

3.2.4 Flow Cytometry

All flow cytometry experiments were conducted with the help of the University of Nottingham flow cytometry staff, Dr David Onion and Nicola Croxall.

All reagent stocks were stored at 4° C in the dark. Ice-cold PBA staining buffer was prepared by adding 1% (w/v) BSA (Bovine Serum Albumin) to PBS (Phosphate Buffer Saline, 137 mM NaCl, 2.7 mM KCl, 8 mM Na2HPO4, 2 mM KH2PO4) and sterile filtering the solution through a 0.2 µm filter. Formaldehyde was diluted in PBS to a concentration of 3% (v/v).

Cells were first stained with the SiR-Tubulin staining kit (Spirochrome, Cytoskeleton Inc., CY-SC002): a staining solution was prepared fresh each time using SiR-Tubulin 1 mM in anhydrous DMSO, further diluted in culture medium with verapamil, a broad-spectrum efflux pump inhibitor, for a final concentration of 1 µM and 10 µM respectively. The solution was applied for 30 minutes at 37° C on the apical cell surface, before proceeding with the antibody staining.

Cells were detached using Tryplee as previously described (see section 3.2.1.1, page 100) and resuspended in PBA, ensuring a single cell suspension. Cell count and viability were assessed using a 1:1 dilution in Trypan Blue Solution, 0.4% (Gibco, 15250061) and a Countess™ 3 Automated Cell Counter (Thermo Fisher Scientific), and the volume of cells in PBA was adjusted to achieve a concentration of 1×10^6 to 1×10^7 cells/mL. Subsequently, 50 µL of cells were placed into the bottom

of a 5 mL FACS tube. The required amount of primary antibody was added to the cells and mixed by pipetting, before incubation on ice in the dark for 30 minutes minimum (maximum overnight). A table of all stains and antibodies used, as well as dilution factor, can be seen in Table 3.1. After incubation, 1.5 mL of PBA was added, and the cells were centrifuged at 300 x g for 5 minutes in a swing-out rotor. The supernatant was removed, and the pellet was vortexed. The centrifugation and vortexing steps were then repeated. The cells were then resuspended in 500 µL of PBA with 3% (v/v) formaldehyde for flow cytometry.

Table 3.1 List of stains and antibodies used for flow cytometry analysis and cell sorting.

Antibody	**Supplier and product code**	**Target**	**Fluorophore**	**Dilution Or Concentration**
Anti-human CD271 (NGFR)	Biolegend (345109)	Nerve growth factor receptor (NGFR)	PE-Cy7	1:100
Anti-human CD66a/c/e	Biolegend (342323)	Carcinoembryonic antigen-related cell adhesion molecule 6 (CEACAM6)	Brilliant Violet 605™	1:100
Anti-human TSPAN8 Antibody	Biolegend (378903)	Tetraspanin 8 (TSPAN8)	PE	1:100
Zombie UV™ Fixable Viability Kit	Biolegend (423107)	Viability dye	Zombie UV	1:100
SiR-Tubulin staining kit	Cytoskeleton (CY-SC002)	Microtubules (microtubule binding drug Docetaxel)	Silicon rhodamine (SiR)	1 µM

For analytical flow cytometry, samples were analysed on the Sony ID7000C Spectral Cell Analyser. For cell sorting, samples were run on the Beckman Coulter Astrios EQ. All data was analysed using Kaluza Analysis Software v2.2 (available at www.mybeckman.uk/flow-cytometry/software/kaluza).

3.2.5 Shark Nanobody Library Biopanning

3.2.5.1 Phage Amplification

An overnight culture of TG1 was set up from a single colony grown on M9 minimal agar plates (2.0 mM $MgSO_4$, 22.2 mM Glucose, 0.1 mM $CaCl_2$, 1X M9

Minimal Salts (Sigma Aldrich, M6030), 1.5% (w/v) agar powder) added to 500 mL fresh 2x TY-G media (0.6% (w/v) tryptone, 1% (w/v) yeast extract, 0.5% (w/v) NaCl, 100 mM glucose, pH 7.0 at 20° C) in a 2 L flask (1:100 dilution) and grown to OD_{600} = 0.6. 10^{12} phages were added, and the culture was incubated at 37° C, 250 rpm for 1 hour. Ampicillin and/or kanamycin were added, and the culture was incubated overnight at 30° C, 150 rpm. The cells were pelleted at 4500 x g, 4° C for 20 minutes twice. PEG salt solution (20% (w/v) polyethylene glycol, 2.5 M NaCl) was added to the culture media (1:5 dilution) and the phage solution was incubated overnight at 4° C. The phages were then pelleted at 17,700 x g, 4° C for 1 hour, before being resuspended in 1 mL sterile PBS. Leftover cells were pelleted out by centrifugation at 4500 x g for 20 minutes, and phages were again precipitated with PEG salt solution at 4° C for 1 hour, before being spun out at 17,700 x g for 30 minutes and resuspended in PBS or PBS 5% (v/v) FBS (Foetal Bovine Serum, Gibco, A5670701).

3.2.5.2 Phage Titre Protocol

An overnight culture of TG1 was set up from a single colony grown on M9 minimal agar plates and used to infect 5 mL of fresh 2x TY-G media (1:5 dilution). The culture was grown to OD_{600} = 0.6. 10 µL of phage solution at various concentrations were used to infect 90 µL of bacterial culture, and incubated at 37° C, 250 rpm for 45 minutes, serial dilutions were then plated on 2x TY-GA plates (0.6% (w/v) tryptone, 1% (w/v) yeast extract, 0.5% (w/v) NaCl, 100 mg/mL ampicillin, 100 mM glucose, 1.5% (w/v) agar powder). 1 µL of highly pure pSEX81 plasmid was transformed into 50 µL TG1 cells as a positive control, and 50 µL of TG1 cells were plated as a negative control. Plates were incubated at 37° C overnight, and colonies were counted either manually or using ImageJ the next day.

3.2.5.3 Biopanning Optimisation

Several biopanning protocols were designed in order to maximise binding and phage output. A schematic representation of the protocols can be seen in Figure 3.2. The protocols were developed based on the relevant literature (Ho and Pastan, 2009; Panagides *et al.*, 2022; Stark *et al.*, 2017; Zadeh *et al.*, 2019).

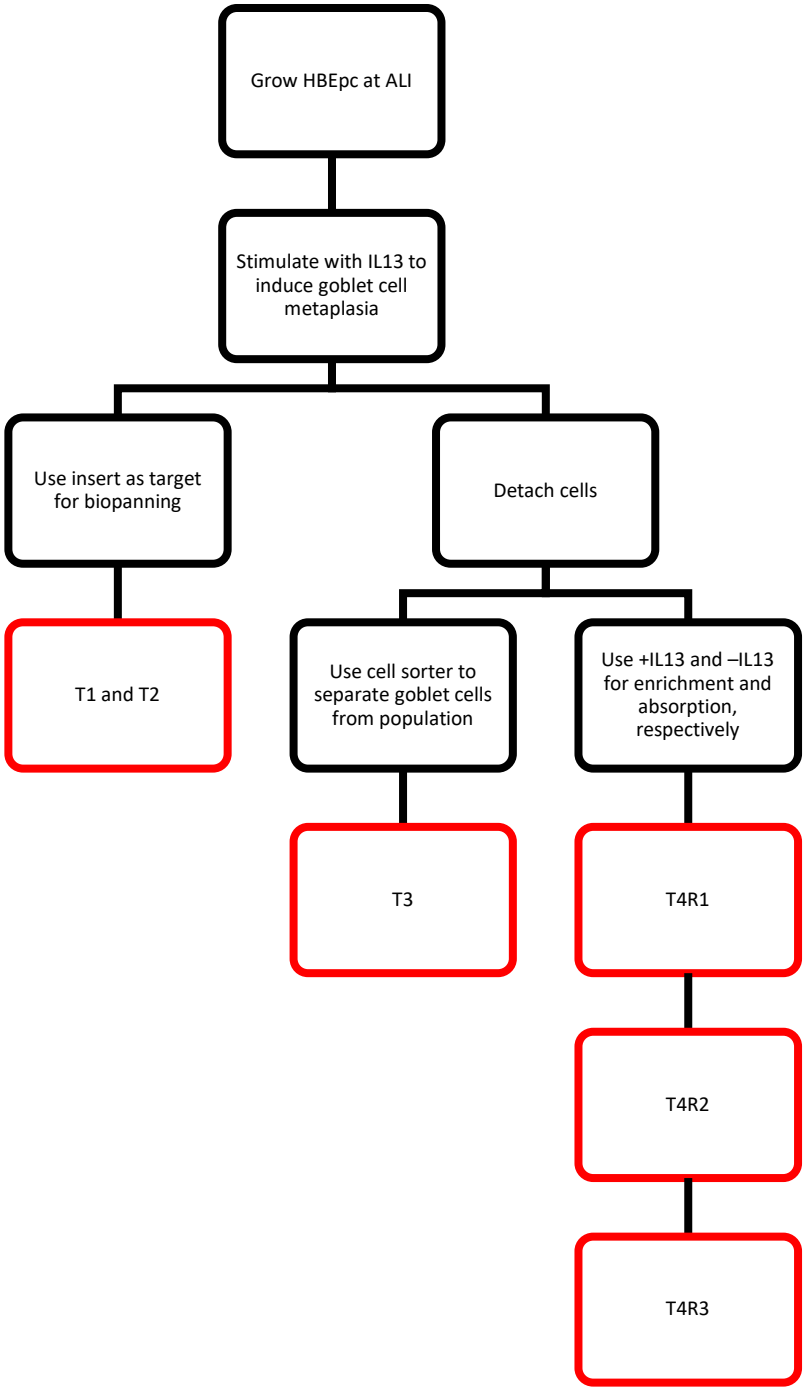


Figure 3.2 Schematic representation of each biopanning protocol developed to isolate goblet cell-specific nanobodies.

Red boxes represent different biopanning experiments: T1 = biopanning experiment 1; T2 = biopanning experiment 2; T3 = biopanning experiment 3; T4R1 = biopanning experiment 4 round 1; T4R2 = biopanning experiment 4 round 2; T4R3 = biopanning experiment 4 round 3. Figure created using Powerpoint.

For biopanning experiments T1 and T2, HBEpc cells were grown at the ALI and goblet cells hyperplasia was induced (see protocol described in 3.2, page 100). The nanobody library was diluted in cell media, and 200 µL of the phage library (10^{14} CFU) was applied to the cells. For T1, the samples were incubated for 2 h at 4° C on an orbital microplate shaker (800 rpm). Following incubation, the cells were washed three times for 5 minutes each with 200 µL of cell media on an orbital microplate shaker (800 rpm). Subsequently, the cells were washed five times with 100 µL of cell media. The phage was eluted by using 200 µL of trypsin buffer (10 mM Tris pH 7.4 at 20° C, 137 mM NaCl, 1 mM CaCl2 and 100 µg/mL Trypsin) for 30 minutes at 37° C on an orbital microplate shaker (800 rpm).

For T2, the samples were incubated with 200 µL of the phage library (10^{14} CFU) for 4 h at 4° C on an orbital microplate shaker (500 rpm). Following incubation, the cells were washed three times for 5 minutes each with 200 µL of cell media on an orbital microplate shaker (500 rpm). Subsequently, the cells were washed five times with 100 µL of cell media. The phage was eluted by using 200 µL of trypsin buffer twice, each for 30 minutes at 37° C on an orbital microplate shaker (500 rpm).

For biopanning experiment T3, ALI-cultured HBEpcs were stimulated for goblet cells hyperplasia and sorted by FACS (see protocol described in 3.2.4, page 102). The cells were then pelleted by centrifugation (5 minutes, 300 rpm). TSPAN8 positive cells were then used for biopanning. The nanobody library was diluted in cell media and cells were resuspended in 500 µL (10^{14} CFU). Incubation ensued for 4 hours at 4° C on an orbital microplate shaker (500 rpm). Afterward, cells were washed thrice for 5 minutes each with 500 µL of cell media. Phage elution was carried out using 500 µL of trypsin buffer for 30 minutes at 37° C.

For T4R1 biopanning experiment, ALI-cultured HBEpcs were stimulated for goblet cells hyperplasia. Following stimulation, cells were detached using 100 µL apical and 500 µL basal TrypLE™ Express Enzymes (Gibco, 12605010) for 20 minutes at 37° C. The detached cells were then spun down and resuspended in PBS supplemented with 5% FBS. The nanobody library was diluted in PBS/5% (v/v) FBS, and the cells were spun down again at 300 x g for 5 minutes before being

resuspended in 500 µL of the nanobody library solution (10^{14} CFU). Incubation followed for 2 hours at 4° C on an orbital microplate shaker (300 rpm). Subsequently, the cells were washed thrice for 5 minutes each with 500 µL of PBS/5% (v/v) FBS, with the final wash involving a change of Eppendorf. Phage elution was then performed using 1 mL trypsin buffer for 30 minutes at 37° C. Absorption round T4R2 was performed against unstimulated ALI-cultured HBEpc. Cells were detached using 100 µL apical and 500 µL basal TrypLE™ Express enzyme for 20 minutes at 37° C. The detached cells were then spun down and resuspended in PBS supplemented with 5% FBS. 10^{11} pfu of the amplified eluate from the previous round (T4R1) were diluted in PBS/5% (v/v) FBS, and the cells were spun down again at 300 x g for 5 minutes before being resuspended in 500 µL of eluate. Cells were incubated for 2 hours at 4° C on an orbital microplate shaker (300 rpm), before being spun down. Unbound phages were collected and amplified for the final round of biopanning.

Final amplification round T4R3 was performed following the same protocol as for T4R1, using 10^{11} pfu of the amplified eluate from the previous round (T4R2).

30 µL of the resulting phage samples was then frozen at -20 °C after glycerol addition to 20% (v/v). The remaining 970 µL were used for amplification and titre, except for T4R3 where the remaining 970 µL were used to infect 4 mL of OD_{600} = 0.6 TG1 cells in 2x TY-G media and plated on a 20x20cm 2x TY-GA plate (0.6% (w/v) tryptone, 1% (w/v) yeast extract, 0.5% (w/v) NaCl, 100 mg/mL ampicillin, 100 mM sterile glucose, 1.5% (w/v) agar powder, pH 7.0 at 20° C).

3.2.6 Western Blotting

ALI differentiated cells (IL-13- and IL-13+) were detached from the insert using TrypLE™ Express Enzyme (Gibco, 12605010) and lysed using 100 µL of RIPA Lysis and Extraction Buffer (Thermo Fisher Scientific™, 89900) per insert. Samples were then diluted in either Novex™ Tris-Glycine SDS Sample Buffer (Invitrogen™, LC2676) or NativePAGE™ Sample Buffer (Invitrogen™, BN2003) and run either on a denaturing Novex™ Tris-Glycine Mini Protein Gels, 4–20%, 1.0 mm (Invitrogen™, XP04205BOX) with Novex™ Tris-Glycine SDS Running Buffer (Invitrogen™, LC2675), or on a native NativePAGE™ 4 to 16%, Bis-Tris, 1.0 mm, Mini Protein Gels (Invitrogen™,

BN1004BOX) with NativePAGE™ Running Buffer (Invitrogen™, BN2001), alongside the Spectra™ Multicolour Broad Range Protein Ladder (Thermo Fisher Scientific™, 26634).

Gels were removed from their running casts and semi-dry transferred onto nitrocellulose membranes (Invitrogen™, LC2009) using Trans-Blot® SD Semi-Dry Transfer Cell with Schafer-Nielsen Transfer Dry Buffer (48 mM Tris, 39 mM glycine, and 1.3 mM SDS, pH 9.0-9.3 at 20° C, Bjerrum and Schafer-Nielsen, 1986).

Membranes were then blocked with 3% (w/v) BSA in TBST (Tris-buffered saline (150 mM NaCl, 50 mM Tris-HCl, pH 7.6 at 20° C) with 0.5% (v/v) Tween 20) overnight at 4° C with gentle rocking. Membranes were then washed (3 times, 10 minutes in TBST at room temperature) before being probed with the appropriate M13K07 phage sample (either clone carrying phages, native phages, or vNAR 5A7 phages, 200 µL of 10^{14} CFU phage preparation) for 2 hours at room temperature with gentle rocking. Membranes were washed again and probed with Anti-M13 Antibody-HRP conjugate (SinoBiological, 11973-MM05T-H). After a final wash, samples were imaged on a LiCor Odyssey® M Imager equipped with a chemiluminescence module using WesternSure® PREMIUM Chemiluminescent Substrate (LiCor, 926–95000). Pictures were taken at the 3 minutes, 5 minutes and 10 minutes exposure time, and the best exposed images were selected.

3.2.7 Sequencing

3.2.7.1 Polymerase Chain Reactions

PCRs requiring high-fidelity output were set up using Phusion® High-Fidelity DNA Polymerase (New-England Biolab, M0530S). Reaction conditions are detailed in Table 3.2, and thermocycling conditions are detailed in Table 3.2.

Table 3.2 Phusion® High-Fidelity DNA PCR reaction conditions

Component	Final concentration
5X Phusion HF or GC Buffer	1x
10 mM dNTPs (New-England Biolab, N0447S)	200 µM
10 µM forward primer	0.5 µM
10 µM reverse primer	0.5 µM
Template DNA	<250 ng
Phusion DNA Polymerase	0.02 u/µL
DMSO (optional)	3%
Nuclease-free water	

Table 3.3 Phusion® High-Fidelity DNA PCR thermocycling conditions

Step	Temperature (°C)	Time (s)	Cycles
Initial denaturation	98	30	x1
Denaturation	98	10	X25-35
Annealing	45–72*	30	
Extension	72	**	
Final extension	72	600	x1
*Annealing temperature was determined for each primer set using the New-England Biolab Tm Calculator v1.12.0. ** Extension time was calculated as 30 seconds/kb.			

3.2.7.2 Bacterial DNA

DNA was extracted from phage-infected bacteria using Monarch® Plasmid Miniprep Kit (New-England Biolab, T1110S). The composition of the buffers is proprietary. 5 mL of overnight cultures in LB were pelleted (60 seconds, 17,900 x g) and resuspended in buffer B1. 200 µL of buffer B2 and 400 µL of buffer B3 were added consecutively to lyse and neutralise the sample before centrifugation (10 minutes, 17,900 x g). The supernatant was applied to the Monarch Spin Column S2D, and spun down (60 seconds, 17,900 x g). Samples were washed using 200 µL of buffer BZ, spun down, and washed again with 400 µL of buffer WZ. DNA was eluted in EB buffer (10 mM Tris, 0.1 mM EDTA, pH 8.5 at 20° C). DNA was quantified using a NanoDrop Microvolume Spectrophotometer (Thermo Fisher Scientific).

Samples were sent to Eurofins Genomics (Germany) alongside appropriate primers for Sanger sequencing. The primers used are listed in Table 3.4. Results were

analysed using SnapGene software 6.1 (from Insightful Science; available at snapgene.com).

Table 3.4 List of primers used for Sanger sequencing.

These primers were used to determine the sequence isolated through biopanning.

Name	Sequence 5′ – > 3′	Size	Description
ForFR1_NcoI	GCA TGA CCA TGG CTC GAG TGG ACC AAA CAC CG	32	vNAR 5A7 library construction. Forward primer with restriction site NcoI.
RevFR4_NotI	GCA TGA GCG GCC GCT TTA TTC ACA GTC ACG GCA GTG CCA T	40	vNAR 5A7 library construction. Reverse primer with restriction site NotI.

Whole plasmid sequencing was performed by the DeepSeq Centre for Genetics and Genomics at the University of Nottingham using their Rapid long read whole genome plasmid analysis with Epi2Me workflows service. Reads were assembled using SnapGene 6.1 (from Insightful Science; available at www.snapgene.com) and Geneious Prime 2024.0.5 (from GraphPad software; available at www.geneious.com).

3.2.7.3 Phage DNA

Purification of phage DNA protocol was adapted from Wilson (1993).

After phage amplification procedure, 200 µL of PEG salt solution was added to 500 µL of the phage containing supernatant and incubated for 20 minutes at room temperature. Phages were spun at 13,800 x g for 10 minutes at 4° C and the supernatant was discarded. The phage pellet was resuspended in 100 µL of iodide buffer (10 mM Tris-HCl (pH 8.0 at 20° C), 1 mM EDTA, 4 M sodium iodide). 250 µL of ethanol was added and the sample was incubated for 20 minutes at room temperature. The sample was spun again (13,800 x g for 10 minutes at 4° C) and the supernatant was discarded. The DNA pellet was washed with 0.5 mL of 70% (v/v) ethanol and briefly dried before being resuspended in 30 µL of EB buffer (10 mM Tris-Cl, pH 8.5 at 20° C) and stored at -20° C. PCR samples were prepared using universal (TruSeq) adapters (see Table 3.5) and Phusion DNA polymerase (New-England Biolab). Indexing and sequencing of all samples on MiSeq with 2 × 300 bp run mode

was then performed by Eurofins. Results were collected and analysed using SnapGene 6.1 (from Insightful Science; available at www.snapgene.com) and Geneious Prime 2024.0.5 (from GraphPad software; available at www.geneious.com).

Table 3.5 List of primers used for next-generation sequencing.

Illumina TruSeq adapters are highlighted in red. These primers were used to validate the diversity of the nanobody library.

Name	Sequence 5' – > 3'	Size	Description
NGS3_for	ACA CTC TTT CCC TAC ACG ACG CTC TTC CGA TCT AAA GAG GAG AAA TTA ACC ATG AAA	57	Forward primer for next generation sequencing amplification, including NGS adapters.
NGS3_rev	GAC TGG AGT TCA GAC GTG TGC TCT TCC GAT CTG AAT TTT CTG TAT GGG ATT TTGC	55	Reverse primer for next generation sequencing amplification, including NGS adapters.

3.2.8 Estimation of Protein Hydrophobicity

The hydrophobicity of proteins was calculated using the hydropathy scale described by Kyte and Doolittle (1982). Scores were calculated using the Expasy ProtScale tool (Gasteiger *et al.*, 2005) and protein 3D structures were generated using UCSF ChimeraX (version 1.9, Pettersen *et al.*, 2004) available at https://www.cgl.ucsf.edu/chimera). HEL-5A7 protein structure was obtained from Stanfield *et al.* (2004), PDB Id: ISQ2.

3.2.9 Reagents

3.2.9.1 Antibiotics

For each antibiotic used, a 1000X concentration stock was prepared in the relevant solvent (Table 3.6). Stocks were stored at -20° C.

Table 3.6 Table of antibiotics used, along with the relevant solvent and working concentration.

Antibiotic	Solvent	Working concentration in µg/mL
Ampicillin	dH_2O	100
Kanamycin	dH_2O	50

3.2.9.2 Enzymes, Buffers, and Solutions

Enzymes used were obtained from New-England Biolab and stored at -20 °C and kept on ice before use. Enzymes were used according to the provider's guidelines and with supplied buffers. The composition of buffers can be seen in Table 3.7. The table also shows the composition of various buffers used. If composition is protected, the supplier was provided.

Table 3.7 Table of buffers with compositions. Buffer pH is measured at room temperature (20° C).

Buffer	**Composition (in dH2O, otherwise specified)**	**Storage**
PBA	3% (w/v) BSA in PBS	4° C
PBS	137 mM NaCl 2.7 mM KCl 8 mM Na2HPO4 2 mM KH2PO4	4° C
M9 minimal agar plates	2.0 mM $MgSO_4$ 22.2 mM Glucose 0.1 mM $CaCl_2$ 1X M9 Minimal Salts 1.5% (w/v) agar powder	Room temperature
5X M9 minimal salts	15 g/L KH_2PO_4 2.5 g/L NaCl 33.9 g/L Na_2HPO_4 5 g/L NH_4Cl	Room temperature
2X TY-G	0.6% (w/v) tryptone 1% (w/v) yeast extract 0.5% (w/v) NaCl 100 mg/mL ampicillin 100 mM sterile glucose pH 7.0	Room temperature
Bjerrum Schafer-Nielsen Transfer Dry Buffer	48 mM Tris 39 mM glycine 1.3 mM SDS pH 9.0-9.3	Room temperature
TBST	150 mM NaCl 50 mM Tris-HCl 0.5% (v/v) Tween 20	4° C
Iodide Buffer	10 mM Tris-HCl (pH 8.0) 1 mM EDTA 4 M sodium iodide	4° C
EB buffer	10 mM Tris-Cl 0.1 mM EDTA pH 8.5	Room temperature

3.3 Results and Discussion

3.3.1 Cell Culture

Human Bronchial Epithelial primary cells (HBEpc) were used as a model for biopanning. Commercially obtained healthy samples were cultured according to established protocols. Each sample contained approximately 500,000 cells at passage 2, and cells were passaged at a 1:3 ratio. However, to obtain a sufficient number of cells for air-liquid interface culture, cells were taken to passage eight. At this level of passage, the air-liquid interface failed to establish a proper layer of epithelium. The resulting gaps within the cell layer allowed for media to permeate through the membrane, preventing the differentiation of the primary cells into the different subgroups. Those gaps are visible in Figure 3.3. In Figure 3.3 (A), the full surface of the insert was coated in cells, this confluence was achieved at the liquid-liquid interface three days after seeding. After removal of the apical media, gaps started to appear with cell clumps visibly forming (Figure 3.3 (B)). Figure 3.3 (C) shows the surface of the inserts two to three days later, gaps had widened, and media was permeating through the membrane from the basal into the apical chamber. After detaching, the viability of the cells highly decreased and very few could be recovered for subsequent analysis.

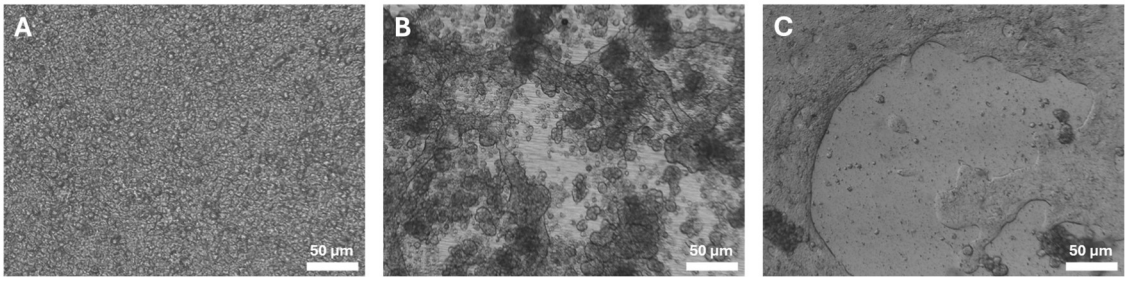


Figure 3.3 Confocal microscopy of HBEpc culture.

A: Cells after reaching confluence on the insert at the liquid-liquid interface. The whole surface of the insert is covered with cells and no gaps are visible. B: cells 3 days after removing the media from the apical chamber to establish ALI. Some cells have become rounded and have detached from the insert surface, creating gaps within the cell layer. C: 2 to 3 days later, gaps have become wider, and the cell layer starts to detach from the insert altogether.

Expanding HBEpc by passaging can alter the cells' phenotypes, as shown by (Wu *et al.*, 2023). Specifically, it was demonstrated that passaging HBEpc impaired CFTR-mediated airway-surface liquid secretion, increased transepithelial resistance and decreased the permeability of the epithelium to water. Overall, the expression of over 300 genes was significantly impacted by only 2 passages, including genes involved in cell growth and differentiation. Therefore, it is likely that the higher number of passages employed here (8 in total before transferring to ALI inserts) significantly impacted the cells and prevented the formation of a functional airway epithelium model. Unfortunately, the use of cells at a lower passage in this context was not possible due to prohibitive costs.

To mitigate this problem, commercially obtained *in vitro* tissue model of the human upper airway epithelium cultured at the air-liquid interface (MucilAir™, Epithelix) were used in lieu of in-house cultured HBEpc. The ready to use MucilAir™ eliminated the need for culturing HBEpc, reducing costs of primary cells, as well as media and other culture reagents.

As previously discussed, goblet cells are the primary site of mucus secretion in AHDs, and therefore an obvious target for the delivery of mucus production and secretion inhibitors. To increase the proportion of goblet cells within the *in vitro* tissue model, interleukin 13 (IL-13) treatment was used. IL-13 stimulation on human

bronchial epithelium notably impacts epithelial structure and function, which is relevant to airway hypersecretory diseases (AHDs). IL-13 promotes mucus production and cell proliferation, and reduces epithelial barrier integrity, resulting in increased susceptibility to environmental allergens. It also increases apoptosis in epithelial cells and promotes fibrosis-related responses, leading to airway remodelling and chronic inflammation characteristic of asthma (Kondo *et al.*, 2006, 2002).

Research demonstrates IL-13's critical role in asthma by activating immune and airway responses via the IL-13/STAT6 signalling pathway, with effects spanning eosinophilia, airway hyper-responsiveness, and mucus production. IL-13 binds the IL-13Ra1/IL-4Ra receptor complex, activating STAT6, which drives the transcription of multiple pro-inflammatory and remodelling genes. Further downstream, IL-13 stimulation upregulates chloride channel accessory protein 1 (CLCA1) in the bronchial epithelium, linking to the MAPK13 (p38 MAP kinase) pathway, which exacerbates mucus production and inflammation (Alevy *et al.*, 2012; Fujisawa *et al.*, 2008). CLCA1 overexpression has been associated with increased mucus secretion and reduced epithelial barrier integrity, while MAPK13 activation contributes to cellular responses involved in chronic inflammation. Venkayya *et al.* (2002) showed Th2 cytokines' direct action on resident airway cells, inducing airway hyperresponsiveness even without inflammatory cells through IL-4/IL-13 signalling. Kuperman *et al. (*2002) expanded on IL-13's direct effects, showing that STAT6 activation in epithelial cells alone could drive airway hyperresponsiveness and mucus production. Together, these studies highlight IL-13 as a key driver of goblet cells hyperplasia and mucus hypersecretion. IL-13 treatment was therefore used to achieve biologically relevant diseased airway modelling and increase the proportion of goblet cells within the samples.

3.3.2 Analytical Flow Cytometry

To demonstrate the effect of IL-13 on HBEpc cultured at the ALI (MucilAir inserts), analytical flow cytometry was used. A five-colour panel was designed based on the literature (Bonser *et al.*, 2021). Extracellular targets were selected for analytical flow cytometry so that the same panel could be used for fluorescence-

activated cell sorting (FACS) later on. To target goblet cells, TSPAN8, a member of the tetraspanin family, was selected. TSPAN8 was identified from cell-type-specific RNA transcripts and plays a significant role in goblet cells within the bronchial epithelium by influencing mucus production and secretion. The nerve growth factor receptor (NGFR), also known as CD271, was used as a reliable marker for basal cells in epithelial tissues. NGFR expression in basal cells makes it a useful marker because basal cells serve as progenitors in epithelial layers, giving rise to specialised cells, such as goblet and ciliated cells (Bravo *et al.*, 2013). To accurately distinguish secretory cells from other epithelial cell types, CEACAM6 (carcinoembryonic antigen-related cell adhesion molecule 6) marker was used. It is highly expressed on the surface of secretory cells, where it participates in cell adhesion, immune responses, and cell signalling. Finally, to reliably mark ciliated cells, SiR-Tubulin, a fluorogenic, cell-permeable dye that selectively binds to microtubules derived from the microtubule-binding drug Docetaxel, was used. It effectively stains endogenous microtubules, a key structural component within cilia that are made up of microtubule-based axoneme. The resulting panel and cell classification are as follows: ciliated cells = $NGFR^-$, $SiR\text{-}Tubulin^+$, $CEACAM6^-$, $TSPAN8^-$; basal cells = $NGFR^+$, $SiR\text{-}Tubulin^-$, $CEACAM6^-$, $TSPAN8^-$; secretory cells = $NGFR^-$, $SiR\text{-}Tubulin^-$, $CEACAM6^+$, $TSPAN8^-$; goblet cells = $NGFR^-$, SiR–$Tubulin^-$, $CEACAM6^+$, $TSPAN8^+$.

Cells were prepared according to established protocols and analysed using SONY ID7000C Spectral Cell Analyser (n=2). The resulting data was collected and analysed. Cells were first gated to exclude debris by delimitating the largest population based on forward scatter (FSC) and side scatter (SSC) properties, identifying cells by their size (FSC) and granularity or complexity (SSC): debris exhibit lower granularity and complexity than cells, as well as smaller sizes. The second gate compared SSC width versus SSC height to discriminate single cells from cell doublets or clumps. Single cells tend to display a narrower SSC width relative to SSC height, while doublets or clusters show increased width due to the larger combined cell size. Setting a gate to exclude events with high SSC width selected only single-cell populations so that further analysis reflected individual cells rather than aggregates. Finally, the last gate selected live, intact cells within the initial cell population. This

gate was based on the ZombieUV viability dye that distinguished live cells from dead ones or apoptotic cells. By excluding dead cells at this stage, the subsequent analysis will be based only on viable cells, improving the accuracy and relevance of the data (Figure 3.4).

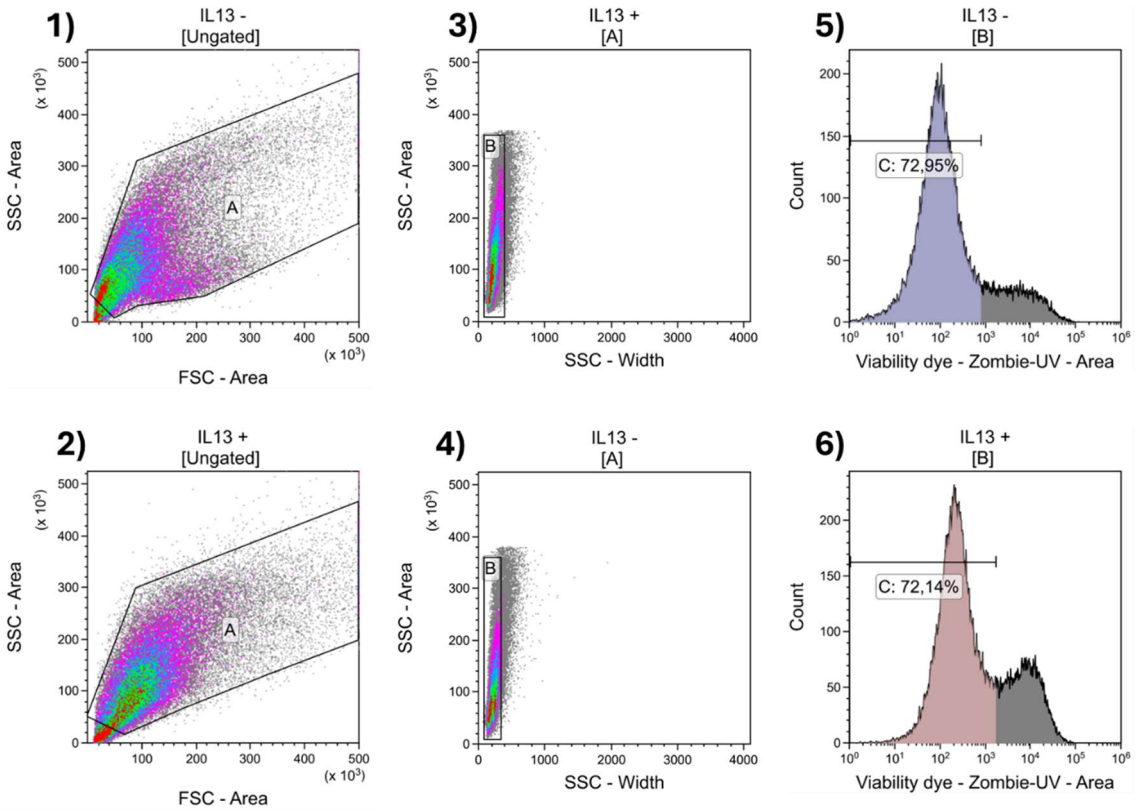


Figure 3.4 Flow cytometry gating strategy for isolating a single, viable cell population of HBEpc cultured at ALI with (IL-13+) or without (IL-13-) interleukin 13 treatment.

(1 and 2) Initial gate (A) based on forward scatter (FSC) and side scatter (SSC) to exclude debris, allowing for selection of intact cells. (3 and 4) SSC width vs. SSC height gate (B) to remove doublets or clumped cells, isolating single cells. (5 and 6) Final gate using a viability dye to distinguish live cells from dead or apoptotic ones, refining the population for accurate analysis. Each gate progressively narrows the sample to focus on single, live cells for further study. Similar gates were used for repeats and can be viewed in appendix 3, Figure A. 10.

Gated populations were then analysed for fluorescent markers. To correct for spectral overlap between fluorophores, compensation was performed by flow cytometry technician Nicola Croxall. When multiple fluorescent markers are used,

some of their emission spectra can overlap, causing signal spillover into unintended detection channels. Compensation adjusts for this by subtracting the overlapping signal, ensuring that each fluorophore is accurately measured in its designated channel. Single-colour samples that contain beads labelled with only one fluorophore were used to determine compensation. Single-colour controls helped determine how much signal each fluorophore contributes to neighbouring channels due to spectral overlap. This correction is essential for accurate data analysis in multicolour experiments, and compensation values as well as single-colour controls can be seen in appendix 3, Figure A. 8.

As described above, each cell subset presented a specific fluorescent signature. To set precise gating, Fluorescence-minus-one, or FMO, controls (samples stained with all fluorophores except one) were used. FMOs showed the level of background signal expected when a specific marker was absent and allowed for the accurate discrimination between a true positive and background fluorescence or signal spillage. Setting gates using this method ensured only cells positive for a specific marker could be selected. FMO controls can be viewed in appendix 3, Figure A. 9.

In Figure 3.5, data from the first analytical flow cytometry repeat can be viewed. Cells were stained with all colours and plotted SiR-Tubulin vs. NGFR and CEACAM6 vs. TSPAN8. In the unstimulated (IL-13-) sample, a large population of $NGFR^+$ $SiR\text{-}Tubulin^-$ cells can be observed. This large group corresponds to basal cells. Basal cells are stem-like undifferentiated cells that can serve as progenitors and differentiate into other cell types. A large population of $NGFR^-$ $SiR\text{-}Tubulin^+$ can also be seen, corresponding to ciliated cells. In the IL-13+ sample, a notable reduction in the basal cell population can be observed. This is likely a result of the IL-13 stimulation, resulting in the differentiation of basal cells into specialised cell types. The CEACAM6 vs. TSPAN8 plots reveal a shift after IL-13 stimulation. While only a small population of $CEACAM6^+$ $TSPAN8^+$ cells, identified as goblet cells, could be observed in the unstimulated sample, a noticeable shift can be seen in the stimulated sample.

These results are consistent with histogram plots (Figure 3.6) of cell counts for each of the 4 markers. For the basal cell marker NGFR, a drop of 20.57% in positivity could be seen when cells were stimulated with IL-13, clearly indicating that the proportion of basal cells in the sample was lower. On the other hand, positivity to the SiR-Tubulin, CEACAM6 and TSPAN8 markers increased by 25.74%, 31.61% and 14.23%, respectively, indicating a higher proportion of ciliated, secretory and goblet cells in the sample. Together, these results confirm the role of IL-13 in airway remodelling previously described in the literature.

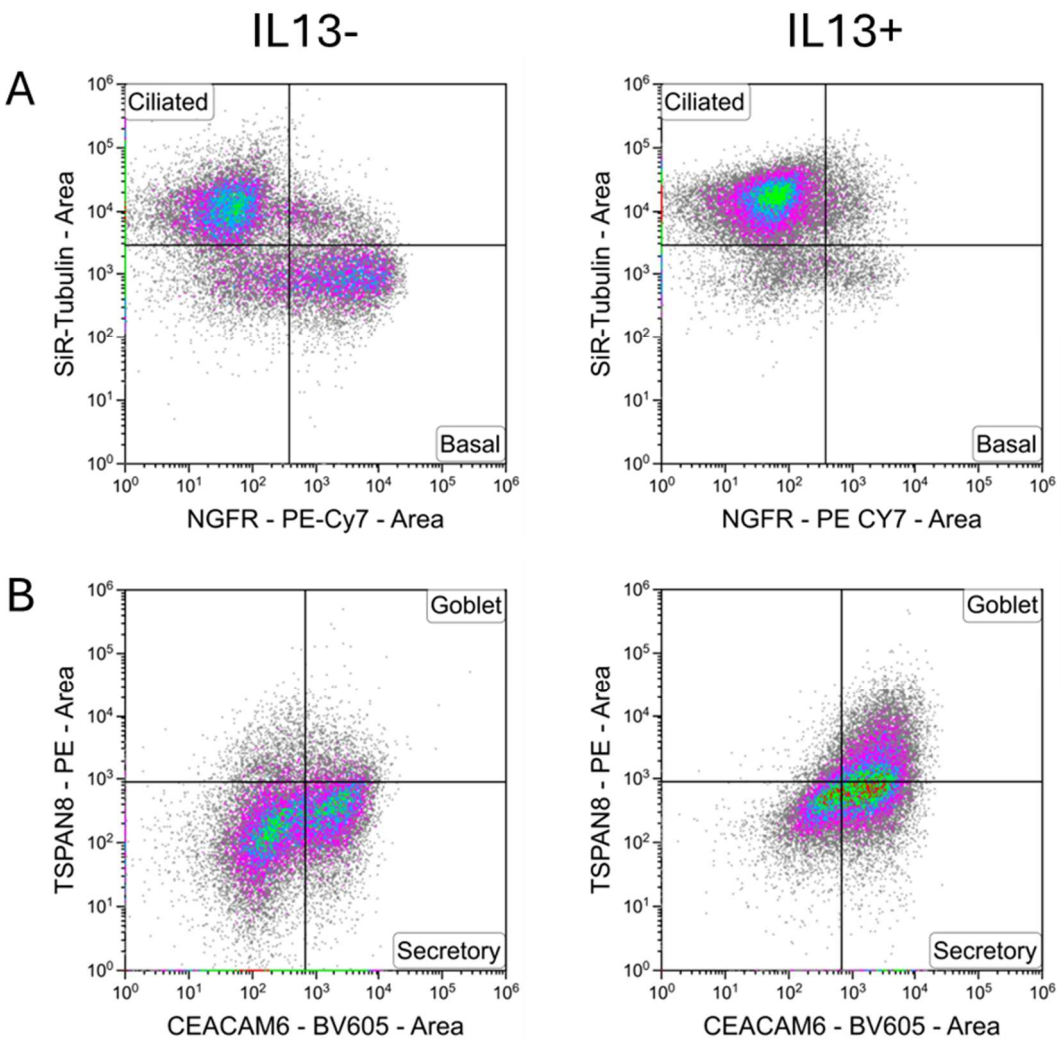


Figure 3.5 Flow cytometry analysis of IL-13- and IL-13+ cell populations stained with a multicolour panel for cell type identification.

Gates were determined using fluorescence-minus-one (FMO) controls to accurately distinguish positive and negative populations for each marker. (A) SiR-Tubulin vs. NGFR plots. A noticeable shift can be observed in NGFR$^+$ population after stimulation with IL-13, revealing a decrease in the proportion of basal cells in the sample, accompanied by an increase of SiR-Tubulin$^+$ cells classified as ciliated cells. (B) CEACAM6 vs. TSPAN8 plots. An increase in the proportion of TSPAN8$^+$ cells reveals a higher proportion of goblet cells in the sample after stimulation with IL-13. Data shown are representative of two independent experiments.

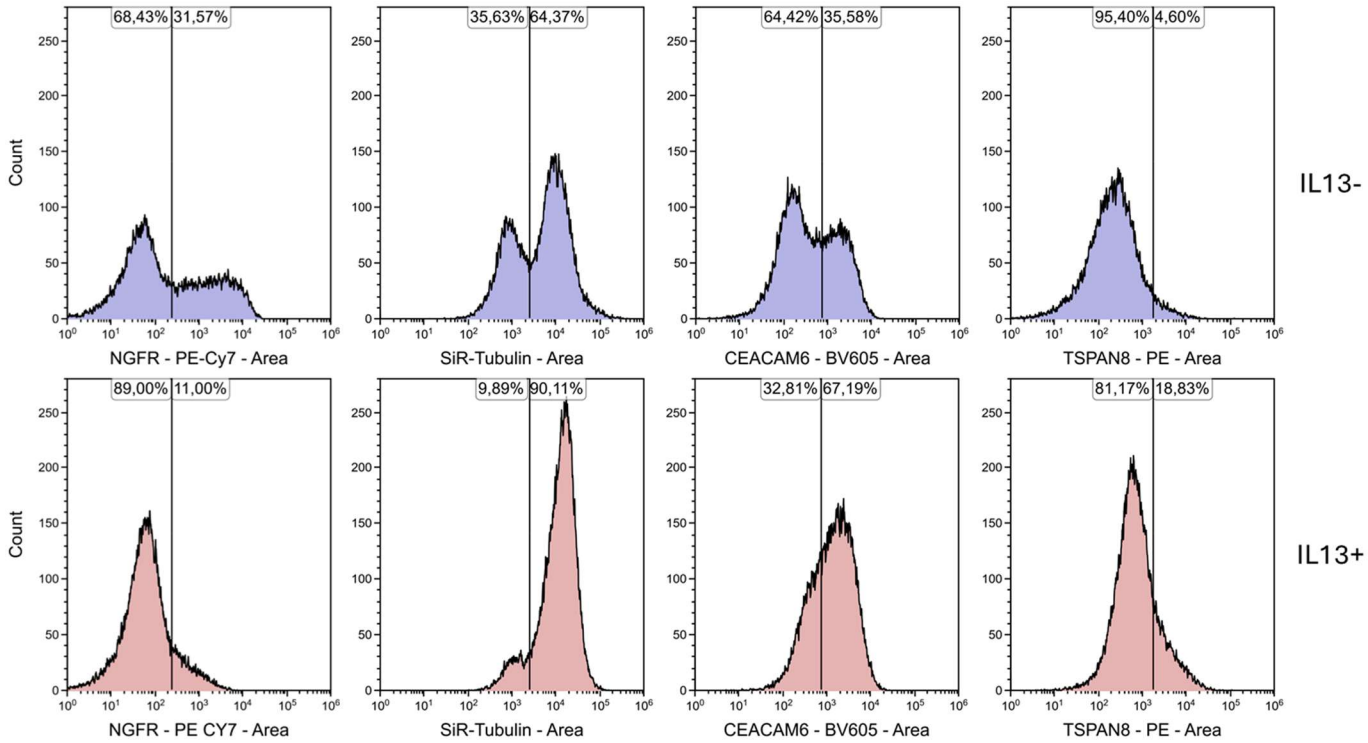


Figure 3.6 Histograms of cell counts for each of the 4 markers, in unstimulated (in blue) and IL-13 stimulated samples (in red).

Gates were determined using fluorescence-minus-one (FMO) controls to accurately distinguish positive and negative populations for each marker. Without stimulation, a higher proportion of cells are positive for the NGFR marker, indicating a higher proportion of basal cells in the sample. In IL-13 stimulated samples, the proportion of cells positive for SiR-Tubulin, CEACAM6 and TSPAN8 increases, indicating an increase of ciliated, secretory and goblet cells in the population. Data shown are representative of two independent experiments.

To quantify these shifts, cell culture, stimulation and staining were repeated a further two times. The corresponding plots can be seen in appendix 3 (Figure A. 10 and Figure A. 11). The second set of cells was run on the Sony ID7000C Spectral Cell Analyser, as for the first experiment, and yielded comparable results. The last set of cells was run on the Beckman Coulter Astrios EQ for cell sorting. In this experiment, a malfunction of the red laser was observed, specifically affecting the detection of the SiR-Tubulin marker. The SiR-Tubulin marker, which binds to tubulin structures and fluoresces in the far-red spectrum, typically requires excitation by a red laser (~640 nm) for optimal detection. However, due to the red laser malfunction, excitation of the SiR-Tubulin marker did not occur, resulting in an absence of detectable fluorescence signal in the SiR-Tubulin channel. This led to a lack of distinguishable data for tubulin-stained cells in the far-red fluorescence spectrum, despite successful staining confirmed in control samples run on the Sony ID7000C Spectral Cell Analyser. Other markers relying on lasers outside of the red spectrum continued to function as expected, confirming that the issue was specific to the red laser. This was also confirmed by flow cytometry facility staff.

A percentage of cells that were marked as either basal, ciliated, secretory of goblet were collected for each experiment, apart for SiR-Tubulin positive cell percentage for the final run and can be seen in Figure 3.7. The data clearly reflected the observation made from flow cytometry plots, with the percentage of basal cells decreasing on average from 10.67% to 1.07% between unstimulated and IL-13 stimulated samples, reflecting the remodelling of the airway driven by IL-13 treatment. Notably, the percentage of goblet cells increased from 3.77% to 17.92% on average, a five-fold increase in IL-13 stimulated samples. Multiple t-tests were used to confirm the significance of the various shifts, and the p-values were corrected using the Holm-Šídák method with an alpha value of 0.05. The Holm–Šidák correction was applied to account for multiple comparisons and control the family-wise error rate across the four groups. No significant shift could be ascertained for the percentage of secretory cells (p value = 0.2318, t ratio = 1.250, dF = 14, adjusted p value = 0.2318). A slightly significant difference was observed for basal (p value = 0.0105, t ratio = 2.951, dF = 14, adjusted p value = 0.0312) and ciliated cells (p value

= 0.0167, t ratio = 2.718, dF = 14, adjusted p value = 0.0330). Finally, a higher significance of difference was observed in the percentages of goblet cells (p value = 0.0007, t ratio = 4.348, dF = 14, adjusted p value = 0.0027). These findings are consistent with the literature and confirm the remodelling effect of IL-13 on human bronchial airway epithelium. This increased number of goblet cells will be used to facilitate the biopanning process, either by separating goblet cell populations from the remaining sample by fluorescence-activated cell sorting, or by using stimulated and unstimulated ALI inserts as biopanning targets, for enrichment and absorption, respectively.

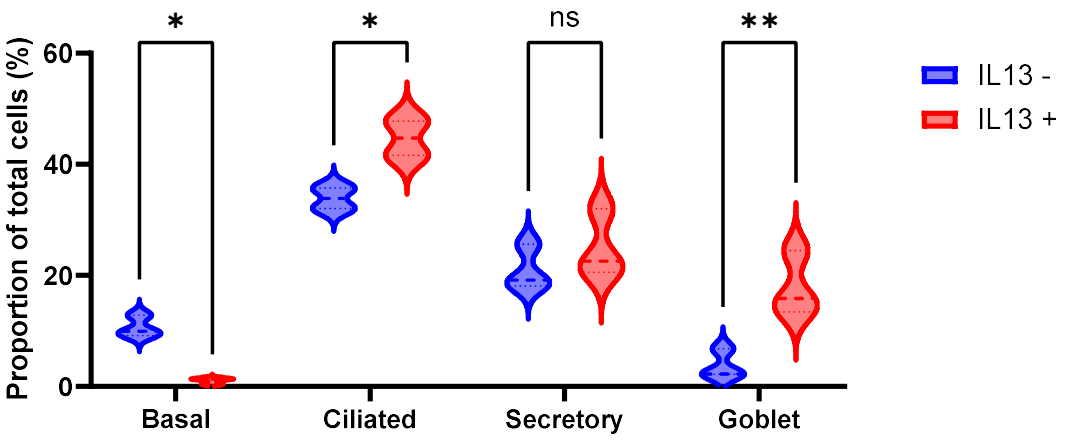


Figure 3.7 Percentage of total cells identified as either basal, ciliated, secretory or goblet cells by flow cytometry.

*Violin plots show the distribution of the data; solid lines indicate the mean; dashed line indicate standard deviation. Results are repeats of three experiments, apart for percentage of ciliated cells, which is a result of two experiments. A moderately significant difference can be observed for basal (mean shift from 10.67% to 1.07% between IL13+ and IL13-) and ciliated cells (mean shift from 33.89% to 44.72% between IL13+ and IL13-) percentages in unstimulated (blue) and stimulated (red) samples, while a higher significance of difference can be observed for goblet cells (mean shift from 3.77% to 17.92% between IL13+ and IL13-). No significant shift was observed for secretory cells (mean shift from 20.98% to 25.05% between IL13+ and IL13-). These findings are consistent with IL-13 stimulation studies in the literature. NS: non-significant; *: p<0.05; **: p<0.01.*

3.3.3 Fluorescence Activated Cell Sorting (FACS)

In order to use goblet cells as the target of biopanning experiments, the cells need to be separated from the remaining subtypes. To achieve this separation, fluorescence activated cell sorting (FACS) was used. The cell marker panel used was the same as for analytical flow cytometry experiments, using nerve growth factor receptor (NGFR), also known as CD271, CEACAM6 (carcinoembryonic antigen-related cell adhesion molecule 6), also known as CD66c, SiR-Tubulin, a fluorogenic, cell-permeable dye that selectively binds to microtubules derived from the microtubule-binding drug Docetaxel, and TSPAN8 (tetraspanin 8). The resulting panel and cell classification are as follows: ciliated cells = $NGFR^-$, $SiR\text{-}Tubulin^+$, $CEACAM6^-$, $TSPAN8^-$;

basal cells = $NGFR^+$, SiR-$Tubulin^-$, $CEACAM6^-$, $TSPAN8^-$; secretory cells = $NGFR^-$, SiR–$Tubulin^–$, $CEACAM6^+$, $TSPAN8^-$; goblet cells = $NGFR^-$, SiR–$Tubulin^-$, $CEACAM6^+$, $TSPAN8^+$. The results of this experiment were used in Figure 3.7.

A similar gating process was used for FACS, apart from the second gate that was set using Forward-Scatter (FSC) height versus width. FSC-H vs. FSC-W gating is more robust and commonly used because it focuses on cell size differences rather than granularity or complexity and therefore is more accurate when separating single cells from clumps and aggregates. This is highly relevant in cell sorting experiment, as single cells need to be isolated so that they can be accurately sorted individually, to ensure the homogeneity of the sorted samples. Gating graphs can be seen in Figure 3.8.

Data from the FACS run can be seen in Figure 3.9. The analysis revealed distinct changes in cell populations across all markers between the IL-13- and IL-13+ samples, reflecting cellular specialisation within the sample. A marked decrease in $TSPAN8^-$ cells was observed in the IL-13+ sample compared to the IL-13- sample. Additionally, the population of $TSPAN8^-$ $CEACAM6^+$ cells (representing secretory cells that are not goblet cells) disappeared, reflecting the airway remodelling triggered by IL-13 stimulation. A failure in the red laser, which is responsible for detecting SiR-Tubulin signals, resulted in the inability to identify SiR-Tubulin-positive cells as ciliary, introducing a limitation in this aspect of the analysis. Finally, the CEACAM6 vs. NGFR plots demonstrated the disappearance of NGFR+ basal cells following IL-13 treatment, further confirming cellular specialisation induced by this treatment. The number of cells sorted for each population is summarised in the accompanying table, reflecting the outcomes of the gating and specialisation processes. This comprehensive gating and sorting approach underscores the dynamic changes in cellular composition within the sample and allowed for the isolation of goblet cells to be used for subsequent biopanning experiments. FACS yielded 83591 $TSPAN8^+$ $CEACAM6^+$ cells from the IL13- population, and 26692 cells from the IL-13+ sample. It is speculated that these numbers might be too low for biopanning experiments.

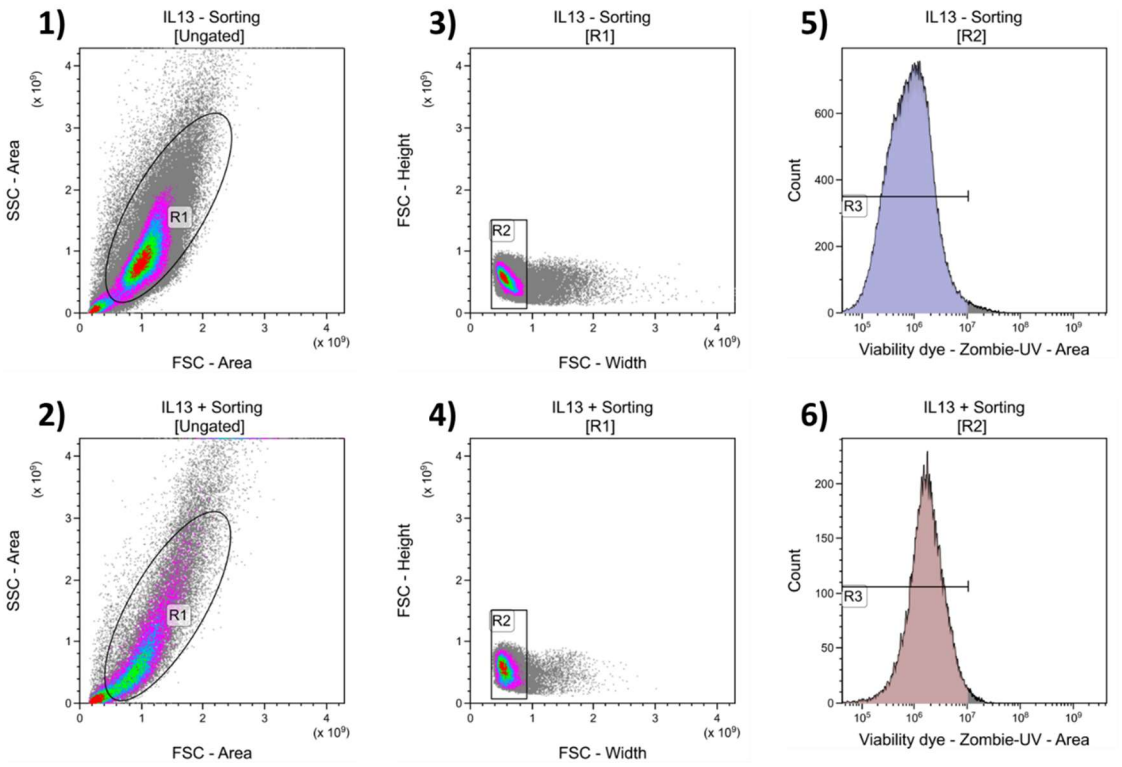
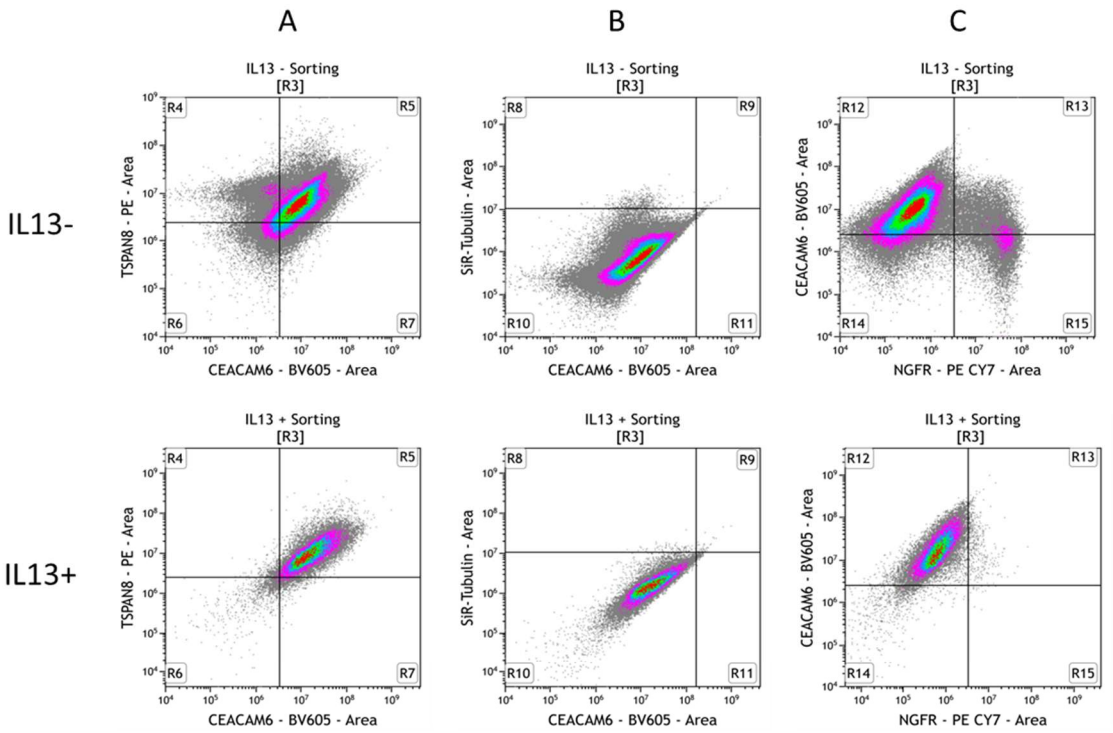


Figure 3.8 Flow cytometry gating strategy for sorting HBEpc cultured at ALI with (IL-13+) or without (IL-13-) interleukin 13 treatment into specific cell subpopulation.

(1 and 2) Initial gate (A) based on forward scatter (FSC) and side scatter (SSC) to exclude debris, allowing for selection of intact cells. (3 and 4) FSC width vs. FSC height gate (B) to remove doublets or clumped cells, isolating single cells. (5 and 6) Final gate using a viability dye to distinguish live cells from dead or apoptotic ones, refining the population for accurate analysis. Each gate progressively narrows the sample to focus on single, live cells for further study.



D

	TSPAN8+/CEACAM6+ (R1 R2 R3 R5)	Tubulin + (R1 R2 R3 R9)	CD271 + (R1 R2 R3 R15)
IL13-	83591	178	13607
IL13+	26692	1	16

Figure 3.9 Fluorescence activated cell sorting of IL-13- and IL-13+ cell populations stained with a multicolour panel for cell type identification.

Gates were based off previous experiments. (A) TSPAN8 vs. CEACAM6 plots. A decrease in the number TSPAN8$^-$ cells can be observed, while the population of cells being TSPAN8$^-$ CEACAM6$^+$ (secretory cells that are not goblet cells) seems to disappear, indicating a specialisation of the cells within the sample. (B) SiR-Tubulin vs. CEACAM6 plots. Very few CEACAM6$^+$ cells were detected. A failure in the red laser, responsible for the SiR-Tubulin signal, prevented any cells from being labelled as SiR-Tubulin$^+$, and therefore identified as ciliary. (C) CEACAM6 vs. NGFR plots. The population of NGFR$^+$ cells (basal) disappears with IL-13+ treatment, confirming the specialisation of the sample. (D) Cells were sorted according to the following gates: TSPAN8$^+$/CD66$^+$ (R1 R2 R3 R5); SiR-Tubulin$^+$ (R1 R2 R3 R9); NGFR$^+$ (R1 R2 R3 R15) and the number of cells obtained are reported in this table.

3.3.4 Biopanning

Whole cell panning was employed to improve the chances of isolating binders to physiologically relevant targets. The first biopanning strategies employed therefore relied on the cell culture inserts themselves. Following stimulation with IL-13 to induce goblet cell metaplasia, MucilAir inserts were used as targets for biopanning and incubated with the library-carrying phages at low temperatures (4° C) to reduce non-specific interactions. The first experiment (T1) yielded no binders: no colonies could be observed on the titre before or after amplification. While it is possible that the phage library may not contain high-affinity binders to the target antigen, it was previously demonstrated that this particular library was highly diverse, and therefore should be sufficient for this particular application (see 2.3.3, page 86). Another potential explanation for the lack of binders could be the incomplete digestion of the trypsin, although the trypsin buffer used is the same as suggested in the literature.

To remedy this, a longer incubation time to allow for more complete binding (4 hours instead of 2) was used for T2. A gentler shake was also used (500 rpm instead of 800 rpm) to optimise binding. Finally, the trypsinisation was done twice to ensure all phages bound phages could be eluted. This resulted in a small number of colonies observed in the phage titre, meaning only around 100 phages were collected. This number is too low to have generated a sufficient number of binders and would not allow for further rounds of biopanning.

To try to increase binding, FACS sorted cells were used. The isolated goblet cells were used as a base for biopanning experiment T3. For this purpose, only IL-13+ stimulated goblet cells were used. Since IL-13 plays a central role in driving mucus hypersecretion, induces goblet cell differentiation and increases mucin production, particularly MUC5AC, a major component of mucus, targeting IL-13-stimulated goblet cells ensures that the nanobodies generated are specifically active against the pathological changes associated with mucus overproduction. Goblet cells stimulated by IL-13 will express disease-relevant targets, such as upregulated mucins or receptors involved in hypersecretion pathways. This increases the likelihood of

identifying nanobodies that bind specifically to proteins or pathways critical for the hypersecretion process (e.g. STAT6, EGFR signalling), rather than generic goblet cell markers or irrelevant proteins.

The low number of cells collected from FACS (only 26692 from the IL-13+ sample) proved difficult to manipulate through the several washes. Each wash necessitated spinning down of the cells, removal of the buffer and resuspension. However, the low number of cells created a very small pellet, meaning proper buffer removal was hard to achieve. This also limited the number of exposed targets for nanobodies to bind to. As a result, only approximately 600 phages were counted from the titre of T3. While this is still insufficient, the improvement from experiments T1 and T2 was encouraging. Therefore, continuing to apply a strategy such as the one described in Stark, Venet and Schmid (2017) seemed the best course of action.

In order to increase the number of cells available, it was decided to detach all cells from the inserts and use these as targets for biopanning. By combining rounds of amplification (on IL-13+ samples) and rounds of absorption where phages that were not specific to the IL-13+ phenotype could be eliminated from the sample (using IL-13- samples), only nanobodies specific to the IL-13+ phenotype could be selected. The first round (T4R1) was an amplification round. IL-13 treated cells were detached from the insert and used as targets for biopanning using protocol adapted from Stark, Venet and Schmid (2017). The eluted phages were titred and yielded 4.2×10^4 CFU ($\pm 2.8 \times 10^4$). This was considered high enough to proceed with the following rounds of biopanning. The next round (T4R2) was an absorption round, and untreated cells were detached and used as targets for biopanning. This round yielded a lower titre of 2.6×10^3 CFU, meaning over 93% of binders were absorbed. The final round (T4R3) was another amplification round, designed to only select the best binders. The obtained eluted phages were not amplified, instead they were used to inoculate 4 mL of log-phase TG1 cells and plated on a large (20x20cm) 2x TY-GA plate. Following overnight incubation, eight colonies were observed (equivalent to 8.25 CFU titre). Each colony was picked up and plated on an individual 2x TY-GA plate. Out of those eight, two colonies appeared to be contamination and did not grow again. The remaining six colonies were grown again and the phagemids were repackaged in

M13K07 phage for further testing. The titre resulting from each experiment can be seen in Figure 3.10. All plates can be viewed in appendix 2 (Figure A. 7).

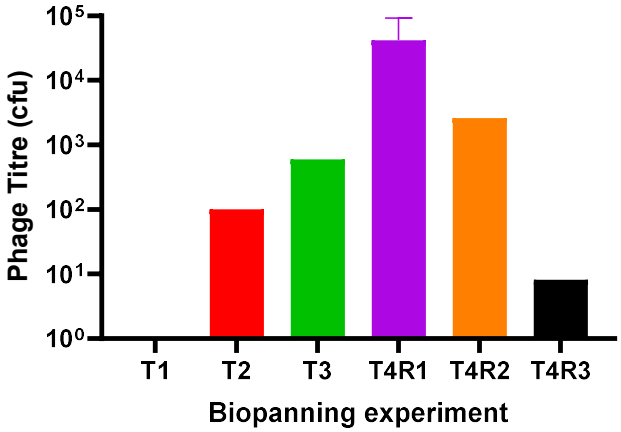


Figure 3.10 Phage titre as CFU of each experiment of biopanning.

Experiments T1 and T2, based on biopanning the whole cell culture inserts, yielded no or very few binders. Experiment T3 yielded a higher number of binders, but the low number of cells available for this experiment made manipulation difficult. Enrichment round T4R1 based on IL13+ cell sample yielded a high number of binders. Following absorption round T4R2 removed potentially irrelevant binders. Finally, enrichment round T4R3 narrowed down binders, yielding 8 clones.

3.3.5 Investigation of Potential Binders

3.3.5.1 Confirming Binding Nanobodies

To confirm the binding of each isolated phagemid, the clones were grown up and infected with M13K07 helper phage to repackage the phagemids. Those phages were then used in a western blot against IL-13+ and IL-13- ALI HBEpc cell lysates, run on either a Tris-Glycine denaturing gradient gel (4 to 20%), or a Bis-Tris native gradient gel (4 to 16%) to retain the protein structures, alongside a colorimetric protein ladder. HEL was also run as a positive control. The ran samples were then transferred onto nitrocellulose membranes, blocked, and then probed with clones packaged by M13K07 helper phages, native M13K07 phages as a negative control, and PpSEX81_5A7 as a positive control. After several washes, the membranes were probed with anti-M13 antibody-HRP (1:1000), washed again and imaged by chemiluminescence.

In

Figure 3.11, the results of the denaturing western blot can be seen. A band can be observed for clones 3 in the IL-13+ lane (lane 1), while a similar band is slightly visible in the IL-13- lane (lane 2) but is slightly hidden by over-exposure of the membrane. The band appears to be between 40 kDa and 50 kDa. A similar band can be seen more clearly for clone 5, while a faint band can be seen for clone 6, again around the 40–50 kDa mark. No bands could be observed on the native M13K07 membrane. The positive control HEL probed with PpSEX81_5A7 also revealed no bands. On the other hand, the native western blot (Figure 3.12) showed no bands in any of the lanes.

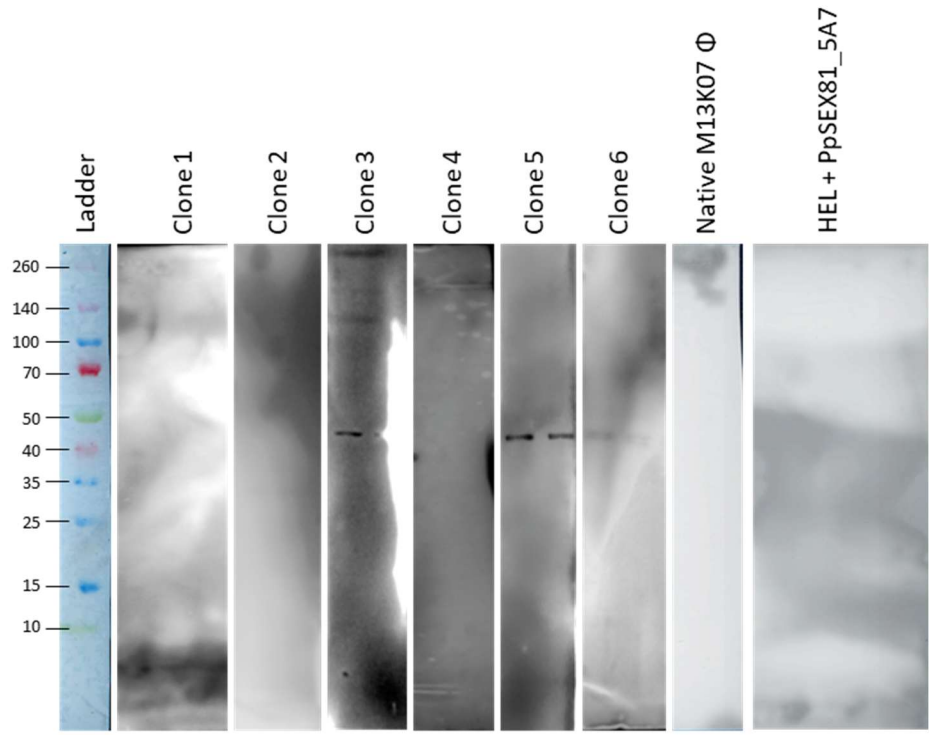


Figure 3.11 Western blot of IL-13+ (column 1), IL-13- (column 2) lysates, and HEL (column 3, final membrane only).

Samples were run on a denaturing Tris-glycine SDS-PAGE gel, transferred onto a nitrocellulose membrane, and probed with either clone packaged by M13K07 phages, native M13K07 phages or PpSEX81_5A7 followed by anti-M13 antibody-HRP and imaged by chemiluminescence. The first membrane shows Thermo Fisher Scientific Spectra Multicolour Broad Range Protein Ladder.

The lack of bands in the HEL probed with 5A7 carrying M13K07, despite a positive ELISA assay (see section 2.3.1, page 62) was unexpected. While ELISAs tend to be much more sensitive than western blot, this lack of signal could also reflect the specific structure of HEL. With a size of 14.33 kDa, HEL presents a mostly hydrophilic surface, with multiple hydrophobic binding pockets. vNAR 5A7 CDR1 and CDR3 bind into the hydrophobic pockets of HEL (Stanfield et al., 2004) as can be seen in Figure 3.13. When run on a denaturing Tris-glycine SDS-PAGE gel, HEL would lose its tertiary structure, and those binding pockets would therefore no longer be available for vNAR 5A7 carrying M13K07 phages to bind to, offering a possible explanation for the lack of signal in the positive control in

Figure 3.11. This could also mean that possible binding of clones 1, 2 and 4 might not be visible on a denaturing western blot; other assays such as Enzyme Linked Immunosorbent Assay (ELISAs) should be considered to confirm binding of isolated nanobodies.

The samples run on a native Bis-Tris PAGE gel showed no bands for any of the M13K07 phages (Figure 3.12). Bis-Tris PAGE allows for the separation of proteins under native (non-denaturing) conditions. This allows for proteins to maintain their structure and activity, such as enzymatic activity, binding properties, or interactions with other molecules (Eubel *et al.*, 2005; Schägger and von Jagow, 1991). Bis-Tris PAGE also operates at a pH of around 6.4–7.2, which is closer to physiological conditions compared to other systems like Tris-Glycine (pH ~8.3). Therefore, it would be expected that clones and positive control would be able to bind to their target. For clones, it is a possibility that the cell lysis process was sufficient to disturb the binding of target proteins, preventing any binding; however, this is unlikely. The transfer of the proteins onto the membrane was potentially incomplete, as only a partial colorimetric ladder could be obtained. It is therefore possible that not all proteins transferred properly onto the membrane, explaining the lack of signal observed. Due to the high cost of MucilAir™ inserts, and the amount of lysates required per gel, this experiment could not be repeated.

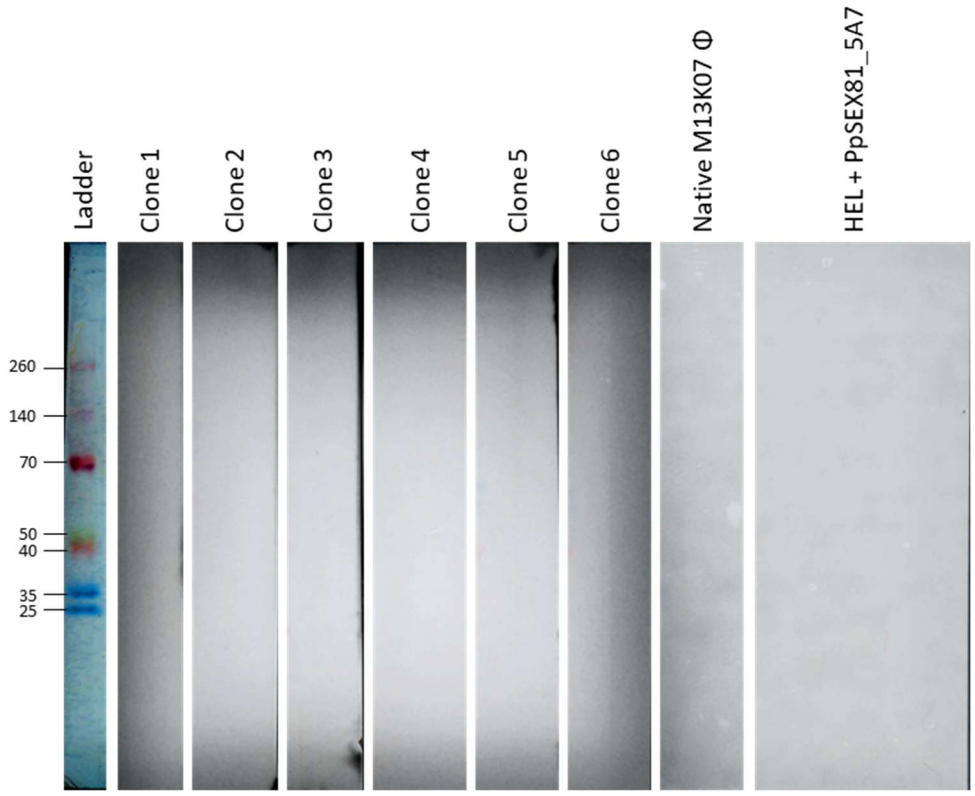


Figure 3.12 Western blot of IL-13+ (column 1), IL-13- (column 2) lysates, and HEL (column 3, final membrane only).

Samples were run on a native Bis-Tris PAGE gel, transferred onto a nitrocellulose membrane, and probed with either clone packaged by M13K07 phages, native M13K07 phages or PpSEX81_5A7 followed by anti-M13 antibody-HRP and imaged by chemiluminescence. The first membrane shows Thermo Fisher Scientific Spectra Multicolour Broad Range Protein Ladder.

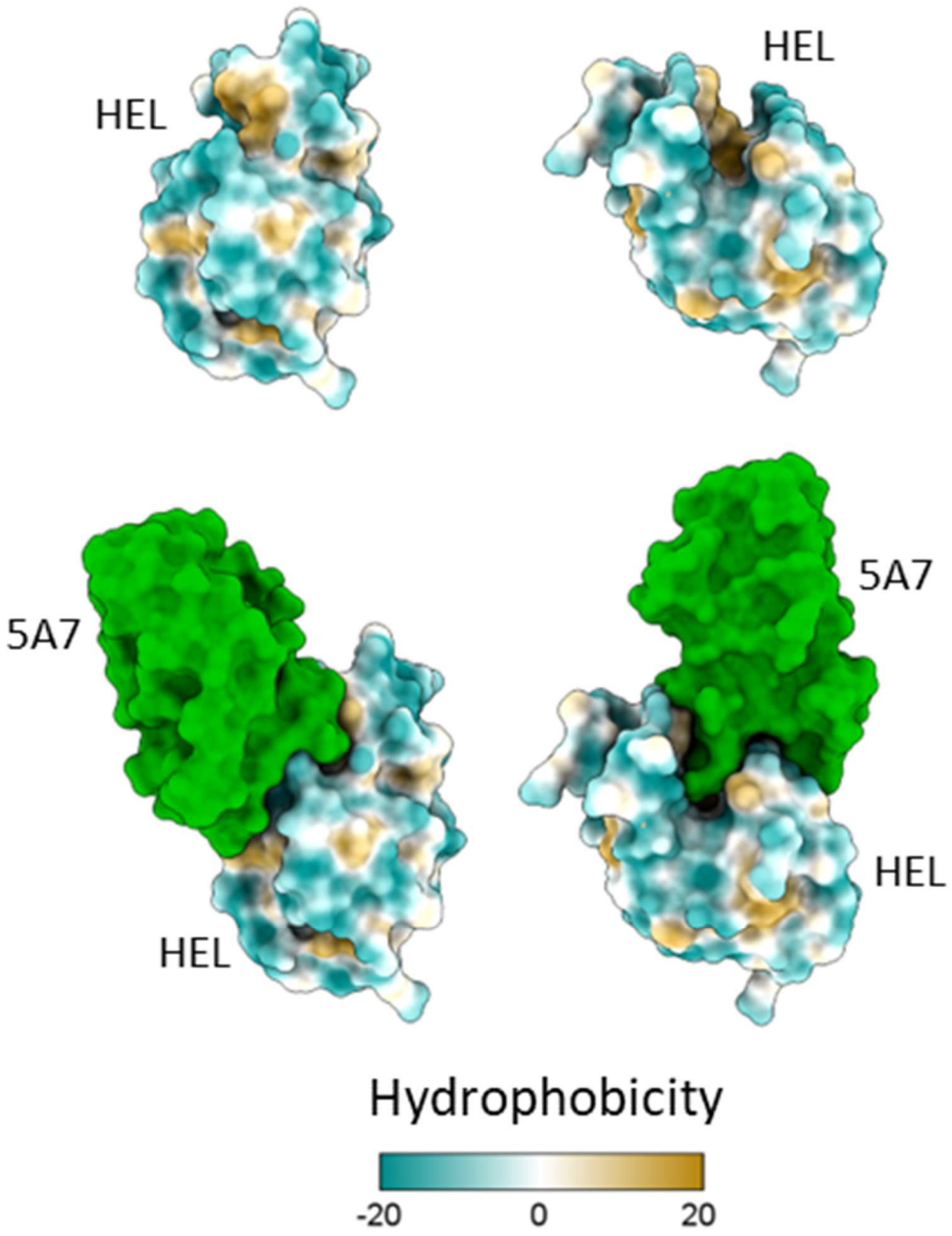


Figure 3.13 Molecular surface representation of vNAR 5A7 bound to HEL highlighting hydrophobicity.

The surface HEL is shown, coloured according to hydrophobicity: hydrophobic regions are depicted in orange and hydrophilic regions in blue. vNAR 5A7 is shown as surface representation in green, bound to HEL, illustrating its interaction with the hydrophobic or hydrophilic regions of HEL. PDB accession ID: 1SQ2.

3.3.5.2 Sequencing and Sequence Consensus

To confirm the selection of binders through the multiple rounds of biopanning, clones, as well as multiple colonies for each round of T4 biopanning, were first picked up and grown on a 96-well agar plate containing ampicillin, before being sent to the PlateSeq Supreme Sanger Sequencing Service at Eurofins, alongside primers ForFR1_NcoI and RevFR4_NotI. Unfortunately, Eurofins was unable to sequence any of the colonies sent. While the exact reasons for this technical failure are unknown, it is possible that DNA variation might have appeared in the sequences, preventing the binding of the primers.

M13K07 packaged clones were also prepared for PCR. The DNA was extracted, and a PCR reaction was set up using the NGS primers NGS3_for and NGS3_rev. Unfortunately, no amplification could be obtained, despite several optimisation of the protocol, including temperature gradients, increased cycle numbers and different enzymes. This means samples could not be sent for next generation sequencing. This confirmed that usual primers were unable to bind to the isolated DNA. This could indicate the presence of unexpected DNA variation at the primers binding sites.

To circumvent the issue, the six clones were then grown in *E. coli*; only five out of the six clones could be grown again; clone 3 unfortunately did not yield any colonies when streaked on a plate, meaning that despite showing a binder on the western blot, it could not be sent for sequencing. Plasmids were prepped and sent for whole plasmid sequencing at the University of Nottingham DeepSeq Service, and plasmids were sequenced using MinION™ Flow Cells on and the EPI2ME analysis platform. This allowed for the full sequence of the plasmid to be obtained for analysis. Reads were trimmed for low quality and assembled against pSEX81-5A7 plasmid as a template (see Figure 3.14).

Assembled reads were highly conserved through most of the sequence apart from a segment starting towards the end of the ColE1 origin gene and ending after the 5A7 domain. Here, the reads were highly diverse, resulting in a low percentage identity. While this was expected over the 5A7 region due to the introduced diversity, the ColE1 origin region should be completely conserved across clones: no diversity

was introduced, and the gene is essential to plasmid replication in *E. coli*. This high level of variability explains why amplification through PCR was unsuccessful, as primer binding sequences appeared to have not been conserved.

Errors in sequencing can produce low-quality reads, base calling errors or biases, especially in repetitive regions. While sequences were trimmed for low quality before any assembly was performed, inaccurate sequencing could still result in misaligned sequences. GC-rich or repetitive regions are known for interfering with sequencing and could lead to a lower accuracy in sequencing. In the pSEX81_5A7 sequence, several regions have noticeably high GC content (>60%) with some of these regions reaching as high as 74% GC content (Figure 3.15). Multiple copy plasmids such as pSEX81 can also present challenges in sequencing, inserts containing repeating sequences, which might be the case for many of the variants generated through the library may be unstable and result in insert deletion or mutations. Mis-assembly is unlikely, as most of the pSEX81 sequence was conserved with high percentage identity, but it is possible that the addition could result in incorrect joining of fragments and create chimeric sequences that do not align properly with the reference.

The most likely explanation for these results lies with the isolated clones themselves. The presence of heterologous sequences in the samples could result in unreadable sequencing results. Foreign DNA contamination in the lab is a likely explanation. Phage contamination, especially, is notoriously hard to prevent in laboratory settings. Bacteriophages such as M13K07 are highly resistant to harsh conditions, such as desiccation, UV radiation, and temperature fluctuations. Their small size (~20–200 nm) and high abundance make them particularly difficult to eliminate from lab equipment and shared facilities. Finally, phage contamination is often undetectable prior to sequencing. Despite all precautions being taken when handling samples and decontaminating lab spaces, phage contamination is a probable explanation for the sequencing results.

Another possible explanation would be the occurrence of recombination events between similar sequences, resulting in rearrangements or

insertions/deletions or nucleotides within the sequence. When introducing genetic diversity through the nanobody sequence, it is a possibility that certain generated sequences matched with other regions of the plasmid, causing homologous recombination between similar sequences. Finally, natural mutations, such as substitutions, insertions, or deletions, may accumulate in the plasmid during its propagation.

Despite seemingly positive results in western blot analysis, the inability to sequence the corresponding DNA indicates a fundamental issue with the molecular construct. As a result, the rounds of biopanning cannot be considered as having successfully isolated binders for the surface of IL-13 stimulated ALI cultured HBEpc.

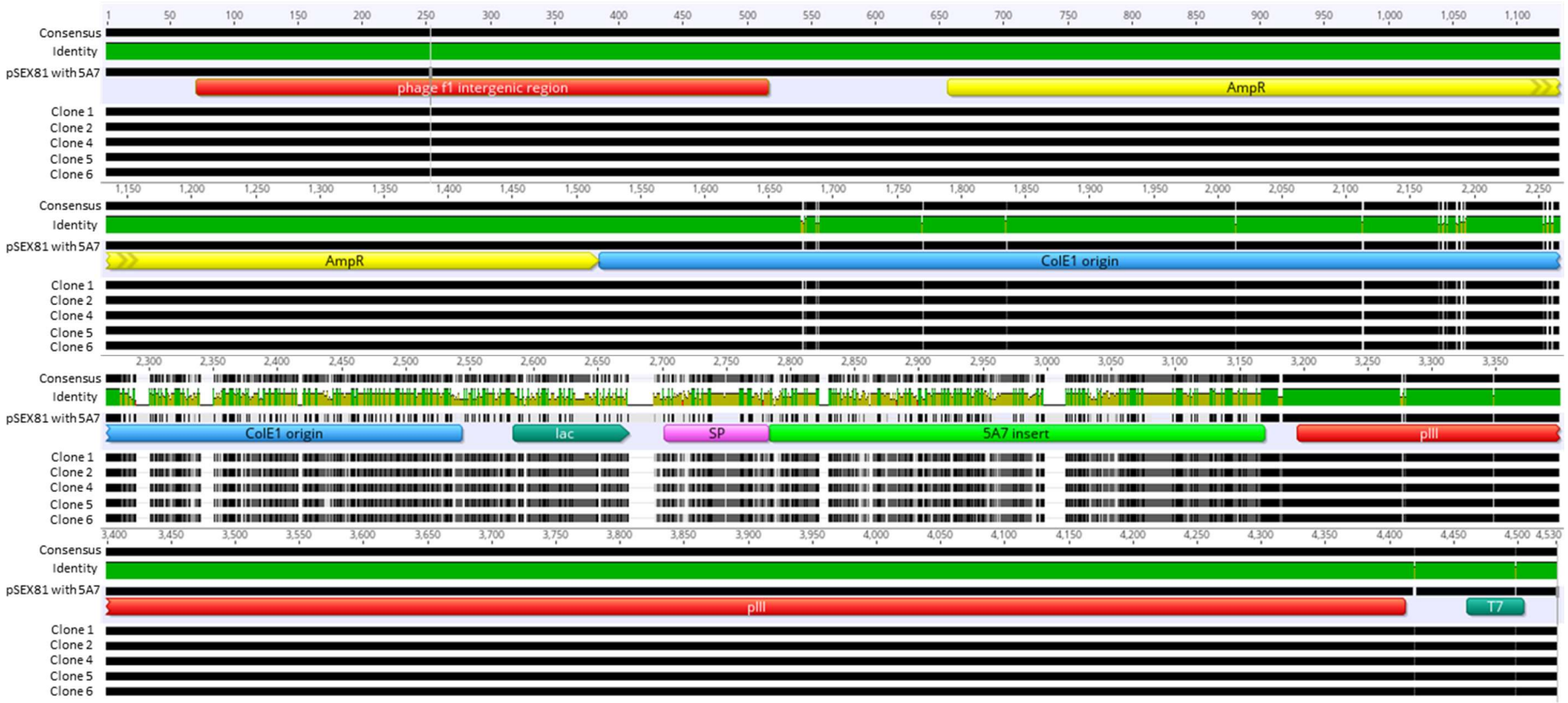


Figure 3.14 Alignment of plasmid assembly against pSEX81_5A7.

Conservation is shown as grey scale, with black being 100% and white 0%. A highly disturbed

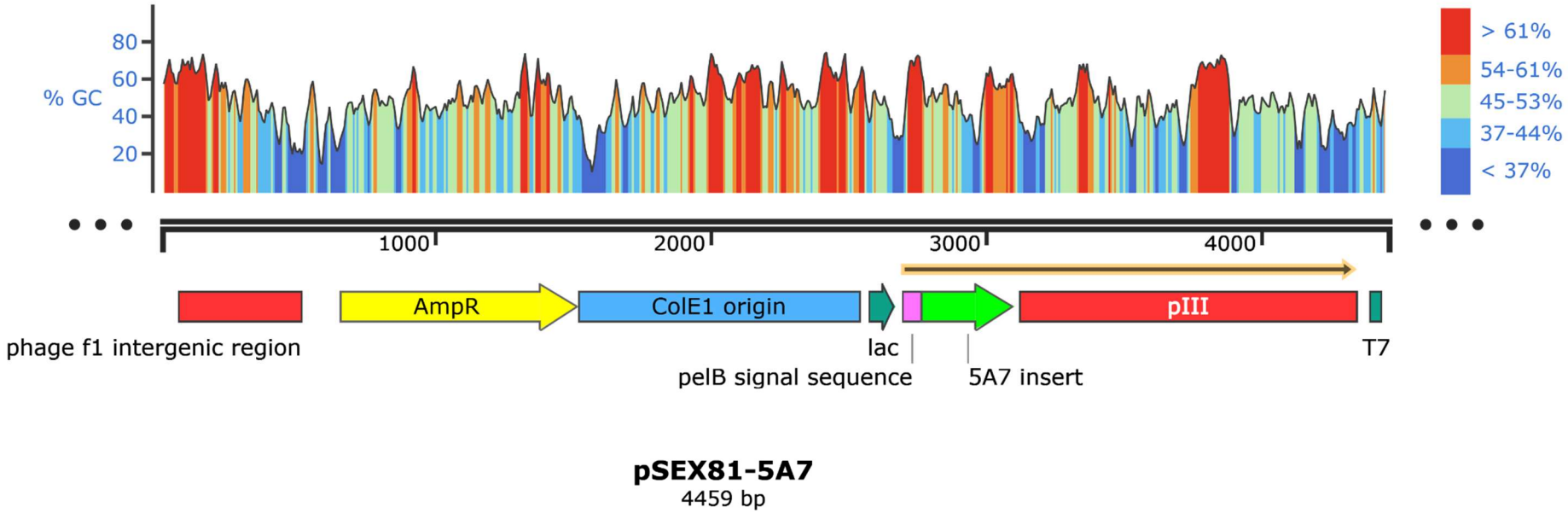


Figure 3.15 GC Content Across the ColE1 Origin Sequence in pSEX81 as plasmid replication origin.

The x-axis represents the nucleotide position within the sequence, while the y-axis indicates the GC content as a percentage, calculated using a sliding window of 25 nucleotides. The low percentage identity region in alignment contains several high GC content (>61%) regions.

3.3.5.3 Challenges in Isolating Nanobodies from Phage Display Libraries

While phage nanobody libraries are powerful tools, as previously explained, they remain notoriously difficult to use. Target presentation, especially when using whole-cell antigen presentation, can yield irrelevant or low-quality binders due to misfolded or improperly presented targets. This appeared to be the best strategy when targeting a specific phenotype, however, but further optimisation and protocol enhancements are necessary to ensure the reliability of the technique. The stringency of the selection requires a balance between specificity and retention to ensure sufficient binders are retained while eliminating non-specific binders. High background noise from phages adhering to plasticware or blocking agents can be the cause of such non-specific binders. While phages were diluted in the same plastic and blocking buffer prior to exposure to the sample to avoid non-specific binding, binding to media remnants or other compounds still present in the sample (such as cell detaching reagents) is a possibility. Such non-specific binders can then be further enriched by phage amplification, resulting in the overrepresentation of irrelevant clones in subsequent rounds of biopanning.

Another possible caveat of phage nanobody selection lies in the complexity of the protocols. While library preparation was successfully validated through next-generation sequencing in this attempt, successful selection often depends on subtle changes to protocols, such as pH, salt concentrations, or washing conditions. While these conditions were chosen based on existing protocols in the literature (Panagides *et al.*, 2022; Stark *et al.*, 2017; Zadeh *et al.*, 2019), these protocols might not be generalisable to the specific experimental design applied in this project.

Several issues can also arise from biopanning. False positives are a possibility: clones that were isolated through biopanning might not be strong or specific binders. This is particularly likely here, as positive binding was observed on some of the western blots, but accurate DNA sequences could not be confirmed by NGS. Additionally, even if correct binders are identified through phage biopanning, they might not exhibit the appropriate level of affinity, specificity or stability: isolated

binders often require downstream binding optimisation through selected mutagenesis to obtain the most appropriate binders. Validating antibodies and antibody-derived binders such as nanobodies is a complex process involving multiple assays. Western blots are initially used to assess the specificity of the compound; blocking peptides covering the protein sequence can also be used to confirm binding in immunohistochemistry, using knockout cell lines as negative control. These assays should be repeated using multiple cell lines to confirm accurate target binding. Tissue microarrays can also be used to confirm the binding of the target in a variety of samples, they can be used to ensure reproducibility of the antibody (or nanobody) binding. Here, additional repeats of the initial western blot experiments could confirm the results obtained.

Finally, utilising phagemids over phage vectors might have reduced the titre significantly in binder experiments. When utilising phagemids with helper phages, only one of the pIII proteins expresses the nanobody, resulting in a lower average affinity. This effect was partially mitigated by the use of the Hyperphages system in the first round of biopanning, allowing for all pIII proteins to express a copy of the nanobody. Utilising his system for all the rounds of biopanning might yield a higher number of binders, which might be particularly helpful for whole cell antigen display that tend to yield a low titre (Breitling *et al.*, 2010; Chasteen *et al.*, 2006).

3.4 Conclusion

Human bronchial epithelial cells (HBEpc) were cultured at the air- liquid interface as a model for the human airway epithelium, and IL-13 stimulation was successfully used to simulate the hypersecretory phenotype observed in AHDs: flow cytometry analysis revealed an increase in the percentage of goblet cells in the sample from 3.77% to 17.92% post IL-13 stimulation. Several biopanning methodologies relying on whole cell panning were employed in order to isolate binders to the IL-13+ phenotype. Unfortunately, no conclusive sequences could be obtained from the isolated clones. Potential explanations for this lack of identified binders are discussed in Chapter 5 (page 193), alongside future work.

Chapter 4 Functionalisation of Target-Specific Nanobodies

4.1 Introduction

4.1.1 Protein Expression and Purification

Recombinant protein expression technology relies on the development of DNA cloning by Stanley Cohen and Herbert Boyer in 1973, allowing for foreign DNA packaged into plasmids to be transformed into bacteria (notably *Escherichia coli*), subsequently allowing for the expression of recombinant proteins in prokaryotic systems (Cohen *et al.*, 1973). A seminal example of the application of this technology is the expression of human insulin in *E. coli* in 1978 by David Goeddel and his colleagues of Genentech, which allowed for rapid and cost-effective insulin production and vastly increasing the availability of this life-saving drug.

Later on, the discovery of strong promoters capable of increasing gene expression, such as the lac operon and T7 promoter, further facilitated recombinant protein expression (Davanloo *et al.*, 1984; Shapiro *et al.*, 1969; Studier and Moffatt, 1986). Alternative expression systems such as the yeast *Saccharomyces cerevisiae* (Beggs, 1978; Brake *et al.*, 1984), *Spodoptera frugiperda* 9 insect cells, or the mammalian Chinese hamster ovary cells (Geisse and Kocher, 1999), offered new possibilities for post-translational modifications and native protein folding of complex proteins.

Advances in protein expression coincided with the development of protein purification technologies. Notably, the development of modern ion exchange chromatography, which separates proteins based on their charge (Small *et al.*, 1975) as well as affinity chromatography, which uses specific binding interactions between the protein of interest and a ligand attached to the chromatography matrix (reviewed in Hage *et al.*, 2015). For example, nickel ion affinity chromatography relies on the ability of metal ions to bind poly-histidine residues. Nickel ions can be easily

immobilised onto an agarose bead matrix functionalised with a chelator, such as nitrilotriacetic acid, to isolate poly-histidine tagged proteins from crude lysate. The combination of these techniques allows for rapid and cost-effective production of recombinant proteins and has therefore been used numerous times for the production of therapeutic molecules, particularly antibodies.

4.1.2 Bioconjugation Methods

Bioconjugation is a chemical strategy that involves the formation of a stable covalent bond between two biomolecules or between a biomolecule and a synthetic molecule. This strategy allows for the functionalisation of purified recombinant proteins to create conjugates with enhanced or novel functionalities. For example, the conjugation of antibodies with fluorescent markers has been widely used as a diagnostic tool in flow cytometry and western blotting. As mentioned previously, antibody drug conjugates that combine the targeting ability of antibodies with the therapeutic action of drugs have been developed for the treatment of various pathologies. Finally, bioconjugation is an important tool in the development of cellular imaging technologies by labelling biomolecules with isotopes or fluorescent markers, allowing for rapid and accurate target identification for *in vivo* and *in vitro* imaging.

Several bioconjugation methods are commonly used, as previously discussed. Amide coupling involves the reaction of primary amines with N-hydroxy succinimide (NHS) esters or carbodiimides and carboxylic acids to form stable amine bonds and has been widely used for the conjugation of antibodies with fluorophores. On the other hand, the reaction of maleimides with free sulphydryl groups (found in cysteine residues) can form stable thioether bonds between synthetic and biological molecules. Technologies such as ELISAs rely heavily on biotinylation, where biotin is conjugated to antibodies through amide coupling or maleimide chemistry, and on streptavidin/biotin interactions when the biotinylated target is detected using fluorophore-labelled streptavidin. Finally, copper catalysed azide-alkyne cycloaddition (or ‘click chemistry’) methodologies have been developed and awarded the Nobel Prize in Chemistry in 2022.

While these bioconjugation methods play a vital role in enabling various applications of antibodies, such as immunofluorescence, Western blotting, ELISA, flow cytometry, and *in vivo* imaging, the unspecific labelling of amino acids can lead to a loss of affinity when the labels inadvertently bind the variable domains of immunoglobulins. To remedy this issue, sequence-specific bioconjugation methods, such as Sortase A conjugation, can be used.

4.1.3 Sortase A Conjugation

Sortase A conjugation is a bioconjugation technique that utilises the enzyme Sortase A, a transpeptidase enzyme derived from *Staphylococcus aureus,* to covalently attach various molecules to a protein of interest, typically an antibody. In the cell, Sortase A catalyses the anchoring of surface proteins to the cell wall of bacteria.

In the context of bioconjugation, Sortase A recognises and cleaves a specific peptide sequence called the LPXTG motif (where X is any amino acid) on the target protein. This cleavage results in the formation of a transient acyl-enzyme intermediate, which subsequently reacts with a synthetic oligoglycine-containing molecule, often referred to as a 'sortag' or 'Sortase A tag.' The sortag carries the desired functional group, such as fluorophores, biotin, or other small molecules.

By employing Sortase A conjugation, a variety of molecules can be specifically attached to the LPXTG motif engineered into the protein of interest. This method allows for precise and controlled labelling, and offers mild reaction conditions, high specificity, and the ability to produce homogeneous bioconjugates, making it an attractive alternative to traditional bioconjugation techniques (Figure 4.1).

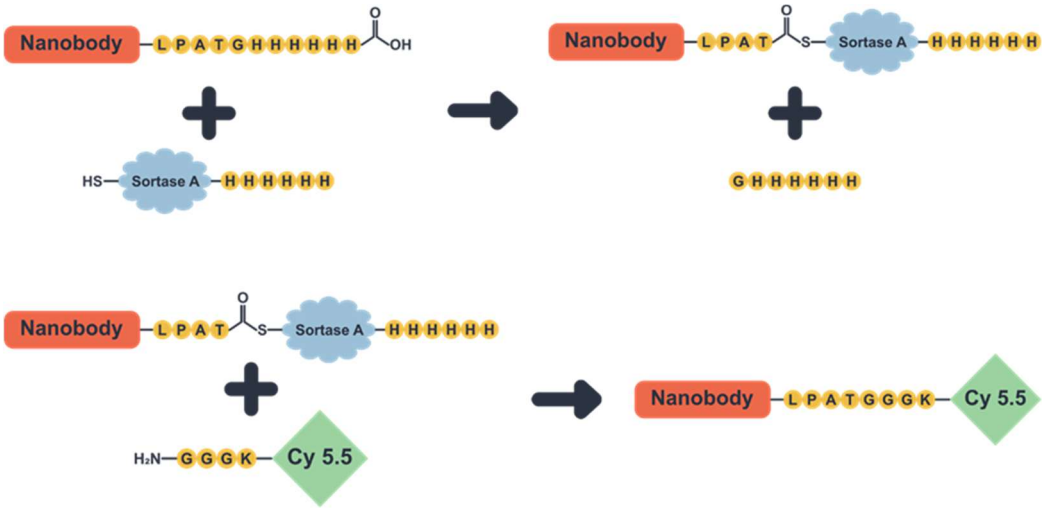


Figure 4.1 Functionalisation of a nanobody with a Cy5.5 fluorophore catalysed by Sortase A.

Sortase A targets recognition site LPXTG (here, LPATG) and cleaves the poly-histidine tag, allowing for the conjugation of the Cy5.5 fluorophore coupled to an oligoglycine to be conjugated onto the nanobody.

4.1.4 Solid Phase Peptide Synthesis

Before the advent of Solid Phase Peptide Synthesis (SPPS), peptides were synthesised using solution-phase methods. These methods were laborious, time-consuming, and often resulted in low yields and purification challenges due to the need for isolating intermediates at each step, as well as solubility problems, which often prevented the elongation of the peptide chain (Coin *et al.*, 2007; Jaradat, 2018). In 1963, Bruce Merrifield introduced SPPS: by attaching the initial amino acid to an insoluble polymer resin (such as polystyrene beads), it allows for iterative coupling of amino acids and easy washing away of reagents and byproducts (Merrifield, 1964, 1963). He was subsequently awarded the Nobel Prize in Chemistry in 1984 for his discovery.

The initial SPPS methodology employed the Boc/Bzl/HF technique: Boc (tert-butyloxycarbonyl) was used as the temporary protecting group for the amino group of amino acids, and Bzl (benzyl) protecting groups for the side chains. The synthesised peptide was then cleaved from the resin using hydrofluoric acid (HF). However, HF being extremely corrosive and requiring the use of HF-resistant equipment drove the

development of alternative chemistries. In 1970, orthogonal Fmoc/tBu (9-fluorenylmethyloxycarbonyl/tert-butyloxycarbonyl) chemistry was developed by Carpino and Han (1970). In Fmoc/tBu peptide synthesis, the Fmoc protecting group can easily be removed using a mild base, such as piperidine. Amino acids are activated for coupling using dicyclohexylcarbodiimide or HBTU (Hexafluorophosphate Benzotriazole Tetramethyl Uronium), for example (Singh *et al.*, 2023). Following the iterative addition of amino acids, the peptide can then be cleaved from the resin using mild basic conditions.

Further advances in the field included the development of novel sidechain protective groups (such as tritylamines or methyltrityl), as well as advances in resin and linker chemistry (such as Rink Amide resin). Finally, automated peptide synthesisers developed in the 1980s allowed for higher throughputs by automating the iterative cycles of deprotection, washing, and coupling, significantly reducing manual labour and errors. They can also employ microwave reactors to increase reaction rates and accelerate synthesis (Pedersen *et al.*, 2012).

The development of SPPS led to significant advances in the field of biological research, as it allowed for the easy production of peptides, hormones and synthetic antigens. It also facilitated research into protein structure, function, and interactions. Peptide-based therapeutics, such as insulin analogues, HIV protease inhibitors, and antimicrobial peptides, were developed using SPPS (Dhayalan *et al.*, 2017; Limal *et al.*, 1998; Mäde *et al.*, 2014). Finally, this technique has been used to create peptide-based materials, such as hydrogels and nanomaterials, for various biomedical applications (Fu *et al.*, 2021).

4.1.5 Aim and Objectives

The aim of this chapter is to label previously isolated nanobodies with a fluorescent tag at the C'-terminus to allow for the detection of the nanobody target. A fluorescent label will be designed and synthesised for Sortase A bioconjugation. Sortase A enzyme will be obtained by bacterial protein expression and purification. The previously isolated vNAR 5A7 nanobody will be expressed in a bacterial system before being purified by liquid chromatography.

4.2 Materials and Methods

4.2.1 Peptide Synthesis

Amino acids purchased from Merck (Novabiochem); all solvents high grade. Syntheses were performed on a 0.25 mmole scale. Reagent abbreviations are presented in the table below (Table 4.1).

Table 4.1 Reagent abbreviations and full names.

Abbreviation	Full reagent name
DCM	Dichloromethane
DMF	N,N-Dimethylformamide
Oxyma	Ethyl cyano(hydroxyimino)acetate
DIC	N,N'-Diisopropylcarbodiimide
TFA	Trifluoroacetic acid
TIS	Triisopropylsilane
DIPEA	N,N-Diisopropylethylamine
NMP	N-Methyl-2-pyrrolidone

4.2.1.1 Manual FMOC-SPPS

4.2.1.1.1 Resin Loading

Fritted syringes *(Torviq, USA)* were used and the various solutions of reagents and washing solvents taken up via stainless steel needles. The syringes were capped and agitated on a rotating table at room temperature during coupling.

Rink amide resin (Novabiochem, loading capacity 0.710 mmole/g) was swollen in DCM for 30 minutes, before being washed with DCM (5 × 3 mL) and DMF (5 × 3 mL). Removal of the Fmoc group followed by treatment with 20% (v/v) piperidine/DMF (2 × 5 minutes). The resin was washed with DMF (5 × 3 mL), DCM (5 × 3 mL) and DMF (5 × 3 mL). DIC (4 eq. over resin loading) and Oxyma (4 eq.) were added to a solution of Fmoc-AA-OH (4 eq.) in DMF. After 5 minutes of pre-activation, the mixture was added to the resin. After 2 hours, the resin was washed with DMF (5 × 3 mL), DCM (5 × 3 mL) and DMF (5 × 3 mL), capped with acetic anhydride/pyridine (1:9 v/v) (2 × 3 minutes) and washed with DMF (5 × 3 mL), DCM (5 × 3 mL) and DMF (5 × 3 mL).

4.2.1.1.2 General Amino Acid Coupling

A pre-activated solution of protected amino acid (4 eq.), DIC (4 eq.) and Oxyma (4 eq.) in DMF was added to the resin. After 1 h, the resin was washed with DMF (5 × 3 mL), DCM (5 × 3 mL) and DMF (5 × 3 mL). For precious amino acids, 2 eq. of all reagents were used, and the coupling left overnight.

The resin was subsequently capped: Acetic anhydride/pyridine (1:9 v/v) was added to the resin (3 mL). After 3 minutes the resin was washed with DMF (5 × 3 mL), DCM (5 × 3 mL) and DMF (5 × 3 mL). The resin was then treated with 20% (v/v) piperidine/DMF (3 mL, 2 × 3 minutes) and washed with DMF (5 × 3 mL), DCM (5 × 3 mL) and DMF (5 × 3 mL).

4.2.1.1.3 Final Deprotection and Cleavage

Once the sequence was completed, the N-terminal Fmoc group was removed by treatment with 20% (v/v) piperidine/DMF (2 × 5 minutes) and the resin was washed with DMF (10 x) and CH_2Cl_2 (10x) and then dried in vacuo.

A mixture of TFA, TIS and water (90:5:5 v/v/v) was added to the resin to cleave the peptide. After 2 h, the solution was plunged into a 50 mL falcon tube and evaporated under a stream of N_2 to <5 mL (if required). Diethyl ether (approximately 30 mL) was added to precipitate the peptide and the solution centrifuged. The supernatant was discarded, and the pellet dissolved in 0.1% (v/v) TFA in water/MeCN for HPLC purification.

4.2.1.2 Automated FMOC SPPS

The automated Microwave Peptide Synthesiser Biotage® Initiator+ Alstra™ was used for all automated FMOC SPPS. Rink amide was loaded onto the system using the usual Fmoc-deprotection/coupling procedure. Amino acids were prepared at 0.5 M in DMF (4 eq. per coupling), DIC at 0.5 M in DMF (4 eq. per coupling), and Oxyma at 0.5 M in DMF (4 eq. per coupling). Acetic anhydride/DIPEA 0.3 M in NMP was used for capping, and 20% (v/v) piperidine in DMF was used for deprotection. The system parameters are presented in Table 4.2. Each step was followed by a wash step in DMF (45 seconds with mixing).

Table 4.2 Automated FMOC SPPS parameters

Step	Solvent	Temperature (°C)	Duration	Oscillating mixer	Interval (on/off in sec)
Resin swelling	DCM	Room temperature	60 minutes	On	10/30
Fmoc removal	20% piperidine/DMF	Room temperature	Two repeats: 3 minutes then 10 minutes	On	10/15
DIC/Oxyma coupling (microwave)	DMF	75	5 minutes	On	Off
DIC/Oxyma coupling (room temp.)	DMF	Room temperature	60 minutes	On	Off
Capping	Acetic anhydride/DIPEA 0.3 M in NMP	Room temperature	5 minutes	On	Off

A pre-cleave wash with DCM was performed at the end of the synthesis, the reaction vessel then removed from the system and the cleavage step was performed manually (see 4.2.1.1.3).

4.2.2 Conjugation of Cy5.5 to Lysine Residues

A peptide containing Mtt lysine was synthesised and left attached to the resin. The Mtt protective group was deprotected on resin using 25 × 5 mL × 5 minutes washes of 1% (v/v) TFA, 98% (v/v) DCM and 1% (v/v) MeOH. A coupling solution containing 1.2 eq. Cy5.5 NHS ester, 1.2 eq. DIPEA in DMF was prepared and incubated overnight with 1 eq. peptide on resin with shaking. The labelled peptide was then washed with DMF (5 × 3 mL), DCM (5 × 3 mL) and DMF (5 × 3 mL) before final FMOC deprotection and cleavage.

4.2.3 High-Performance Liquid Chromatography

4.2.3.1 Analytical High-Performance Liquid Chromatography

Analytical high-performance liquid chromatography (Analytical HPLC) was performed using a Thermo Ultimate 3000 uHPLC equipped with a UV-Vis detector set

to monitor at 210 nm, 254 nm, 280 nm and 450 nm. Separation was achieved on a Waters SunFire 5 µm, 2.1 mm × 150 mm column (C-18) at a flow rate of 0.6 mL/minute. The column temperature was maintained at 45° C throughout the analysis.

The mobile phase consisted of solvent A (0.1% (v/v) TFA in H_2O) and solvent B (0.1% (v/v) TFA acid in acetonitrile). Various linear gradients were used based on compound elution time and purity. The column was equilibrated with 95% A and 5% B for 10 minutes before sample injection. Chromatograms were analysed using Chromeleon™ 7.2.10 CDS Software before data was exported and processed in GraphPad Prism 10.4.1 (from GraphPad software; available at www.graphpad.com). The chromatograms were analysed by integrating the peak corresponding to the target peptide and comparing its area to the total area of all detected peaks. Purity was calculated as the percentage of the target peak area relative to the total peak area, using the following formula:

$$Purity(\%) = (\frac{AUC\ of\ target\ peak}{Total\ AUC\ of\ all\ peaks}) \times 100$$

4.2.3.2 Preparative Reverse-Phase High-Performance Liquid Chromatography

Preparative reverse-phase high-performance liquid chromatography (prep RP-HPLC) was performed using a Waters 1525 binary pump HPLC. A Waters SunFire 5 µm (C-18) preparative column with 5-µm particle size, 19 mm × 150 mm, flow rate of 6 mL/minute, was used for separation and purification. The column was maintained at room temperature. The mobile phase consisted of solvent A (0.1% (v/v) TFA in H_2O) and solvent B (0.1% (v/v) TFA in acetonitrile). The gradient was optimised based on the retention time and separation parameters identified during analytical HPLC analysis. Fractions were collected manually based on the UV-Vis absorbance profile, and fractions corresponding to the target compound were pooled and analysed for purity using analytical HPLC to confirm successful separation. Samples were then frozen at -80 °C and freeze-dried on a Labconco FreeZone Benchtop Freeze Dryer.

4.2.4 Mass Spectrometry

Mass spectrometry was conducted by the University of Nottingham Mass Spectrometry service run by Ben Pointer-Gleadhill, Tong Liu, Zoe Disley and Lola Ogunyemi.

High-resolution mass spectrometry analyses were performed on a Bruker micrOTOFII mass spectrometer (Bruker Daltonik, Bremen, Germany), interfaced to an Agilent 1200 HPLC (Agilent Technologies, Santa Clara, USA). Samples were presented in solution for analysis by Flow Injection, 1 µL of solution being injected into the ion source of the instrument along with a flow of 0.2 mL/minute of 70% (v/v) methanol/water eluent. The mass spectrometer was operated in electrospray ionisation (ESI) mode, operating in positive or negative ionisation, at a typical resolving power of 8000. The machine interface was provided by Bruker's Compass Open Access QC (v1.4; Bruker Daltonik, Bremen, Germany) and acquired and processed using Bruker Compass (v1.7; Bruker Daltonik, Bremen, Germany).

4.2.5 Protein Expression and Purification

4.2.5.1 Microbiology Techniques

Techniques used in this chapter are consistent with those used previously. See section 2.2.1, page 48.

4.2.5.2 Nanobody Expression System

A Gibson assembly was designed to easily transfer the nanobodies into the expression vector pET52b(+) (Novagen, 71554). Two sets of primers with overlapping ends were designed. The first set was used to amplify the nanobody region from the pSEX81 vector, whereas the second set was used to linearise the pET52(b)+ vector while introducing a functionalisation tag and a histidine tag for easier purification (Table 4.3).

Table 4.3 List of primers used for the Gibson assembly of nanobodies into pET52(b)+ and subsequent analysis

Name	Sequence 5' – > 3'	Size	Description
Gibson_vector_for	GGTATATCTCCTTCTTAAAGTTAAACAAAATTATTTCTAGAGGGGAA	47	Gibson assembly pET-52b forward primer
Gibson_vector_rev	CTTCCTGCCACCGGTCATCACCATCACCACCACTaattaacctagg	25	Gibson assembly pET-52b reverse primer, with tag modifications
Gibson_fragment_for	CTAGAAATAATTTTGTTTAACTTTAAGAAGGAGATATACCatgaaatacctattgcctacgg	62	Gibson assembly nanobody forward primer with vector overhangs
Gibson_fragment_rev	ttaattAGTGGTGGTGATGGTGATGACCGGTGGCAGGAAGattcacagtcacggcagtgccatct	61	Gibson assembly nanobody reverse primer with vector overhangs
T7	TAATACGACTCACTATAGGG	20	T7 promoter, forward primer
T7_term	GCTAGTTATTGCTCAGCGG	19	T7 terminator, reverse primer

This method was tested on the original vNAR_5A7 sequence to validate the experimental design. Fragments and linearised vectors were obtained by PCR using Q5® High-Fidelity DNA Polymerase (New-England Biolab, see method 2.2.2.2, page 51). Reactions were set up using the Gibson Assembly® Master Mix (New-England Biolab) with a fragment:insert ratio of 1:1 (see Table 4.4) and incubated at 50° C for 60 minutes. Obtained assemblies were then transformed into chemically competent DH5α (New-England Biolab, C2987H) and minipreped.

Table 4.4 Reaction conditions for Gibson assembly using the Gibson Assembly® Master Mix (New-England Biolab)

	Sample	Positive control
Total Amount of Fragments	0.02–0.5 pmols	10 µL
Gibson Assembly Master Mix (2X)	10 µL	10 µL
Deionised H_2O	10-X µL	0
Total Volume	20 µL***	20 µL

This assembly should result in the following construct being expressed (see Figure 4.2), with the pelB leader sequence directing the expressed construct to the periplasmic space, the 5A7 nanobody protein followed by the LPXTG Sortase A recognition motif and a 6-histidine tag for easy purification by affinity liquid chromatography.



Figure 4.2 Predicted sequence to be expressed by BL21-AI as a result of a Gibson assembly between plasmid pET52b(+) and 5A7 nanobody in pSEX81.

Primers Gibson_vector_for, Gibson_vector_rev, Gibson_fragment_for and Gibson_fragment_rev were used.

The resulting pET52b_5A7 plasmid was then transformed into electrocompetent BL21-AI™ One Shot® Chemically Competent cells (Invitrogen, C6070-03) for protein expression.

The second methodology employed relied on a synthetic gene obtained from Thermofisher, encoding the 5A7 nanobody sequence alongside a flexible GS linker and the LPXTG Sortase A binding site (sequence can be viewed in Figure 4.3). Each end of the sequence was flanked by Gibson assembly sites matching the primers, designed to modify and amplify the pET101 D-TOPO expression plasmid (listed in Table 4.5). The fragment was then inserted ahead and in frame with the histidine tag encoded in the vector.

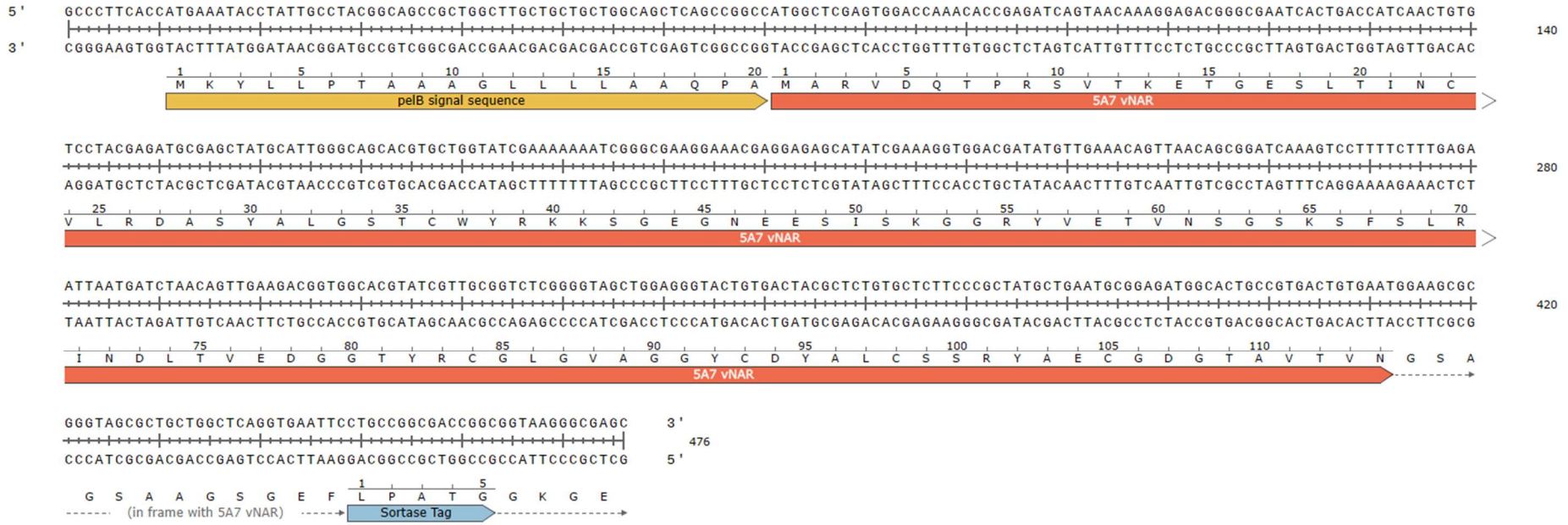


Figure 4.3 Synthetic gene sequence used for the Gibson assembly of the 5A7 alongside relevant linker and tag into pET101

Table 4.5 List of primers used for the Gibson assembly of the 5A7 synthetic gene into pET101.

Name	Sequence 5' – > 3'	Size	Description
pET101_for	GACCGGCGGTAAGGGCGAGCAGGGCGAGCTCAATTCGA	38	Gibson assembly pET101 forward primer
pET101_rev	GGTATTTCATGGTGAAGGGCGGTGAAGGGCTCCTGAATTC	40	Gibson assembly pET101 reverse primer

The resulting pET101_5A7 plasmid was then transformed into electrocompetent BL21-AI™ One Shot® Chemically Competent cells (Invitrogen, C6070-03) for protein expression.

4.2.5.3 Expression of Sortase A

The purification protocol was adapted from the literature (Guimaraes *et al.*, 2013). pET28a-SrtAdelta59 was obtained from Hidde Ploegh (Addgene plasmid # 51138; http://n2t.net/addgene:51138; RRID:Addgene_51138;). The plasmid was transformed into BL21-DE3 Electrocompetent Cells (Sigma Aldrich, CMC0016) and grown to OD600=0.6 in 200 mL LB broth (Lysogeny Broth Lennox, 0.5% (w/v) Tryptone, 0.5% (w/v) Yeast extract, 1% (w/v) Sodium chloride, pH 7.0 at 20° C, Sigma Aldrich, L3022) with 100 µg/mL ampicillin in a 1 L flask. Protein expression was induced using 0.5 mM IPTG (Isopropyl β-D-1-thiogalactopyranoside) for 3 hours (the incubation time was shortened to account for the higher temperature). The culture was then spun down (20 minutes, 5000 x g, 4°C) and the pellet resuspended in protein purification buffer A (50 mM Tris HCl pH 8.0, 150 mM NaCl, 10% (v/v) glycerol, 20 mM imidazole in distilled water) for subsequent purification.

4.2.5.4 5A7 Pilot Overexpression

Plasmids were transformed into BL21-AI™ One Shot® Chemically Competent cells (Invitrogen, C6070-03). Pilot overexpression was set up prior to protein purification to confirm the correct plasmid integration of protein expression by the transformed competent cells. Recombinants were plated on agar and grown overnight. A single colony was picked and transferred to 5 mL of LB with ampicillin and grown overnight. The culture was then diluted (1:100) into fresh LB with

ampicillin and incubated at 37° C with shaking (210 rpm) until OD_{600} = 0.6. Protein expression was then induced using IPTG at various concentrations. The culture was then incubated in the same condition for another 3 hours. Samples prior and post induction were collected, spun down (60 seconds, 17,900 × G) and prepared for SDS-PAGE.

4.2.5.5 5A7 Upscale Overexpression

Plasmids were transformed into BL21-AI™ One Shot® Chemically Competent cells (Invitrogen, C6070-03). Upscale overexpression was set up for protein purification. A single colony was picked and transferred to 5 mL of LB with ampicillin and grown overnight. The culture was then diluted (1:100) into fresh LB with ampicillin and incubated at 37° C with shaking (210 rpm) until OD_{600} = 0.6. Protein expression was then induced using IPTG at the optimum concentration, determined from the pilot overexpression. The culture was then incubated in the same condition for another 3 hours. Cells were pelleted (12 minutes, 4000 x g) and resuspended in the first purification buffer plus 0.5 mM PMSF (phenylmethylsulphonyl fluoride, Thermo Scientific, 36978). This biomass was then fast frozen and stored at -80° C. Cells were then aliquoted in 10 mL samples, and each sample was sonicated for 3 minutes, in 10 seconds intervals with 10 seconds of recovery in between. Cells were then left to incubate on ice for 30 minutes, before being pelleted (30 minutes, 4000 x g). The supernatant was collected and stored on ice before purification. Samples prior and post induction were collected along with a crude lysate sample, supernatant and final pellet, and prepared for SDS-PAGE. If the overexpressed protein was found in the supernatant, the samples were then purified.

4.2.5.6 Estimation of Protein Hydrophobicity

The hydrophobicity of proteins was calculated using the hydropathy scale described by Kyte and Doolittle (1982). Scores were calculated using the Expasy ProtScale tool (Gasteiger *et al.*, 2005) and protein 3D structures were generated using UCSF ChimeraX version 1.9 (Pettersen *et al.*, 2004), available at https://www.cgl.ucsf.edu/chimera). HEL-5A7 protein structure was obtained from Stanfield *et al.* (2004), PDB Id: ISQ2.

4.2.5.7 Purification/FPLC

4.2.5.7.1 Column Maintenance

Columns were stripped with 10 column volumes of 20 mM sodium phosphate, 0.5 M NaCl and 50 mM EDTA, pH 7.4 at 20° C, before recharging with 5 volumes of 0.1M $NiSO_4$ in distilled water. Columns were then rinsed with 5 column volumes distilled water and stored in 20% (v/v) ethanol in distilled water or equilibrated with 5 column volumes of binding buffer.

4.2.5.7.2 Buffers

Buffers were designed following recommendations from column manufacturer (Cytiva), prepared fresh for each use, filter sterilised and stored at 4 °C.

Table 4.6 Composition of buffers for protein purification by FPLC.

Buffers were filter sterilised and stored at 4° C

Buffer name	Composition
Binding buffer A	50 mM Tris HCl pH 8.0, 150 mM NaCl, 10% (v/v) glycerol, 20 mM imidazole in distilled water
Eluting buffer B.1	50 mM Tris HCl pH 8.0, 150 mM NaCl, 10% (v/v) glycerol, 1 M imidazole in distilled water
Eluting buffer B.2	50 mM Tris HCl pH 8.0, 150 mM NaCl, 10% (v/v) glycerol, 500 mM imidazole in distilled water
Binding buffer C	20 mM sodium phosphate, 0.5 M NaCl, 8 M urea, 5 mM DTT, 10% (v/v) glycerol, 20 mM imidazole
Eluting buffer D	20 mM sodium phosphate, 0.5 M NaCl, 8 M urea, 5 mM DTT, 10% (v/v) glycerol, 1 M imidazole

4.2.5.7.3 Purification Protocol

All FPLC experiments were run on a AKTAprime Plus (Cytiva).

Samples were run on HisTrap™ High Performance Nickel-charged chromatography column (Cytiva). Columns were rinsed with dH_2O, and columns were equilibrated with binding buffer. The sample was run on the column and bound proteins were eluted alongside an increasing imidazole gradient using eluting and binding buffer; fractions were collected. Samples from the flow-through, wash-through, and fractions were collected and prepared for an SDS-PAGE. Following the SDS-PAGE, samples containing the desired protein were dialysed overnight in 2 L of binding buffer to remove any imidazole and excessive salts. A second round of

purification was performed if required. Finally, samples were concentrated using appropriate Vivaspin® Centrifugal Concentrator and dialysed in storage buffer (40 mM Tris-HCl pH8.0, 110 mM NaCl, 2.2 mM KCl, 8 mM imidazole, 0.04% (v/v) Tween 20, 20% (v/v) glycerol) before being flash-frozen and stored at -80° C.

4.2.5.8 Protein Concentration Determination

Protein concentrations were determined using a Pierce BCA Protein Assay Kit (Thermo Fisher Scientific, 23225). A BSA (Bovine Serum Albumin) standard curve was prepared with concentrations between 500 µg/mL and 0 µg/mL in triplicates. The working reagent was prepared by mixing equal part of reagent A and B, and 25 µL of either standard or sample of unknown concentration was added to 200 µL of working reagent in a 96-well microplate. The plate was mixed thoroughly on a plate shaker and incubated at 37° C for 30 minutes. The plate was then equilibrated at room temperature, and absorbance was measured at 475 nm on a GloMax® Explorer Microplate reader (Promega). A linear regression was fitted to the standard curve using GraphPad Prism 10.4.1 (from GraphPad software; available at www.graphpad.com); protein sample concentrations were determined using this concentration curve.

4.2.5.9 Protein Gel Electrophoresis and Western Blotting

Samples were diluted in Novex™ Tris-Glycine SDS Sample Buffer (Invitrogen™, LC2676) and run on Novex™ Tris-Glycine Mini Protein Gels, 4–20%, 1.0 mm (Invitrogen™, XP04205BOX) with Novex™ Tris-Glycine SDS Running Buffer (Invitrogen™, LC2675) alongside the Spectra™ Multicolour Broad Range Protein Ladder (Thermo Scientific™, 26634). For Coomassie staining, gels were stained in 50% (v/v) methanol, 10% (v/v) acetic acid, 40% dH_2O and 0.25% (w/v) Coomassie Blue R-250 for 30 minutes to overnight, and de-stained in 50% (v/v) methanol, 10% (v/v) acetic acid and 40% (v/v) dH_2O.

For western blots, gels were removed from their running casts and semi-dry transferred onto nitrocellulose membranes (Invitrogen™, LC2009) using Trans-Blot® SD Semi-Dry Transfer Cell with Bjerrum Schafer-Nielsen Transfer Dry Buffer (48 mM

Tris, 39 mM glycine, and 1.3 mM SDS, pH 9.0-9.3, at 20 ^{o}C, (Bjerrum and Schafer-Nielsen, 1986).

Membranes were then blocked with 3% BSA (Bovine serum Albumin) in TBST (150 mM NaCl, 50 mM Tris-HCl, 0.5% (v/v) Tween 20, pH 7.6 at 20° C) overnight at 4° C with gentle rocking. Membranes were then washed (3 times, 10 minutes in TBST at room temperature) before being probed with the primary antibody (anti-histidine tag antibody produced in rabbit, Sigma SAB5600227, 1:1000 in TBS) for 2 hours at room temperature with gentle rocking. Membranes were washed again and probed with the secondary antibody (swine anti-rabbit IgG-HRP, Dako P0399, 1:4000 in TBS). After a final wash, samples were imaged on a LiCor Odyssey® M Imager equipped with a chemiluminescence module using WesternSure® PREMIUM Chemiluminescent Substrate (LiCor, 926–95000). Pictures were taken at the 3 minutes, 5 minutes and 10 minutes exposure time, and the best images were selected.

4.3 Results and Discussion

4.3.1 Peptide Synthesis

In order to create a fluorophore tag for nanobodies that could be attached by Sortase A conjugation, a short peptide encoding the Sortase A recognition oligoglycine needed to be synthesised. In order to label this oligoglycine with a fluorophore, a free side chain was required. The amino acid lysine is a basic, polar amino acid with a long, flexible aliphatic ε-side chain terminating in a second amino group. This reactive ε-amino group can then be used to attach the dye with amine coupling. The peptide glycine-glycine-glycine-lysine (GGGK) was first synthesised by Fmoc (fluorenylmethyloxycarbonyl protecting group) solid-phase peptide synthesis (SPPS). The lysine used contained an N-methyltrityl (Mtt) protective group on the $(CH_2)_4NH_2$ side chain (CAS Number: 167393-62-6). This Mtt group can be selectively removed using a weak acid. The dye Cy5.5 was selected as the fluorophore of choice, and is a derivative of Cy5, a dye within the cyanine family. Cy5.5 emits in the near-infrared region (694 nm), where biological tissues and samples have reduced autofluorescence, facilitating signal detection in flow cytometry and immunofluorescence experiments. This wavelength was also compatible with the flow cytometry panel designed in the previous chapter. Cy5.5 is water soluble and photostable and is commercially available as the NHS ester for easy labelling of antibodies and peptides.

A rink amide resin (Novabiochem®, loading capacity 0.71 mmole/g) was loaded onto an automatic peptide synthesis system to couple Fmoc-Lys (Mtt)-OH at the 0.25 mmole scale (0.352 g of resin). Diisopropylcarbodiimide (DIC) activated the carboxylic acid group of the amino acid, and the reaction was facilitated by ethyl cyanohydroxyiminoacetate (Oxyma), which stabilised the active ester intermediate formed during the reaction. The resin was then washed using dimethyl fluoride (DMF), dichloromethane (DCM) and DMF, and capped by 10% (v/v) acetic anhydride and 90% (v/v) pyridine to prevent undesired side reactions. After another round of washes, the Fmoc group was deprotected using 20% (v/v) piperidine in DMF and washed again. The next amino acid (Fmoc-Gly-OH, CAS number: 29022-11-5) was

then coupled following the same process. The cycle was repeated until the GGGK(Mtt) peptide was synthesised. A small-scale cleavage was conducted using a small amount of resin and a mixture of 90% (v/v) trifluoroacetic acid (TFA), 5% (v/v) triisopropylsilane (TIS), and 5% (v/v) water to confirm the correct synthesis of peptides. The peptide was precipitated with diethyl ether and resuspended in 0.1% T (v/v) TFA in H_2O. A schematic representation of Fmoc SPPS can be seen in Figure 4.4.

Since cleaving the peptide from the resin requires a strong acid (90% (v/v) TFA, 5% (v/v) TIS, 5% (v/v) H_2O), it is considered that the Mtt protective group would also be removed from the structure (the Mtt group is usually removed by a weak acid, here 1% (v/v) TFA, 98% (v/v) DCM, 1% (v/v) MeOH). The expected structure is presented in Figure 4.5 and the mass spectra can be seen in Figure 4.6. The mass spectra (ESI positive) confirmed the presence of a peak consistent with the $[M+H]^+$ of the GGGK peptide at 539.25. Once the accurate synthesis of the peptide was confirmed, the Mtt protective group was removed overnight from the remaining resin-coupled peptide, and the Cy5.5 fluorophore was coupled (1 eq. peptide, 1.2 eq. Cy5.5 NHS ester, 1.2 eq. DIPEA, in DMF). The Cy5.5 dye is pre-activated with an NHS ester, and thus reactive towards the ε-chain amine.

The peptide was then cleaved from the resin and the sample was sent to mass spectrometry (ESI positive) to confirm the Cy5.5 coupling. Unfortunately, the exact m/z of the compound could not be detected, indicating the coupling was unsuccessful.

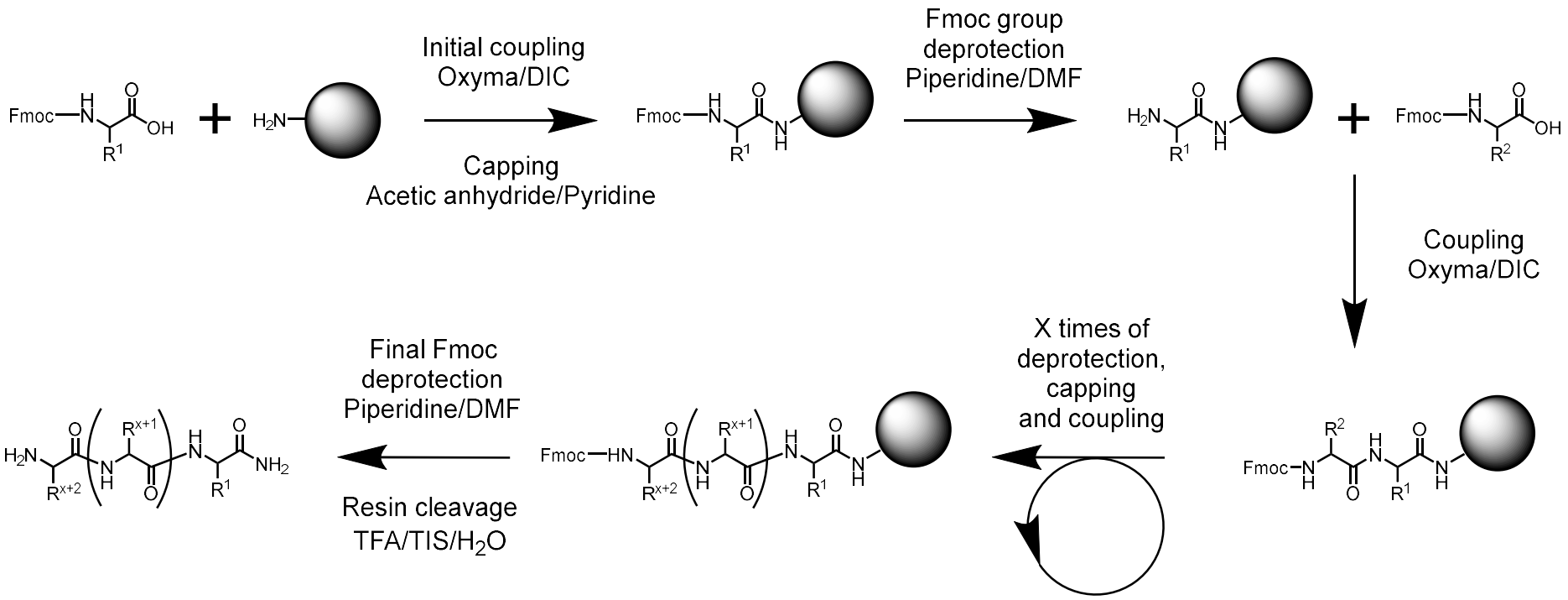


Figure 4.4 Mechanism of Fmoc Solid Phase Peptide Synthesis (Fmoc SPPS).

Fmoc protected amino acids are coupled to a Rink Amide resin (represented by a grey sphere) by amine coupling, facilitated by Oxyma and DIC. The peptide is capped with 10% acetic anhydride and 90% pyridine to prevent undesired side reactions. The Fmoc group is removed by a 20% piperidine in DMF before a new amino acid is coupled. The process is repeated with each amino acid, extending the peptide. After the final coupling, the Fmoc group is removed and the peptide is cleaved from the resin with 90% TFA, 5% TIS and 5% H_2O. Wash steps with DMF and DCM are performed between steps as appropriate. Figure created using ChemDraw 23.1.2 (available at revvitysignals.co), adapted from Jaradat (2018).

.

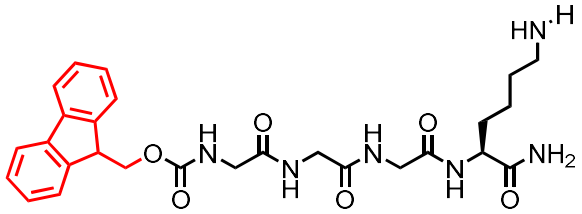


Figure 4.5 Chemical structure of the Fmoc-GGGK peptide following cleavage from rink amide resin in order to check for proper synthesis prior to Cy5.5 coupling.

The Fmoc protective group is highlighted in red. Chemical Formula: $C_{27}H_{34}N_6O_6$, Exact Mass: 538.25.

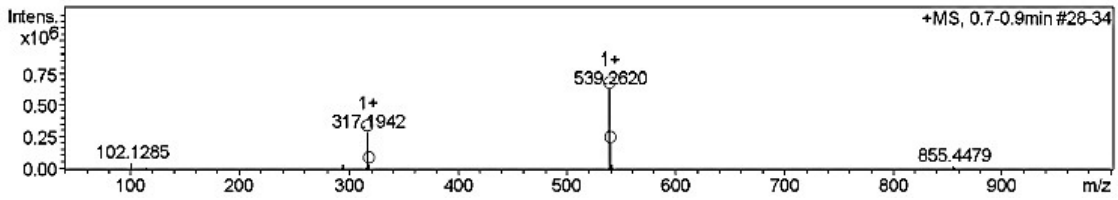


Figure 4.6 Mass Spectra confirming the synthesised Fmoc-GGGK peptide.

The observed ESI-MS (positive) spectrum displays a dominant ion at m/z 539.26, corresponding to the $[M+H]^+$ of GGGK. Additional peaks represent adducts, or fragments. The theoretical molecular weight of the peptide aligns with the observed data, validating the successful synthesis of the compound.

Considering the large size of the resin, it is possible that coupling the Cy5.5 dye to the lysine ε-chain is sterically blocked. To circumvent this issue, an additional three glycine amino acids were placed between the resin and the lysine to allow more space for fluorophore coupling, to yield the following peptide: GGGK(Mtt)GGG. Again, a Rink Amide resin (Novabiochem®, loading capacity 0.710 mmole/g) was loaded onto an automatic peptide synthesis system to couple three Fmoc-Gly-OH, Fmoc-Lys (Mtt)-OH, and again three Fmoc-Gly-OH, at the 0.25 mmole scale (0.352 g of resin). A mini cleave was performed to confirm correct peptide synthesis before Mtt deprotection. The expected structure is presented in Figure 4.7 and the mass spectra can be seen in Figure 4.8. The mass spectra (ESI positive) confirmed the presence of a peak consistent with the $[M+H]^+$ of the GGGKGGG peptide at 710.32.

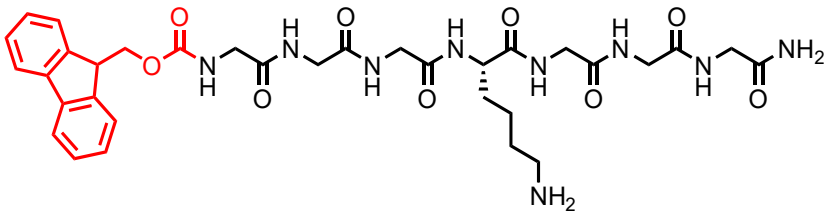


Figure 4.7 Chemical structure of the Fmoc-GGGKGGG peptide following cleavage from rink amide resin in order to check for proper synthesis prior to Cy5.5 coupling.

The Fmoc protective group is highlighted in red. Chemical Formula: $C_{33}H_{43}N_9O_9$, Exact Mass: 709.32.

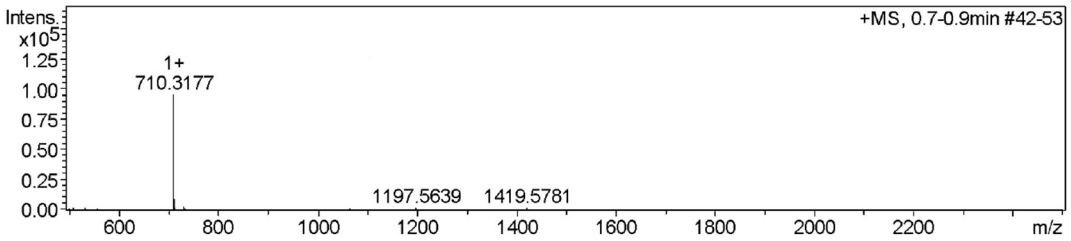


Figure 4.8 Mass Spectra confirming the synthesised Fmoc-GGGKGGG peptide.

The observed ESI-MS (positive) spectrum displays a dominant ion at m/z 710.32, corresponding to the $[M+H]^+$ of Fmoc-GGGKGGG. Additional peaks represent adducts, or fragments. The theoretical molecular weight of the peptide aligns with the observed data, validating the successful synthesis of the compound.

The Mtt protective group was removed (1% (v/v) TFA, 98% (v/v) DCM, 1% (v/v) MeOH) and the Cy5.5 fluorophore was coupled in solution with DIPEA (1 eq. peptide, 1.2 eq. Cy5.5 NHS ester, 1.2 eq. DIPEA, in DMF). The terminal Fmoc group was deprotected and the compound was cleaved from the resin, precipitated and resuspended. The resulting sample was sent to mass spectrometry to confirm Cy5.5 coupling to the peptide. The structure of GGGK(Cy5.5)GGG can be seen in Figure 4.9, and the mass spectra (ESI positive) of the resulting sample can be seen in Figure 4.10. The mass spectra showed a peak at 1052.52, consistent with the m/z of GGGK(Cy5.5)GGG. This confirmed that the compound was synthesised. A schematic representation of the synthesis can be seen in Figure 4.11. However, additional peaks on the mass spectra indicated the presence of contaminants. In order to purify the sample, preparative reverse-phase high-performance liquid chromatography (prep RP-HPLC) was used. The sample was run on a Waters SunFire 5 µm (C-18, 19 mm ×

150 mm) preparative column and run on a 5–95% gradient. Fractions were collected manually at high 210 nm absorbance and prepared for analytical HPLC and mass spectrometry (ESI positive).

Figure 4.12 (A) presents the analytical HPLC (2–95% gradient over 10 minutes) of the fraction that was shown to contain the GGGK(Cy5.5)GGG sample by mass spectrometry. Both the mass spectrometry and analytical HPLC revealed the presence of contaminants in the sample. An additional round of purification by prep RP-HPLC was conducted on a shorter gradient (20–60%) and three fractions were collected: one before the major peak, one of the major peaks, and one after the major peak.

Figure 4.12 (B) presents the analytical HPLC (15–60% gradient over 5 minutes) and mass spectrometry (ESI positive) of the pre-peak sample, (C) of the peak sample, and (D) of the post-peak sample. Both the peak and post-peak sample mass spectra showed the presence of the GGGK(Cy5.5)GGG compound; however, only the peak sample appeared free of contaminants. The corresponding analytical HPLC confirmed one major peak at 6.56 minutes, with an Area Under Curve (AUC) of 771.4. Two additional peaks were detected (not visible on the graph due to their small size) at 0.77 and 8.073 minutes, with AUC of 20.91 and 24.08 respectively. The percentage purity of the sample was calculated using the formula below and confirmed a purity of 94%.

$$Purity(\%) = (\frac{AUC\ of\ target\ peak}{Total\ AUC\ of\ all\ peaks}) \times 100$$

Finally, the sample was freeze-dried and weighed: the synthesis yielded 6.8 mg final mass for an initial synthesis of 22 nmole, corresponding to a final yield of 32.32%.

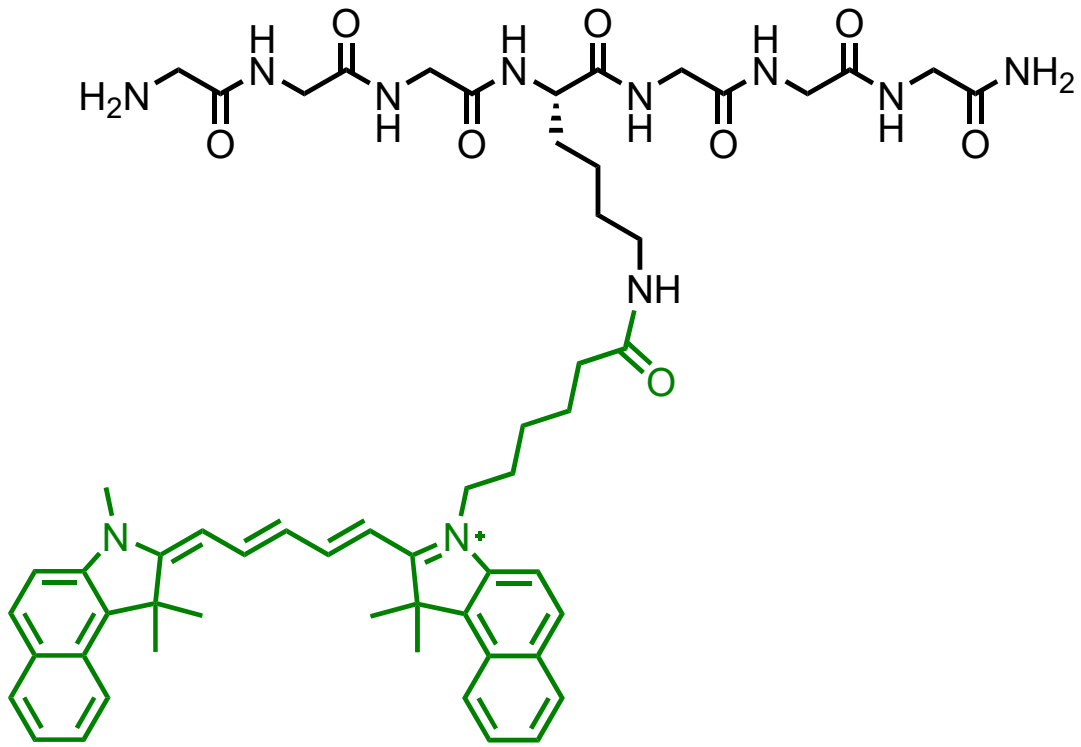


Figure 4.9 Chemical structure of the GGGK(Cy5.5)GGG peptide following cleavage from rink amide resin.

The Cy5.5 dye is highlighted in green. Chemical Formula: $C_{58}H_{74}N_{11}O_8^+$, Exact Mass: 1052.57.

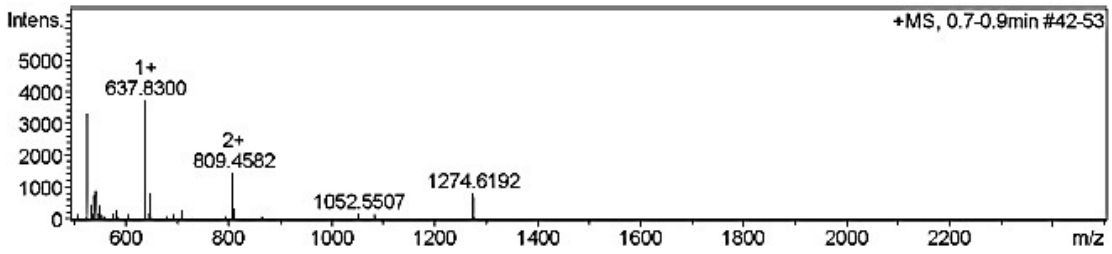


Figure 4.10 Mass Spectra confirming the synthesised GGGK(Cy5.5)GGG-NH_2 peptide.

The observed ESI-MS (positive) spectrum displays an ion at m/z 1052.52, corresponding to the mass of GGGK(Cy5.5)GGG-NH_2. Additional peaks represent adducts, or fragments. The theoretical molecular weight of the peptide aligns with the observed data, validating the successful synthesis of the compound.

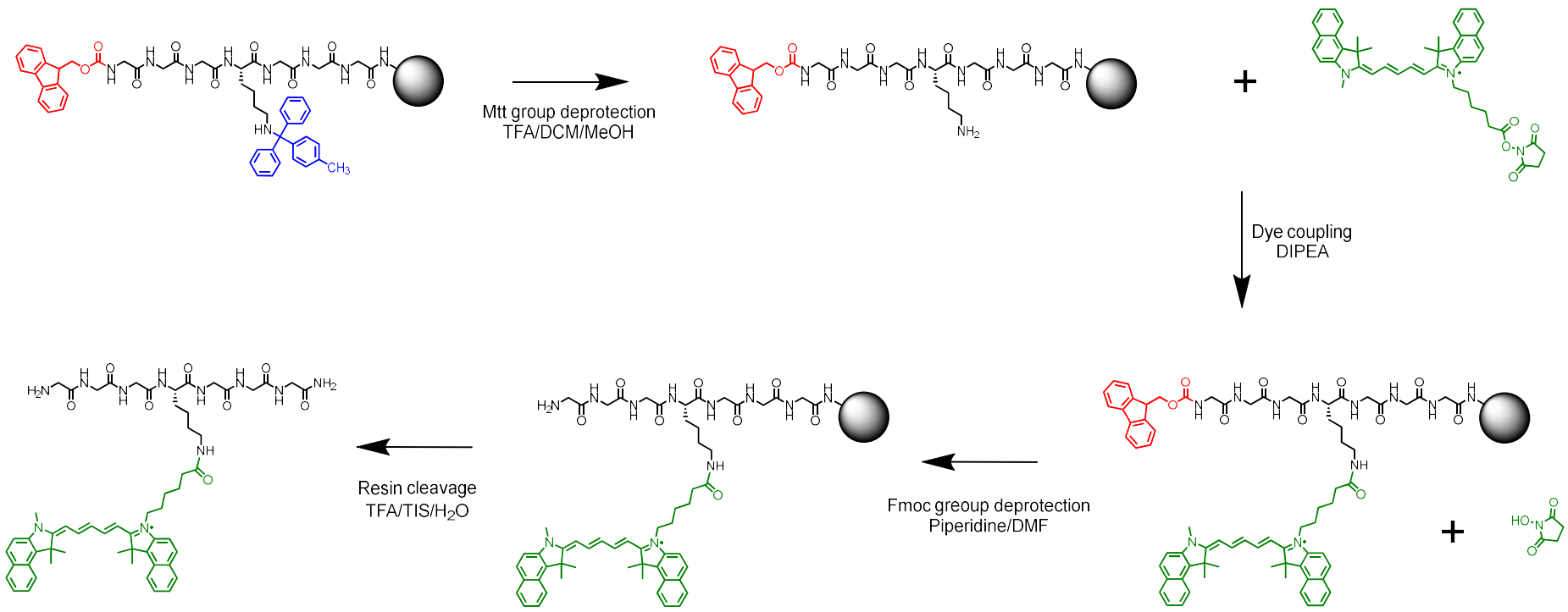
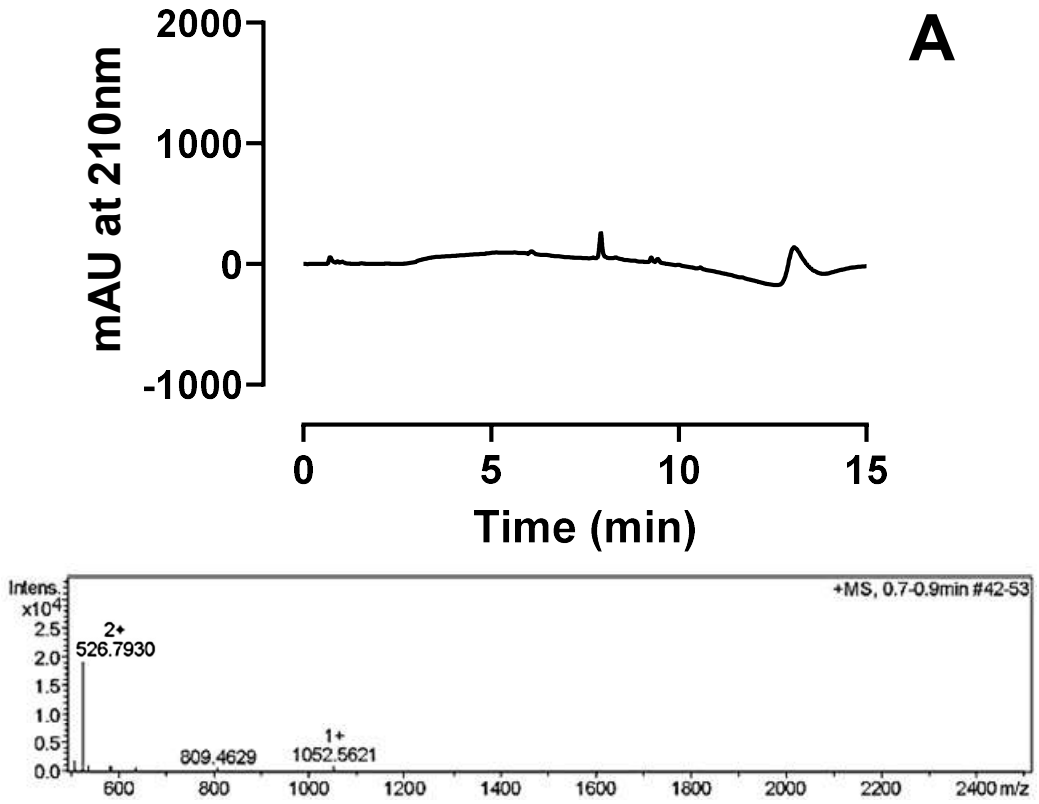
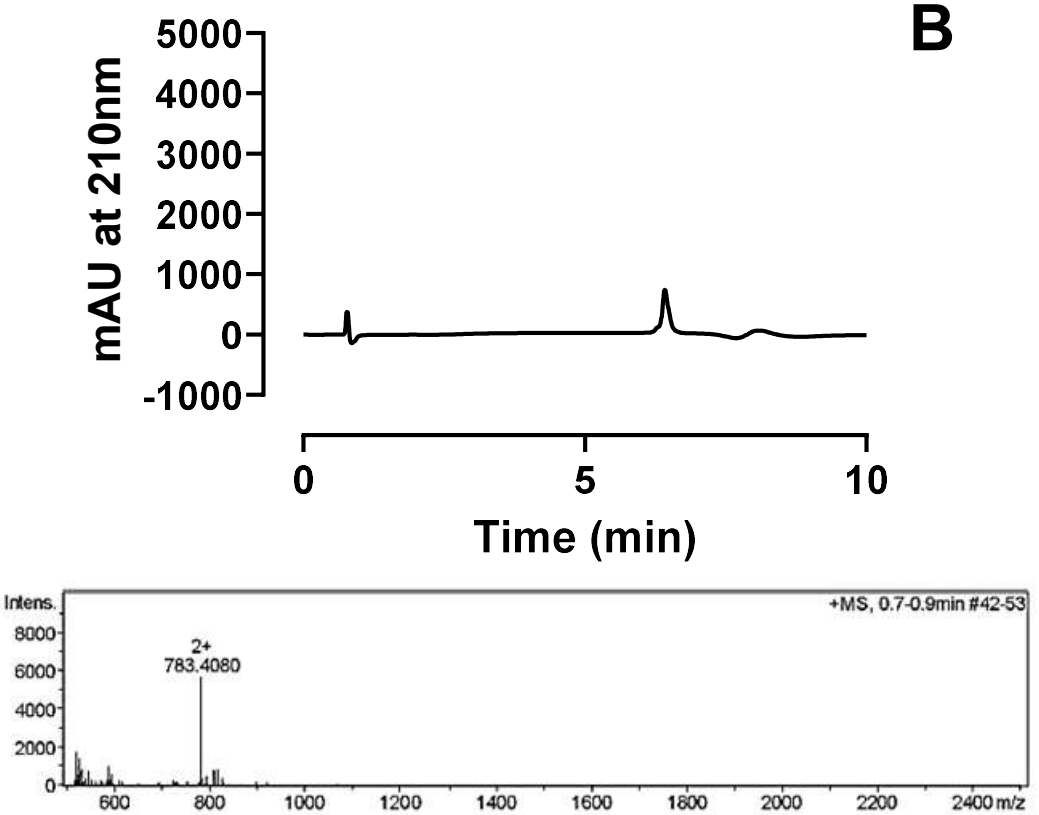
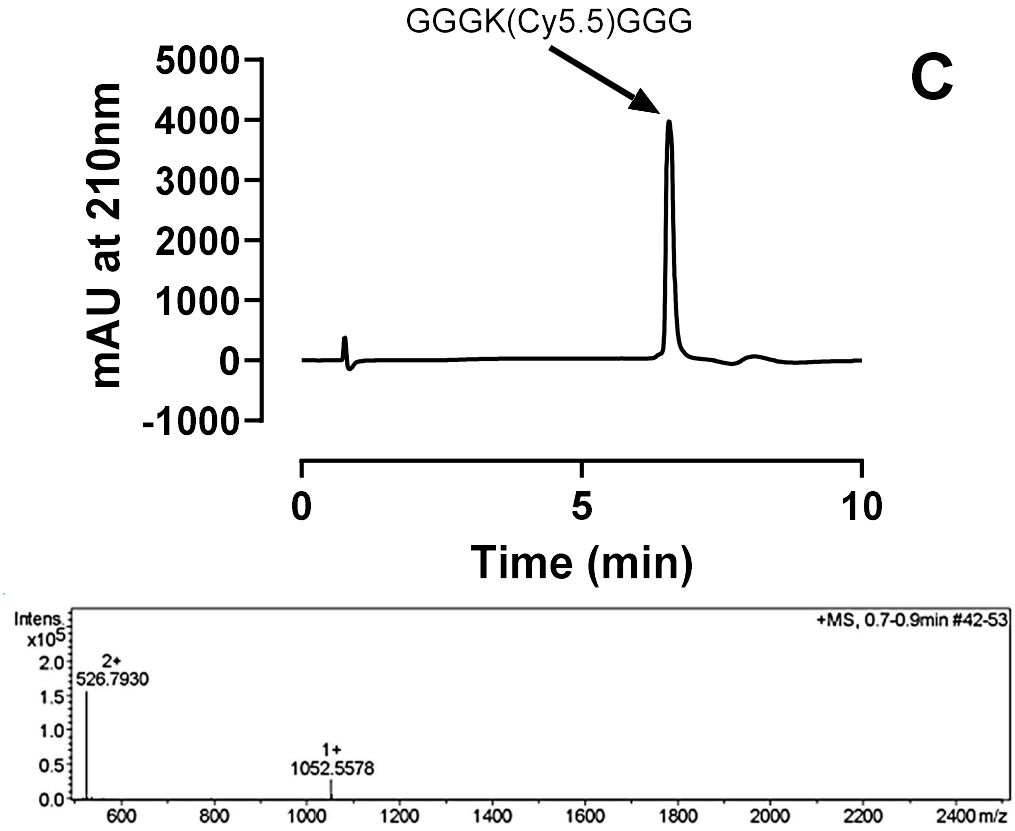


Figure 4.11 Stepwise synthesis of GGGK(Cy5.5)GGG following Fmoc-based solid-phase peptide synthesis (SPPS), followed by dye conjugation through amide coupling to a lysine residue.

The Fmoc group is highlighted in red, the Mtt group in blue, and the Cy5.5 dye in green. The Rink Amide resin is represented by a grey sphere. Following Fmoc SPPS of the GGGK(Mtt)GGG peptide, the Mtt group is deprotected with 1% TFA, 98% DCM and 1% MeOH. Cy5.5 NHS ester is coupled onto the lysine ε-chain, forming a stable amide bond. The final Fmoc group is deprotected with 20% piperidine in DMF, and the completed peptide-dye conjugate is cleaved from the resin using 90% TFA, 5% TIS and 5% H_2O. Excess reagents and unreacted dye are removed via extensive washing.


A
mAU at 210nm
2000
1000
0
-1000
0
5
10
15
Time (min)
Intens.
x10^4
2.5
2.0
1.5
1.0
0.5
0.0
2+
526.7930
809.4629
1+
1052.5621
+MS, 0.7-0.9min #42-53
600
800
1000
1200
1400
1600
1800
2000
2200
2400 m/z


B
mAU at 210nm
5000
4000
3000
2000
1000
0
-1000
0
5
10
Time (min)
Intens.
8000
6000
4000
2000
0
2+
783.4080
+MS, 0.7-0.9min #42-53
600
800
1000
1200
1400
1600
1800
2000
2200
2400 m/z


GGGK(Cy5.5)GGG
C
mAU at 210nm
5000
4000
3000
2000
1000
0
-1000
0
5
10
Time (min)
Intens.
x10^5
2.0
1.5
1.0
0.5
0.0
2+
526.7930
1+
1052.5578
+MS, 0.7-0.9min #42-53
600
800
1000
1200
1400
1600
1800
2000
2200
2400 m/z

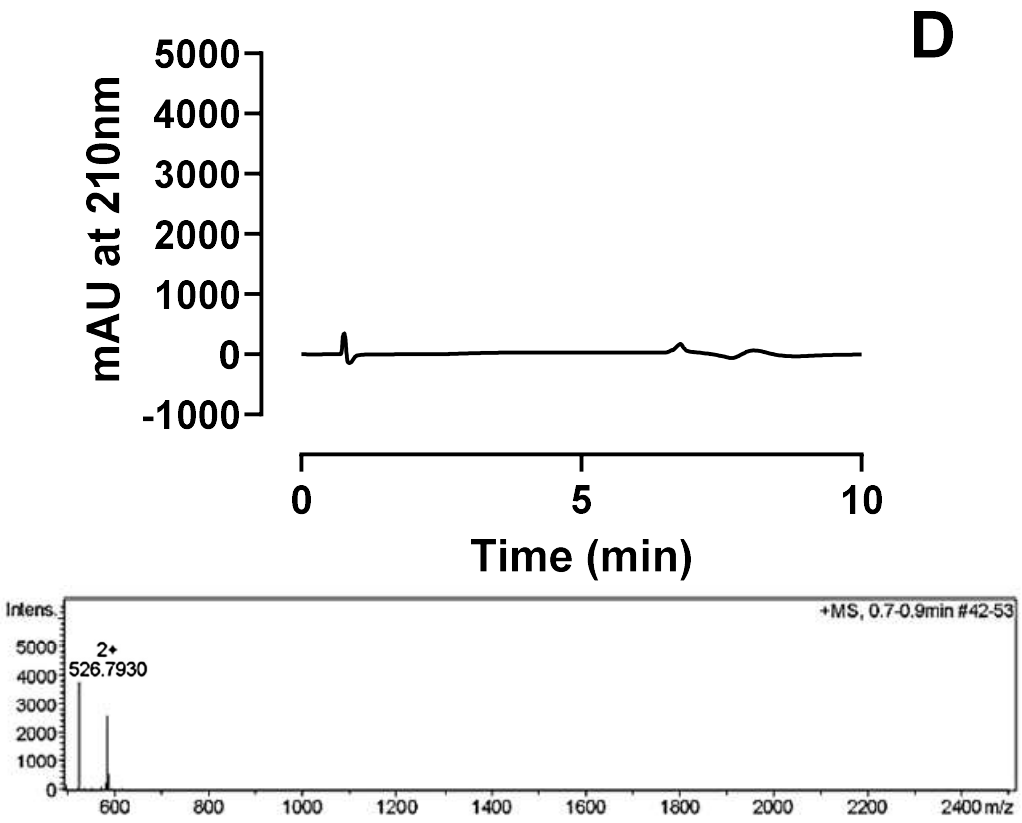

D
mAU at 210nm
5000
4000
3000
2000
1000
0
-1000
0
5
10
Time (min)
Intens.
5000
4000
3000
2000
1000
0
2+
526.7930
+MS, 0.7-0.9min #42-53
600
800
1000
1200
1400
1600
1800
2000
2200
2400 m/z

Figure 4.12 HPLC chromatogram depicting the separation of GGGK(Cy5.5)GGG alongside corresponding MS spectra showing the m/z values of the detected ions.

The predominant ion species are labelled, confirming their identity. A) Sample obtained after the first round of prep RP-HPLC B) Pre-peak sample obtained from the second round of prep RP-HPLC. C) Peak sample obtained from the second round of prep RP-HPLC, confirming the purity of synthesised GGGK(Cy5.5)GGG: 94%. D) Post-peak sample obtained from the second round of prep RP-HPLC.

4.3.2 Sortase A Expression and Purification

The pET28a-SrtAdelta59 was obtained from Addgene (plasmid #51138) and transformed into BL21-DE3 for protein overexpression. Protein overexpression was induced with 0.5 mM IPTG (protocol adapted from Guimaraes *et al.* (2013)) before the cells were collected and sonicated in buffer A.

The sample was run on a 1 mL HisTrap™ High Performance column (Cytiva) using an AKTAprime Plus (Cytiva), and eluted against an imidazole gradient (0 to 100% buffer A to B.1), and 2 mL fractions were collected. A malfunction of the UV detector led to an inaccurate signal (Figure 4.13). To confirm the correct fraction numbers, samples were collected from each fraction (1 to 38) and grouped every 5 fractions. The combined groups were run on an SDS-PAGE gel to confirm the size of the eluted protein (Figure 4.14). A clear band of the appropriate size (20,358.13 Da) can be observed in combined fractions 6 to 10 and 11 to 25. An additional band can be seen at around 40 kDa, indicating the possible presence of a protein dimer. The formation of a Sortase A protein dimer has been reported in the literature (Lu *et al.*, 2007). Such a dimer could impact the protein activity, and the addition of a reducing agent such as DTT might be necessary to ensure optimal activity. Faint bands can also be observed around 60 kDa in every single lane. These bands are likely an artefact of the staining process and were disregarded. In order to confirm the 40 kDa band was indeed a dimer of the Sortase A protein, samples were taken from the grouped fractions 6 to 10 and incubated with various concentrations of DTT for 10 minutes, before being loaded onto an SDS-PAGE gel (Figure 4.15). A consistent reduction in the thickness of the 40 kDa band was observed with increased DTT concentration, confirming the presence of a dimer. The increased sample concentration led to the

appearance of additional bands, indicating the presence of contaminant proteins in the sample. In order to remove these additional proteins, the grouped fractions 6 to 10 and 11 to 15 were pooled, concentrated using a Vivaspin centrifugal concentrator with a 10 kDa limit, dialysed in buffer A, and purified again against a shorter imidazole gradient (20 mM to 500 mM rather than 20 mM to 1 M).

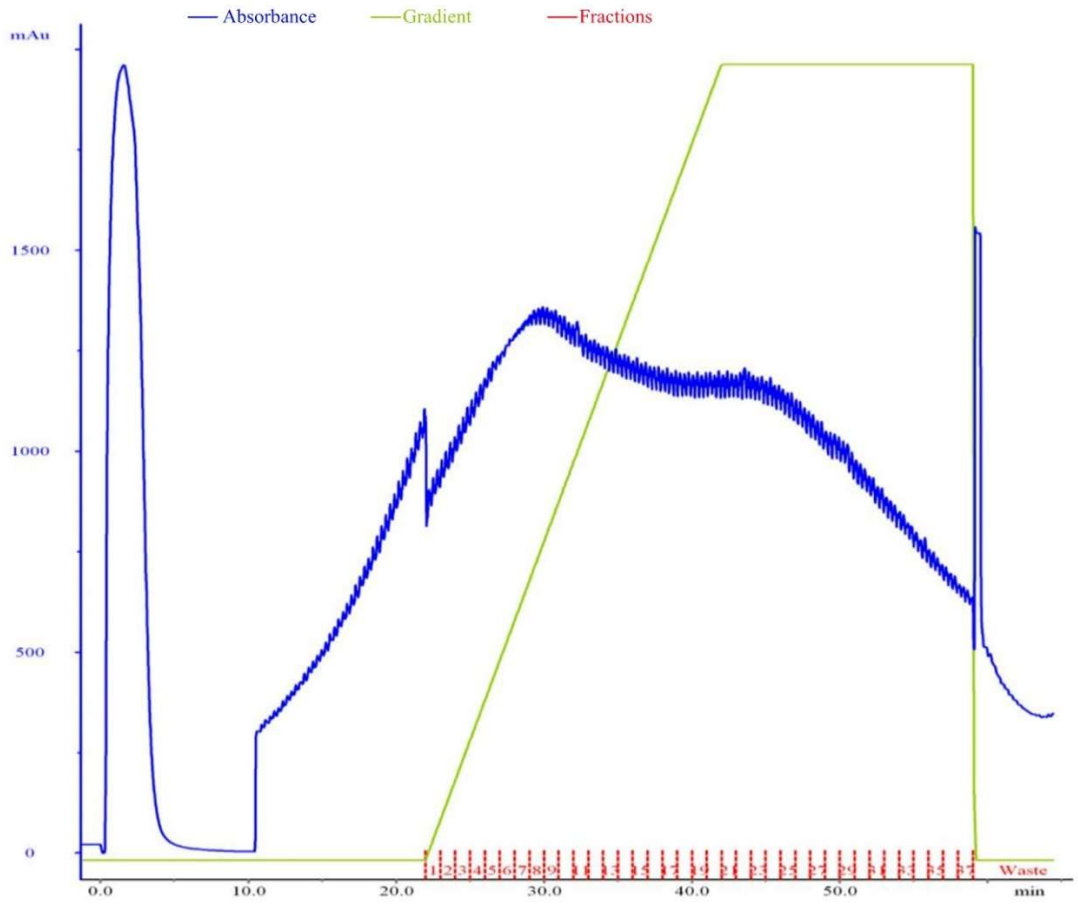


Figure 4.13 Representative chromatogram of Sortase A protein purification using an ÄKTA FPLC system.

The graph shows UV absorbance at 280 nm (blue line), indicative of protein concentration, plotted against elution volume. Concentration gradient (green line) indicates imidazole gradient changes. Collected fractions are labelled in red. Following the initial equilibration phase, a large peak in absorbance can be observed due to sample loading, followed by wash steps. A malfunction of the UV monitor at 10 minutes renders this graph unreliable.

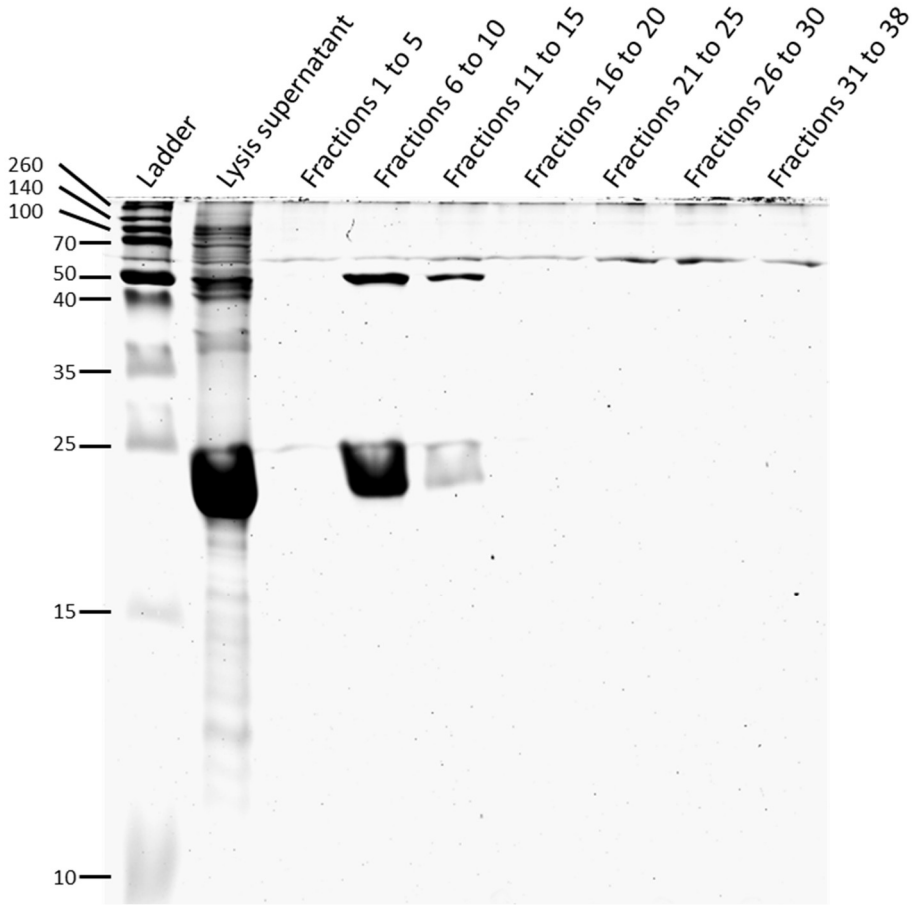


Figure 4.14 SDS-PAGE analysis of fractions collected from the Sortase A protein purification process, stained with Coomassie Brilliant Blue.

Lane 1: Molecular weight marker Spectra™ Multicolour Broad Range Protein Ladder (size in kDa indicated). Lane 2: Lysis supernatant, as loaded onto the purification column. Lane 3 to 8: Fractions collected from the purification process. Bands indicate the presence of proteins, with the target protein prominently visible at approximately 20 kDa, confirming successful purification. Additional bands at around 40 kDa indicate the presence of a potential dimer.

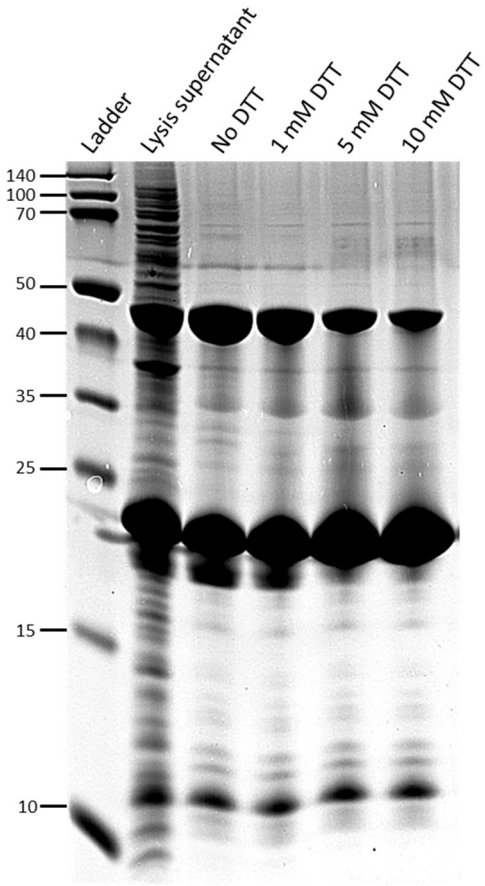


Figure 4.15 SDS-PAGE analysis of fractions collected from the Sortase A protein with various concentrations of DTT to reduce the protein dimer, stained with Coomassie Brilliant Blue. *Lane 1: Molecular weight marker Spectra™ Multicolour Broad Range Protein Ladder (size in kDa indicated). Lane 2: Lysis supernatant, as loaded onto the purification column. Lane 3 to 6: Fractions 11 to 20 collected from the purification process loaded with various concentrations of DTT from 0 mM to 10 mM. Bands indicate the presence of proteins, with the target protein prominently visible at approximately 20 kDa. Faint or additional bands represent co-purified proteins or impurities.*

For the second round of purification, the sample was loaded onto a 1 mL HisTrap™ High Performance column (Cytiva) using an AKTAprime Plus (Cytiva), and eluted against an imidazole gradient (0 to 100% buffer A to B.2), and 2 mL fractions were collected. A single strong peak is visible on the 280 nm absorbance spectra (Figure 4.16). This peak coincided with fractions 11 to 21. The later elution time can be explained by the use of a shorter imidazole gradient (20 mM to 500 mM rather than 20 mM to 1 M). Individual fractions were collected and prepped for SDS-PAGE (Figure 4.17). Once again, a strong band was visible around the 20 kDa mark,

consistent with the size of the Sortase A protein, alongside a band around the 40 kDa mark corresponding to the dimer observed previously. Since no other strong peak was visible on the UV spectra, and no strong bands of other sizes were visible on the SDS-PAGE gel, it was considered the protein was pure enough for its intended use as a conjugation enzyme. Further purification steps, such as ion exchange chromatography, could be considered in the future.

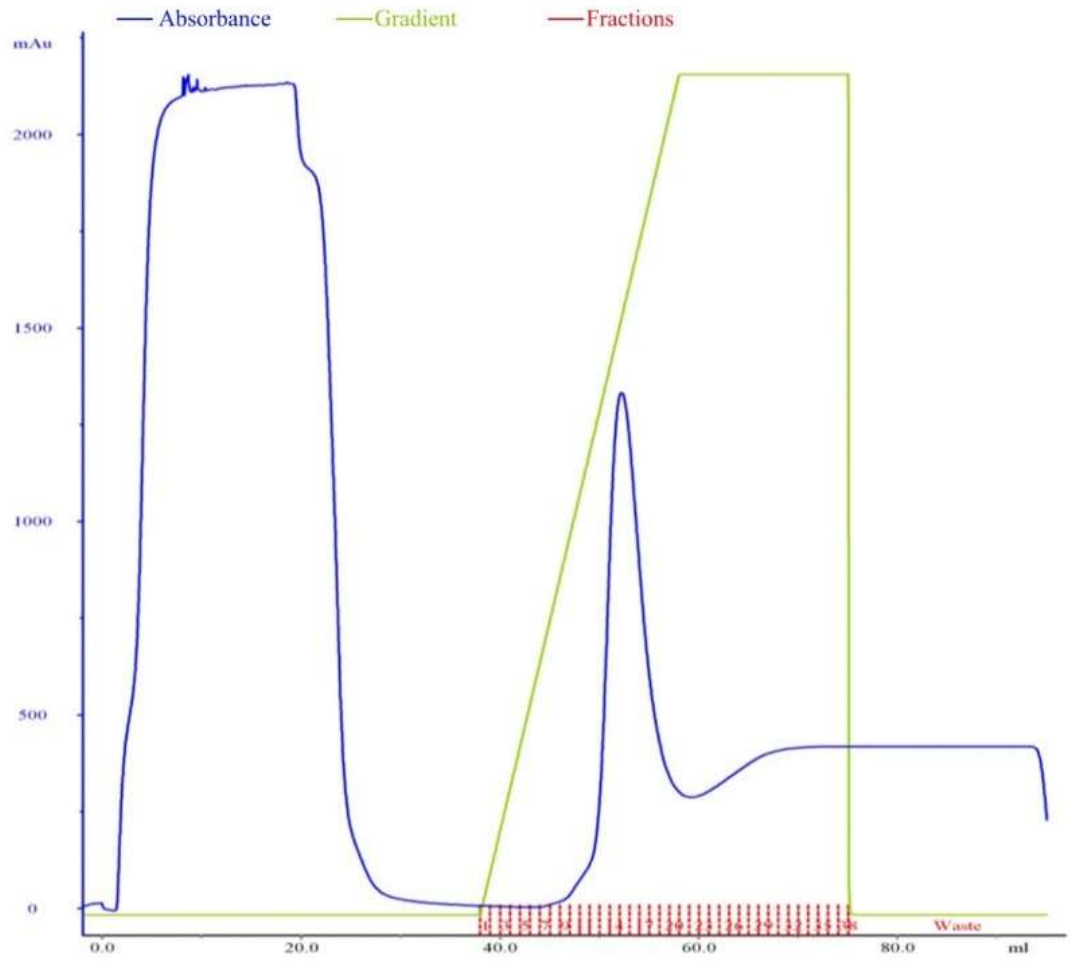


Figure 4.16 Representative chromatogram of Sortase A protein purification using an ÄKTA FPLC system.

The graph shows UV absorbance at 280 nm (blue line), indicative of protein concentration, plotted against elution volume. Concentration gradient (green line) indicates imidazole gradient changes. Collected fractions are labelled in red. Following the initial equilibration phase, a large peak in absorbance can be observed due to sample loading, followed by wash steps. A distinct peak corresponding to the eluted protein under the applied gradient is visible, with target protein elution identified at approximately fractions 11 to 18.

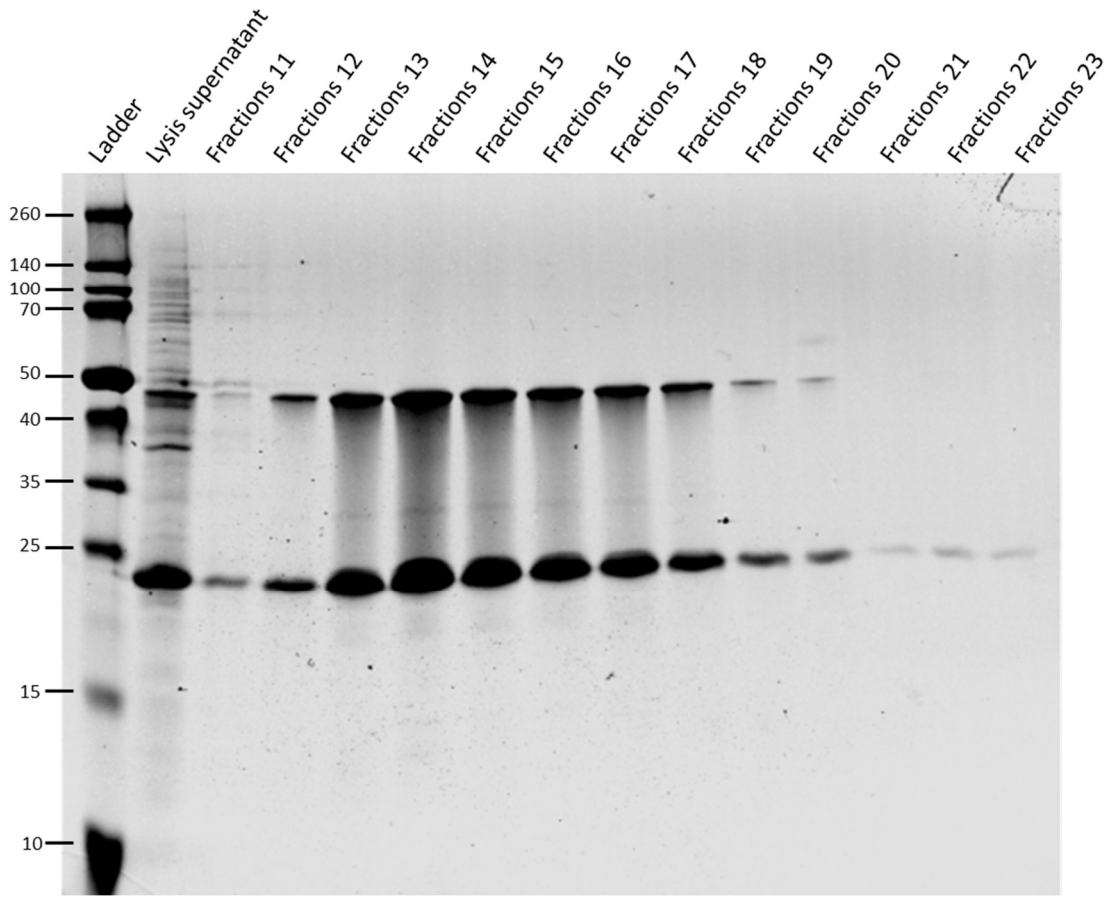


Figure 4.17 SDS-PAGE analysis of fractions collected from the Sortase A protein second purification process, stained with Coomassie Brilliant Blue.

Lane 1: Molecular weight marker Spectra™ Multicolour Broad Range Protein Ladder (size in kDa indicated). Lane 2: Lysis supernatant, as loaded onto the first purification column. Lane 3 to 15: Fractions collected from the purification process. Bands indicate the presence of proteins, with the target protein prominently visible at approximately 20 kDa, confirming successful purification. Additional bands at around 40 kDa indicate the presence of a dimer.

Fractions 12 to 19 were pooled and concentrated using a Vivaspin centrifugal concentrator with a 10 kDa limit down to 4 mL and dialysed in Sortase A storage buffer. A Pierce BCA Protein Assay Kit was used to determine the concentration of the protein. A BSA standard curve was prepared with concentrations between 500 µg/mL and 0 µg/mL in triplicates, and three measurements of the Sortase A sample were made (Figure 4.18). The concentration of the Sortase A sample was extrapolated from the standard curve and determined to be 313.4 ± 13.14 (SD) µg/mL, corresponding to a total of 61.58 ± 2.58 (SD) nmol of protein produced (or 1.253 mg, for a final yield of 6.25mg/L of culture). This yield appeared lower than

previously reported, which could be due to the higher used temperature during protein expression induction, which could have impacted protein solubility (Guimaraes *et al.*, 2013). Additional assays to confirm enzymatic activity will be required to confirm the ligating properties of the purified protein.

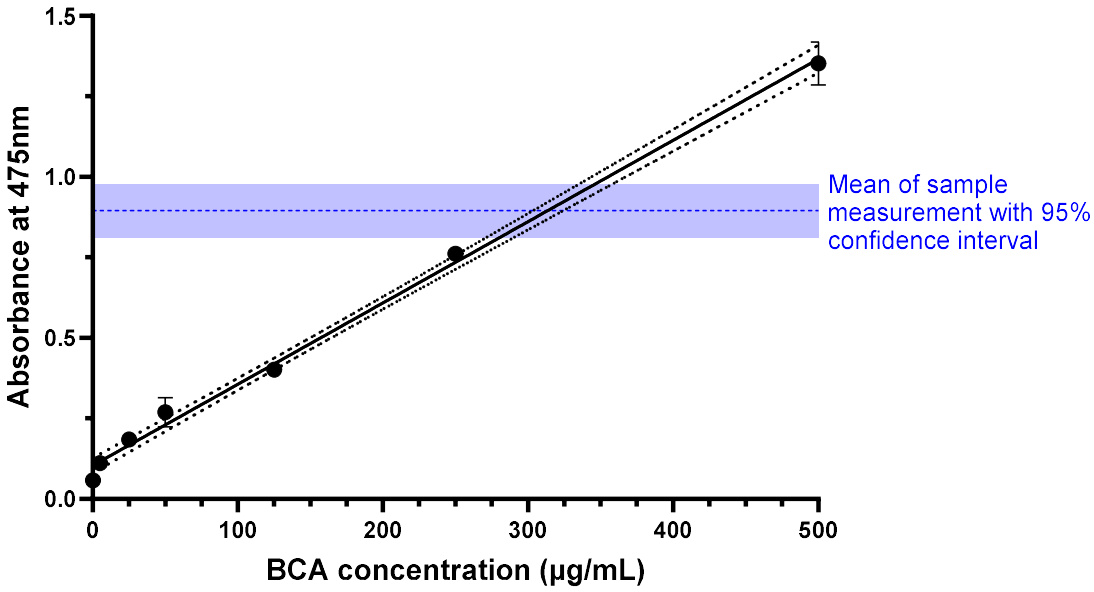


Figure 4.18 Determination of Sortase A protein concentration by Pierce BCA Protein Assay. *A standard curve was generated using seven concentrations of BCA in triplicates; measurements are shown with error bars representing standard deviation. Three measurements of the Sortase A sample were made; the mean measurement is shown as a blue line, with the 95% confidence interval shown in blue shade. The intersection of the standard curve with the mean of the sample measurement corresponded to a final concentration of 313.4 ± 13.14 (SD) µg/mL.*

4.3.3 Nanobody Expression and Purification

4.3.3.1 pET52b(+) Gibson Assembly

Primers Gibson_fragment_for and Gibson_fragment_rev were used to amplify the vNAR_5A7 region out of the pSEX81 vector (Q5® High-Fidelity DNA Polymerase, 30 cycles, Tm = 59° C, predicted amplicon size = 482 bp). This was confirmed by agarose gel showing a band consistent with the expected amplicon size of 482 bp (Figure 4.19). The pET52(b)+ vector was linearised using the Gibson_vector_for and Gibson_vector_rev primers (Q5® High-Fidelity DNA

Polymerase, 30 cycles, Tm = 61° C, predicted amplicon size = 5098 bp). Successful linearisation and modifications were confirmed by Sanger sequencing (Eurofins Genomics, Germany) using T7 and T7-term primers, as well as electrophoresis (Figure 4.20).

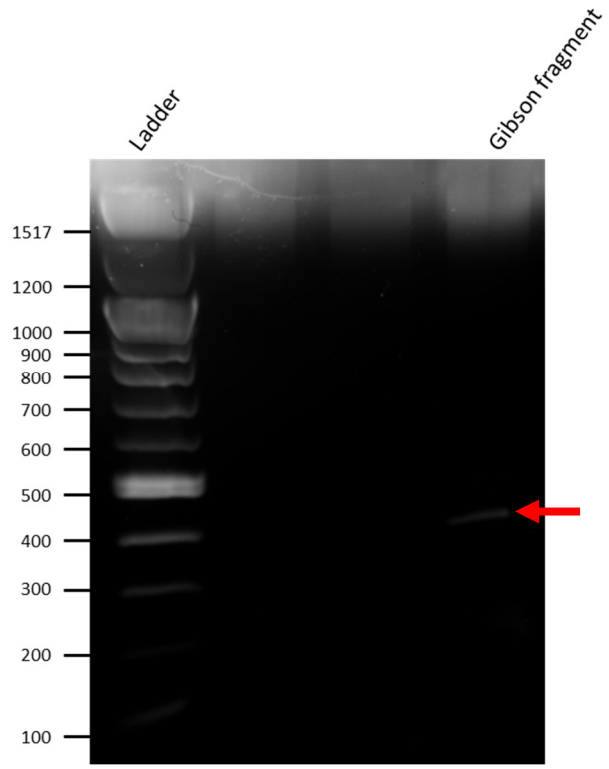


Figure 4.19 1% agarose gel of PCR-amplified Gibson fragment from pSEX81_5A7.

Lane 1: DNA ladder New-England Biolab 100 bp (sizes are indicated in bp). Lane 4: PCR-amplified fragment from pSEX81_5A7 with primers Gibson_fragment_for and Gibson_fragment_rev. A band consistent with the size of the expected fragment (482 bp, highlighted by the red arrow) is visible.

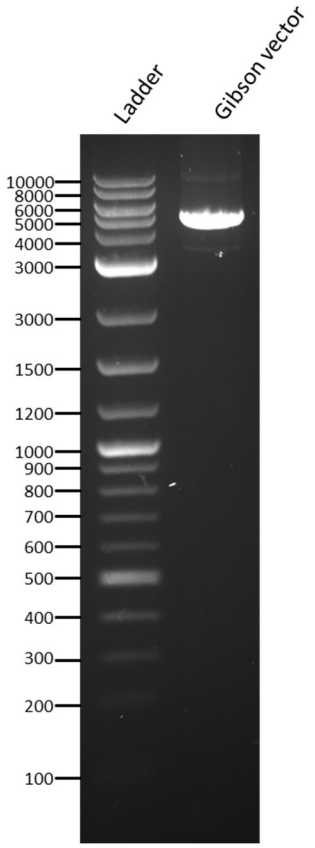


Figure 4.20 1% agarose gel of PCR-linearised vector pet52b(+).

Lane 1: DNA ladder New-England Biolab 1 kb plus (sizes are indicated in bp). Lane 2: Vector pet52b(+) linearised by PCR with primers Gibson_vector_for and Gibson_vector_rev. A band consistent with the size of the expected fragment (5098 bp) is visible.

The assembly was performed using Gibson Assembly® Master Mix (New-England Biolab) and the ligated plasmid was transformed into BL21-AI for protein expression. Pilot protein expression was performed using various concentrations of IPTG (0.1 mM, 0.5 mM and 1 mM). Samples were collected and run on an SDS-PAGE gel (Figure 4.21). No band corresponding to the expected size of the tagged 5A7 nanobody (15,273.18 Da) could be observed, indicating that the tagged 5A7 nanobody protein was not expressed. To confirm this lack of expression, the 1 mM IPTG induced sample was pelleted and sonicated. The resulting lysate was run on an immobilised nickel ion column (His-Trap, Cytiva) using an AKTAprime Plus (Cytiva), Bound proteins were eluted alongside an imidazole gradient. No peak was visible on the UV spectrum obtained from the ÄKTA FPLC (Fast Protein Liquid Chromatography) system (Figure 4.22). This lack of signal indicated the absence of protein eluted from

the column. Several hypothesises could explain the lack of expression. After careful consideration of the plasmid sequence, it was observed that a start codon appeared in the ribosome binding site (RBS) spacer sequence as a result of the Gibson assembly. The presence of a start codon in the RBS spacer sequence introduces ambiguity in translation initiation, leading to potential mis-expression or suppression of the desired protein. This emphasises the importance of carefully designing sequences around the RBS to ensure proper translation of the target gene.

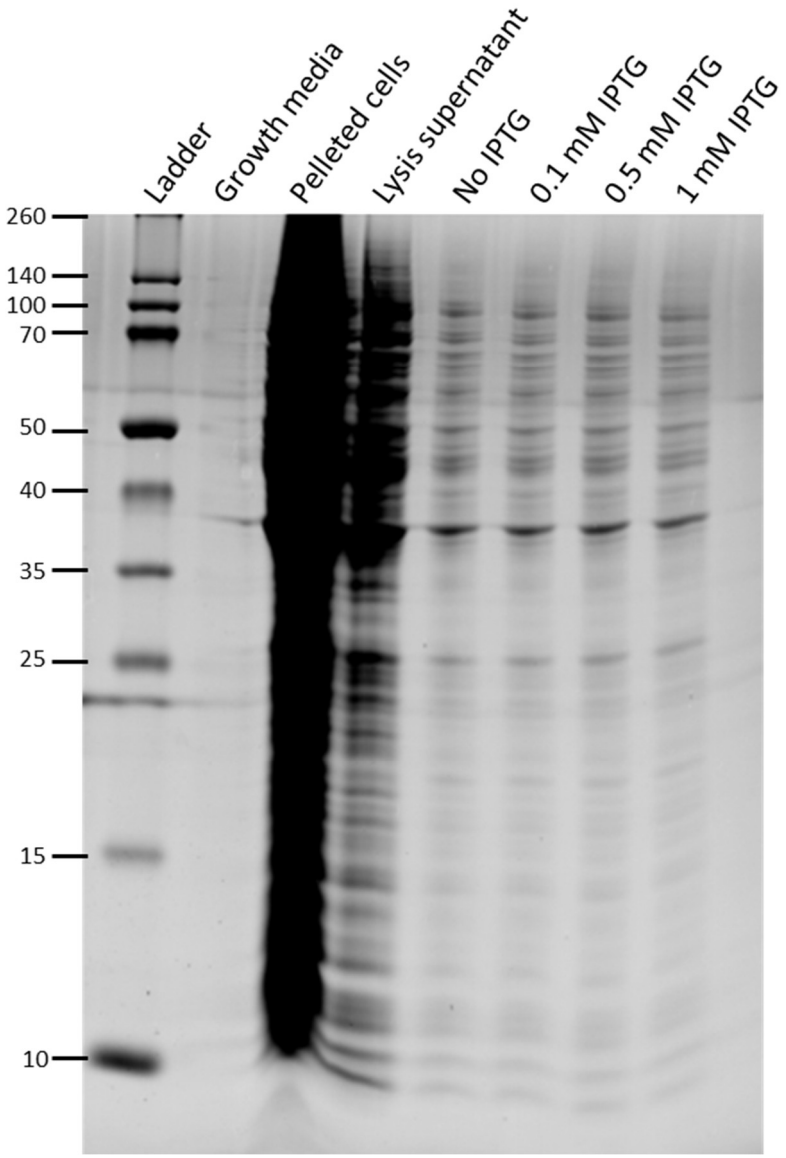


Figure 4.21 SDS-PAGE analysis of 5A7 pilot protein expression from BL21 carrying pET52b_5A7, stained with Coomassie Brilliant Blue.

Lane 1: Molecular weight marker Spectra™ Multicolour Broad Range Protein Ladder (size in kDa indicated). Lane 2: Growth media of BL21 cells carrying pET52b_5A7 prior to induction. Lane 3: Pelleted and lysed BL21 cells carrying pET52b_5A7 prior to induction. Lane 4: Lysis supernatant from BL21 cells carrying pET52b_5A7 prior to induction. Lane 5 to 8: Pelleted and lysed BL21 cells carrying pET52b_5A7 following induction with various concentrations of IPTG. Bands indicate the presence of proteins; no band is visible for the target protein around 15 kDa.

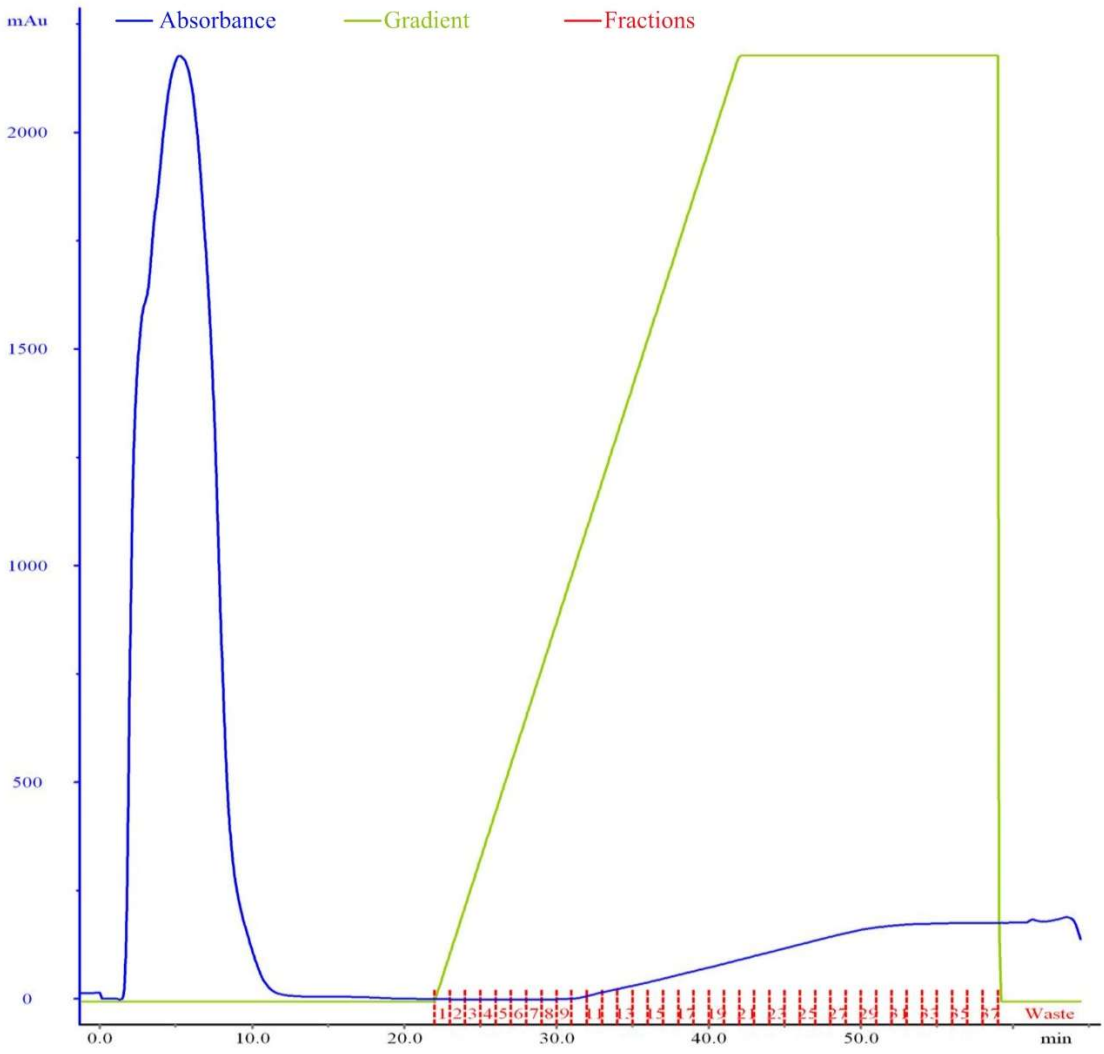


Figure 4.22 Representative chromatogram of 5A7 from pET52b(+) protein purification using an ÄKTA FPLC system.

The graph shows UV absorbance at 280 nm (blue line), indicative of protein concentration, plotted against elution volume. Concentration gradient (green line) indicates imidazole gradient changes. Collected fractions are labelled in red. Following the initial equilibration phase, a large peak in absorbance can be observed due to sample loading, followed by wash steps. No distinct peaks are visible following elution.

4.3.3.2 pET101 D-TOPO Gibson Assembly

A new experimental protocol was designed for the expression of tagged 5A7 nanobody. A synthetic gene encoding for the 5A7 nanobody, alongside an additional glycine and serine rich flexible linker (GSAGSAAGSGEF, as described in Waldo *et al.*, 1999), the Sortase A binding site followed by a 6x histidine tag was designed. The

gene was flanked by Gibson binding sites corresponding to two primers designed to linearised the pET101 D-TOPO expression plasmid. The pET101 d-TOPO plasmid is commercially available as a linear plasmid and was modified and amplified by PCR using primers pET101_for and pET101_rev (Q5® High-Fidelity DNA Polymerase, 30 cycles, Tm = 56° C, predicted amplicon size = 5792 bp).

Gibson assembly was performed using Gibson Assembly® Master Mix (New-England Biolab) and the ligated plasmid was transformed into BL21-AI for protein expression. Pilot protein expression was performed using various concentrations of IPTG (0.1 mM, 0.5 mM and 1 mM). Samples were collected and run on an SDS-PAGE gel (Figure 4.23). Despite the gel being distorted by overloading of the un-induced pellet sample, no band corresponding to the expected size of the new tagged 5A7 nanobody (19,511.78 Da) could be observed, indicating that the new tagged 5A7 nanobody protein was not expressed. To confirm this lack of expression, the 1 mM IPTG was prepared for purification and run on an immobilised nickel ion column (His-Trap, Cytiva) using an AKTAprime Plus (Cytiva). Bound proteins were eluted alongside an imidazole gradient. No peak was visible on the UV spectrum obtained from the ÄKTA FPLC system (Figure 4.24).

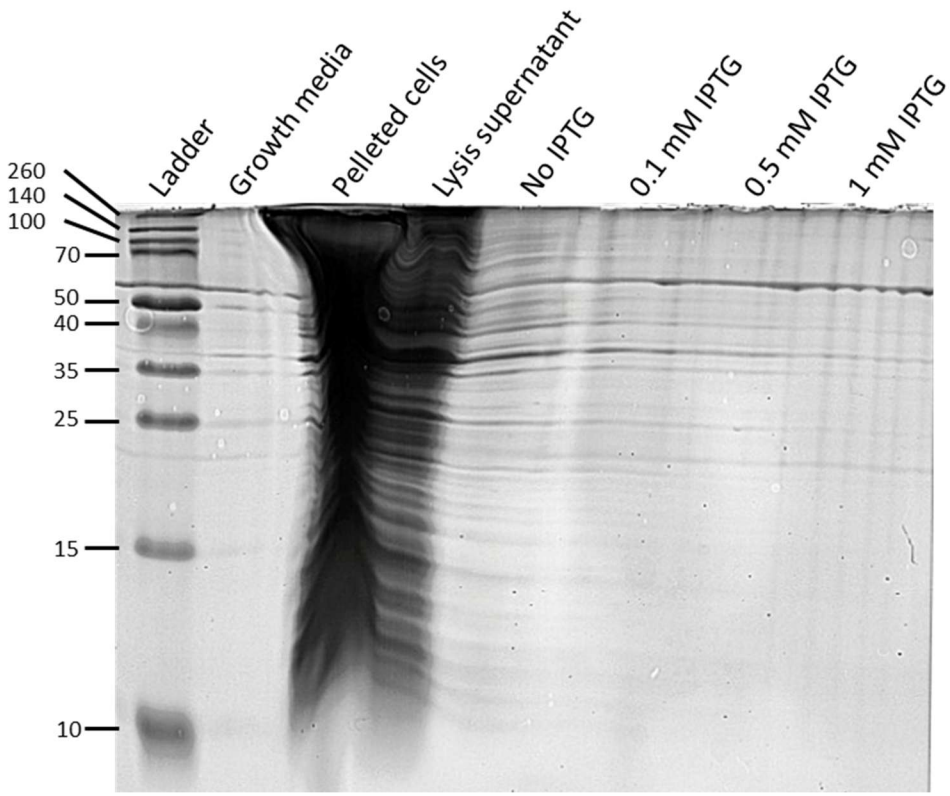


Figure 4.23 SDS-PAGE analysis of 5A7 pilot protein expression from BL21 carrying pET101_5A7, stained with Coomassie Brilliant Blue.

Lane 1: Molecular weight marker Spectra™ Multicolour Broad Range Protein Ladder (size in kDa indicated). Lane 2: Growth media of BL21 cells carrying pET52b_5A7 prior to induction. Lane 3: Pelleted and lysed BL21 cells carrying pET52b_5A7 prior to induction. Lane 4: Lysis supernatant from BL21 cells carrying pET52b_5A7 prior to induction. Lane 5 to 8: Pelleted and lysed BL21 cells carrying pET52b_5A7 following induction with various concentrations of IPTG. Bands indicate the presence of proteins; no band is visible for the target protein around 15 kDa.

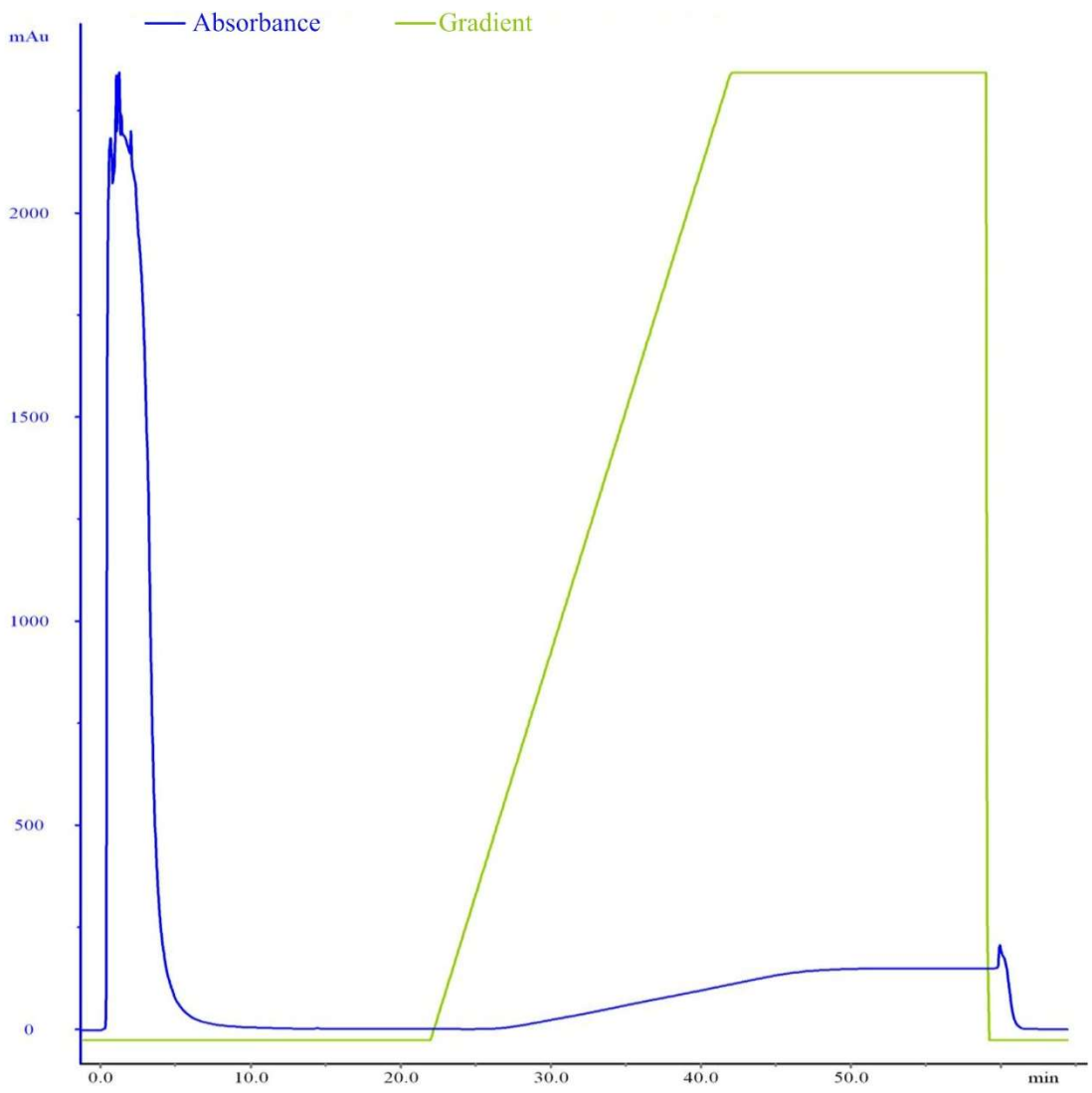


Figure 4.24 Representative chromatogram of 5A7 from pET101_5A7 protein purification using an ÄKTA FPLC system.

The graph shows UV absorbance at 280 nm (blue line), indicative of protein concentration, plotted against elution volume. Concentration gradient (green line) indicates imidazole gradient changes. Following the initial equilibration phase, a large peak in absorbance can be observed due to sample loading, followed by wash steps. No distinct peaks are visible following elution.

Fractions were collected, grouped every 5 mL and prepared for SDS-PAGE (Figure 4.25). Alongside those fractions, lysed cells prior to and after induction, as well as the corresponding growth media, were run. A band that could potentially correspond to the size of 5A7 was observed in the induced lysed cells sample but was not present in the lysis supernatant obtained following sonication and centrifugation

of the induced cells. However, a strong band around 38 kDa was visible in the lysis supernatant. This could potentially indicate that 5A7 aggregates during the lysis process, blocking the histidine tag and preventing purification. In order to rule out aggregation, new lysis purification buffers were designed to include 8 M urea and 5 mM DTT. A new culture was set up, and cells were resuspended in buffer C, and loaded onto an immobilised nickel ion column (His-Trap, Cytiva) for elution with buffer D using an AKTAprime Plus (Cytiva).

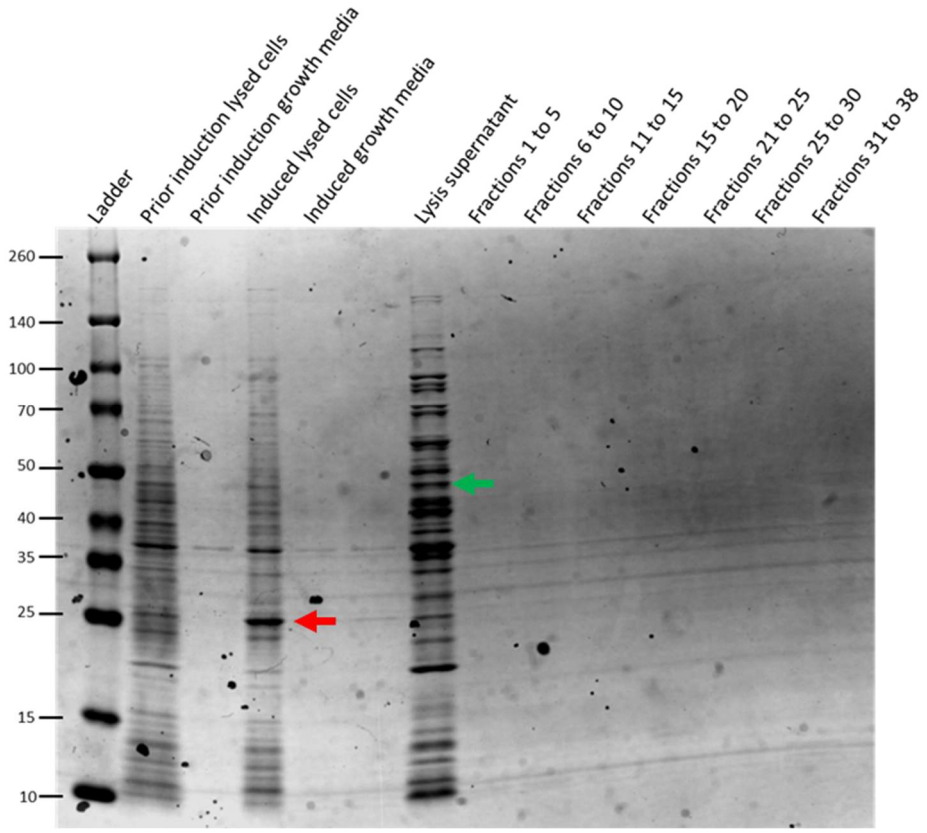


Figure 4.25 SDS-PAGE analysis of fractions collected from the 5A7 from pET101_5A7 protein purification process, stained with Coomassie Brilliant Blue.

Lane 1: Molecular weight marker Spectra™ Multicolour Broad Range Protein Ladder (size in kDa indicated). Lane 2: Lysed BL21 cells carrying pET101_5A7 prior to induction with IPTG. Lane 3: Growth media of BL21 cells carrying pET101_5A7 prior to induction with IPTG. Lane 4: Lysed BL21 cells carrying pET101_5A7 after induction with IPTG. Lane 5: Growth media of BL21 cells carrying pET101_5A7 after induction with IPTG. Lane 7: Lysis supernatant, as loaded onto the first purification column. Lane 8 to 14: Fractions collected from the purification process. Bands indicate the presence of proteins; no band is visible for the target protein around 19 kDa in the fraction samples. A band is visible around the right size in the induced lysed cells sample (red arrow). Additionally, bands around the 38 kDa mark in the lysis supernatant might indicate the presence of aggregated proteins (green arrow).

Once again, no peak was visible on the FPLC spectra (Figure 4.26). To confirm the absence of protein, fractions were grouped and prepared for SDS-PAGE alongside lysis supernatant. No bands could be observed in any of the fractions, but a band corresponding to 19 kDa was visible in the lysis supernatant, as well as the previous band around 38 kDa (Figure 4.27). To confirm whether this band was 5A7, wild type

BL21 lysate, growth media of BL21 pET101_5A7 and the corresponding pellet, as well as lysed cell supernatant were run on an SDS-PAGE gel for analysis by western blot (Figure 4.28). A histidine tagged protein ladder was used as a positive control (BenchMark™ His-tagged Protein Standard), and the membrane was probed with an anti-his antibody, followed by an HRP labelled secondary. Following chemiluminescent imaging, the positive control ladder was clearly visible, but no band could be observed in any of the samples, confirming that 5A7 was not expressed by the BL21 pET101_5A7 cells. In order to ascertain potential solubility issues, the hydrophobicity of 5A7 was investigated. The hydropathy score was calculated and revealed a very slightly hydrophobic molecule (Kyte and Doolittle mean hydropathy score: -0.3352 ± 1.017 (SD)), meaning the protein is likely soluble in water, and therefore solubilisation issues are not responsible for the absence of signal. Due to time constraints, the protein expression and purification of 5A7 had to be abandoned, and the protein was not successfully produced.

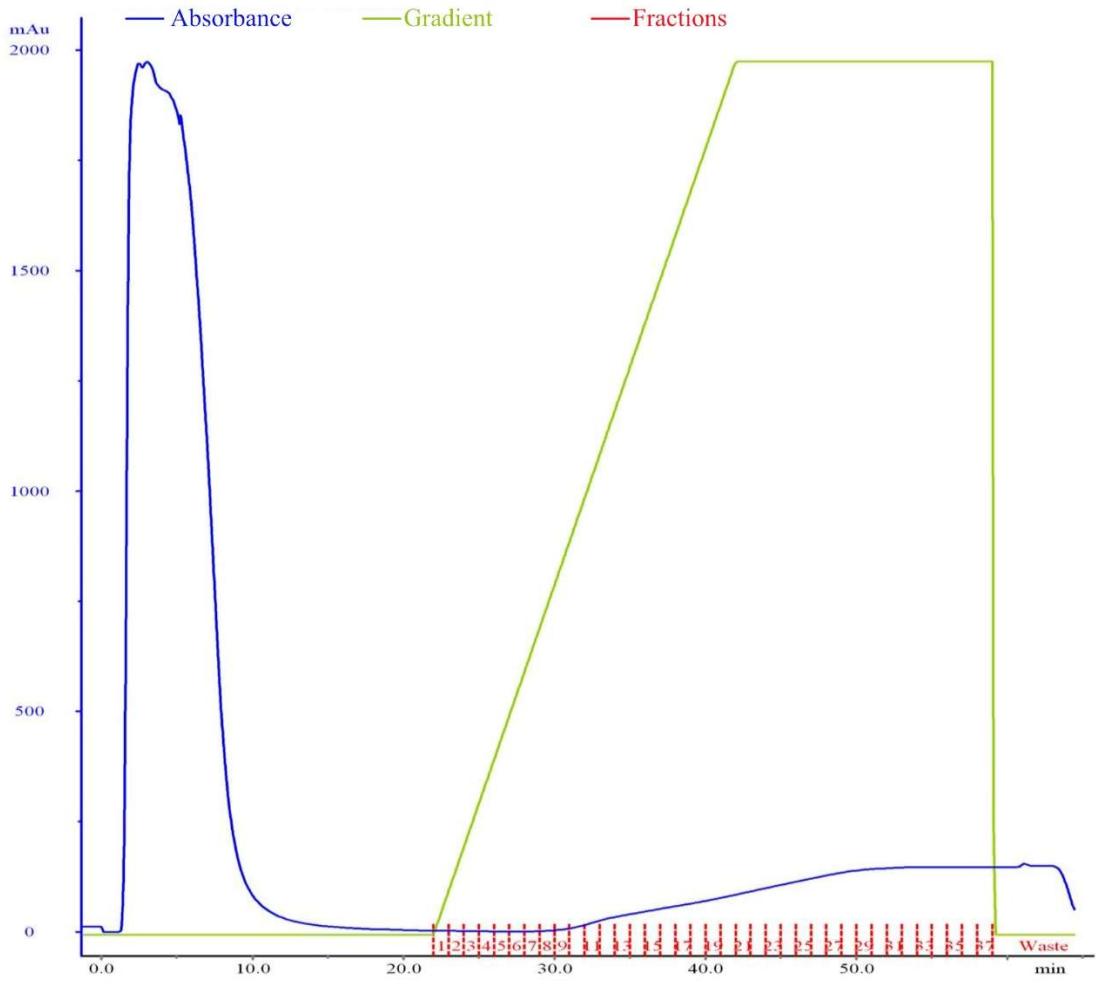


Figure 4.26 Representative chromatogram of 5A7 from pET101_5A7 protein purification with urea treatment using an ÄKTA FPLC system.

The graph shows UV absorbance at 280 nm (blue line), indicative of protein concentration, plotted against elution volume. Concentration gradient (green line) indicates imidazole gradient changes. Following the initial equilibration phase, a large peak in absorbance can be observed due to sample loading, followed by wash steps. No distinct peaks are visible following elution.

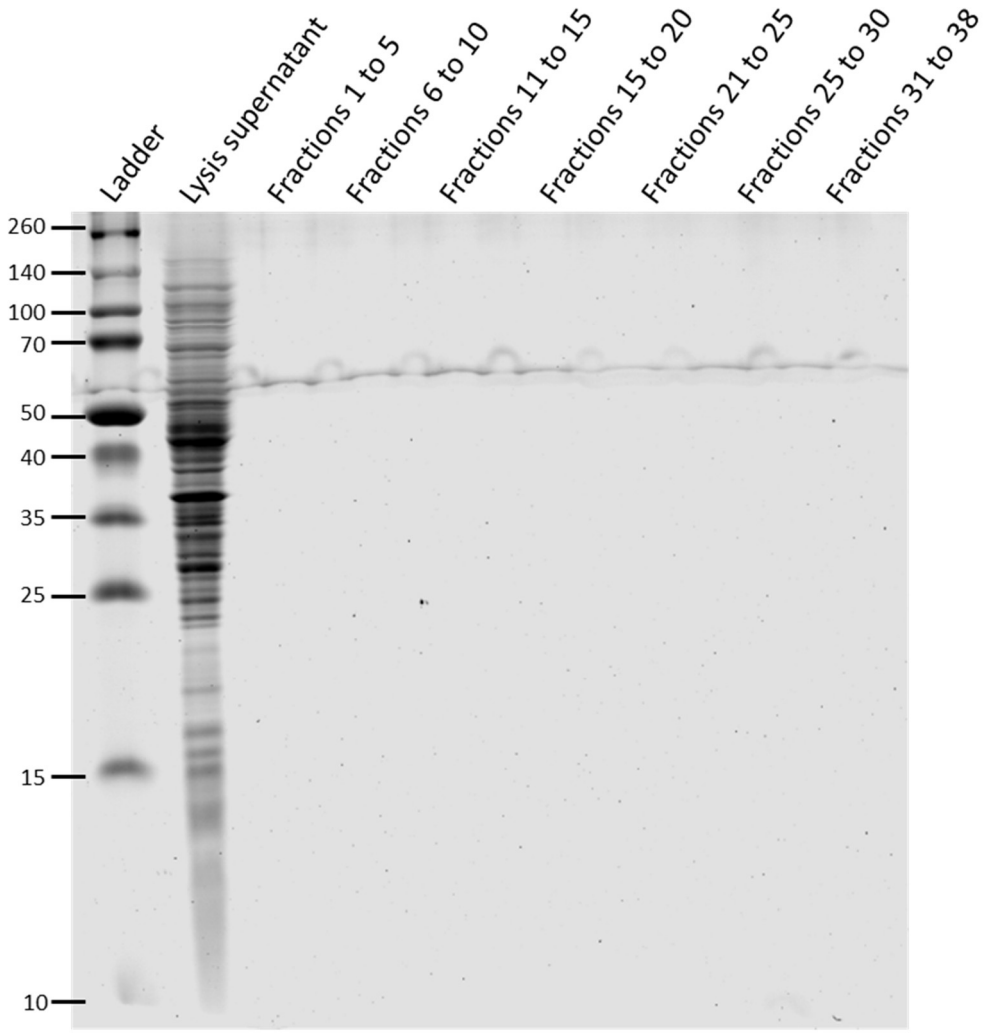


Figure 4.27 SDS-PAGE analysis of fractions collected from the 5A7 from pET101_5A7 protein purification process with urea treatment, stained with Coomassie Brilliant Blue.

Lane 1: Molecular weight marker Spectra™ Multicolour Broad Range Protein Ladder (size in kDa indicated). Lane 2: Lysis supernatant, as loaded onto the first purification column. Lanes 3 to 9: Fractions collected from the purification process. Bands indicate the presence of proteins; no band is visible for the target protein around 19 kDa.

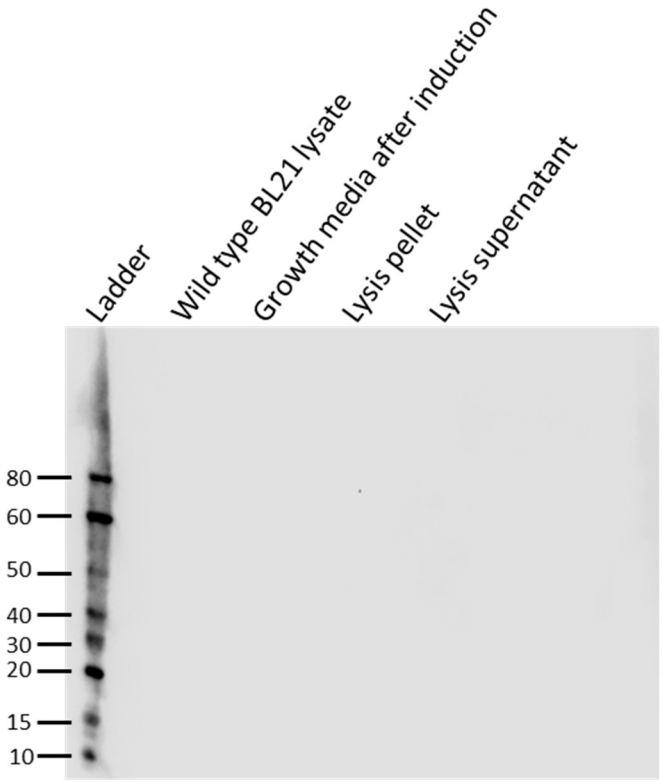


Figure 4.28 Western blot analysis of 5A7 expression.

Lane 1: Positive control his-tagged protein ladder. Lane 2: Lysed wild type BL21 cells. Lane 3: Growth media of BL21 with pET101_5A7 after induction with IPTG. Lane 4: Pellet of BL21 with pET101_5A7 after induction with IPTG and sonication. Lane 5: Supernatant of BL21 with pET101_5A7 after induction with IPTG and sonication. Bands indicate the presence of proteins; no band is visible in any of the samples.

4.4 Conclusion

In order to functionalise the vNAR 5A7 nanobody at the C-terminus, a fluorescent label was designed for Sortase A catalysed coupling. An oligoglycine peptide including an amide-coupling activated lysine was synthesized by solid phase peptide synthesis. The fluorescent marker Cy5.5 was then coupled onto the peptide to create the fluorescent label. The synthesis yielded 6.8 mg of compound, at 94% purity. The Sortase A enzyme was successfully expressed and purified in *E. coli*, yielding 62 nmol of protein. A plasmid encoding for the vNAR 5A7 functionalised with the LPATG Sortase A recognition motif was generated and transformed into E. coli for expression and purification. Despite several optimisation, the vNAR 5A7 protein could not be expressed. The challenges of nanobody expression and purification are discussed in Chapter 5 (page 193), alongside future work.

Chapter 5 General Discussion

5.1 Introduction

The primary aim of this work was to develop a targeted drug delivery platform based on the specificity of nanobodies to specific targets of the mucus secretion pathway, and their functionalisation. As previously stated, hypersecretory diseases (AHDs) share the common pathophysiology of mucus hypersecretion, and impact over 500 million people worldwide. While numerous therapeutic options exist, developing new targeted and symptom-specific biologics is highly relevant in improving patients' outcomes. The overall aim of this thesis was to develop a targeted drug delivery platform utilising goblet cell-specific nanobodies to deliver therapeutic molecules to the site of mucus secretion.

The first step consisted in the construction of a diverse nanobody library based on the IgNAR scaffold isolated from nurse shark *Ginglymostoma cirratum* by introducing genetic diversity into the CDR3 region of the previously isolated vNAR 5A7 (Dooley *et al.*, 2003), utilising a protocol developed by Zadeh *et al.* (2019). Once a library of sufficient diversity was achieved, targets needed to be isolated. The second chapter focused on establishing an airway epithelium model by growing Human Bronchial Epithelium primary cells (HBEpc) at the air-liquid interface (ALI), in order to isolate goblet cell populations for whole cell panning (WCP). Optimisation of the biopanning protocol was required. As no specific binders were identified, the third chapter consisted in the functionalisation of vNAR 5A7 with a fluorescent tag by Sortase A bioconjugation.

While a highly diverse nanobody library was successfully created, and goblet cell populations isolated from an airway epithelium model, unsuccessful biopanning resulted in no specific binders being identified. Despite this setback, the functionalisation experiments were pursued using the original vNAR 5A7. A fluorescent label was synthesised, but unsuccessful expression and purification of vNAR 5A7 prevented the Sortase A bioconjugation of the label.

The key findings of this thesis will be discussed here, contextualised with existing literature. Future directions, recommendations and lessons learned will also be discussed.

5.2 Interpretation of Key Findings

5.2.1 Development of a Diverse Nanobody Library

In order to generate a novel diverse nanobody library, a variable heavy domain only scaffold had to be selected. The literature has identified such scaffolds in camelids (V_HH) and nurse sharks (vNAR) (Greenberg *et al.*, 1995; Hamers-Casterman *et al.*, 1993).

Here, the protocol developed by Zadeh *et al.* (2019) was used in order to introduce genetic diversity into the complementarity-determining region 3 (CDR3) or vNAR 5A7. Randomised primers were designed, and polymerase chain reaction was used to create a genetically diverse collection of nanobody fragments.

Nanobodies rely heavily on their complementarity-determining regions (CDRs) for antigen binding. Introducing genetic diversity into these CDRs is crucial for generating libraries for nanobody discovery and optimisation. Numerous technologies exist to introduce diversity into DNA sequences. DNA damage can be induced by chemical agents such as ethyl methane sulfonate or exposure to UV light. Coupled with the use of bacterial mutator strains with defective DNA repair systems, the mutation rate can be greatly increased, increasing diversity. However, these approaches affect the entire DNA sequence and, therefore, are not best suited for selected CDRs diversification. Random mutagenesis can be achieved by engineering error-prone PCRs using low-fidelity polymerases or altering dNTP and $MgCl_2$ concentrations. While this approach is more focused, results are unreliable and would result in poor library diversity. Additionally, this approach risks the introduction of stop codons within the complementarity-determining region, which would produce incomplete antibody fragments with low to null binding probability.

De novo synthesis of CDRs with controlled diversity focuses on specific residues or regions within the CDRs for mutagenesis by replacing targeted codons with all possible amino acids via NNK codons (where N has an equal chance of standing for adenine (A), cytosine (C), guanine (G), and thymine (T), and K has an equal chance of standing for thymine or guanine). NNK codons can code for the 20 amino acids, and one stop codon (TAG) or amber codon. SupE *E. coli* strains (like TG1) can translate the amber codon into glutamine (Bossi, 1983; Jacobs *et al.*, 2015). Trinucleotide synthesis can also be used to precisely control amino acid composition and reduce stop codons. This biological chemistry approach, similar to solid phase peptide synthesis, allows for the synthesis of nucleotide strands by sequentially adding trinucleotide phosphoramidites to a growing DNA chain. Trinucleotides are mixed in specified ratios for controlled diversity, ensuring that each amino acid appears at desired frequencies (Suchsland *et al.*, 2021).

Genetic diversity can also be inserted following the identification of potential binders in order to improve characteristics such as specificity, affinity, stability or hydrophilicity. Sequentially mutating each CDR region (known as CDR walking) can be used to refine binding properties while retaining overall structural integrity. Computational modelling uses structural or sequence information to predict beneficial mutations in CDRs. Site-targeted mutagenesis can then be used to either introduce specific biases to mimic natural antibody repertoires or optimise physicochemical properties (e.g. hydrophobicity, charge) or improve binding capabilities.

Each methodology has its strengths and limitations, with choices often dictated by the desired library size, sequence diversity, and structural constraints of the nanobody scaffold.

Here the NNK codon was used, and randomised primers introduced genetic diversity into the vNAR 5A7 CDR3. This method was selected based on its ease of use and high effectiveness, combined with its time and cost-efficient properties. The use of ultra competent TG1 cells was essential to ensuring a highly diverse library by increasing the number of clones isolated. While traditionally libraries reported in the

literature express their diversity in colony forming units (CFU), these numbers are better used to reflect the transformation competency of the cell line used, and not the true diversity of the library. Methods like transformation efficiency, fingerprinting, and sequencing small samples (a few hundred elements) provided rudimentary and limited insights, as complexity does not scale linearly with sample size.

Next generation sequencing (NGS) has emerged as a new tool to fully assess the diversity of nanobody libraries (Fantini *et al.*, 2017; Wang *et al.*, 2022). Large number of sequences can be isolated and analysed, giving a more accurate picture of library diversity. This method was employed here, narrowing an initial $7.42 \times 10^9 \pm 1.88 \times 10^9$ (SE) CFU transformation titre to $2.56 \times 10^9 \pm 6.49 \times 10^8$ (SE), or a 30-fold difference. This library size was consistent with commercially available libraries, and similar libraries discussed in the literature (Almagro *et al.*, 2019; Cabanillas-Bernal *et al.*, 2019; Tsai *et al.*, 2023; Yan *et al.*, 2014).

Additional diversity could be achieved by increasing the number of primers used for NNK codon diversification and increasing the number of cysteine loops within the CDR3. Other parts of the vNAR sequence could also be targeted. Four hypervariable loops (CDR1, CDR3, HV2, and HV4, depicted in Figure 5.1) are responsible for the large repertoire diversity observed in shark nanobodies, and while studies have shown that CDR3 was the primary site of nanobody diversity, randomisation of the other hyperloops might increase the overall diversity of the library and yield better binders (Barelle and Porter, 2015; Feng *et al.*, 2018; Fernández-Quintero *et al.*, 2021).

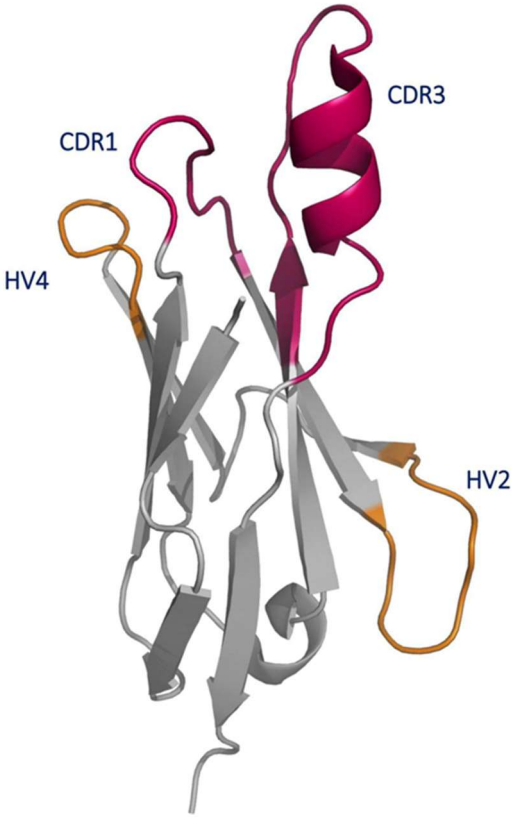


Figure 5.1 3D structure of a vNAR showing the four hypervariable loops.

CDR1 and CDR3 are highlighted in red, HV2 and HV4 in orange. Adapted from Fernández-Quintero et al. (2021), published in Frontiers in Molecular Biosciences. © 2021, licensed under CC BY.

5.2.2 Establishing an Airway Epithelium Model

The isolation of nanobodies specific to the site of mucus secretion in the airway necessitated a relevant *in vitro* model for the human airway epithelium.

Immortalised cell lines such as BEAS-2B, Calu-3 or A549 are often used in respiratory research. They are readily available, easy to culture and handle and suitable for high-throughput screening and mechanistic studies due to their reproducibility. However, immortalised cell lines do not fully replicate the complexity of primary cells due to their abnormal (or absent) differentiation and phenotype. Primary Human Bronchial Epithelial cells (HBEpc) derived from human donors and differentiated at the air-liquid interface (ALI) to form a pseudostratified epithelium resembling native airway tissue; more closely mimic the structure and function of

native airway epithelium. They can produce mucus, cilia, and innate immune responses and are often used to study Airway Hypersecretory Diseases (AHDs). While they offer a more accurate model, their availability can be limited, and variability due to donor differences needs to be accounted for. Here, their expensive maintenance cost was mitigated by the use of commercially available ALI HBEpc inserts, ensuring good quality cells were used in following experiments.

A previously described flow cytometry panel was used to isolate goblet cells from the general cell populations (Bonser *et al.*, 2021). In order to increase the population of goblet cells, IL-13 was used to induce epithelium remodelling and drive the differentiation of mucus-secreting phenotypes (Kondo *et al.*, 2006, 2002). These combined methodologies allowed for a five-fold increase in the percentage of goblet cells in IL-13 stimulated samples (17.92%) compared to unstimulated (3.77%). These results were comparable to those obtained by other studies (Bonser *et al.*, 2021; Davis and Wypych, 2021; Deprez *et al.*, 2020) and confirm the remodelling effect of IL-13 treatment on the airway epithelium.

This increase in the proportion of goblet cells is especially significant in this context. Stimulated inserts modelled the airway physiology of AHDs and could be used as a biopanning target to identify key phenotype differences. Isolated goblet cells could also be used for more precise targeting of mucus hypersecretion sites. Being able to isolate a higher number of cells is critical to successful biopanning. Live cells are difficult to manipulate due to their size and fragility, increasing the number of cells available in the sample would help facilitate the biopanning process.

5.2.3 Whole Cell Biopanning

Stimulated and unstimulated inserts were used as targets for the first biopanning experiments, as models for the diseased and healthy airway epithelium, respectfully. However, this approach yielded a very low number of binders, insufficient for more than one round of biopanning, and parameters were modified to increase the number of clones isolated. A second attempt using goblet cells isolated by fluorescence-activated cell sorting yielded similar results. Despite IL-13 stimulation, the number of isolated cells remained low and led to difficulties in sample manipulation, especially when washing and eluting phages. The final approach utilised detached cells from IL-13 stimulated and unstimulated inserts. This allowed for a higher number of cells while keeping a relevant phenotype difference. After a first enrichment round against the IL-13 stimulated cells, an absorption round against unstimulated cells was performed to eliminate binders to IL-13-unaffected targets. A final enrichment round was then performed to further select high affinity binders.

The number of binders was satisfactory after the first round of biopanning (4.2×10^4 CFU). The absorption round eliminated over 93% of binders, further narrowing the phage pool to 2.6×10^3 CFU. Following the last enrichment round, eight clones were identified and prepared for sequencing alongside phage samples from each round of biopanning. Despite several tries, relevant sequences could not be amplified by PCR and therefore were not sequenced. In order to extract data from the isolated clones, phagemid DNA was extracted from bacterial culture and sent for whole plasmid sequencing. Upon analysis of the phagemid sequences, it appeared that a significant portion of the vNAR region was highly disturbed, as well as part of the *E. coli* origin of replication gene. While this explained why the vNAR sequence could not be amplified by PCR due to the primers not being able to bind to the sequence, this unexpected result revealed that no relevant binders were identified through the biopanning experiments. Several possible explanations for these lack of results are discussed below.

First of all, the complexity of Whole Cell Panning (WCP) might have played a role. WCP is a powerful strategy for selecting antibodies against antigens presented in their native conformation on the surface of whole cells. This approach allows for the identification of antibodies targeting complex and physiologically relevant structures, including post-translational modifications, multimeric proteins, and membrane-localised antigens. As WCP does not rely on purified proteins, binders for novel or poorly characterised antigens can be identified alongside their relevant antibody, and complex proteins can be targeted without the need for complex expression and purification protocols. WCP can also identify binders to a diverse range of surface molecules, such as RNA, for example. RNA has been shown to play a critical role in neutrophil recruitment (Zhang *et al.*, 2024) and it has been shown that neutrophils play a key role in asthma pathophysiology (Ray and Kolls, 2017). Utilising WCP could allow for the identification of such RNA, while identifying the relevant antibody at the same time. This type of target-agnostic approach allows for unbiased antibody discovery, making WCP particularly valuable in fields like oncology and immunology (Stark *et al.*, 2017).

Despite its potential, WCP faces several technical and biological challenges. Cell surfaces are highly dynamic, and proteins may undergo internalisation, shedding, or glycosylation changes, affecting the stability and accessibility of target antigens during the selection process. Additionally, cell viability and stability are of particular concern, as cellular processes such as cell lysis leading to the release of intracellular components during panning can interfere with selection. The use of detergents during the wash steps especially might impact cellular physiology. Insufficient washing steps can lead to non-specific phage retention, while overly stringent conditions may result in the loss of rare but genuine binders.

Addressing these challenges involves careful optimisation of selection protocols. Negative selection using off-target cells, differential antigen expression profiling, and pre-clearing steps can enhance specificity.

The display methodology used might also have contributed to the unsuccessfulness of the panning experiments. As previously discussed, phage display

is a powerful tool for antibody discovery, but notable limitations can hinder its effectiveness. Abundant or adhesive surface components can lead to background interactions. This is particularly relevant when using WCP combined with phage display. While phages were blocked with the same solutions, cells were washed and stored in Eppendorfs identical to the ones used for panning, there is still a possibility of interactions between phage particles and container or cell growth media remnants. Biases can then be introduced by the positive selection of these background binders. While one of the intended purposes of the absorption round was to remove such binders, it is possible that a strong bias in phage amplification from the first round of biopanning rendered the process difficult.

Other display methodologies have been employed with vNAR 5A7 derived nanobodies. Tsai *et al.* (2023) used *Saccharomyces cerevisiae* yeast display strain EBY100 to display a vNAR 5A7 library bound to the Green Fluorescent Protein (GFP). This allowed for the monitoring of vNAR expression by fluorescence-activated cell sorting (FACS), ensuring all yeasts carried a potential binder on their surface and limiting background contamination. When compared, vNAR phage and yeast display systems present key differences in sequence diversity and CDR3 characteristics. vNAR phage-displayed library tend to show higher sequence diversity, whereas the yeast-displayed libraries show higher retention of unique sequences in later rounds of biopanning (Takeda *et al.*, 2023).

One key technical issue specific to phage-displayed libraries is the carryover of phages lacking a displayed nanobody. Preventing this type of 'bald' phage contamination is critical to the efficiency of the biopanning process. These 'bald' phages are the result of the incorporation of the native pIII encoded by the phage genome over the nanobody-pIII construct, leading to many phages lacking the nanobody in their coat (Ledsgaard *et al.*, 2018). Several technologies have been developed to mitigate this issue. Modified phages such as CT phages, Hyperphage, Ex-phage and Phaberge have been developed (Baek, 2002; Kramer *et al.*, 2003; Rondot *et al.*, 2001; Soltes *et al.*, 2003). These phages lack a functional copy of the pIII encoding gene and rely solely on phagemid-encoded pIII fusions, ensuring only insert-containing phagemids are packaged. This results in all copies of the pIII fusion

protein being displayed is coupled with the phagemid encoded antibody fragment. Here, an Hyperphage system was used to prevent the apparition of 'bald' phage contaminants. Hyperphage systems have been successfully used to isolate binding antibody fragments in the past: Meyer *et al.* (2011) isolated antibody fragments from the naïve human antibody gene library HAL7 specific to the outer membrane protein D of *Salmonella Typhimurium*, while Kirsch *et al.* (2008) used the Hyperphage system to isolate human antibody fragments for the detection and diagnosis of Venezuelan equine encephalitis virus. While these systems can ensure that all phages amplified by library containing bacteria do come from repackaged phagemids, they do not prevent empty phagemids from being packaged. Self-ligating plasmids resulting from improper ligation at the fragment introduction stage could still contaminate the genetic material of the library. While the NGS library analysis performed to assess the quality and diversity of the library did not reveal any sequence mapping to the empty pSEX81 vector, empty vector contamination is still a possibility.

While pIII-deficient systems prevent the apparition of 'bald' phages, other issues might arise from their use. Structural limitations of the fused antibody fragments can lead to instability of the pIII protein, reducing the functional incorporation of pIII-fused nanobodies into the phage coat. In systems where all pIII proteins display an antibody fragment, the selection by avidity can obscure the intrinsic affinity of individual ligands, making high-affinity clones harder to identify. Phages displaying multiple low-affinity ligands may bind tightly to targets through cumulative interactions (Rondot *et al.*, 2001). Hyperphages also tend to show reduced titres and infectivity when compared to native M13KO7. Here the initial avidity round was followed directly by an absorption round, before a final affinity-based enrichment round. Increasing the number of affinity-based rounds might help improve the number of binders identified, although this might have not been helpful here, as none of the clones displayed expected vNAR sequences.

5.2.4 Chemical Synthesis of a Fluorescent Label for the Functionalisation of Nanobodies by Sortase A Conjugation

The chemical synthesis of a fluorescent label, including a Sortase A oligoglycine recognition site, was achieved through solid-phase peptide synthesis and amide coupling. Amide coupling is a commonly used antibody labelling methodology, due to its ease of use and low cost, and could have been used here to remove the need for Sortase A conjugation. However, when directly labelling amino acids of antibodies or antibody fragments, there is a possibility for the label to obstruct key antibody binding sites. This is especially of concern when working with shark vNAR, as their small size strongly limits the number of binding sites available. In the case of vNAR 5A7, the protein is only 114 amino acids long. Bioconjugation by Sortase A ensures the nanobody will be labelled and the C-terminus, preventing the fluorescent dye Cy5.5 from binding to amino acids within any of the four hypervariable loops. (Schumacher *et al.*, 2018).

While the proposed synthesis was relatively simple, adjustments had to be made to facilitate the binding of the Cy5.5 dye to the GGGK peptide in solid phase. Solid phase simplifies the synthesis by allowing for the removal of contaminants and unbound amino acids in a syringe, as opposed to liquid phase, where preparatory HPLC is required after every coupling stage. But the size of the resin can sterically affect binding reactions. This was the case here, and the issue was circumvented by extending the peptide chain to create space between the resin the reactive lysine residue.

A Sortase A encoding plasmid was commercially obtained, and Sortase A enzyme was easily purified following established protocols (Guimaraes *et al.*, 2013).

5.2.5 Expression and Purification of the vNAR 5A7

Functionalisation of vNAR 5A7 required the expression and purification of the protein engineered with the LPXTG Sortase A recognition site and a histidine tag for easy purification by nickel-ion immobilised chromatography. Unfortunately, despite

several optimisations, vNAR 5A7 could not be expressed in *E. coli*. This was an unexpected outcome, as nanobodies are usually easy to express in bacterial systems. vNAR 5A7 has been successfully expressed before in mammalian HEK293 cells (Cummins *et al.*, 2008; Steven *et al.*, 2017). Häsler *et al.* (2016) reported the purification of vNAR 5A7 but gave little details on the methods used to achieve this. The original vNAR 5A7 paper from Dooley, Flajnik and Porter (2003) reported bacterial expression of the nanobody tagged with a human constant kappa (HuCκ) domain and a hexa-histidine tag in *E. coli* X1-Blue cells. It is possible that the addition of HuCκ improved the expression of vNAR 5A7 by limiting aggregation.

The expression and purification of single-chain antibody fragments can present unique challenges. Poor plasmid design, suboptimal codon optimisation, or weak promoter activity can lead to poor expression of the protein. This was originally the case here, with the first design resulting in a start codon appearing in the ribosome binding site (RBS) spacer sequence as a result of the Gibson assembly. It was hypothesised that this codon led to improper expression of the protein and a new system was designed. Another common issue is the folding issues of nanobodies when directed to *E. coli* cytoplasm where the fragments tend to aggregate or form insoluble inclusion bodies. The inclusion of a pelB leader can direct the protein to the bacterial periplasm, leveraging its oxidising environment to facilitate disulphide bond formation and preventing aggregation (Kipriyanov, 2009). Both systems accounted for this pelB leader, and the sequence was included in the vector design. This was insufficient here, as no expression could be detected after Western Blot analysis. The insolubility of antibody fragments can also be a challenge. Here, hydrophobicity was measured and revealed that, while vNAR 5A7 was slightly hydrophobic, this was not enough to prevent solubilisation in water. Additionally, the use of DTT and urea showed that aggregation was not the limiting factor of vNAR 5A7 expression and purification (Malpiedi *et al.*, 2013).

There is a possibility of degradation of the histidine tag by host proteases during expression. PMSF (phenylmethanesulfonyl fluoride, a serine-protease inhibitor, was added prior to lysis by sonication in order to prevent any such degradation, but studies have shown that PMSF alone is not always sufficient to

prevent protein degradation. Future optimisation of the solubilisation and purification buffers is required for full expression and purification of vNAR 5A7 (Amrein and Stossel, 1980). For example, the addition of dithiothreitol to inhibit thiol-protease could help improve this system.

Finally, there is a possibility that the Sortase linker motif could interfere with protein purification in this case. The addition of amino acids at the protein C terminus could affect the protein structure or folding, leading to aggregation or altered solubility. Moreover, the proximity of the linker to the histidine tag could interfere with histidine binding to immobilised nickel ions. The introduction of a protease cleavage site could have also led to the separation of the histidine tag from the vNAR 5A7 protein, preventing purification by immobilised nickel ions columns. Placing an additional histidine tag at the N terminus could potentially circumvent this issue (Young *et al.*, 2012).

Methods such as the co-expression of molecular chaperones have been shown to significantly improve solubility and reduce toxicity during the expression and purification of antibody fragments (Hayhurst and Harris, 1999). Fusion to another protein, such as the maltose-binding protein, can also help overcome the folding challenges of nanobody expression (Salema and Fernández, 2013). Fusion to proteins might be difficult here, and the free C terminus is required for functionalisation by Sortase A, but enzymatic digestion sites could be engineered to sever additional protein domains. Careful optimisation of expression and purification workflows is necessary here to ensure the successful production of vNAR 5A7 nanobodies.

5.3 Future Directions

When considering the identification of mucus secretion specific binders, two potential directions are conceivable. Careful optimisation of whole cell panning methodology, including modification of buffers, architecture of rounds or cell panning conditions, might help identify binding phages. Another possible avenue would be the prior identification of target proteins by analysis of the genomic landscape of diseased airway epithelium. Purification of such proteins could allow for

panning of these targets by immobilisation on a surface, bypassing the difficulties of whole cell panning completely. While this approach is more common and easier to implement, it does lack the native characteristics of whole cell panning when considering surface proteins. However, it might be sufficient to identify binders to the mucus secretion site. It is important to remember that naïve libraries never achieve the same level of affinity as observed in immunised animals thanks to the complexity of the antibody maturation process. Therefore, following the identification of such binders by screening of the library produced here, careful optimisation of the binding domains by site-specific mutagenesis, and binding evaluation using surface plasma resonance and ELISA techniques will be required to improve the specificity and affinity of the binders. By modifying key amino acids, binding properties can be optimised. In silico prediction of binding sites might be key in identifying the appropriate amino acids to target.

If whole-cell panning is sufficiently optimised for selecting binders, identifying the antigen will also be necessary. Techniques such as immunofluorescence might be required to confirm the localisation of the antigen in the airway epithelium, and mass spectrometry would allow for the characterisation of these targets. X-ray crystallography could also be considered to resolve the nanobody-antigen binding sites.

Optimisation of nanobody expression and purification systems will also be required to create a reliable pipeline for nanobody production. Other expression systems should be considered: purification of nanobodies from phage expression might be a particularly appropriate method, considering nanobody-presenting phages are produced as part of the panning process

5.4 Conclusion

This work was successful in developing a highly diverse nanobody library, which could be used for the selection of vNAR nanobodies to a wide range of targets. The whole cell panning of disease model airway epithelium was unsuccessful; the flow cytometry data obtained as part of the development of such a model were consistent with results observed in the literature and confirmed the remodelling effect of IL-13 reported previously. A methodology for the chemical synthesis of a functional fluorescent compound for targeted labelling of the C-terminus of nanobodies was also developed, and while conjugation could not be tested due to the unsuccessful production of nanobody proteins, it remains a valid methodology for future work.

In addition to this thesis work, a portion of time of was dedicated to participating in the COVID-19 research effort during the pandemic lockdown. At that time, no lab-based PhD research was allowed within the university but volunteering to support the COVID-19 research effort was permitted. This work is discussed in additional Chapter 6.

Chapter 6 Contribution to the COVID-19 Research Effort

6.1 Introduction

6.1.1 Coronaviruses

Coronaviruses are enveloped, positive-strand RNA viruses of the family *Coronaviridae,* from the order *Nidovirales* and are divided into four genera: *Alphacoronavirus, Betacoronavirus, Gammacoronavirus and Deltacoronavirus* ("Coronaviruses," 2019). Virion particles are spherical to pleomorphic, with a size ranging from 65 to 140 nm in diameter. All coronaviruses possess the same lipid envelope; enclosing three structural proteins: M, S and E. The membrane (M) protein makes up most of the envelope, it is composed of three transmembrane domains and is responsible for organising the assembly of new virions by establishing the viral shape of coronaviruses. The spike (S) protein contains the receptor binding domains that allows viruses to anchor onto the host's cells surface (S1) as well as a fusion domain (S2) which initiates viral entry following S1 receptor binding and cleavage. The smaller envelope (E) multifunctional protein involved in viral assembly. Inside the envelope, a nucleocapsid (N) protein encloses the virus' genetic material by binding to and packaging RNA (Schoeman and Fielding, 2019). The large genome of coronaviruses (26-32 kb) is positive sense, meaning it can act as messenger RNA and be translated into viral proteins by the host's cells. It encodes for the four structural proteins mentioned, as well as two open reading frames which account for two thirds of the genome size: ORF1a and ORF1b. These ORFs encode several proteins involved in virion replication (Sawicki *et al.*, 2007). Accessory proteins unique to each coronavirus are also encode into the genome and can contribute to immune evasion. For example, in SARS-CoV, ORF6 blocks the nuclear import of STAT1 (Signal Transducer and Activator of Transcription 1), a key component of the interferon pathway (Frieman *et al.*, 2007).

Coronaviruses are responsible for a range of diseases in both humans and animals, primarily impacting the respiratory, gastrointestinal, hepatic, and neurological systems. In humans, coronaviruses cause respiratory infections, with symptoms ranging from a simple cold to severe pneumonia requiring hospitalisation. The lethality of coronaviruses varies across strains (Su *et al.*, 2016).

Previously known coronaviruses include the *Betacoronavirus* Severe Acute Respiratory Syndrome Coronavirus 1, or SARS-CoV-1, which originated in China in early 2003. The infection appeared in a Guangdong animal market, spreading to over 30 countries in 8 months, and was distinct from previously known human or animal coronaviruses (Nicholls *et al.*, 2003). A zoonotic origin was speculated, and the virus was detected at nearby farms (Kan *et al.*, 2005; Xu *et al.*, 2004). Later on, bats were identified as the primary reservoir of SARS-CoV-1 (Li *et al.*, 2005). The global death toll of SARS-CoV-1 was 774 deaths out of 8,096 confirmed cases across 29 countries (*SARS : how a global epidemic was stopped*, 2006). This results in a case fatality rate of approximately 9.6%. The outbreak was contained by mid-2003 through public health measures, including isolation, quarantine, and contact tracing. Another notable example of coronavirus is the Middle East Respiratory Coronavirus (from the genus *Betacoronavirus)*, abbreviated to MERS-CoV. Patients presented with a new flu-like respiratory illness in Saudi Arabia in April 2012. The causative pathogen was identified as a novel coronavirus (Zaki *et al.*, 2012). The source of the virus was again linked to bats, with camels as an intermediary (Corman *et al.*, 2014). From April 2012 to date, a total of 2613 laboratory-confirmed cases of MERS-CoV were reported globally, with 957 associated deaths as of July 2025, for a case fatality rate of 36% (“Communicable disease threats report, 28 June - 4 July 2025, week 27,” 2025). The majority of these cases were reported from Saudi Arabia. Finally, endemic human coronaviruses (HCoVs) are coronaviruses that circulate widely in the human population, typically causing mild respiratory illnesses causing symptoms like runny nose, sore throat, cough, and fever, but can be more severe in vulnerable populations such as children, the elderly, or immunocompromised patients. They are a cause of ‘common colds’ and have been with humans for many years (Otieno *et al.*, 2022). *Alphacoronavirus* HCoV-229E was first identified in 1966 and relies on the cellular

receptor Aminopeptidase N (CD13) for viral entry. It is one of the first coronavirus isolated from humans and has been shown to circulate seasonally (Gaunt *et al.*, 2010; Tyrrell and Bynoe, 1966). HCoV-NL36, also a member of the genus *Alphacoronavirus*, was first identified in an infant suffering from bronchiolitis, and is particularly common amongst children (Dijkman *et al.*, 2012; Van Der Hoek *et al.*, 2004). HCoV-OC43 is *Betacoronavirus* closely related to bovine coronavirus BCoV and is hypothesized to have crossed from cattle to human around 1890 (Vijgen *et al.*, 2005). Finally, *Betacoronavirus* HCoV-HKU1 was identified in a patient in Hong Kong in 2005, and has been shown to cause both respiratory and gastrointestinal issues (Woo *et al.*, 2005).

6.1.2 Emergence and Characteristics of SARS-CoV-2

In December 2019, several patients presenting with fever, cough, myalgia or fatigue and pneumonia with abnormal findings on chest computed tomography scans presented to a hospital in Wuhan, China (Huang *et al.*, 2020; Zhu *et al.*, 2020). The virus was rapidly sequenced and identified as a novel coronavirus, later named Severe Acute Respiratory Syndrome Coronavirus 2, abbreviated to SARS-CoV-2, while the disease was termed Coronavirus disease 2019 (COVID-19) (Wu *et al.*, 2020). The virus rapidly spread worldwide, infecting millions within months, and the UK confirmed its first case on 31 January 2020. To date, 778,252,838 cases have been reported to the World Health Organisation, alongside 7,097,572 confirmed deaths as of 22 June 2025 ("WHO COVID-19 dashboard," 2025).

SARS-CoV-2 is a single-stranded positive-sense RNA virus with a genome of approximately 29.9 kb in length. A schematic representation of a SARS-CoV-2 genome and virion can be seen in Figure 6.1. Alongside those 4 proteins, the SARS-CoV-2 genome contains two open reading frames (ORFs) encoding polyproteins. ORF1a encodes two proteases: a chymotrypsin-like (3CL) main protease and a papain-like protease. Both play a role in cleavage and maturation of viral polyproteins (Osipiuk *et al.*, 2021). ORF1b encodes an RNA-dependent polymerase, alongside a helicase, essential for RNA replication and viral proliferation.

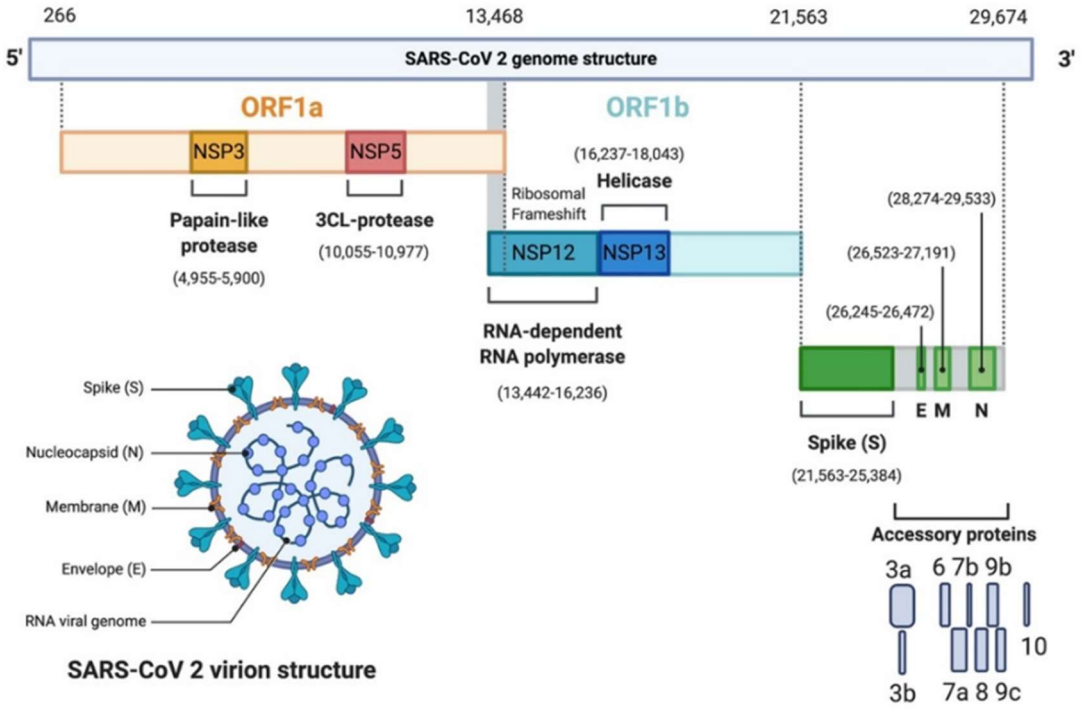


Figure 6.1 Schematic representation of SARS-CoV-2's genome, showing the two ORFs alongside the 4 genes encoding the structural proteins S, E, M and N. A schematic virion structure is also shown.

From Alanagreh, Alzoughool and Atoum (2020). published in Pathogens. © 2022, licensed under CC BY.

SARS-CoV-2 achieves viral entry by binding to the extracellular receptors angiotensin-converting enzyme 2 (ACE2) and transmembrane protease serine 2 (TMPRSS2) through the S1 domain of the spike protein (see Figure 6.2 (1), Shang *et al.*, 2020). Alternative receptors have also been identified, such as CD147 extracellular matrix metalloproteinase inducer (EMMPRIN), on cells with low level of ACE2 expression (Lim *et al.*, 2022). Once inside the cell, the virion sheds its envelope and releases its RNA. The two ORFs are translated into polyproteins subsequently processed into 16 individual Non-Structural Proteins (NSPs) by the two encoded proteases to form the viral replication complex (see Figure 6.2 (2) and (3)). RNA-dependent RNA polymerase synthesises viral RNA (Figure 6.2 (4) and (5)). Viral RNA is then repackaged by the nucleocapsid (N) protein and translocated to the endoplasmic reticulum, before moving to the Golgi apparatus for glycosylation and progression into exocytic vesicles (Figure 6.2 (5) and (6)). The newly created virions

then exit the cell through exocytosis (Kung *et al.*, 2022). The mechanism of infection and replication of SARS-CoV-2 is presented in Figure 6.2.

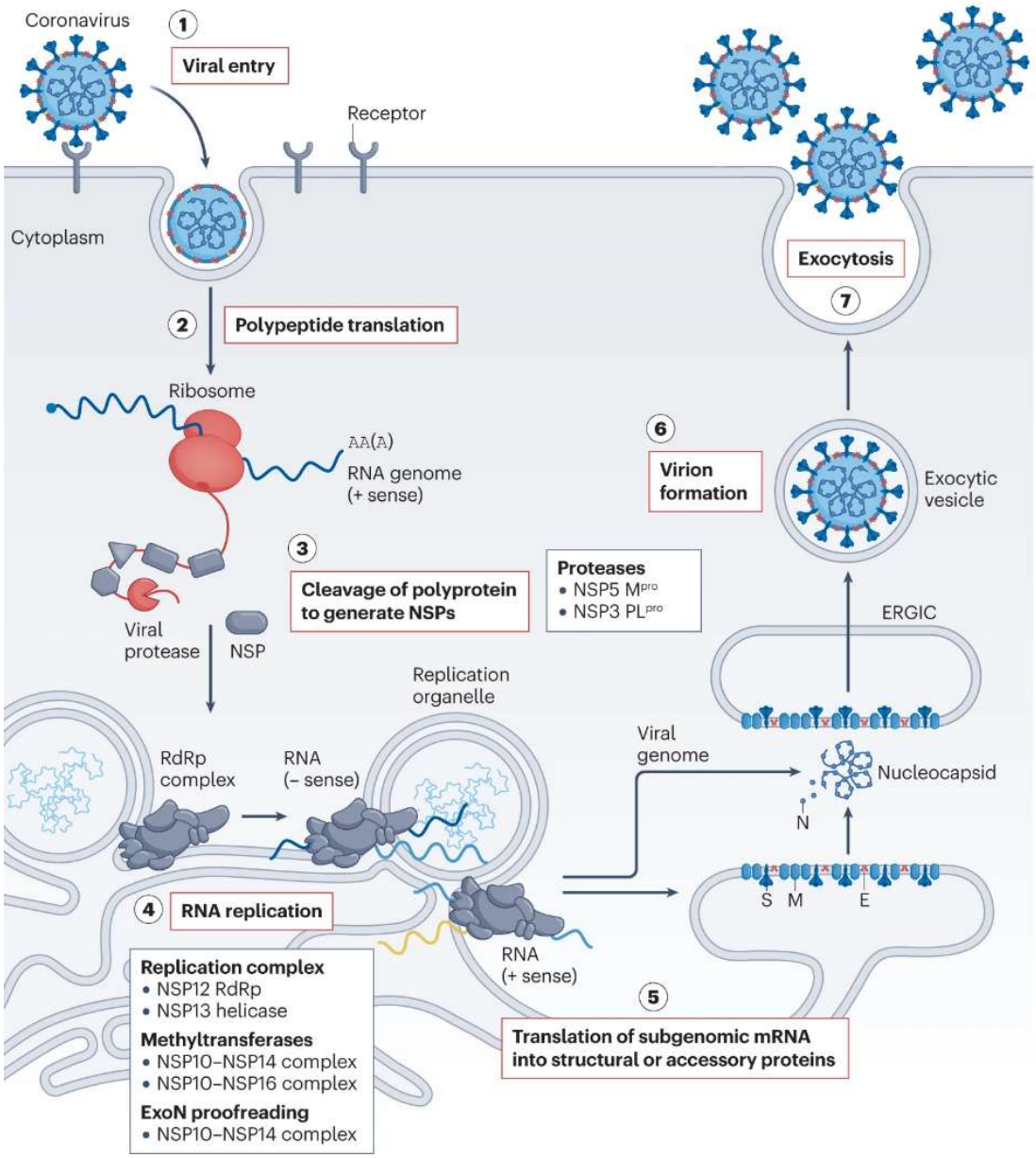


Figure 6.2 SARS-CoV-2 infection and replication mechanism.

(1) The virion enters the cells through endocytosis. (2) Polyproteins are translated and (3) cleaved by proteases. (4) Viral RNA undergoes replication. (5) Structural proteins are translated, and the RNA is repackaged in the endoplasmic reticulum. (6) the virion forms in the Golgi apparatus and is excreted 7° by exocytosis. RdRp: RNA-dependent RNA polymerase; NSP: Non-structural protein; Mpro: main 3CL protease; P: phosphorylation; PLpro: papain-like protease. Adapted from (Shelke et al., 2025). Springer Nature. © 2023. Licensed for use in this thesis through the Copyright Clearance Center.

6.1.3 Clinical Manifestations and Transmission

Patients presenting with symptomatic COVID-19 first experience flu-like symptoms such as headache, fatigue, dry cough, and sore throat. Gastrointestinal symptoms are also relatively common. Anosmia, or loss of smell, has emerged as a distinguishing characteristic of COVID-19, occurring in approximately 55% of infections (Walker *et al.*, 2020). In severe cases, patients developed acute respiratory distress syndrome due to severe interstitial pneumonia, sometimes accompanied by thrombotic and/or cardiac complications (Huang *et al.*, 2020; Jin *et al.*, 2020). Risk factors included advanced age, neutropenia, organ dysfunction, and high fever. Severe cases typically involve preexisting conditions like diabetes, hypertension, and chronic heart disease (Dessie and Zewotir, 2021).

Viral transmission occurred via multiple routes: direct contact, droplets, aerosols, fomite, faecal-oral, blood-borne, and mother-to-child, which greatly facilitated the spread of the virus (Kirubananthan *et al.*, 2021). Additionally, asymptomatic presentations accelerated transmission: asymptomatic patients carried unknowingly a similar upper-respiratory tract viral load as symptomatic patients, accelerating the spread of the disease (Ra *et al.*, 2021; You *et al.*, 2024).

6.1.4 Academic Contribution to the COVID19 Research Effort: The PANTHER Study

COVID-19 had profound implications, causing a global health crisis, economic disruptions, and social challenges, with millions of lives affected (*World Development Report 2022: Finance for an Equitable Recovery*, 2022). Research was critical to understanding the virus's transmission, develop effective treatments, and create vaccines at unprecedented speeds, helping to mitigate its impact.

The PANdemic Tracking of HEalthcare woRkers (PANTHER) team was established in 2020 to contribute to the ongoing research effort with the aim of generating data and knowledge on susceptibility to, immunity from and transmission of Sars-Cov2. Headed by Professor Ben Ollivere, Professor Ana Valdes and Professor Guru Aithal, a study was designed to collect blood samples from healthcare workers

(HCWs) at two Nottingham hospitals: City Hospital and Queen's Medical Centre. Over 600 HCWs volunteered to take part in this study and provided the team with samples and relevant demographic information. Figure 6.3 presents the overall study objectives.

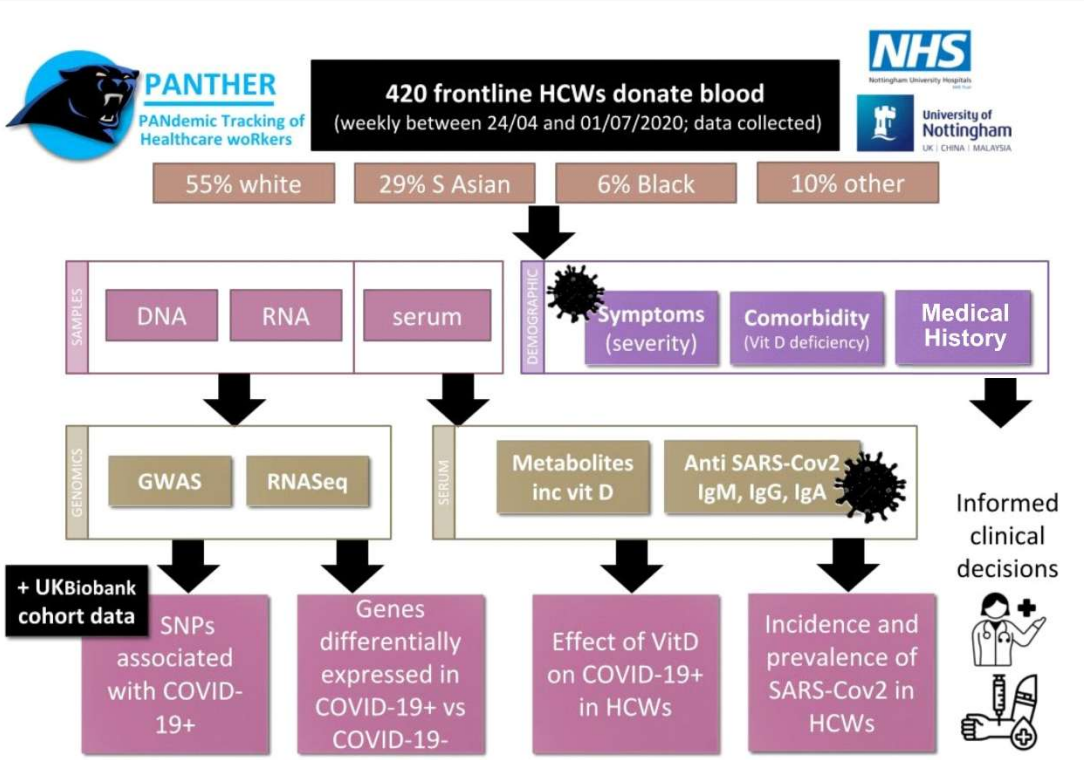


Figure 6.3 PANTHER team study objectives as part of the SARS-CoV-2 COVID19 research effort.

From https://pantherstudy.org.uk/studies-bame/

6.2 Aim, Objectives and Acknowledgements

This chapter reviews and synthesises findings from longitudinal studies to elucidate the long-term effects of COVID-19 on health outcomes, conducted at the University of Nottingham in 2020 and 2021. This work was highly collaborative, and this author's contribution is limited to the processing of serum samples from the Nottingham-based participants, Enzyme-linked immunosorbent assays (ELISAs) and data management, but does not include in-depth data analysis. This work contributed to the publication of the papers below, and key findings from these papers will be presented for context.

6.3 Materials and Methods

6.3.1 Sample Collection and Processing

The PANTHER team recruited 633 healthcare workers (including nurses, doctors, allied health professionals and other frontline health-care workers) from Nottingham City Hospital and Queen's Medical Centre for this study. Written informed consent was obtained, and participants were asked to fill in questionnaires and provide blood samples over a period of 10 weeks between 23 March 2020 and 10 July 2020, under a Human Tissue Authority licence (licence number: 11035). Blood serum samples were immediately spun and stored at -80 °C, before being handed in to this author for processing. Certain participants accessed the Pfizer-BioNTech mRNA vaccine (BNT162b2) early vaccination programme, and vaccination status was also recorded.

Serum samples were aliquoted and deactivated with 1% (v/v) Triton X-100 (Sigma Aldrich, T8787) in a Class II biosafety cabinet to maintain a sterile environment and ensure operator protection. Samples were processed immediately or stored at -20 °C.

6.3.2 Enzyme-Linked Immunosorbent Assays

Procedures below were conducted on liquid-handling Bio-Tec Precision XS (or Precision) six place robots.

Enzyme-linked immunosorbent assays (ELISAs) were designed to test the serum immunoglobulin response of participants to the Covid19 spike protein S1 segment, as well as the nucleocapsid protein. Nunc MaxiSorp 384 well plates were coated with 20 µL SARS-CoV-2 spike protein S1 (Sinobiological, Cat. 40591-V08H), SARS-CoV-2 nucleocapsid protein (Sinobiological, Cat: 40588-V08B), or a combination of both, at 0.5 µg/mL, in carbonate-bicarbonate buffer. Plates were sealed and incubated overnight at 4° C. Plates were then washed three times in PBST (phosphate buffered saline, 0.05% (v/v) Tween 20) using a Wellwash™ Versa Microplate Washer (Thermo Fisher Scientific) immediately blocked with 100 µL of blocking solution (3%

(w/v) skimmed milk powder in PBS, 0.05% (w/v) sodium azide). Plates were again sealed and incubated overnight at 4° C. Inactivated serum samples were diluted to 1:600 in low-cross buffer (Tris-buffered saline, pH 7.4 at 20° C, 300 mM NaCl, 0.1% (v/v) Triton-x100, 5% (v/v) glycerol). Plates were washed 3x in PBST and incubated with 50 µL serum samples in duplicates for 1 hour at room temperatures. Samples from patients with known active infections and either strong, mild or low antibody response were used as positive controls, while serum controls from known uninfected participants were used as negatives, alongside a no-serum blank. At the time, no National Institute for Biological Standards and Control (NIBSC) or World Health Organisation (WHO) serum positives were available as controls. All controls were run in duplicates on each assay plate. Plates were washed 3x in PBST and incubated with 20 µL of either Anti-Human IgG (F_c specific)−Peroxidase antibody (Sigma, A0170), Anti-Human IgA (α-chain specific)−Peroxidase antibody (Sigma, A0295) or Anti-Human IgM (µ-chain specific)−Peroxidase antibody (Sigma, A0420) for 1 hour at room temperature. Plates were washed 3x in PBST and incubated for 20 minutes with 40 µL Ultra-TMB solution (Sigma, T4444) at room temperature in the dark. The reaction was stopped with 40 µL 2N H_2SO_4.

Plates were read at 450 nm on a GloMax® Explorer Microplate reader (Promega). Data were exported to an excel spreadsheet for processing.

6.3.3 Data Analysis

ELISA reads were matched to participants' anonymised number, and stored in excel spreadsheets. To determine seropositivity cutoff, twice the median of the negative controls of the corresponding plate was calculated. The 99th percentile of the negative control was also calculated to identify 'indeterminate' samples. Calculations and plots were generated using GraphPad Prism 10.4.1 (from GraphPad software; available at www.graphpad.com).

6.4 Results and Discussion

For each sample collected, IgG seropositivity was tested against SARS-CoV-2 nucleocapsids and spike protein S1 segment. If the participants showed positivity at any point, then the entire sample set for that patient was tested for IgG, IgA and IgM. Results were collected and plotted, with 2 times the median of negative samples used as a cutoff line for seropositivity. Given the volume of data generated for all 633 participants, representative data from a single participant is presented below to illustrate the research process and findings. Figure 6.4 shows ELISA results for a single participant. While the participant did not display COVID-19 symptoms at the time the samples were taken, seropositivity to nucleocapsid was observed for IgG in weeks 1 to 3, indicating the participant was exposed and/or infected with SARS-CoV-2. Seropositivity to spike protein S1 segment was also observed in week 1 and 2 for IgG and IgA. As this data was collected before any vaccination against the virus could be rolled out, seropositivity could only be a result of direct exposure to SARS-CoV-2.

This data was used as part of further research on SARS-CoV-2. Firstly, seropositivity data were used to understand the impact of ethnicity, job role, socio-economic status, basic demographics, and symptomatic presentation on participants' seropositivity. Secondly, the effect of Human Leukocyte Antigen (HLA) subtypes on patients' immune response was investigated. Finally, seropositivity data prior and post infection and/or vaccination with one or more doses of the Pfizer-BioNTech mRNA vaccine (BNT162b2) were considered.

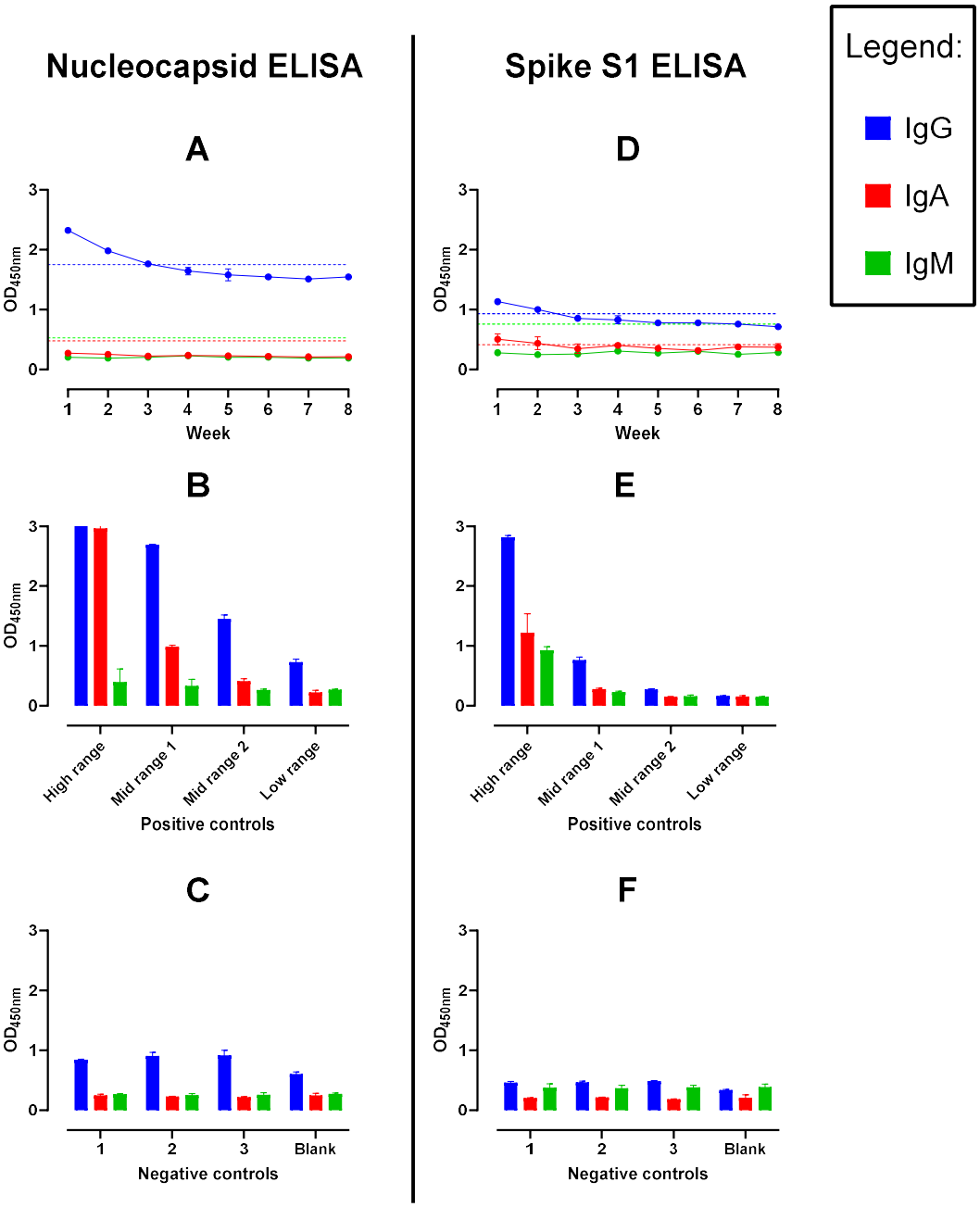


Figure 6.4 Representative data showing weekly samples for a single participant.

ELISAs were used to determine seropositivity of the participant to SARS-CoV-2 nucleocapsids and spike protein S1 segment IgG, IgA and IgM antibodies. A: Seropositivity of the participant to SARS-CoV-2 nucleocapsids: the participant was IgG seropositive in week 1 to 3, with antibody levels dropping below the threshold thereafter. B: Positive controls for SARS-CoV-2 nucleocapsid seropositivity for IgG, IgA and IgM antibodies. C: Negative controls for SARS-CoV-2 nucleocapsid seropositivity for IgG, IgA and IgM antibodies. D: Seropositivity of the participant to SARS-CoV-2 spike protein S1 segment: the participant was IgG seropositive in week 1 and 2, and also showed low-level IgA seropositivity, with antibody levels dropping below the threshold thereafter. E: Positive controls for SARS-CoV-2 spike protein S1 segment seropositivity for IgG, IgA and IgM antibodies. F: Negative controls for SARS-CoV-2 spike protein S1 segment seropositivity for IgG, IgA and IgM antibodies.

6.4.1 Longitudinal Assessment of Symptoms and Risk of SARS-CoV-2 Infection in Healthcare Workers across 5 Hospitals to Understand Ethnic Differences in Infection Risk

Full refence: Valdes, A.M., Moon, J.C., Vijay, A., Chaturvedi, N., Norrish, A., Ikram, A., Craxford, S., Cusin, L.M., Nightingale, J., Semper, A. and Brooks, T., 2021. Longitudinal assessment of symptoms and risk of SARS-CoV-2 infection in healthcare workers across 5 hospitals to understand ethnic differences in infection risk. *EClinicalMedicine*, *34*.

In order to understand the ethnic disparities in SARS-CoV-2 seroprevalence, 1,364 HCWs were recruited across 5 UK hospitals by the PANTHER and COVIDsortium (COVID-Consortium) teams. Early data suggested that the rates of hospitalisation and mortality might vary across ethnic groups. While these disparities were attributed to comorbidities, socio-economic status or healthcare access, the lack of community-wide studies limited the amount of data available. Moreover, inconsistent testing and case reporting limited sample sizes and data accuracy. In order to bridge this gap in the research, HCWs were used as a controlled cohort facing high infection risks to study potential ethnic differences in seroprevalence and disease outcomes.

The study was designed to follow 1,364 HCWs for 13 weeks (London) and 10 weeks (Nottingham), with sample and symptom data collected weekly or biweekly. Demographic data were collected, and the cohort appeared to be predominantly female (71.6%) with an average age of 40.7 years. The participants were primarily white (73.5%), with Asian ethnicities representing the second-largest group (15.1% divided across 9.4% South Asian and 5.7% East Asian), black ethnicities represented the smallest group, with 4.3%, and 2% of participants identified with other or mixed ethnicities. Serological assays (ELISAs) were used to determine seropositivity to SARS-CoV-2 spike S1 segment and nucleocapsid proteins. Seroprevalence was 21.3% in London and 18.2% in Nottingham, with no significant difference between locations.

Logistic regressions were used to identify any associations between seroprevalence and ethnicity, while adjusting for demographic, socio-economic, and occupational factors. Adjusting for these biases allowed for the determination of true correlation between ethnicity and seroprevalence, while mitigating the effects of sex, age, income, geographical disparities and job role. The observed higher seropositivity rate observed in Black HCWs (42%) when compared to White HCWs (19%) was found to be significant, even after adjusting for these cofounders (OR=2.61, p=0.0009), however no similar differences could be observed between Asian HCWs, White HCWs and other/mixed HCWs.

No association between age, sex, body mass index, role or Index of Multiple Deprivation (IMD) and seropositivity was found, but HCWs working in intensive therapy units were less likely to be found seropositive (OR=0.44 95%CI 0.24, 0.77; p=0.0035). A potential explanation for this effect is the priority usage of personal protective equipment.

In conclusion, Black HCWs showed higher SARS-CoV-2 seroprevalence than their White counterparts. This suggests that biological differences in immune response might have an impact on infection susceptibility. Further studies with larger sample sizes and more specific ethnic categories are needed to confirm these findings. Additionally, this cohort faced higher infection risks than the general population due to their occupation, which should be taken into account when

considering these findings. Overall, this study supported the need for further research into ethnic variations in COVID-19 immunity.

6.4.2 HLA-DR Polymorphism in SARS-CoV-2 Infection and Susceptibility to Symptomatic COVID-19.

Full reference: Astbury, S., Reynolds, C.J., Butler, D.K., Muñoz-Sandoval, D.C., Lin, K.M., Pieper, F.P., Otter, A., Kouraki, A., Cusin, L., Nightingale, J. and Vijay, A., 2022. HLA-DR polymorphism in SARS-CoV-2 infection and susceptibility to symptomatic COVID-19. *Immunology*, *166*(1), pp.68-77.

The same cohort of 1,364 HCWs was used to investigate the potential links between human leukocyte antigen (HLA) class II polymorphisms and the immune response to and infection rates of SARS-CoV-2. The HCWs were genotyped using the Illumina Infinium Global Screening Array and HLA alleles were imputed using the HLA Genotype Imputation with Attribute Bagging (HIBAG). Seroprevalence was determined using the previously described ELISAs to the spike protein S1 segment and nucleocapsid protein detecting IgG. T cell ELISpot assays were used for T-cell response analysis using participants peripheral blood mononuclear cells and serum.

No population-level effects of HLA polymorphism in SARS-CoV-2 seroprevalence could be ascertained. However, participants carrying HLA-DRB1*13:02 were more likely to report symptoms of COVID-19 (OR = 6·74, 95% confidence interval 2·03–22·31; P = 0·002), indicating a potential genetic predisposition influencing disease severity. However, no link between DRB1 alleles and anti-spike serology could be established. Lower T-cell responses to the nucleocapsid protein were observed in HLA-DRB1*15:02 carrier, but these findings were not significant, likely due to the lower sample size used. Following vaccination, HLA DRB1*15:01 was associated with increased spike T-cell responses after a first dose of the Pfizer-BioNTech mRNA vaccine (BNT162b2) (p=0.0026) but a similar effect was not observed after the second dose.

In conclusion, HLA class II polymorphisms, particularly HLA-DRB1*13:02, influence the likelihood of symptomatic COVID-19, and HLA-DRB1*15:01 enhances T-cell responses to spike protein post-vaccination. Although a large number of participants took part in the study, the limited diversity of HLA alleles restricted discovery. Further studies are needed to fully understand the role of host genetics in the outcomes in SARS-CoV-2 infection and vaccination.

6.4.3 Two Doses of the SARS-CoV-2 BNT162b2 Vaccine Enhance Antibody Responses to Variants in Individuals with Prior SARS-CoV-2 Infection

Full reference: Urbanowicz, R.A., Tsoleridis, T., Jackson, H.J., Cusin, L., Duncan, J.D., Chappell, J.G., Tarr, A.W., Nightingale, J., Norrish, A.R., Ikram, A. and Marson, B., 2021. Two doses of the SARS-CoV-2 BNT162b2 vaccine enhance antibody responses to variants in individuals with prior SARS-CoV-2 infection. *Science translational medicine*, *13*(609), p.eabj0847.

Following the distribution of vaccines against SARS-CoV-2, rates of infection, morbidity and mortality of COVID19 were reduced. Uncertainty remained over the protective effects of such vaccines against newly emerged variants. This study aimed to investigate whether repeated antigenic exposure, through natural infection or vaccination with the Pfizer-BioNTech mRNA vaccine (BNT162b2) enhanced antibody potency against SARS-CoV-2 variants. Four variants were considered, the initial lineage A from Wuhan, B.1, B.1.351 (or β variant) first reported in South Africa, and the P.1 (or γ variant) first identified in Brazil. The data collected by the PANTHER team was used to select 45 individuals who received both doses of the BNT162b2 vaccine with complete serology, of which 25 had no history of prior infection with SARS-CoV-2, and 20 tested positive either on a polymerase chain reaction (PCR) or serological test. There were no differences in age or body mass index amongst selected participants, but the group was 80% female.

ELISAs for spike protein IgG were used to determine the concentration of antibodies specific to lineages A, B.1 and B.1.351. Antibody concentration was shown to be higher in individuals who had prior infection with SARS-CoV-2 after a first dose of vaccines ($p<0.0001$, $p<0.001$, and $p<0.0001$ respectively). No significant difference could be observed between the naïve and prior infection group after two doses of vaccine. However, antibody titres showed that individuals with a history of prior infection had a higher median effective concentration (EC50) antibody titre against the S1 region of the spike protein than naïve individuals after two doses of vaccine ($p = 0.0034$). Antibody titres against the receptor binding domain (RBD) revealed no significant difference between the two groups after two doses of the vaccine, indicating that epitopes outside of the RBD are responsible for the antibody response.

Virus neutralisation assays were used to determine whether participants antibody levels were sufficient to neutralise infection across all three variants. Past infection resulted in an increased neutralisation potency variants A, B1.1.351 and P.1 ($p = 0.0008$, $p = 0.0019$ and $p = 0.0074$, respectively). However, neutralisation against lineage A was significantly higher than against lineage B.1.351 ($P = 0.0345$) and P.1 ($P = 0.0302$), but this was not the case for individuals with a history of prior infection.

The study focused on a specific cohort (mostly female healthcare workers) and used an extended vaccine dosing interval (10–12 weeks), which may differ from other populations and dosing schedules. Analysis was limited to IgG antibody responses, without exploring T cells or broader immune responses. Variants such as B.1.617.2 (δ variant first recorded India) were not studied, necessitating further research on emerging strains.

In conclusion, repeated antigenic exposure, via infection or vaccination, enhances antibody responses against SARS-CoV-2 and its variants. Further studies are necessary to consider variants such as δ (B.1.617.2), as well as other immunoglobulins responses, such as IgA or IgM. This study showed that booster vaccinations are pivotal in maintaining broad and potent immunity, particularly as new variants emerge.

6.5 Conclusion

These studies showed that leveraging samples from healthcare workers is highly relevant to the study of new emerging infections. HCWs provided a large cohort of participants that could be easily and repeatedly accessed by researchers and generated a large amount of data that contributed to enhancing the knowledge base of the ongoing pandemic. These studies discussed the role of ethnicity, HLA subtype and prior infection in serological response to SARS-CoV-2 infection and contributed to the global research effort by providing key insights into SARS-CoV-2 immunology.

References

Abe, M., Goto, T., Kosaka, M., Wolfenbarger, D., Weiss, D.T., Solomon, A., 2001. Differences in kappa to lambda (κ:λ) ratios of serum and urinary free light chains. Clin. Exp. Immunol. 111, 457–462. https://doi.org/10.1046/j.1365-2249.1998.00487.x

Adeloye, D., Chua, S., Lee, C., Basquill, C., Papana, A., Theodoratou, E., Nair, H., Gasevic, D., Sridhar, D., Campbell, H., Chan, K.Y., Sheikh, A., Rudan, I., 2015. Global and regional estimates of COPD prevalence: Systematic review and meta-analysis. J. Glob. Health 5. https://doi.org/10.7189/jogh.05.020415

Adler, K.B., Tuvim, M.J., Dickey, B.F., 2013. Regulated mucin secretion from airway epithelial cells. Front. Endocrinol. 4, 1–9. https://doi.org/10.3389/fendo.2013.00129

Alanagreh, L., Alzoughool, F., Atoum, M., 2020. The human coronavirus disease covid-19: Its origin, characteristics, and insights into potential drugs and its mechanisms. Pathogens 9. https://doi.org/10.3390/pathogens9050331

Aldini, G., Altomare, A., Baron, G., Vistoli, G., Carini, M., Borsani, L., Sergio, F., 2018. N-Acetylcysteine as an antioxidant and disulphide breaking agent: the reasons why. Free Radic. Res. 52, 751–762. https://doi.org/10.1080/10715762.2018.1468564

Alevy, Y.G., Patel, A.C., Romero, A.G., Patel, D.A., Tucker, J., Roswit, W.T., Miller, C.A., Heier, R.F., Byers, D.E., Brett, T.J., Holtzman, M.J., 2012. IL-13-induced airway mucus production is attenuated by MAPK13 inhibition. J. Clin. Invest. 122, 4555–4568. https://doi.org/10.1172/JCI64896

Alfaleh, M.A., Alsaab, H.O., Mahmoud, A.B., Alkayyal, A.A., Jones, M.L., Mahler, S.M., Hashem, A.M., 2020. Phage Display Derived Monoclonal Antibodies: From Bench to Bedside. Front. Immunol. 11. https://doi.org/10.3389/fimmu.2020.01986

Alley, S.C., Okeley, N.M., Senter, P.D., 2010. Antibody-drug conjugates: targeted drug delivery for cancer. Curr. Opin. Chem. Biol. 14, 529–537. https://doi.org/10.1016/j.cbpa.2010.06.170

Almagro, J.C., Pedraza-Escalona, M., Arrieta, H.I., Pérez-Tapia, S.M., 2019. Phage display libraries for antibody therapeutic discovery and development. Antibodies 8. https://doi.org/10.3390/antib8030044

Amrein, P.C., Stossel, T.P., 1980. Prevention of Degradation of Human Polymorphonuclear Leukocyte Proteins by Diisopropylfluorophosphate.

Andersen, D.H., 1938. Cystic Fibrosis Of The Pancreas And Its Relation To Celiac Disease. Am. J. Dis. Child. 56, 344–344. https://doi.org/10.1001/archpedi.1938.01980140114013

Andrew, S., 2010. FastQC: a quality control tool for high throughput sequence data (version 0.12.1). Babraham Inst. Camb.

Arbabi Ghahroudi, M., Desmyter, A., Wyns, L., Hamers, R., Muyldermans, S., 1997. Selection and identification of single domain antibody fragments from camel heavy-chain antibodies. FEBS Lett. 414, 521–526. https://doi.org/10.1016/S0014-5793(97)01062-4

Baek, H., 2002. An improved helper phage system for efficient isolation of specific antibody molecules in phage display. Nucleic Acids Res. 30, 18e–118. https://doi.org/10.1093/nar/30.5.e18

Barderas, R., Benito-Peña, E., 2019. The 2018 Nobel Prize in Chemistry: phage display of peptides and antibodies. Anal. Bioanal. Chem. 411, 2475–2479. https://doi.org/10.1007/S00216-019-01714-4/FIGURES/2

Barelle, C., Porter, A., 2015. VNARs: An Ancient and Unique Repertoire of Molecules That Deliver Small, Soluble, Stable and High Affinity Binders of Proteins. Antibodies 4, 240–258. https://doi.org/10.3390/antib4030240

Barnes, P.J., 2013. Theophylline. Am. J. Respir. Crit. Care Med. 188, 901–906. https://doi.org/10.1164/rccm.201302-0388PP

Beck, A., Wurch, T., Bailly, C., Corvaia, N., 2010. Strategies and challenges for the next generation of therapeutic antibodies. Nat. Rev. Immunol. 10, 345–352. https://doi.org/10.1038/nri2747

Beggs, J.D., 1978. Transformation of yeast by a replicating hybrid plasmid. Nature 275, 104–109. https://doi.org/10.1038/275104a0

Bell, A.;, Wang, Z.J.;, Arbabi-Ghahroudi, M.;, Chang, T.A.;, Durocher, Y.;, Trojahn, U.;, Baardsnes, J.;, Jaramillo, M.L.;, Li, S.;, Baral, T.N.;, O'Connor-McCourt, M.;, Mackenzie, R.;, Zhang, J., 2010. Differential tumor-targeting abilities of three single-domain antibody formats. Cancer Lett. 289, 81–90. https://doi.org/10.1016/j.canlet.2009.08.003

Benatuil, L., Perez, J.M., Belk, J., Hsieh, C.-M., 2010. An improved yeast transformation method for the generation of very large human antibody libraries. Protein Eng. Des. Sel. PEDS 23, 155–9. https://doi.org/10.1093/protein/gzq002

Benedek, T.G., 2011. History of the development of corticosteroid therapy. Clin. Exp. Rheumatol. 29, S-12.

Bennett, W.D., Henderson, A.G., Donaldson, S.H., 2016. Hydrator therapies for chronic bronchitis: Lessons from cystic fibrosis. Ann. Am. Thorac. Soc. 13, S186–S190. https://doi.org/10.1513/AnnalsATS.201509-652KV

Bessette, P.H., Rice, J.J., Daugherty, P.S., 2004. Rapid isolation of high-affinity protein binding peptides using bacterial display. Protein Eng. Des. Sel. PEDS 17, 731–9. https://doi.org/10.1093/protein/gzh084

Birch, J.R., Racher, A.J., 2006. Antibody production. Adv. Drug Deliv. Rev. 58, 671–685. https://doi.org/10.1016/j.addr.2005.12.006

Bjerrum, O.J., Schafer-Nielsen, C., 1986. Buffer systems and transfer parameters for semi dry electroblotting with a horizontal apparatus, in: Dunn, M.J. (Ed.), . Presented at the Proceedings of the Fifth Meeting of the International Electrophoresis Society, Verlag Chemie, Verlagsgesellschaft, Weinheim, FRG, pp. 315–327.

Boder, E.T., Wittrup, K.D., 1997. Yeast surface display for screening combinatorial polypeptide libraries. Nat. Biotechnol. 15, 553–557. https://doi.org/10.1038/nbt0697-553

Boekhout, A.H., Beijnen, J.H., Schellens, J.H.M., 2011. Trastuzumab. The Oncologist 16, 800–810. https://doi.org/10.1634/theoncologist.2010-0035

Bonser, L.R., Koh, K.D., Johansson, K., Choksi, S.P., Cheng, D., Liu, L., Sun, D.I., Zlock, L.T., Eckalbar, W.L., Finkbeiner, W.E., Erle, D.J., 2021. Flow-Cytometric Analysis and Purification of Airway Epithelial-Cell Subsets. Am. J. Respir. Cell Mol. Biol. 64, 308–317. https://doi.org/10.1165/rcmb.2020-0149MA

Bossi, L., 1983. Context effects: Translation of UAG codon by suppressor tRNA is affected by the sequence following UAG in the message. J. Mol. Biol. 164, 73–87. https://doi.org/10.1016/0022-2836(83)90088-8

Bourdin, A., Burgel, P.-R.R., Chanez, P., Garcia, G., Perez, T., Roche, N., 2009. Recent advances in COPD: pathophysiology, respiratory physiology and clinical aspects, including comorbidities. Eur. Respir. Rev. 18, 198–212. https://doi.org/10.1183/09059180.00005509

Bowers, P.M., Horlick, R.A., Kehry, M.R., Neben, T.Y., Tomlinson, G.L., Altobell, L., Zhang, X., Macomber, J.L., Krapf, I.P., Wu, B.F., McConnell, A.D., Chau, B., Berkebile, A.D., Hare, E., Verdino, P., King, D.J., 2014. Mammalian cell display for the discovery and optimization of antibody therapeutics. Methods San Diego Calif 65, 44–56. https://doi.org/10.1016/j.ymeth.2013.06.010

Bragg, P.D., Hou, C., 1975. Subunit composition, function, and spatial arrangement in the Ca2+- and Mg2+-activated adenosine triphosphatases of Escherichia coli and Salmonella typhimurium. Arch. Biochem. Biophys. 167, 311–321. https://doi.org/10.1016/0003-9861(75)90467-1

Brake, A.J., Merryweather, J.P., Coit, D.G., Heberlein, U.A., Masiarz, F.R., Mullenbach, G.T., Urdea, M.S., Valenzuela, P., Barr, P.J., 1984. Alpha-factor-directed synthesis and secretion of mature foreign proteins in Saccharomyces cerevisiae. Proc. Natl. Acad. Sci. 81, 4642–4646. https://doi.org/10.1073/pnas.81.15.4642

Bravo, D.T., Soudry, E., Edward, J.A., Le, W., Nguyen, A.L., Hwang, P.H., Sanyal, M., Nayak, J.V., 2013. Characterization of human upper airway epithelial progenitors. Int. Forum Allergy Rhinol. 3, 841–847. https://doi.org/10.1002/alr.21205

Breitling, F., Broders, O., Helmsing, S., Hust, M., Dübel, S., 2010. Improving Phage Display Throughput by Using Hyperphage, Miniaturized Titration and pVIII (g8p) ELISA. Antib. Eng. 197–206. https://doi.org/10.1007/978-3-642-01144-3_14

Breitling, F., Dübel, S., Seehaus, T., Klewinghaus, I., Little, M., 1991. A surface expression vector for antibody screening. Gene 104, 147–153. https://doi.org/10.1016/0378-1119(91)90244-6

Bush, A., Floto, R.A., 2019. Pathophysiology, causes and genetics of paediatric and adult bronchiectasis. Respirology 24, 1053–1062. https://doi.org/10.1111/resp.13509

Cabanillas-Bernal, O., Dueñas, S., Ayala-Avila, M., Rucavado, A., Escalante, T., Licea-Navarro, A.F., 2019. Synthetic libraries of shark vNAR domains with different cysteine numbers within the CDR3. PLoS ONE 14. https://doi.org/10.1371/journal.pone.0213394

Carbajal, M., Teneback, C.C., 2022. Environmental and Infectious Causes of Bronchiectasis. pp. 85–115. https://doi.org/10.1007/978-3-031-12926-1_4

Carpino, L.A., Han, G.Y., 1970. 9-Fluorenylmethoxycarbonyl function, a new base-sensitive amino-protecting group. J. Am. Chem. Soc. 92, 5748–5749. https://doi.org/10.1021/ja00722a043

Castelli, M.S., McGonigle, P., Hornby, P.J., 2019. The pharmacology and therapeutic applications of monoclonal antibodies. Pharmacol. Res. Perspect. 7. https://doi.org/10.1002/prp2.535

Chalmers, J.D., 2018. New Insights Into the Epidemiology of Bronchiectasis. Chest 154, 1272–1273. https://doi.org/10.1016/j.chest.2018.08.1051

Chalmers, J.D., Chang, A.B., Chotirmall, S.H., Dhar, R., McShane, P.J., 2018. Bronchiectasis. Nat. Rev. Dis. Primer 4, 45–45. https://doi.org/10.1038/s41572-018-0042-3

Chasteen, L., Ayriss, J., Pavlik, P., Bradbury, A.R.M., 2006. Eliminating helper phage from phage display. Nucleic Acids Res. 34. https://doi.org/10.1093/nar/gkl772

Chen, L., Wang, T., Zhang, J.Y., Zhang, S.F., Liu, D.S., Xu, D., Wang, X., Chen, Y.J., Wen, F.Q., 2009. Toll-like Receptor 4 Relates to Lipopolysaccharide-induced Mucus Hypersecretion in Rat Airway. Arch. Med. Res. 40, 10–17. https://doi.org/10.1016/j.arcmed.2008.10.005

Chen, S.-H., Prakash, S., Helgason, E., Gilchrist, C.L., Kenner, L.R., Srinivasan, R., Sterne-Weiler, T., Hafner, M., Piskol, R., Dueber, E.C., Hamidi, H., Endres, N., Ye, X., Fairbrother, W.J., Wertz, I.E., 2023. Constitutive protein degradation induces acute cell death via proteolysis products. bioRxiv 2023.02.06.527237-2023.02.06.527237. https://doi.org/10.1101/2023.02.06.527237

Cherf, G.M., Cochran, J.R., 2015. Applications of yeast surface display for protein engineering. Methods Mol. Biol. 1319, 155–175. https://doi.org/10.1007/978-1-4939-2748-7_8

Cohen, S.N., Chang, A.C.Y., Boyer, H.W., Helling, R.B., 1973. Construction of biologically functional bacterial plasmids in vitro. Proc. Natl. Acad. Sci. U. S. A. 70, 3240–3244. https://doi.org/10.1073/pnas.70.11.3240

Coin, I., Beyermann, M., Bienert, M., 2007. Solid-phase peptide synthesis: From standard procedures to the synthesis of difficult sequences. Nat. Protoc. 2, 3247–3256. https://doi.org/10.1038/nprot.2007.454

Communicable disease threats report, 28 June - 4 July 2025, week 27 [WWW Document], 2025. URL https://www.ecdc.europa.eu/en/publications-data/communicable-disease-threats-report-28-june-4-july-2025-week-27 (accessed 7.8.25).

Cooney, A.L., McCray, P.B., Sinn, P.L., 2018. Cystic Fibrosis Gene Therapy: Looking Back, Looking Forward. Genes 9, 538–538. https://doi.org/10.3390/genes9110538

Corman, V.M., Ithete, N.L., Richards, L.R., Schoeman, M.C., Preiser, W., Drosten, C., Drexler, J.F., 2014. Rooting the Phylogenetic Tree of Middle East Respiratory Syndrome Coronavirus by Characterization of a Conspecific Virus from an African Bat. J. Virol. 88, 11297–11303. https://doi.org/10.1128/jvi.01498-14

Coronaviruses: General Features (Coronaviridae), 2019. , in: Encyclopedia of Virology. Elsevier, pp. 193–197. https://doi.org/10.1016/b978-0-12-814515-9.00139-9

Cummins, E., Luxenberg, D.P., McAleese, F., Widom, A., Fennell, B.J., Darmanin-Sheehan, A., Whitters, M.J., Bloom, L., Gill, D., Cunningham, O., 2008. A simple high-throughput purification method for hit identification in protein screening. J. Immunol. Methods 339, 38–46. https://doi.org/10.1016/j.jim.2008.07.016

Cystic Fibrosis Worldwide, 2020. What is Cystic Fibrosis?

Daraee, H., Etemadi, A., Kouhi, M., Alimirzalu, S., Akbarzadeh, A., 2016. Application of liposomes in medicine and drug delivery. Artif. Cells Nanomedicine Biotechnol. 44, 381–391. https://doi.org/10.3109/21691401.2014.953633

Davanloo, P., Rosenberg, A.H., Dunn, J.J., Studier, F.W., 1984. Cloning and expression of the gene for bacteriophage T7 RNA polymerase. Proc. Natl. Acad. Sci. U. S. A. 81, 2035–2039. https://doi.org/10.1073/pnas.81.7.2035

David Row, R., Roark, T.J., Philip, M.C., Perkins, L.L., Antos, J.M., 2015. Enhancing the efficiency of sortase-mediated ligations through nickel-peptide complex formation. Chem. Commun. 51, 12548–12551. https://doi.org/10.1039/c5cc04657b

Davis, J.D., Wypych, T.P., 2021. Cellular and functional heterogeneity of the airway epithelium. Mucosal Immunol. 14, 978–990. https://doi.org/10.1038/s41385-020-00370-7

de Beer, M.A., Giepmans, B.N.G., 2020. Nanobody-Based Probes for Subcellular Protein Identification and Visualization. Front. Cell. Neurosci. 14, 1–16. https://doi.org/10.3389/fncel.2020.573278

Deprez, M., Zaragosi, L.-E., Truchi, M., Becavin, C., Ruiz García, S., Arguel, M.-J., Plaisant, M., Magnone, V., Lebrigand, K., Abelanet, S., Brau, F., Paquet, A., Pe'er, D., Marquette, C.-H., Leroy, S., Barbry, P., 2020. A Single-Cell Atlas of the Human Healthy Airways. Am. J. Respir. Crit. Care Med. 202, 1636–1645. https://doi.org/10.1164/rccm.201911-2199OC

Desmyter, A., Transue, T.R., Ghahroudi, M.A., Dao Thi, M.-H., Poortmans, F., Hamers, R., Muyldermans, S., Wyns, L., Thi, M.H.D., Poortmans, F., Hamers, R., Muyldermans, S., Wyns, L., 1996. Crystal structure of a camel single-domain V(H) antibody fragment in complex with lysozyme. Nat. Struct. Mol. Biol. 3, 803–811. https://doi.org/10.1038/nsb0996-803

Dessie, Z.G., Zewotir, T., 2021. Mortality-related risk factors of COVID-19: a systematic review and meta-analysis of 42 studies and 423,117 patients. BMC Infect. Dis. 21. https://doi.org/10.1186/s12879-021-06536-3

Detalle, L., Stohr, T., Palomo, C., Piedra, P.A., Gilbert, B.E., Mas, V., Millar, A., Power, U.F., Stortelers, C., Allosery, K., Melero, J.A., Depla, E., 2016. Generation and Characterization of ALX-0171, a Potent Novel Therapeutic Nanobody for the Treatment of Respiratory Syncytial Virus Infection. Antimicrob. Agents Chemother. 60, 6–13. https://doi.org/10.1128/AAC.01802-15

Dhayalan, B., Mandal, K., Rege, N., Weiss, M.A., Eitel, S.H., Meier, T., Schoenleber, R.O., Kent, S.B.H., 2017. Scope and Limitations of Fmoc Chemistry SPPS-Based Approaches to the Total Synthesis of Insulin Lispro via Ester Insulin. Chem. – Eur. J. 23, 1709–1716. https://doi.org/10.1002/chem.201605578

Diaz, M., Greenberg, A.S., Flajnik, M.F., 1998. Somatic hypermutation of the new antigen receptor gene (*NAR*) in the nurse shark does not generate the repertoire: Possible role in antigen-driven reactions in the absence of germinal centers. Proc. Natl. Acad. Sci. 95, 14343–14348. https://doi.org/10.1073/pnas.95.24.14343

Diaz, M., Stanfield, R.L., Greenberg, A.S., Flajnik, M.F., 2002. Structural analysis, selection, and ontogeny of the shark new antigen receptor (IgNAR): identification of a new locus preferentially expressed in early development. Immunogenetics 54, 501–512. https://doi.org/10.1007/s00251-002-0479-z

Dijkman, R., Jebbink, M.F., Gaunt, E., Rossen, J.W.A., Templeton, K.E., Kuijpers, T.W., Van Der Hoek, L., 2012. The dominance of human coronavirus OC43 and NL63 infections in infants. J. Clin. Virol. 53, 135–139. https://doi.org/10.1016/j.jcv.2011.11.011

Dooley, H., Flajnik, M.F., Porter, A.J., 2003. Selection and characterization of naturally occurring single-domain (IgNAR) antibody fragments from immunized sharks by phage display. Mol. Immunol. 40, 25–33. https://doi.org/10.1016/S0161-5890(03)00084-1

Drulis-Kawa, Z., Dorotkiewicz-Jach, A., 2010. Liposomes as delivery systems for antibiotics. Int. J. Pharm. 387, 187–198. https://doi.org/10.1016/j.ijpharm.2009.11.033

Duclos, G.E., Teixeira, V.H., Autissier, P., Gesthalter, Y.B., Reinders-Luinge, M.A., Terrano, R., Dumas, Y.M., Liu, G., Mazzilli, S.A., Brandsma, C.-A., Van Den Berge, M., Janes, S.M., Timens, W., Lenburg, M.E., Spira, A., Campbell, J.D., Beane, J., 2019. Characterizing smoking-induced transcriptional heterogeneity in the human bronchial epithelium at single-cell resolution, Sci. Adv.

Dumoulin, M., Conrath, K., Van Meirhaeghe, A., Meersman, F., Heremans, K., Frenken, L.G.J., Muyldermans, S., Wyns, L., Matagne, A., 2009. Single-domain antibody fragments with high conformational stability. Protein Sci. 11, 500–515. https://doi.org/10.1110/ps.34602

Ehrlich, P., 1910. Anwendung und wirkung von salvarsan. Dtsch Med Wochenschr 2437–2438.

Ellwood, P., Asher, M.I., Billo, N.E., Bissell, K., Chiang, C.Y., Ellwood, E.M., El-Sony, A., García-Marcos, L., Mallol, J., Marks, G.B., Pearce, N.E., Strachan, D.P., 2017. The Global Asthma Network rationale and methods for Phase I global surveillance: prevalence, severity, management and risk factors. Eur. Respir. J. 49. https://doi.org/10.1183/13993003.01605-2016

Eubel, H., Braun, H.-P., Millar, Ah., 2005. Blue-native PAGE in plants: a tool in analysis of protein-protein interactions. Plant Methods 1, 11–11. https://doi.org/10.1186/1746-4811-1-11

Ewing, B., Green, P., 1998. Base-Calling of Automated Sequencer Traces Using Phred. II. Error Probabilities. Genome Res. 8, 186–194. https://doi.org/10.1101/GR.8.3.186

Ewing, B., Hillier, L.D., Wendl, M.C., Green, P., 1998. Base-Calling of Automated Sequencer Traces Using Phred. I. Accuracy Assessment. Genome Res. 8, 175–185. https://doi.org/10.1101/GR.8.3.175

Fahy, J.V., Dickey, B.F., Francisco, S., 2010. Airway Mucus Function and Dysfunction. New-Engl. J. Med. 363, 2233–2247. https://doi.org/10.1056/NEJMra0910061

Fanen, P., Wohlhuter-Haddad, A., Hinzpeter, A., 2014. Genetics of cystic fibrosis: CFTR mutation classifications toward genotype-based CF therapies. Int. J. Biochem. Cell Biol. 52, 94–102. https://doi.org/10.1016/j.biocel.2014.02.023

Fantini, M., Pandolfini, L., Lisi, S., Chirichella, M., Arisi, I., Terrigno, M., Goracci, M., Cremisi, F., Cattaneo, A., 2017. Assessment of antibody library diversity through next generation sequencing and technical error compensation. PLoS ONE 12(5). https://doi.org/10.1371/journal.pone.0177574

Fay, F., Scott, C.J., 2011. Antibody-targeted nanoparticles for cancer therapy. Immunotherapy 3, 381–394. https://doi.org/10.2217/imt.11.5

Feng, M., Bian, H., Wu, X., Fu, T., Fu, Y., Hong, J., Fleming, B.D., Flajnik, M.F., Ho, M., 2018. Construction and next-generation sequencing analysis of a large phage-displayed VNARsingle-domain antibody library from six naïve nurse sharks. Antib. Ther. 1, 1–11. https://doi.org/10.1093/abt/tby011

Fernández-Quintero, M.L., Seidler, C.A., Quoika, P.K., Liedl, K.R., 2021. Shark Antibody Variable Domains Rigidify Upon Affinity Maturation—Understanding the Potential of Shark Immunoglobulins as Therapeutics. Front. Mol. Biosci. 8. https://doi.org/10.3389/fmolb.2021.639166

Frieman, M., Yount, B., Heise, M., Kopecky-Bromberg, S.A., Palese, P., Baric, R.S., 2007. Severe acute respiratory syndrome coronavirus ORF6 antagonizes STAT1 function by sequestering nuclear import factors on the rough endoplasmic reticulum/Golgi membrane. J. Virol. 81, 9812–9824. https://doi.org/10.1128/JVI.01012-07

Fu, K., Wu, H., Su, Z., 2021. Self-assembling peptide-based hydrogels: Fabrication, properties, and applications. Biotechnol. Adv. 49, 107752. https://doi.org/10.1016/j.biotechadv.2021.107752

Fujisawa, T., Ide, K., Holtzman, M.J., Suda, T., Suzuki, K., Kuroishi, S., Chida, K., Nakamura, H., 2008. Involvement of the p38 MAPK pathway in IL-13-induced mucous cell metaplasia in mouse tracheal epithelial cells. Respirology 13, 191–202. https://doi.org/10.1111/j.1440-1843.2008.01237.x

Gainkam, L.O.T., Huang, L., Caveliers, V., Keyaerts, M., Hernot, S., Vaneycken, I., Vanhove, C., Revets, H., De Baetselier, P., Lahoutte, T., 2008. Comparison of the Biodistribution and Tumor Targeting of Two 99m Tc-Labeled Anti-EGFR Nanobodies in Mice, Using Pinhole SPECT/Micro-CT. J. Nucl. Med. • 49, 788–795. https://doi.org/10.2967/jnumed.107.048538

Garner, M.M., Chrambach, A., 1992. Resolution of circular, nicked circular and linear DNA, 4.4 kb in length, by electrophoresis in polyacrylamide solutions. ELECTROPHORESIS 13, 176–178. https://doi.org/10.1002/elps.1150130136

Gasteiger, E., Hoogland, C., Gattiker, A., Duvaud, S., Wilkins, M.R., Appel, R.D., Bairoch, A., 2005. Protein Identification and Analysis Tools on the Expasy Server, in: Walker, J.M. (Ed.), The Proteomics Protocols Handbook. pp. 561–607.

Gaunt, E.R., Hardie, A., Claas, E.C.J., Simmonds, P., Templeton, K.E., 2010. Epidemiology and Clinical Presentations of the Four Human Coronaviruses 229E, HKU1, NL63, and OC43 Detected over 3 Years Using a Novel Multiplex Real-Time PCR Method. J. Clin. Microbiol. 48, 2940–2947. https://doi.org/10.1128/jcm.00636-10

Geisse, S., Kocher, H.P., 1999. Protein expression in mammalian and insect cell systems, in: Methods in Enzymology. pp. 19–42. https://doi.org/10.1016/S0076-6879(99)06004-8

Gould-Fogerite, S., Kheiri, M.T., Zhang, F., Wang, Z., Scolpino, J., Feketeova, E., Canki, M., Mannino, R.J., 1998. Targeting immune response induction with cochleate and liposome-based vaccines. Adv. Drug Deliv. Rev. 32, 273–287. https://doi.org/10.1016/S0169-409X(98)00014-3

Goulet, D.R., Atkins, W.M., 2020. Considerations for the Design of Antibody-Based Therapeutics. J. Pharm. Sci. 109, 74–103. https://doi.org/10.1016/j.xphs.2019.05.031

Greenberg, A.S., Avila, D., Hughes, M., Hughes, A., McKinney, E.C., Flajnik, M.F., 1995. A new antigen receptor gene family that undergoes rearrangement and extensive somatic diversification in sharks. Nature 374, 168–173. https://doi.org/10.1038/374168a0

Grimaldi, N., Andrade, F., Segovia, N., Ferrer-Tasies, L., Sala, S., Veciana, J., Ventosa, N., 2016. Lipid-based nanovesicles for nanomedicine. Chem. Soc. Rev. 45, 6520–6545. https://doi.org/10.1039/C6CS00409A

Guimaraes, C.P., Witte, M.D., Theile, C.S., Bozkurt, G., Kundrat, L., Blom, A.E.M., Ploegh, H.L., 2013. Site-specific C-terminal and internal loop labeling of proteins using sortase-mediated reactions. Nat. Protoc. 8, 1787–1799. https://doi.org/10.1038/nprot.2013.101

Guo, J., Garratt, A., Hill, A., 2022. Worldwide rates of diagnosis and effective treatment for cystic fibrosis. J. Cyst. Fibros. 21, 456–462. https://doi.org/10.1016/j.jcf.2022.01.009

Guseh, J.S., Bores, S.A., Stanger, B.Z., Zhou, Q., Anderson, W.J., Melton, D.A., Rajagopal, J., 2009. Notch signaling promotes airway mucous metaplasia and inhibits alveolar development. Development 136, 1751–1759. https://doi.org/10.1242/dev.029249

Ha, E.V.S.S., Rogers, D.F., 2016. Novel Therapies to Inhibit Mucus Synthesis and Secretion in Airway Hypersecretory Diseases. Pharmacology 97, 84–100. https://doi.org/10.1159/000442794

Haga, D.S., 1995. Immunoassays. Anal. Chem. 67, 455–462.

Hage, D.S., Matsuda, R.E., Hage, D.S., Matsuda, R., 2015. Affinity Chromatography. Springer New York, New York, NY. https://doi.org/10.1007/978-1-4939-2447-9

Hakim, A., Adcock, I.M., Usmani, O.S., 2012. Corticosteroid Resistance and Novel Anti-Inflammatory Therapies in Chronic Obstructive Pulmonary Disease. Drugs 72, 1299–1312. https://doi.org/10.2165/11634350-000000000-00000

Hamers-Casterman, C., Atarhouch, T., Muyldermans, S., Robinson, G., Hamers, C., Bajyana Songa, E., Bendahman, N., Hamerst, R., HamersCasterman, C., Atarhouch, T., Muyldermans, S., Robinson, G., Hamers, C., Bajyana Songa, E., Bendahman, N., Hamerst, R., Hamers-Casterman, C., Atarhouch, T., Muyldermans, S., Robinson, G., Hamers, C., Bajyana Songa, E., Bendahman, N., Hamerst, R., Hamers-Casterman, A., T., Muyldermans, S., Robinson, G., Hamers, C., Bajyana, E., Bendahman, N., Hamilton, R., 1993. Naturally occurring antibodies devoid of light chains. Lett. Nat. 363, 446–448.

Hanes, J., Plückthun, A., 1997. In vitro selection and evolution of functional proteins by using ribosome display. Proc. Natl. Acad. Sci. U. S. A. 94, 4937–4942. https://doi.org/10.1073/PNAS.94.10.4937

Hanes, J., Schaffitzel, C., Knappik, A., Plückthun, A., 2000. Picomolar affinity antibodies from a fully synthetic naive library selected and evolved by ribosome display. Nat. Biotechnol. 18, 1287–1292. https://doi.org/10.1038/82407

Harmsen, M.M., De Haard, H.J., 2007. Properties, production, and applications of camelid single-domain antibody fragments. Appl. Microbiol. Biotechnol. 77, 13–22. https://doi.org/10.1007/s00253-007-1142-2

Häsler, J., Flajnik, M.F., Williams, G., Walsh, F.S., Rutkowski, J.L., 2016. VNAR single-domain antibodies specific for BAFF inhibit B cell development by molecular mimicry. Mol. Immunol. 75, 28–37. https://doi.org/10.1016/j.molimm.2016.05.009

Hayhurst, A., Harris, W.J., 1999. Escherichia coli Skp Chaperone Coexpression Improves Solubility and Phage Display of Single-Chain Antibody Fragments.

Heilmann, C., Barington, T., 1989. Distribution of κ and λ Light Chain Isotypes among Human Blood Immunoglobulin-Secreting Cells after Vaccination with Pneumococcal Polysaccharides. Scand. J. Immunol. 29, 159–164. https://doi.org/10.1111/j.1365-3083.1989.tb01112.x

Herbst, R.S., Soria, J.C., Kowanetz, M., Fine, G.D., Hamid, O., Gordon, M.S., Sosman, J.A., McDermott, D.F., Powderly, J.D., Gettinger, S.N., Kohrt, H.E.K., Horn, L., Lawrence, D.P., Rost, S., Leabman, M., Xiao, Y., Mokatrin, A., Koeppen, H., Hegde, P.S., Mellman, I., Chen, D.S., Hodi, F.S., 2014. Predictive correlates of response to the anti-PD-L1 antibody MPDL3280A in cancer patients. Nature 515, 563–567. https://doi.org/10.1038/nature14011

Hermanson, G.T., 2013. Bioconjugate techniques. Academic press.

Higuchi, K., Araki, T., Matsuzaki, O., Sato, A., Kanno, K., Kitaguchi, N., Ito, H., 1997. Cell display library for gene cloning of variable regions of human antibodies to hepatitis B surface antigen. J. Immunol. Methods 202, 193–204. https://doi.org/10.1016/S0022-1759(97)00010-0

Hill, D.B., Button, B., Rubinstein, M., Boucher, R.C., 2022. Physiology and pathophysiology of human airway mucus. Physiol. Rev. 102, 1757–1836. https://doi.org/10.1152/physrev.00004.2021

Ho, M., Pastan, I., 2009. Mammalian Cell Display for Antibody Engineering, in: Methods in Molecular Biology (Clifton, N.J.). Humana Press, pp. 337–352. https://doi.org/10.1007/978-1-59745-554-1_18

Hoogenboom, H.R., De Bruïne, A.P., Hufton, S.E., Hoet, R.M., Arends, J.-W., Roovers, R.C., De Bruı¨nebruı¨ne, A.P., Hufton, S.E., Hoet, R.M., Arends, J.-W., Roovers, R.C., 1998. Antibody phage display technology and its applications. Immunotechnology 4, 1–20.

Huang, C., Wang, Y., Li, X., Ren, L., Zhao, J., Hu, Y., Zhang, L., Fan, G., Xu, J., Gu, X., Cheng, Z., Yu, T., Xia, J., Wei, Y., Wu, W., Xie, X., Yin, W., Li, H., Liu, M., Xiao, Y., Gao, H., Guo, L., Xie, J., Wang, G., Jiang, R., Gao, Z., Jin, Q., Wang, J., Cao, B., 2020. Clinical features of patients infected with 2019 novel coronavirus in Wuhan, China. The Lancet 395, 497–506. https://doi.org/10.1016/S0140-6736(20)30183-5

Huang, L., Gainkam, L.O.T., Caveliers, V., Vanhove, C., Keyaerts, M., De Baetselier, P., Bossuyt, A., Revets, H., Lahoutte, T., Baetselier, P., Bossuyt, A., Revets, H., Lahoutte, T., 2008. SPECT Imaging with 99mTc-Labeled EGFR-Specific Nanobody for In Vivo Monitoring of EGFR Expression. Mol. Imaging Biol. 10, 167–175. https://doi.org/10.1007/s11307-008-0133-8

Irving, B., Chiu, H., Maecker, H., Mariathasan, S., Lehar, S.M., Wu, Y., Cheung, J., 2012. Anti-PD-L1 antibodies, compositions and articles of manufacture.

Ito, K., Lim, S., Caramori, G., Cosio, B., Chung, K.F., Adcock, I.M., Barnes, P.J., Beavo, J.A., 2002. A molecular mechanism of action of theophylline: Induction of histone deacetylase activity to decrease inflammatory gene expression. Proc. Natl. Acad. Sci. U. S. A. 99, 8921–8926. https://doi.org/10.1073/pnas.132556899

Jacobs, T.M., Yumerefendi, H., Kuhlman, B., Leaver-Fay, A., 2015. SwiftLib: rapid degenerate-codon-library optimization through dynamic programming. Nucleic Acids Res. 43, e34–e34. https://doi.org/10.1093/nar/gku1323

Jain, T., Sun, T., Durand, S., Hall, A., Houston, N.R., Nett, J.H., Sharkey, B., Bobrowicz, B., Caffry, I., Yu, Y., Cao, Y., Lynaugh, H., Brown, M., Baruah, H., Gray, L.T., Krauland, E.M., Xu, Y., Vásquez, M., Wittrup, K.D., 2017. Biophysical properties of the clinical-stage antibody landscape. Proc. Natl. Acad. Sci. U. S. A. 114, 944–949. https://doi.org/10.1073/pnas.1616408114

James, S.L., Abate, D., Abate, K.H., Abay, S.M., Abbafati, C., Abbasi, N., Abbastabar, H., Abd-Allah, F., Abdela, J., Abdelalim, A., Abdollahpour, I., Abdulkader, R.S., Abebe, Z., Abera, S.F., Abil, O.Z., Abraha, H.N., Abu-Raddad, L.J., Abu-Rmeileh, N.M.E., Accrombessi, M.M.K., Acharya, D., Acharya, P., Ackerman, I.N., Adamu, A.A., Adebayo, O.M., Adekanmbi, V., Adetokunboh, O.O., Adib, M.G., Adsuar, J.C., Afanvi, K.A., Afarideh, M., Afshin, A., Agarwal, G., Agesa, K.M., Aggarwal, R., Aghayan, S.A., Agrawal, S., Ahmadi, A., Ahmadi, M., Ahmadieh, H., Ahmed, M.B., Aichour, A.N., Aichour, I., Aichour, M.T.E., Akinyemiju, T., Akseer, N., Al-Aly, Z., Al-Eyadhy, A., Al-Mekhlafi, H.M., Al-Raddadi, R.M., Alahdab, F., Alam, K., Alam, T., Alashi, A., Alavian, S.M., Alene, K.A., Alijanzadeh, M., Alizadeh-Navaei, R., Aljunid, S.M., Alkerwi, A., Alla, F., Allebeck, P., Alouani, M.M.L., Altirkawi, K., Alvis-Guzman, N., Amare, A.T., Aminde, L.N., Ammar, W., Amoako, Y.A., Anber, N.H., Andrei, C.L., Androudi, S., Animut, M.D., Anjomshoa, M., Ansha, M.G., Antonio, C.A.T., Anwari, P., Arabloo, J., Arauz, A., Aremu, O., Ariani, F., Armoon, B., Ärnlöv, J., Arora, A., Artaman, A., Aryal, K.K., Asayesh, H., Asghar, R.J., Ataro, Z., Atre, S.R., Ausloos, M., Avila-Burgos, L., Avokpaho, E.F.G.A., Awasthi, A., Ayala Quintanilla, B.P., Ayer, R., Azzopardi, P.S., Babazadeh, A., Badali, H., Badawi, A., Bali, A.G., Ballesteros, K.E., Ballew, S.H., Banach, M., Banoub, J.A.M., Banstola, A., Barac, A., Barboza, M.A., Barker-Collo, S.L., Bärnighausen, T.W., Barrero, L.H., Baune, B.T., Bazargan-Hejazi, S., Bedi, N., Beghi, E., Behzadifar, Masoud, Behzadifar, Meysam, Béjot, Y., Belachew, A.B., Belay, Y.A., Bell, M.L., Bello, A.K., Bensenor, I.M., Bernabe, E., Bernstein, R.S., Beuran, M., Beyranvand, T., Bhala, N., Bhattarai, S., Bhaumik, S., Bhutta, Z.A., Biadgo, B., Bijani, A., Bikbov, B., Bilano, V., Bililign, N., Bin Sayeed, M.S., Bisanzio, D., Blacker, B.F., Blyth, F.M., Bou-Orm, I.R., Boufous, S., Bourne, R., Brady, O.J., Brainin, M., Brant, L.C., Brazinova, A., Breitborde, N.J.K., Brenner, H., Briant, P.S., Briggs, A.M., Briko, A.N., Britton, G., Brugha, T., Buchbinder, R., Busse, R., Butt, Z.A., Cahuana-Hurtado, L., Cano, J., Cárdenas, R., Carrero, J.J., Carter, A., Carvalho,

F., Castañeda-Orjuela, C.A., Castillo Rivas, J., Castro, F., Catalá-López, F., Cercy, K.M., Cerin, E., Chaiah, Y., Chang, A.R., Chang, H.Y., Chang, J.C., Charlson, F.J., Chattopadhyay, A., Chattu, V.K., Chaturvedi, P., Chiang, P.P.C., Chin, K.L., Chitheer, A., Choi, J.Y.J., Chowdhury, R., Christensen, H., Christopher, D.J., Cicuttini, F.M., Ciobanu, L.G., Cirillo, M., Claro, R.M., Collado-Mateo, D., Cooper, C., Coresh, J., Cortesi, P.A., Cortinovis, M., Costa, M., Cousin, E., Criqui, M.H., Cromwell, E.A., Cross, M., Crump, J.A., Dadi, A.F., Dandona, L., Dandona, R., Dargan, P.I., Daryani, A., Das Gupta, R., Das Neves, J., Dasa, T.T., Davey, G., Davis, A.C., Davitoiu, D.V., De Courten, B., De La Hoz, F.P., De Leo, D., De Neve, J.W., Degefa, M.G., Degenhardt, L., Deiparine, S., Dellavalle, R.P., Demoz, G.T., Deribe, K., Dervenis, N., Des Jarlais, D.C., Dessie, G.A., Dey, S., Dharmaratne, S.D., Dinberu, M.T., Dirac, M.A., Djalalinia, S., Doan, L., Dokova, K., Doku, D.T., Dorsey, E.R., Doyle, K.E., Driscoll, T.R., Dubey, M., Dubljanin, E., Duken, E.E., Duncan, B.B., Duraes, A.R., Ebrahimi, H., Ebrahimpour, S., Echko, M.M., Edvardsson, D., Effiong, A., Ehrlich, J.R., El Bcheraoui, C., El Sayed Zaki, M., El-Khatib, Z., Elkout, H., Elyazar, I.R.F., Enayati, A., Endries, A.Y., Er, B., Erskine, H.E., Eshrati, B., Eskandarieh, S., Esteghamati, A., Esteghamati, S., Fakhim, H., Fallah Omrani, V., Faramarzi, M., Fareed, M., Farhadi, F., Farid, T.A., Farinha, C.S.E., Farioli, A., Faro, A., Farvid, M.S., Farzadfar, F., Feigin, V.L., Fentahun, N., Fereshtehnejad, S.M., Fernandes, E., Fernandes, J.C., Ferrari, A.J., Feyissa, G.T., Filip, I., Fischer, F., Fitzmaurice, C., Foigt, N.A., Foreman, K.J., Fox, J., Frank, T.D., Fukumoto, T., Fullman, N., Fürst, T., Furtado, J.M., Futran, N.D., Gall, S., Ganji, M., Gankpe, F.G., Garcia-Basteiro, A.L., Gardner, W.M., Gebre, A.K., Gebremedhin, A.T., Gebremichael, T.G., Gelano, T.F., Geleijnse, J.M., Genova-Maleras, R., Geramo, Y.C.D., Gething, P.W., Gezae, K.E., Ghadiri, K., Ghasemi Falavarjani, K., Ghasemi-Kasman, M., Ghimire, M., Ghosh, R., Ghoshal, A.G., Giampaoli, S., Gill, P.S., Gill, T.K., Ginawi, I.A., Giussani, G., Gnedovskaya, E.V., Goldberg, E.M., Goli, S., Gómez-Dantés, H., Gona, P.N., Gopalani, S.V., Gorman, T.M., Goulart, A.C., Goulart, B.N.G., Grada, A., Grams, M.E., Grosso, G., Gugnani, H.C., Guo, Y., Gupta, P.C., Gupta, Rahul, Gupta, Rajeev, Gupta, T., Gyawali, B., Haagsma, J.A., Hachinski, V., Hafezi-Nejad, N., Haghparast Bidgoli, H., Hagos, T.B., Hailu, G.B., Haj-Mirzaian, Arvin, Haj-Mirzaian, Arya, Hamadeh, R.R., Hamidi, S., Handal, A.J., Hankey, G.J., Hao, Y., Harb, H.L., Harikrishnan, S., Haro, J.M., Hasan, M., Hassankhani, H., Hassen, H.Y., Havmoeller, R., Hawley, C.N., Hay, R.J., Hay, S.I., Hedayatizadeh-Omran, A., Heibati, B., Hendrie, D., Henok, A., Herteliu, C., Heydarpour, S., Hibstu, D.T., Hoang, H.T., Hoek, H.W., Hoffman, H.J., Hole, M.K., Homaie Rad, E., Hoogar, P., Hosgood, H.D., Hosseini, S.M., Hosseinzadeh, M., Hostiuc, M., Hostiuc, S., Hotez, P.J., Hoy, D.G., Hsairi, M., Htet, A.S., Hu, G., Huang, J.J., Huynh, C.K., Iburg, K.M., Ikeda, C.T., Ileanu, B., Ilesanmi, O.S., Iqbal, U., Irvani, S.S.N., Irvine, C.M.S., Mohammed, Sheikh, Islam, S., Islami, F., Jacobsen, K.H., Jahangiry, L., Jahanmehr, N., Jain, S.K., Jakovljevic, M., Javanbakht, M., Jayatilleke, A.U., Jeemon, P., Jha, R.P., Jha, V., Ji, J.S., Johnson, C.O., Jonas, J.B., Jozwiak, J.J., Jungari, S.B., Jürisson, M., Kabir, Z., Kadel, R., Kahsay, A., Kalani, R., Kanchan, T., Karami, M., Karami Matin, B., Karch, A., Karema, C., Karimi, N., Karimi, S.M., Kasaeian, A., Kassa, D.H., Kassa, G.M., Kassa, T.D., Kassebaum, N.J., Katikireddi, S.V., Kawakami, N., Kazemi Karyani, A.,

Keighobadi, M.M., Keiyoro, P.N., Kemmer, L., Kemp, G.R., Kengne, A.P., Keren, A., Khader, Y.S., Khafaei, B., Khafaie, M.A., Khajavi, A., Khalil, I.A., Khan, E.A., Khan, M.S., Khan, M.A., Khang, Y.H., Khazaei, M., Khoja, A.T., Khosravi, A., Khosravi, M.H., Kiadaliri, A.A., Kiirithio, D.N., Kim, C.I., Kim, D., Kim, P., Kim, Y.E., Kim, Y.J., Kimokoti, R.W., Kinfu, Y., Kisa, A., Kissimova-Skarbek, K., Kivimäki, M., Knudsen, A.K.S., Kocarnik, J.M., Kochhar, S., Kokubo, Y., Kolola, T., Kopec, J.A., Kosen, S., Kotsakis, G.A., Koul, P.A., Koyanagi, A., Kravchenko, M.A., Krishan, K., Krohn, K.J., Kuate Defo, B., Kucuk Bicer, B., Kumar, G.A., Kumar, M., Kyu, H.H., Lad, D.P., Lad, S.D., Lafranconi, A., Lalloo, R., Lallukka, T., Lami, F.H., Lansingh, V.C., Latifi, A., Lau, K.M.M., Lazarus, J.V., Leasher, J.L., Ledesma, J.R., Lee, P.H., Leigh, J., Leung, J., Levi, M., Lewycka, S., Li, S., Li, Y., Liao, Y., Liben, M.L., Lim, L.L., Lim, S.S., Liu, S., Lodha, R., Looker, K.J., Lopez, A.D., Lorkowski, S., Lotufo, P.A., Low, N., Lozano, R., Lucas, T.C.D., Lucchesi, L.R., Lunevicius, R., Lyons, R.A., Ma, S., Macarayan, E.R.K., Mackay, M.T., Madotto, F., Magdy Abd El Razek, H., Magdy Abd El Razek, M., Maghavani, D.P., Mahotra, N.B., Mai, H.T., Majdan, M., Majdzadeh, R., Majeed, A., Malekzadeh, R., Malta, D.C., Mamun, A.A., Manda, A.L., Manguerra, H., Manhertz, T., Mansournia, M.A., Mantovani, L.G., Mapoma, C.C., Maravilla, J.C., Marcenes, W., Marks, A., Martins-Melo, F.R., Martopullo, I., März, W., Marzan, M.B., Mashamba-Thompson, T.P., Massenburg, B.B., Mathur, M.R., Matsushita, K., Maulik, P.K., Mazidi, M., McAlinden, C., McGrath, J.J., McKee, M., Mehndiratta, M.M., Mehrotra, R., Mehta, K.M., Mehta, V., Mejia-Rodriguez, F., Mekonen, T., Melese, A., Melku, M., Meltzer, M., Memiah, P.T.N., Memish, Z.A., Mendoza, W., Mengistu, D.T., Mengistu, G., Mensah, G.A., Mereta, S.T., Meretoja, A., Meretoja, T.J., Mestrovic, T., Mezerji, N.M.G., Miazgowski, B., Miazgowski, T., Millear, A.I., Miller, T.R., Miltz, B., Mini, G.K., Mirarefin, M., Mirrakhimov, E.M., Misganaw, A.T., Mitchell, P.B., Mitiku, H., Moazen, B., Mohajer, B., Mohammad, K.A., Mohammadifard, N., Mohammadnia-Afrouzi, M., Mohammed, M.A., Mohammed, Shafiu, Mohebi, F., Moitra, M., Mokdad, A.H., Molokhia, M., Monasta, L., Moodley, Y., Moosazadeh, M., Moradi, G., Moradi-Lakeh, M., Moradinazar, M., Moraga, P., Morawska, L., Moreno Velásquez, I., Morgado-Da-Costa, J., Morrison, S.D., Moschos, M.M., Mousavi, S.M., Mruts, K.B., Muche, A.A., Muchie, K.F., Mueller, U.O., Muhammed, O.S., Mukhopadhyay, S., Muller, K., Mumford, J.E., Murhekar, M., Musa, J., Musa, K.I., Mustafa, G., Nabhan, A.F., Nagata, C., Naghavi, M., Naheed, A., Nahvijou, A., Naik, G., Naik, N., Najafi, F., Naldi, L., Nam, H.S., Nangia, V., Nansseu, J.R., Nascimento, B.R., Natarajan, G., Neamati, N., Negoi, I., Negoi, R.I., Neupane, S., Newton, C.R.J., Ngunjiri, J.W., Nguyen, A.Q., Nguyen, Ha Thu, Nguyen, H.L.T., Nguyen, Huong Thanh, Nguyen, L.H., Nguyen, M., Nguyen, N.B., Nguyen, S.H., Nichols, E., Ningrum, D.N.A., Nixon, M.R., Nolutshungu, N., Nomura, S., Norheim, O.F., Noroozi, M., Norrving, B., Noubiap, J.J., Nouri, H.R., Nourollahpour Shiadeh, M., Nowroozi, M.R., Nsoesie, E.O., Nyasulu, P.S., Odell, C.M., Ofori-Asenso, R., Ogbo, F.A., Oh, I.H., Oladimeji, O., Olagunju, A.T., Olagunju, T.O., Olivares, P.R., Olsen, H.E., Olusanya, B.O., Ong, K.L., Ong, S.K., Oren, E., Ortiz, A., Ota, E., Otstavnov, S.S., øverland, S., Owolabi, M.O., Mahesh, P.A., Pacella, R., Pakpour, A.H., Pana, A., Panda-Jonas, S., Parisi, A., Park, E.K., Parry, C.D.H., Patel, S., Pati, S., Patil, S.T.,

Patle, A., Patton, G.C., Paturi, V.R., Paulson, K.R., Pearce, N., Pereira, D.M., Perico, N., Pesudovs, K., Pham, H.Q., Phillips, M.R., Pigott, D.M., Pillay, J.D., Piradov, M.A., Pirsaheb, M., Pishgar, F., Plana-Ripoll, O., Plass, D., Polinder, S., Popova, S., Postma, M.J., Pourshams, A., Poustchi, H., Prabhakaran, D., Prakash, S., Prakash, V., Purcell, C.A., Purwar, M.B., Qorbani, M., Quistberg, D.A., Radfar, A., Rafay, A., Rafiei, A., Rahim, F., Rahimi, K., Rahimi-Movaghar, A., Rahimi-Movaghar, V., Rahman, M., Ur Rahman, M.H., Rahman, M.A., Rahman, S.U., Rai, R.K., Rajati, F., Ram, U., Ranjan, P., Ranta, A., Rao, P.C., Rawaf, D.L., Rawaf, S., Reddy, K.S., Reiner, R.C., Reinig, N., Reitsma, M.B., Remuzzi, G., Renzaho, A.M.N., Resnikoff, S., Rezaei, S., Rezai, M.S., Ribeiro, A.L.P., Robinson, S.R., Roever, L., Ronfani, L., Roshandel, G., Rostami, A., Roth, G.A., Roy, A., Rubagotti, E., Sachdev, P.S., Sadat, N., Saddik, B., Sadeghi, E., Saeedi Moghaddam, S., Safari, H., Safari, Y., Safari-Faramani, R., Safdarian, M., Safi, S., Safiri, S., Sagar, R., Sahebkar, A., Sahraian, M.A., Sajadi, H.S., Salam, N., Salama, J.S., Salamati, P., Saleem, K., Saleem, Z., Salimi, Y., Salomon, J.A., Salvi, S.S., Salz, I., Samy, A.M., Sanabria, J., Sang, Y., Santomauro, D.F., Santos, I.S., Santos, J.V., Santric Milicevic, M.M., Sao Jose, B.P., Sardana, M., Sarker, A.R., Sarrafzadegan, N., Sartorius, B., Sarvi, S., Sathian, B., Satpathy, M., Sawant, A.R., Sawhney, M., Saxena, S., Saylan, M., Schaeffner, E., Schmidt, M.I., Schneider, I.J.C., Schöttker, B., Schwebel, D.C., Schwendicke, F., Scott, J.G., Sekerija, M., Sepanlou, S.G., Serván-Mori, E., Seyedmousavi, S., Shabaninejad, H., Shafieesabet, A., Shahbazi, M., Shaheen, A.A., Shaikh, M.A., Shams-Beyranvand, M., Shamsi, M., Shamsizadeh, M., Sharafi, H., Sharafi, K., Sharif, M., Sharif-Alhoseini, M., Sharma, M., Sharma, R., She, J., Sheikh, A., Shi, P., Shibuya, K., Shigematsu, M., Shiri, R., Shirkoohi, R., Shishani, K., Shiue, I., Shokraneh, F., Shoman, H., Shrime, M.G., Si, S., Siabani, S., Siddiqi, T.J., Sigfusdottir, I.D., Sigurvinsdottir, R., Silva, J.P., Silveira, D.G.A., Singam, N.S.V., Singh, J.A., Singh, N.P., Singh, V., Sinha, D.N., Skiadaresi, E., Slepak, E.L.N., Sliwa, K., Smith, D.L., Smith, M., Soares Filho, A.M., Sobaih, B.H., Sobhani, S., Sobngwi, E., Soneji, S.S., Soofi, M., Soosaraei, M., Sorensen, R.J.D., Soriano, J.B., Soyiri, I.N., Sposato, L.A., Sreeramareddy, C.T., Srinivasan, V., Stanaway, J.D., Stein, D.J., Steiner, C., Steiner, T.J., Stokes, M.A., Stovner, L.J., Subart, M.L., Sudaryanto, A., Sufiyan, M.B., Sunguya, B.F., Sur, P.J., Sutradhar, I., Sykes, B.L., Sylte, D.O., Tabarés-Seisdedos, R., Tadakamadla, S.K., Tadesse, B.T., Tandon, N., Tassew, S.G., Tavakkoli, M., Taveira, N., Taylor, H.R., Tehrani-Banihashemi, A., Tekalign, T.G., Tekelemedhin, S.W., Tekle, M.G., Temesgen, H., Temsah, M.H., Temsah, O., Terkawi, A.S., Teweldemedhin, M., Thankappan, K.R., Thomas, N., Tilahun, B., To, Q.G., Tonelli, M., Topor-Madry, R., Topouzis, F., Torre, A.E., Tortajada-Girbés, M., Touvier, M., Tovani-Palone, M.R., Towbin, J.A., Tran, B.X., Tran, K.B., Troeger, C.E., Truelsen, T.C., Tsilimbaris, M.K., Tsoi, D., Tudor Car, L., Tuzcu, E.M., Ukwaja, K.N., Ullah, I., Undurraga, E.A., Unutzer, J., Updike, R.L., Usman, M.S., Uthman, O.A., Vaduganathan, M., Vaezi, A., Valdez, P.R., Varughese, S., Vasankari, T.J., Venketasubramanian, N., Villafaina, S., Violante, F.S., Vladimirov, S.K., Vlassov, V., Vollset, S.E., Vosoughi, K., Vujcic, I.S., Wagnew, F.S., Waheed, Y., Waller, S.G., Wang, Y., Wang, Y.P., Weiderpass, E., Weintraub, R.G., Weiss, D.J., Weldegebreal, F., Weldegwergs, K.G., Werdecker, A., West, T.E.,

Whiteford, H.A., Widecka, J., Wijeratne, T., Wilner, L.B., Wilson, S., Winkler, A.S., Wiyeh, A.B., Wiysonge, C.S., Wolfe, C.D.A., Woolf, A.D., Wu, S., Wu, Y.C., Wyper, G.M.A., Xavier, D., Xu, G., Yadgir, S., Yadollahpour, A., Yahyazadeh Jabbari, S.H., Yamada, T., Yan, L.L., Yano, Y., Yaseri, M., Yasin, Y.J., Yeshaneh, A., Yimer, E.M., Yip, P., Yisma, E., Yonemoto, N., Yoon, S.J., Yotebieng, M., Younis, M.Z., Yousefifard, M., Yu, C., Zadnik, V., Zaidi, Z., Zaman, S.B., Zamani, M., Zare, Z., Zeleke, A.J., Zenebe, Z.M., Zhang, K., Zhao, Z., Zhou, M., Zodpey, S., Zucker, I., Vos, T., Murray, C.J.L., 2018. Global, regional, and national incidence, prevalence, and years lived with disability for 354 Diseases and Injuries for 195 countries and territories, 1990-2017: A systematic analysis for the Global Burden of Disease Study 2017. The Lancet 392, 1789–1858. https://doi.org/10.1016/S0140-6736(18)32279-7

Jaradat, D.M.M., 2018. Thirteen decades of peptide synthesis: key developments in solid phase peptide synthesis and amide bond formation utilized in peptide ligation. Amino Acids 50, 39–68. https://doi.org/10.1007/s00726-017-2516-0

Jaramillo, A.M., Azzegagh, Z., Tuvim, M.J., Dickey, B.F., 2018. Airway mucin secretion. Ann. Am. Thorac. Soc. 15, S164–S170. https://doi.org/10.1513/AnnalsATS.201806-371AW

Jenne, J.W., Wyze, E., Rood, F.S., Macdonald, F.M., Minneapolis, M., 1972. Pharmacokinetics of theophylline application to adjustment of the clinical dose of aminophylline. Clin. Pharmacol. Ther. 13, 349–360. https://doi.org/10.1002/cpt1972133349

Jin, X., Lian, J.S., Hu, J.H., Gao, J., Zheng, L., Zhang, Y.M., Hao, S.R., Jia, H.Y., Cai, H., Zhang, X.L., Yu, G.D., Xu, K.J., Wang, X.Y., Gu, J.Q., Zhang, S.Y., Ye, C.Y., Jin, C.L., Lu, Y.F., Yu, X., Yu, X.P., Huang, J.R., Xu, K.L., Ni, Q., Yu, C.B., Zhu, B., Li, Y.T., Liu, J., Zhao, H., Zhang, X., Yu, L., Guo, Y.Z., Su, J.W., Tao, J.J., Lang, G.J., Wu, X.X., Wu, W.R., Qv, T.T., Xiang, D.R., Yi, P., Shi, D., Chen, Y., Ren, Y., Qiu, Y.Q., Li, L.J., Sheng, J., Yang, Y., Yang, Y., Yang, Y., 2020. Epidemiological, clinical and virological characteristics of 74 cases of coronavirus-infected disease 2019 (COVID-19) with gastrointestinal symptoms. Gut 69, 1002–1009. https://doi.org/10.1136/gutjnl-2020-320926

Joint Formulary Committee, 2024. British National Formulary (online). Lond. BMJ Pharm. Press.

Joo, N.S., Lee, D.J., Winges, K.M., Rustagi, A., Wine, J.J., 2004. Regulation of Antiprotease and Antimicrobial Protein Secretion by Airway Submucosal Gland Serous Cells. J. Biol. Chem. 279, 38854–38860. https://doi.org/10.1074/jbc.M407077200

Kaleli, N.E., Karadag, M., Kalyoncu, S., 2019. Phage display derived therapeutic antibodies have enriched aliphatic content: Insights for developability issues. Proteins Struct. Funct. Bioinforma. 87, 607–618. https://doi.org/10.1002/prot.25685

Kan, B., Wang, M., Jing, H., Xu, H., Jiang, X., Yan, M., Liang, W., Zheng, H., Wan, K., Liu, Q., Cui, B., Xu, Y., Zhang, E., Wang, H., Ye, J., Li, G., Li, M., Cui, Z., Qi, X., Chen, K., Du, L., Gao, K., Zhao, Y., Zou, X., Feng, Y.-J., Gao, Y.-F., Hai, R., Yu, D., Guan, Y., Xu, J., 2005. Molecular Evolution Analysis and Geographic Investigation of Severe Acute Respiratory Syndrome Coronavirus-Like Virus in Palm Civets at an Animal Market and on Farms. J. Virol. 79, 11892–11900. https://doi.org/10.1128/jvi.79.18.11892-11900.2005

Ke, Y., Reddel, R.R., Gerwin, B.I., Miyashita, M., McMenamin, M., Lechner, J.F., Harris, C.C., 1988. Human bronchial epithelial cells with integrated SV40 virus T antigen genes retain the ability to undergo squamous differentiation. Differentiation 38, 60–66. https://doi.org/10.1111/j.1432-0436.1988.tb00592.x

Kende, M., Alving, C.R., Rill, ', Wayne L., Swartz, G.M., Canonico', P.G., Rill, W.L., Swartz, G.M., Canonico, P.G., 1985. Enhanced efficacy of liposome-encapsulated ribavirin against Rift Valley fever virus infection in mice. Antimicrob. Agents Chemother. 27, 903–907. https://doi.org/10.1128/AAC.27.6.903

Keyt, B.A., Baliga, R., Sinclair, A.M., Carroll, S.F., Peterson, M.S., 2020. Structure, Function, and Therapeutic Use of IgM Antibodies. Antibodies 9, 53. https://doi.org/10.3390/antib9040053

Kim, Y., Ho, S.O., Gassman, N.R., Korlann, Y., Landorf, E.V., Collart, F.R., Weiss, S., 2008. Efficient Site-Specific Labeling of Proteins via Cysteines. Bioconjug. Chem. 19, 786–791. https://doi.org/10.1021/bc7002499

Kipriyanov, S.M., 2009. High-Level Periplasmic Expression and Purification of scFvs, in: Antibody Phage Display. Humana Press, New Jersey, pp. 333–341. https://doi.org/10.1385/1-59259-240-6:333

Kirsch, M.I., Hülseweh, B., Nacke, C., Rülker, T., Schirrmann, T., Marschall, H.-J., Hust, M., Dübel, S., 2008. Development of human antibody fragments using antibody phage display for the detection and diagnosis of Venezuelan equine encephalitis virus (VEEV). BMC Biotechnol. https://doi.org/10.1186/1472-6750-8-66

Kirubananthan, L., Illuri, R., Rajendran, R., Chandrasekaran, P.R., 2021. Mechanism and transmission routes of COVID-19, in: Environmental and Health Management of Novel Coronavirus Disease (COVID-19). Elsevier, pp. 65–88. https://doi.org/10.1016/B978-0-323-85780-2.00013-5

Knight, D.A., Holgate, S.T., 2003. The airway epithelium: Structural and functional properties in health and disease. Respirology 8, 432–446. https://doi.org/10.1046/j.1440-1843.2003.00493.x

Köhler, G., Milstein, C., 1975. Continuous cultures of fused cells secreting antibody of predefined specificity. Nature 256, 495–497. https://doi.org/10.1038/256495a0

Kondo, M., Tamaoki, J., Takeyama, K., Isono, K., Kawatani, K., Izumo, T., Nagai, A., 2006. Elimination of IL-13 Reverses Established Goblet Cell Metaplasia into Ciliated Epithelia in Airway Epithelial Cell Culture. Allergol. Int. 55, 329–336. https://doi.org/10.2332/allergolint.55.329

Kondo, M., Tamaoki, J., Takeyama, K., Nakata, J., Nagai, A., 2002. Interleukin-13 induces goblet cell differentiation in primary cell culture from guinea pig tracheal epithelium. Am. J. Respir. Cell Mol. Biol. 27, 536–541. https://doi.org/10.1165/rcmb.4682

Kontermann, R.E., 2004. Intrabodies as therapeutic agents. Methods 34, 163–170. https://doi.org/10.1016/j.ymeth.2004.04.002

Kramer, R.A., Cox, F., van der Horst, M., van der Oudenrijn, S., Res, P.C.M., Bia, J., Logtenberg, T., de Kruif, J., 2003. A novel helper phage that improves phage display selection efficiency by preventing the amplification of phages without recombinant protein. Nucleic Acids Res. 31, e59–e59. https://doi.org/10.1093/nar/gng058

Krishn, S.R., Ganguly, K., Kaur, S., Batra, S.K., 2018. Ramifications of secreted mucin MUC5AC in malignant journey: A holistic view. Carcinogenesis 39, 633–651. https://doi.org/10.1093/carcin/bgy019

Kung, Y.-A., Lee, K.-M., Chiang, H.-J., Huang, S.-Y., Wu, C.-J., Shih, S.-R., 2022. Molecular Virology of SARS-CoV-2 and Related Coronaviruses. Microbiol. Mol. Biol. Rev. 86. https://doi.org/10.1128/mmbr.00026-21

Kuperman, D.A., Huang, X., Koth, L.L., Chang, G.H., Dolganov, G.M., Zhu, Z., Elias, J.A., Sheppard, D., Erle, D.J., 2002. Direct effects of interleukin-13 on epithelial cells cause airway hyperreactivity and mucus overproduction in asthma. Nat. Med. 8, 885–889. https://doi.org/10.1038/nm734

Kyte, J., Doolittle, R.F., 1982. A simple method for displaying the hydropathic character of a protein. J. Mol. Biol. 157, 105–132. https://doi.org/10.1016/0022-2836(82)90515-0

Lagowala, D.A., Kwon, S., Sidhaye, V.K., Kim, D.-H., 2021. Human microphysiological models of airway and alveolar epithelia. Am. J. Physiol. Lung Cell. Mol. Physiol. 321, L1072–L1088. https://doi.org/10.1152/ajplung.00103.2021

Ledsgaard, L., Kilstrup, M., Karatt-Vellatt, A., McCafferty, J., Laustsen, A.H., 2018. Basics of antibody phage display technology. Toxins 10. https://doi.org/10.3390/toxins10060236

Lee, R.E., Miller, S.M., Mascenik, T.M., Lewis, C.A., Dang, H., Boggs, Z.H., Tarran, R., Randell, S.H., 2020. Assessing Human Airway Epithelial Progenitor Cells for Cystic Fibrosis Cell Therapy. Am. J. Respir. Cell Mol. Biol. 63, 374–385. https://doi.org/10.1165/rcmb.2019-0384oc

Levardon, H., Yonker, L.M., Hurley, B.P., Mou, H., 2018. Expansion of Airway Basal Cells and Generation of Polarized Epithelium. Bio-Protoc. 8, e2877. https://doi.org/10.21769/BioProtoc.2877

Li, W., Shi, Z., Yu, M., Ren, W., Smith, C., Epstein, J.H., Wang, H., Crameri, G., Hu, Z., Zhang, H., Zhang, J., McEachern, J., Field, H., Daszak, P., Eaton, B.T., Zhang, S., Wang, L.-F., 2005. Bats Are Natural Reservoirs of SARS-Like Coronaviruses. Science 310, 676–679. https://doi.org/10.1126/science.1118391

Lillehoj, E.P., Kato, K., Lu, W., Kim, K.C., 2013. Cellular and Molecular Biology of Airway Mucins, in: Physiology & Behavior. pp. 139–202. https://doi.org/10.1016/B978-0-12-407697-6.00004-0

Lim, S., Zhang, M., Chang, T.L., 2022. ACE2-Independent Alternative Receptors for SARS-CoV-2. Viruses 14, 2535. https://doi.org/10.3390/v14112535

Limal, D., Briand, J. -P, Dalbon, P., Jolivet, M., 1998. Solid-phase synthesis and on-resin cyclization of a disulfide bond peptide and lactam analogues corresponding to the major antigenic site of HIV gp41 protein. J. Pept. Res. 52, 121–129. https://doi.org/10.1111/j.1399-3011.1998.tb01366.x

Lipovsek, D., Plückthun, A., 2004. In-vitro protein evolution by ribosome display and mRNA display. J. Immunol. Methods 290, 51–67. https://doi.org/10.1016/j.jim.2004.04.008

Lode, H.N., Xiang, R., Becker, J.C., Gillies, S.D., Reisfeld, R.A., 1998. Immunocytokines: A promising approach to cancer immunotherapy. Pharmacol. Ther. 80, 277–292. https://doi.org/10.1016/S0163-7258(98)00033-3

Lu, C., Zhu, J., Wang, Y., Umeda, A., Cowmeadow, R.B., Lai, E., Moreno, G.N., Person, M.D., Zhang, Z., 2007. Staphylococcus aureus sortase a exists as a dimeric protein in vitro. Biochemistry 46, 9346–9354. https://doi.org/10.1021/bi700519w

Mäde, V., Els-Heindl, S., Beck-Sickinger, A.G., 2014. Automated solid-phase peptide synthesis to obtain therapeutic peptides. Beilstein J. Org. Chem. 10, 1197–1212. https://doi.org/10.3762/bjoc.10.118

Malpiedi, L.P., Díaz, C.A., Nerli, B.B., Pessoa, A., 2013. Single-chain antibody fragments: Purification methodologies. Process Biochem. 48, 1242–1251. https://doi.org/10.1016/j.procbio.2013.06.008

Mann, S., Chen, Y.P.P., 2010. Bacterial genomic G + C composition-eliciting environmental adaptation. Genomics 95, 7–15. https://doi.org/10.1016/j.ygeno.2009.09.002

Marshall, B., Faro, A., Elbert, A., Fink, A., Sewall, A., Loeffler, D., Fernandez, G., Ostrenga, J., Petren, K., Wu, R., 2018. Cystic Fibrosis Foundation Patient Registry 2018 Annual Data Report Bethesda, Maryland© 2019 Cystic Fibrosis Foundation. 2018.

Mashoof, S., Criscitiello, M., 2016. Fish Immunoglobulins. Biology 5, 45. https://doi.org/10.3390/biology5040045

Massa, S., Vikani, N., Betti, C., Ballet, S., Vanderhaegen, S., Steyaert, J., Descamps, B., Vanhove, C., Bunschoten, A., van Leeuwen, F.W.B.B., Hernot, S., Caveliers, V., Lahoutte, T., Muyldermans, S., Xavier, C., Devoogdt, N., 2016. Sortase A-mediated site-specific labeling of camelid single-domain antibody-fragments: a versatile strategy for multiple molecular imaging modalities. Contrast Media Mol. Imaging 11, 328–339. https://doi.org/10.1002/cmmi.1696

Massa, S., Xavier, C., De Vos, J., Caveliers, V., Lahoutte, T., Muyldermans, S., Devoogdt, N., 2014. Site-Specific Labeling of Cysteine-Tagged Camelid Single-Domain Antibody-Fragments for Use in Molecular Imaging. Bioconjug. Chem. 25, 979–988. https://doi.org/10.1021/bc500111t

Mathers, C.D., Loncar, D., 2006. Projections of Global Mortality and Burden of Disease from 2002 to 2030. PLoS Med. 3, 2011–2030. https://doi.org/10.1371/journal.pmed.0030442

Mattheakis, L.C., Bhattt, R.R., Dower, W.J., 1994. An in vitro polysome display system for identifying ligands from very large peptide libraries. Biochemistry 91, 9022–9026.

Mazor, Y., Van Blarcom, T., Mabry, R., Iverson, B.L., Georgiou, G., 2007. Isolation of engineered, full-length antibodies from libraries expressed in Escherichia coli. Nat. Biotechnol. 25, 563–565. https://doi.org/10.1038/nbt1296

McCafferty, J., Griffiths, A.D., Winter, G., Chiswell, D.J., 1990. Phage antibodies: filamentous phage displaying antibody variable domains. Nature 348, 552–554. https://doi.org/10.1038/348552a0

Mendoza, M.N., Jian, M., King, M.T., Brooks, C.L., 2020. Role of a noncanonical disulfide bond in the stability, affinity, and flexibility of a VHH specific for the Listeria virulence factor InlB. Protein Sci. 29, 1004–1017. https://doi.org/10.1002/pro.3831

Merrifield, R.B., 1964. Solid Phase Peptide Synthesis. II. The Synthesis of Bradykinin. J. Am. Chem. Soc. 86, 304–305. https://doi.org/10.1021/ja01056a056

Merrifield, R.B., 1963. Solid Phase Peptide Synthesis. I. The Synthesis of a Tetrapeptide. J. Am. Chem. Soc. 85, 2149–2154. https://doi.org/10.1021/ja00897a025

Meyer, T., Stratmann-Selke, J., Meens, J., Schirrmann, T., Gerlach, G.F., Frank, R., Dübel, S., Strutzberg-Minder, K., Hust, M., 2011. Isolation of scFv fragments specific to OmpD of Salmonella Typhimurium. Vet. Microbiol. 147, 162–169. https://doi.org/10.1016/j.vetmic.2010.06.023

Michi, A.N., Proud, D., 2021. A toolbox for studying respiratory viral infections using air-liquid interface cultures of human airway epithelial cells. Am. J. Physiol.-Lung Cell. Mol. Physiol. 321, L263–L279. https://doi.org/10.1152/ajplung.00141.2021

Minchinton, A.I., Tannock, I.F., 2006. Drug penetration in solid tumours Andrew. Nat. Rev. 6, 583–592. https://doi.org/10.1038/nrc1893

Mishani, E., Hagooly, A., 2009. Strategies for molecular imaging of epidermal growth factor receptor tyrosine kinase in cancer. J. Nucl. Med. 50, 1199–1202. https://doi.org/10.2967/jnumed.109.062117

Mohiuddin, T.M., Zhang, C., Sheng, W., Al-Rawe, M., Zeppernick, F., Meinhold-Heerlein, I., Hussain, A.F., 2023. Near Infrared Photoimmunotherapy: A Review of Recent Progress and Their Target Molecules for Cancer Therapy. Int. J. Mol. Sci. 24. https://doi.org/10.3390/ijms24032655

Moniaux, N., 2001. Structural organization and classification of the human mucin genes. Front. Biosci. 6, d1192–d1192. https://doi.org/10.2741/Moniaux

Montuschi, P., Peters-Golden, M.L., 2010. Leukotriene modifiers for asthma treatment. Clin. Exp. Allergy 40, 1732–1741. https://doi.org/10.1111/j.1365-2222.2010.03630.x

Morillas, H.N., Zariwala, M., Knowles, M.R., 2007. Genetic Causes of Bronchiectasis: Primary Ciliary Dyskinesia. Respiration 74, 252–263. https://doi.org/10.1159/000101783

Morrow, T., Felcone, L.H., 2004. Defining the difference: What Makes Biologics Unique. Biotechnol. Healthc. 1, 24–9.

Mucenski, M.L., Nation, J.M., Thitoff, A.R., Besnard, V., Xu, Y., Wert, S.E., Harada, N., Taketo, M.M., Stahlman, M.T., Whitsett, J.A., 2005. B-Catenin Regulates Differentiation of Respiratory Epithelial Cells in Vivo. Am. J. Physiol. - Lung Cell. Mol. Physiol. 289, 971–979. https://doi.org/10.1152/ajplung.00172.2005

Mulhall, A.M., Droege, C.A., Ernst, N.E., Panos, R.J., Zafar, M.A., 2015. Phosphodiesterase 4 inhibitors for the treatment of chronic obstructive pulmonary disease: A review of current and developing drugs. Expert Opin.

Investig. Drugs 24, 1597–1611. https://doi.org/10.1517/13543784.2015.1094054

Muyldermans, S., Atarhouch, T., Saldanha, J., Barbosa, J.A.R.G., Hamers, R., 1994. Sequence and structure of V H domain from naturally occurring camel heavy chain immunoglobulins lacking light chains. Protein Eng. Des. Sel. 7, 1129–1135. https://doi.org/10.1093/protein/7.9.1129

Muyldermans, S., Baral, T.N., Retamozzo, V.C., De Baetselier, P., De Genst, E., Kinne, J., Leonhardt, H., Magez, S., Nguyen, V.K., Revets, H., Rothbauer, U., Stijlemans, B., Tillib, S., Wernery, U., Wyns, L., Hassanzadeh-Ghassabeh, Gh., Saerens, D., 2009. Camelid immunoglobulins and nanobody technology. Vet. Immunol. Immunopathol. 128, 178–183. https://doi.org/10.1016/j.vetimm.2008.10.299

Nadel, J.A., 2001. Role of epidermal growth factor receptor activation in regulating mucin synthesis. Respir. Res. 2, 85–89. https://doi.org/10.1186/rr43

Nguyen, S.V., Puthuveetil, N.P., Petrone, J.R., Kirkland, J.L., Gaffney, K., Tabron, C.L., Wax, N., Duncan, J., King, S., Marlow, R., Reese, A.L., Yarmosh, D.A., McConnell, H.H., Fernandes, A.S., Bagnoli, J., Benton, B., Jacobs, J.L., 2024. The ATCC genome portal: 3,938 authenticated microbial reference genomes. Microbiol. Resour. Announc. 13. https://doi.org/10.1128/mra.01045-23

Nicholls, J., Dong, X.P., Jiang, G., Peiris, M., 2003. SARS: Clinical virology and pathogenesis. Respirology 8. https://doi.org/10.1046/j.1440-1843.2003.00517.x

Nicod, L.P., 2005. Lung defences: an overview: TABLE 1—. Eur. Respir. Rev. 14, 45–50. https://doi.org/10.1183/09059180.05.00009501

Nisonoff, A., Rivers, M.M., 1961. Recombination of a mixture of univalent antibody fragments of different specificity. Arch. Biochem. Biophys. 93, 460–462. https://doi.org/10.1016/0003-9861(61)90296-X

Nord, K., Gunneriusson, E., Ringdahl, J., Ståhl, S., Uhlén, M., Nygren, P.-Å.Å., 1997. Binding proteins selected from combinatorial libraries of an α-helical bacterial receptor domain. Nat. Biotechnol. 15, 772–777. https://doi.org/10.1038/nbt0897-772

Nuttall, S.D., Krishnan, U.V., Doughty, L., Nathanielsz, A., Ally, N., Pike, R.N., Hudson, P.J., Kortt, A.A., Irving, R.A., 2002. A naturally occurring NAR variable domain binds the Kgp protease from Porphyromonas gingivalis. FEBS Lett. 516, 80–86. https://doi.org/10.1016/S0014-5793(02)02506-1

Nuttall, S.D., Krishnan, U.V., Hattarki, M., De Gori, R., Irving, R.A., Hudson, P.J., 2001. Isolation of the new antigen receptor from wobbegong sharks, and use as a scaffold for the display of protein loop libraries. Mol. Immunol. 38, 313–326. https://doi.org/10.1016/S0161-5890(01)00057-8

Olusanya, T.O.B., Ahmad, R.R.H., Ibegbu, D.M., Smith, J.R., Elkordy, A.A., Haj Ahmad, R., Ibegbu, D.M., Smith, J.R., Elkordy, A.A., 2018. Liposomal Drug Delivery Systems and Anticancer Drugs. Molecules 23, 907–907. https://doi.org/10.3390/molecules23040907

Oray, M., Abu Samra, K., Ebrahimiadib, N., Meese, H., Foster, C.S., 2016. Long-term side effects of glucocorticoids. Expert Opin. Drug Saf. 15, 457–465. https://doi.org/10.1517/14740338.2016.1140743

Ordovas-Montanes, J., Dwyer, D.F., Nyquist, S.K., Buchheit, K.M., Vukovic, M., Deb, C., Wadsworth, M.H., Hughes, T.K., Kazer, S.W., Yoshimoto, E., Cahill, K.N., Bhattacharyya, N., Katz, H.R., Berger, B., Laidlaw, T.M., Boyce, J.A., Barrett, N.A., Shalek, A.K., 2018. Allergic inflammatory memory in human respiratory epithelial progenitor cells. Nature 560, 649–654. https://doi.org/10.1038/s41586-018-0449-8

Osipiuk, J., Azizi, S.A., Dvorkin, S., Endres, M., Jedrzejczak, R., Jones, K.A., Kang, S., Kathayat, R.S., Kim, Y., Lisnyak, V.G., Maki, S.L., Nicolaescu, V., Taylor, C.A., Tesar, C., Zhang, Y.A., Zhou, Z., Randall, G., Michalska, K., Snyder, S.A., Dickinson, B.C., Joachimiak, A., 2021. Structure of papain-like protease from SARS-CoV-2 and its complexes with non-covalent inhibitors. Nat. Commun. 12. https://doi.org/10.1038/s41467-021-21060-3

Otieno, J.R., Cherry, J.L., Spiro, D.J., Nelson, M.I., Trovão, N.S., 2022. Origins and Evolution of Seasonal Human Coronaviruses. Viruses 14. https://doi.org/10.3390/v14071551

Paggiaro, P., Bacci, E., 2011. Montelukast in asthma: A review of its efficacy and place in therapy. Ther. Adv. Chronic Dis. 2, 47–58. https://doi.org/10.1177/2040622310383343

Panagides, N., Zacchi, L.F., De Souza, M.J., Morales, R.A.V., Karnowski, A., Liddament, M.T., Owczarek, C.M., Mahler, S.M., Panousis, C., Jones, M.L., Fercher, C., 2022. Evaluation of Phage Display Biopanning Strategies for the Selection of Anti-Cell Surface Receptor Antibodies. Int. J. Mol. Sci. 23. https://doi.org/10.3390/ijms23158470

Pant, N., Hultberg, A., Zhao, Y., Svensson, L., Pan-Hammarström, Q., Johansen, K., Pouwels, P.H., Ruggeri, F.M., Hermans, P., Frenken, L., Borén, T., Marcotte, H., Hammarström, L., Pan-Hammarström, Q., Johansen, K., Pouwels, P.H., Ruggeri, F.M., Hermans, P., Frenken, L., Borén, T., Marcotte, H., Hammarström, L., 2006. Lactobacilli expressing variable domain of llama heavy-chain antibody fragments (lactobodies) confer protection against rotavirus-induced diarrhea. J. Infect. Dis. 194, 1580–1588. https://doi.org/10.1086/508747

Park, J.W., 2002. Liposome-based drug delivery in breast cancer treatment. Breast Cancer Res. 4, 95–95. https://doi.org/10.1186/bcr432

Parthiban, K., Perera, R.L., Sattar, M., Huang, Y., Mayle, S., Masters, E., Griffiths, D., Surade, S., Leah, R., Dyson, M.R., McCafferty, J., 2019. A comprehensive search of functional sequence space using large mammalian display libraries created by gene editing. mAbs 11, 884–898. https://doi.org/10.1080/19420862.2019.1618673

Pedersen, S.L., Tofteng, A.P., Malik, L., Jensen, K.J., 2012. Microwave heating in solid-phase peptide synthesis. Chem Soc Rev 41, 1826–1844. https://doi.org/10.1039/c1cs15214a

Pelaia, C., Vatrella, A., Bruni, A., Terracciano, R., Pelaia, G., 2018. Benralizumab in the treatment of severe asthma: design, development and potential place in therapy. Drug Des. Devel. Ther. 12, 619–628. https://doi.org/10.2147/DDDT.S155307

Pettersen, E.F., Goddard, T.D., Huang, C.C., Couch, G.S., Greenblatt, D.M., Meng, E.C., Ferrin, T.E., 2004. UCSF Chimera—A visualization system for exploratory research and analysis. J. Comput. Chem. 25, 1605–1612. https://doi.org/10.1002/jcc.20084

Plasschaert, L.W., Žilionis, R., Choo-Wing, R., Savova, V., Knehr, J., Roma, G., Klein, A.M., Jaffe, A.B., 2018. A single-cell atlas of the airway epithelium reveals the CFTR-rich pulmonary ionocyte. Nature 560, 377–381. https://doi.org/10.1038/s41586-018-0394-6

Plückthun, A., 2012. Ribosome display: A perspective. Methods Mol. Biol. 805, 13–28.

Proud, D. (Ed.), 2008. The pulmonary epithelium in health and disease. John Wiley & Sons, Chichester, England ; Hoboken, NJ.

Quint, J.K., Millett, E.R.C., Joshi, M., Navaratnam, V., Thomas, S.L., Hurst, J.R., Smeeth, L., Brown, J.S., 2016. Changes in the incidence, prevalence and mortality of bronchiectasis in the UK from 2004 to 2013: A population-based cohort study. Eur. Respir. J. 47, 186–193. https://doi.org/10.1183/13993003.01033-2015

Ra, S.H., Lim, J.S., Kim, G.U., Kim, M.J., Jung, J., Kim, S.H., 2021. Upper respiratory viral load in asymptomatic individuals and mildly symptomatic patients with SARS-CoV-2 infection. Thorax 76, 61–63. https://doi.org/10.1136/thoraxjnl-2020-215042

Ramalho, A.S., Amato, F., Gentzsch, M., 2023. Patient-derived cell models for personalized medicine approaches in cystic fibrosis. J. Cyst. Fibros. Off. J. Eur. Cyst. Fibros. Soc. 22 Suppl 1, S32–S38. https://doi.org/10.1016/j.jcf.2022.11.007

Ramamoorthy, S., Cidlowski, J.A., 2016. Corticosteroids-Mechanisms of Action in Health and Disease. Rheum Clin North AM 42, 15–31. https://doi.org/10.1016/j.rdc.2015.08.002

Rashidian, M., Wang, L., Edens, J.G., Jacobsen, J.T., Hossain, I., Wang, Q., Victora, G.D., Vasdev, N., Ploegh, H., Liang, S.H., 2016. Enzyme-Mediated Modification of Single-Domain Antibodies for Imaging Modalities with Different Characteristics. Angew. Chem. 128, 538–543. https://doi.org/10.1002/ange.201507596

Ray, A., Kolls, J.K., 2017. Neutrophilic Inflammation in Asthma and Association with Disease Severity. Trends Immunol. 38, 942–954. https://doi.org/10.1016/j.it.2017.07.003

Raybould, M.I.J., Turnbull, O.M., Suter, A., Guloglu, B., Deane, C.M., 2024. Contextualising the developability risk of antibodies with lambda light chains using enhanced therapeutic antibody profiling. Commun. Biol. 7, 62–62. https://doi.org/10.1038/s42003-023-05744-8

Reeves, S.R., Barrow, K.A., White, M.P., Rich, L.M., Naushab, M., Debley, J.S., 2018. Stability of gene expression by primary bronchial epithelial cells over increasing passage number. BMC Pulm. Med. 18. https://doi.org/10.1186/s12890-018-0652-2

Revets, H., De Baetselier, P., Muyldermans, S., 2005. Nanobodies as novel agents for cancer therapy. Expert Opin. Biol. Ther. 5, 111–124. https://doi.org/10.1517/14712598.5.1.111

Richard, G., Meyers, A.J., McLean, M.D., Arbabi-Ghahroudi, M., MacKenzie, R., Hall, J.C., 2013. In Vivo Neutralization of α-Cobratoxin with High-Affinity Llama Single-Domain Antibodies (VHHs) and a VHH-Fc Antibody. PLoS ONE 8, e69495–e69495. https://doi.org/10.1371/journal.pone.0069495

Richards, D.A., 2018. Exploring alternative antibody scaffolds: Antibody fragments and antibody mimics for targeted drug delivery. Drug Discov. Today Technol. 30, 35–46. https://doi.org/10.1016/j.ddtec.2018.10.005

Ridolo, E., Pucciarini, F., Nizi, M.C., Makri, E., Kihlgren, P., Panella, L., Incorvaia, C., 2020. Mabs for treating asthma: omalizumab, mepolizumab, reslizumab, benralizumab, dupilumab. Hum. Vaccines Immunother. 16, 2349–2356. https://doi.org/10.1080/21645515.2020.1753440

Ries, J., Kaplan, C., Platonova, E., Eghlidi, H., Ewers, H., 2012. A simple, versatile method for GFP-based super-resolution microscopy via nanobodies. Nat. Methods 9, 582–584. https://doi.org/10.1038/nmeth.1991

Riordan, J.R., Rommens, J.M., Kerem, B.-S., Alon, N., Rozmahel, R., Grzelczak, Z., Zielenski, J., Lok, S., Plavsic, N., Chou, J.-L., Drumm, M.L., Iannuzzi, M.C., Collins, F.S., Tsui, L.-C., 1989. Identification of the Cystic Fibrosis Gene: Cloning and Characterization of Complementary DNA. Science 245, 1066–1073. https://doi.org/10.1126/science.2475911

Rogers, D.F., 2004. Airway mucus hypersecretion in asthma: an undervalued pathology? Curr. Opin. Pharmacol. 4, 241–250. https://doi.org/10.1016/j.coph.2004.01.011

Rogers, D.F., 1994. Airway goblet cells: responsive and adaptable front-line defenders. Eur. Respir. J. 7, 1690–1706.

Rondot, S., Koch, J., Breitling, F., Dübel, S., 2001. A helper phage to improve single-chain antibody presentation in phage display. Nat. Biotechnol. 19, 75–78. https://doi.org/10.1038/83567

Roovers, R.C., Vosjan, M.J.W.D., Laeremans, T., el Khoulati, R., De Bruin, R.C.G., Ferguson, K.M., Verkleij, A.J., Van Dongen, G.A.M.S., Van Bergen En Henegouwen, P.M.P., 2011. A biparatopic anti-EGFR nanobody efficiently inhibits solid tumour growth. Int. J. Cancer 129, 2013–2024. https://doi.org/10.1002/ijc.26145

Rosenwasser, Y., Berger, I., Loewy, Z.G., 2022. Therapeutic Approaches for Chronic Obstructive Pulmonary Disease (COPD) Exacerbations. Pathogens 11, 1–22. https://doi.org/10.3390/pathogens11121513

Rosowski, S., Becker, S., Toleikis, L., Valldorf, B., Grzeschik, J., Demir, D., Willenbücher, I., Gaa, R., Kolmar, H., Zielonka, S., Krah, S., 2018. A novel one-step approach for the construction of yeast surface display Fab antibody libraries. Microb. Cell Factories 17, 3–3. https://doi.org/10.1186/s12934-017-0853-z

Rostovtsev, V.V., Green, L.G., Fokin, V.V., Sharpless, K.B., 2002. A Stepwise Huisgen Cycloaddition Process: Copper(I)-Catalyzed Regioselective "Ligation" of Azides and Terminal Alkynes. Angew. Chem. Int. Ed. 41, 2596–2599. https://doi.org/10.1002/1521-3773(20020715)41:14<2596::AID-ANIE2596>3.0.CO;2-4

Roux, K.H., Greenberg, A.S., Greene, L., Strelets, L., Avila, D., Mckinney, E.C., Flajnik, M.F., 1998. Structural analysis of the nurse shark (new) antigen receptor (NAR): Molecular convergence of NAR and unusual mammalian immunoglobulins. Proc. Natl. Acad. Sci. 95, 11804–11809. https://doi.org/10.1073/pnas.95.20.11804

Ruiz García, S., Deprez, M., Lebrigand, K., Cavard, A., Paquet, A., Arguel, M.-J., Magnone, V., Truchi, M., Caballero, I., Leroy, S., Marquette, C.-H., Marcet, B., Barbry, P., Zaragosi, L.-E., 2019. Novel dynamics of human mucociliary differentiation revealed by single-cell RNA sequencing of nasal epithelial cultures. Development 146. https://doi.org/10.1242/dev.177428

Rumfelt, L.L., Diaz, M., Lohr, R.L., Mochon, E., Flajnik, M.F., 2004. Unprecedented Multiplicity of Ig Transmembrane and Secretory mRNA Forms in the Cartilaginous Fish. J. Immunol. 173, 1129–1139.

Ryman, J.T., Meibohm, B., 2017. Pharmacokinetics of Monoclonal Antibodies. CPT Pharmacomet. Syst. Pharmacol. 6, 576–588. https://doi.org/10.1002/psp4.12224

Saggy, I., Wine, Y., Shefet-Carasso, L., Nahary, L., Georgiou, G., Benhar, I., 2012. Antibody isolation from immunized animals: Comparison of phage display and antibody discovery via v gene repertoire mining. Protein Eng. Des. Sel. 25, 539–549. https://doi.org/10.1093/protein/gzs060

Salema, V., Fernández, L.Á., 2013. High yield purification of nanobodies from the periplasm of E. coli as fusions with the maltose binding protein. Protein Expr. Purif. 91, 42–48. https://doi.org/10.1016/j.pep.2013.07.001

SARS : how a global epidemic was stopped, 2006. . World Health Organization, Western Pacific Region.

Sawicki, S.G., Sawicki, D.L., Siddell, S.G., 2007. A Contemporary View of Coronavirus Transcription. J. Virol. 81, 20–29. https://doi.org/10.1128/jvi.01358-06

Schägger, H., von Jagow, G., 1991. Blue native electrophoresis for isolation of membrane protein complexes in enzymatically active form. Anal. Biochem. 199, 223–231. https://doi.org/10.1016/0003-2697(91)90094-A

Scheinfeld, N., 2003. Adalimumab (HUMIRA): a review. J. Drugs Dermatol. JDD 2, 375–7.

Schikowski, T., Mills, I.C., Anderson, H.R., Cohen, A., Hansell, A., Kauffmann, F., Krämer, U., Marcon, A., Perez, L., Sunyer, J., Probst-Hensch, N., Künzli, N., Kramer, U., Marcon, A., Perez, L., Sunyer, J., Probst-Hensch, N., Kunzli, N., 2014. Ambient air pollution: a cause of COPD? Eur. Respir. J. 43, 250–263. https://doi.org/10.1183/09031936.00100112

Schleimer, R.P., Kato, A., Kern, R., Kuperman, D., Avila, P.C., 2007. Epithelium: At the interface of innate and adaptive immune responses. J. Allergy Clin. Immunol. 120, 1279–1284. https://doi.org/10.1016/j.jaci.2007.08.046

Schmitz, K.R., Bagchi, A., Roovers, R.C., Van Bergen En Henegouwen, P.M.P., Ferguson, K.M., 2013. Structural Evaluation of EGFR Inhibition Mechanisms for Nanobodies/VHH Domains. Structure 21, 1214–1224. https://doi.org/10.1016/j.str.2013.05.008

Schoeman, D., Fielding, B.C., 2019. Coronavirus envelope protein: current knowledge. Virol. J. 16. https://doi.org/10.1186/s12985-019-1182-0

Schulman, E.S., 2001. Development of a Monoclonal Anti-Immunoglobulin E Antibody (Omalizumab) for the Treatment of Allergic Respiratory Disorders. Am. J. Respir. Crit. Care Med. 164, S6–S11. https://doi.org/10.1164/ajrccm.164.supplement_1.2103025

Schumacher, D., Helma, J., Schneider, A.F.L.L., Leonhardt, H., Hackenberger, C.P.R.R., 2018. Nanobodies: Chemical Functionalization Strategies and Intracellular Applications. Angew. Chem. - Int. Ed. 57, 2314–2333. https://doi.org/10.1002/anie.201708459

Schwimmer, L.J., Huang, B., Giang, H., Cotter, R.L., Chemla-Vogel, D.S., Dy, F.V., Tam, E.M., Zhang, F., Toy, P., Bohmann, D.J., Watson, S.R., Beaber, J.W., Reddy, N., Kuan, H.-F., Bedinger, D.H., Rondon, I.J., 2013. Discovery of diverse and functional antibodies from large human repertoire antibody libraries. J. Immunol. Methods 391, 60–71. https://doi.org/10.1016/j.jim.2013.02.010

Scott, J.P., Peters-Golden, M., 2013. Antileukotriene agents for the treatment of lung disease. Am. J. Respir. Crit. Care Med. 188, 538–544. https://doi.org/10.1164/rccm.201301-0023PP

Shang, J., Wan, Y., Luo, C., Ye, G., Geng, Q., Auerbach, A., Li, F., 2020. Cell entry mechanisms of SARS-CoV-2. Proc. Natl. Acad. Sci. 117, 11727–11734. https://doi.org/10.1073/pnas.2003138117

Shapiro, J., Machattie, L., Eron, L., Ihler, G., Ippen, K., Beckwith, J., 1969. Isolation of Pure lac Operon DNA*. Nature 224, 768–774. https://doi.org/10.1038/224768a0

Sharma, M., Stucki, A.O., Verstraelen, S., Stedeford, T.J., Jacobs, A., Maes, F., Poelmans, D., Van Laer, J., Remy, S., Frijns, E., Allen, D.G., Clippinger, A.J., 2023. Human cell-based in vitro systems to assess respiratory toxicity: a case study using silanes. Toxicol. Sci. Off. J. Soc. Toxicol. 195, 213–230. https://doi.org/10.1093/toxsci/kfad074

Shelke, S., Shivange, V., Darekar, A., 2025. Antiviral Drug Development in The Post-COVID Era: Innovations, Challenges, and Future Perspectives in Pharmacy. https://doi.org/10.5281/ZENODO.15257666

Silva, S., Bicker, J., Falcão, A., Fortuna, A., 2023. Air-liquid interface (ALI) impact on different respiratory cell cultures. Eur. J. Pharm. Biopharm. 184, 62–82. https://doi.org/10.1016/j.ejpb.2023.01.013

Singh, M., Nalawade, S.A., Kumar, Drgk.R.P., Veeresh, K., Pahan, S., Dey, S., Gopi, H.N., 2023. HBTU Mediated Synthesis of α,β-Unsaturated γ-Lactams from E-α,β-Unsaturated γ-Amino Acids. Eur. J. Org. Chem. 26. https://doi.org/10.1002/ejoc.202300682

Small, Hamish., Stevens, T.S., Bauman, W.C., 1975. Novel ion exchange chromatographic method using conductimetric detection. Anal. Chem. 47, 1801–1809. https://doi.org/10.1021/ac60361a017

Smith, G.P., 1985. Filamentous Fusion Phage: Novel Expression Vectors That Display Cloned Antigens on the Virion Surface. Science 228, 1315–1317. https://doi.org/10.1126/science.4001944

Smith, G.P., Petrenko, V.A., 1997. Phage Display. Chem. Rev. 97, 391–410.

Smyth, D.G., Blumenfeld, O.O., Konigsberg, W., Derek Smyth, B.G., Konigsberg, W., 1964. Reactions of N-Ethylmaleimide with Peptides and Amino Acids. Biochem. J. 91, 589–595.

Soltes, G., Barker, H., Marmai, K., Pun, E., Yuen, A., Wiersma, E.J., 2003. A new helper phage and phagemid vector system improves viral display of antibody Fab fragments and avoids propagation of insert-less virions. J. Immunol. Methods 274, 233–244. https://doi.org/10.1016/S0022-1759(02)00294-6

Spina, D., 2014. Current and novel bronchodilators in respiratory disease. Curr. Opin. Pulm. Med. 20, 73–86. https://doi.org/10.1097/MCP.0000000000000012

Ståhl, E.E., Lindberg, A., Jansson, S.-A.A., Rönmark, E., Svensson, K., Andersson, F., Löfdahl, C.-G.G., Lundbäck, B., 2005. Health-related quality of life is related to COPD disease severity. Health Qual. Life Outcomes 3, 56–56. https://doi.org/10.1186/1477-7525-3-56

Stanfield, R.L., Dooley, H., Flajnik, M.F., Wilson, I.A., 2004. Crystal Structure of a Shark Single-Domain Antibody V Region in Complex with Lysozyme. Science 305, 1770–1773. https://doi.org/10.1126/science.1101148

Stark, Y., Venet, S., Schmid, A., 2017. Whole Cell Panning with Phage Display, in: Tiller, T. (Ed.), Synthetic Antibodies. Methods in Molecular Biology. Humana Press, New York, NY, pp. 67–91. https://doi.org/10.1007/978-1-4939-6857-2_5

Steeland, S., Vandenbroucke, R.E., Libert, C., 2016. Nanobodies as therapeutics: big opportunities for small antibodies. Drug Discov. Today 21, 1076–1113. https://doi.org/10.1016/j.drudis.2016.04.003

Steven, J., Müller, M.R., Carvalho, M.F., Ubah, O.C., Kovaleva, M., Donohoe, G., Baddeley, T., Cornock, D., Saunders, K., Porter, A.J., Barelle, C.J., 2017. In vitro maturation of a humanized shark VNAR domain to improve its biophysical properties to facilitate clinical development. Front. Immunol. 8. https://doi.org/10.3389/fimmu.2017.01361

Stewart, C.E., Torr, E.E., Mohd Jamili, N.H., Bosquillon, C., Sayers, I., 2012. Evaluation of Differentiated Human Bronchial Epithelial Cell Culture Systems for Asthma Research. J. Allergy 2012, 1–11. https://doi.org/10.1155/2012/943982

Studier, F.W., Moffatt, B.A., 1986. Use of bacteriophage T7 RNA polymerase to direct selective high-level expression of cloned genes. J. Mol. Biol. 189, 113–130. https://doi.org/10.1016/0022-2836(86)90385-2

Su, S., Wong, G., Shi, W., Liu, J., Lai, A.C.K., Zhou, J., Liu, W., Bi, Y., Gao, G.F., 2016. Epidemiology, Genetic Recombination, and Pathogenesis of Coronaviruses. Trends Microbiol. 24, 490–502. https://doi.org/10.1016/j.tim.2016.03.003

Suchsland, R., Appel, B., Virta, P., Müller, S., 2021. Synthesis of fully protected trinucleotide building blocks on a disulphide-linked soluble support. RSC Adv. 11, 3892–3896. https://doi.org/10.1039/d0ra10941j

Sun, Y., Huang, T., Hammarström, L., Zhao, Y., 2020. The Immunoglobulins: New Insights, Implications, and Applications. Annu. Rev. Anim. Biosci. 8, 145–169. https://doi.org/10.1146/annurev-animal-021419-083720

Tabtimmai, L., Suphakun, P., Srisook, P., Kiriwan, D., Phanthong, S., Kiatwuthinon, P., Chaicumpa, W., Choowongkomon, K., 2019. Cell-penetrable nanobodies (transbodies) that inhibit the tyrosine kinase activity of EGFR leading to the impediment of human lung adenocarcinoma cell motility and survival. J. Cell. Biochem. 120, 18077–18087. https://doi.org/10.1002/jcb.29111

Takeda, H., Ozawa, T., Zenke, H., Ohnuki, Y., Umeda, Y., Zhou, W., Tomoda, H., Takechi, A., Narita, K., Shimizu, T., Miyakawa, T., Ito, Y., Sawasaki, T., 2023. VNAR development through antigen immunization of Japanese topeshark (Hemitriakis japanica). Front. Bioeng. Biotechnol. 11. https://doi.org/10.3389/fbioe.2023.1265582

Tanha, J., Dubuc, G., Hirama, T., Narang, S.A., MacKenzie, C.R., 2002. Selection by phage display of llama conventional VH fragments with heavy chain antibody VHH properties. J. Immunol. Methods 263, 97–109. https://doi.org/10.1016/S0022-1759(02)00027-3

Thakur, A., Mei, S., Zhang, N., Zhang, K., Taslakjian, B., Lian, J., Wu, S., Chen, B., Solway, J., Chen, H.J., 2024. Pulmonary neuroendocrine cells: crucial players in respiratory function and airway-nerve communication. Front. Neurosci. 18, 1438188. https://doi.org/10.3389/fnins.2024.1438188

Tijink, B.M., Laeremans, T., Budde, M., Walsum, M.S., Dreier, T., de Haard, H.J., Leemans, C.R., Van Dongen, G.A.M.S., Stigter-Van Walsum, M., Dreier, T., de Haard, H.J., Leemans, C.R., Van Dongen, G.A.M.S., 2008. Improved tumor targeting of anti–epidermal growth factor receptor Nanobodies through albumin binding: taking advantage of modular Nanobody technology. Mol. Cancer Ther. 7, 2288–2297. https://doi.org/10.1158/1535-7163.MCT-07-2384

Tildy, B.E., Rogers, D.F., 2015. Therapeutic options for hydrating airway mucus in cystic fibrosis. Pharmacology 95, 117–132. https://doi.org/10.1159/000377638

Tiller, T., Schuster, I., Deppe, D., Siegers, K., Strohner, R., Herrmann, T., Berenguer, M., Poujol, D., Stehle, J., Stark, Y., Heßling, M., Daubert, D., Felderer, K., Kaden, S., Kölln, J., Enzelberger, M., Urlinger, S., 2013. A fully synthetic human Fab antibody library based on fixed VH/VL framework pairings with favorable biophysical properties. mAbs 5, 445–470.

Tokuhara, D., Álvarez, B., Mejima, M., Hiroiwa, T., Takahashi, Y., Kurokawa, S., Kuroda, M., Oyama, M., Kozuka-Hata, H., Nochi, T., Sagara, H., Aladin, F., Marcotte, H., Frenken, L.G.J., Iturriza-Gómara, M., Kiyono, H., Hammarström, L., Yuki, Y., 2013. Rice-based oral antibody fragment prophylaxis and therapy against rotavirus infection. J. Clin. Invest. 123, 3829–3838. https://doi.org/10.1172/JCI70266

Tornøe, C.W., Christensen, C., Meldal, M., 2002. Peptidotriazoles on solid phase: [1,2,3]-Triazoles by regiospecific copper(I)-catalyzed 1,3-dipolar cycloadditions of terminal alkynes to azides. J. Org. Chem. 67, 3057–3064. https://doi.org/10.1021/jo011148j

Tsai, C.H., Wang, K.T., Guo, X., Wu, T.M., 2023. Yeast Surface Dual Display Platform for Rapid Discovery of Shark VNAR from a Semi-Synthetic Library Followed by Next-Generation Sequencing. Appl. Sci. Switz. 13. https://doi.org/10.3390/app132011520

Tsao, P.N., Vasconcelos, M., Izvolsky, K.I., Qian, J., Lu, J., Cardoso, W.V., 2009. Notch signaling controls the balance of ciliated and secretory cell fates in developing airways. Development 136, 2297–2307. https://doi.org/10.1242/dev.034884

Turner, J., Jones, C.E., 2009. Regulation of mucin expression in respiratory diseases. Biochem. Soc. Trans. 37, 877–881. https://doi.org/10.1042/BST0370877

Tyrrell, D.A.J., Bynoe, M.L., 1966. Cultivation Of Viruses From A High Proportion Of Patients With Colds. The Lancet 287, 76–77. https://doi.org/10.1016/s0140-6736(66)92364-6

Valldorf, B., Hinz, S.C., Russo, G., Pekar, L., Mohr, L., Klemm, J., Doerner, A., Krah, S., Hust, M., Zielonka, S., 2022. Antibody display technologies: selecting the cream of the crop. Biol. Chem. 403, 455–477. https://doi.org/10.1515/hsz-2020-0377

Van De Donk, N.W.C.J., Dhimolea, E., 2012. Brentuximab vedotin. mAbs 4, 458–465. https://doi.org/10.4161/mabs.20230

Van Der Hoek, L., Pyrc, K., Jebbink, M.F., Vermeulen-Oost, W., Berkhout, R.J.M., Wolthers, K.C., Wertheim-van Dillen, P.M.E., Kaandorp, J., Spaargaren, J., Berkhout, B., 2004. Identification of a new human coronavirus. Nat. Med. 10, 368–373. https://doi.org/10.1038/nm1024

van der Vaart, J.M., Pant, N., Wolvers, D., Bezemer, S., Hermans, P.W., Bellamy, K., Sarker, S.A., van der Logt, C.P.E.E., Svensson, L., Verrips, C.T., Hammarstrom, L., Van Klinken, B.J.W.W., 2006. Reduction in morbidity of rotavirus induced diarrhoea in mice by yeast produced monovalent llama-derived antibody fragments. Vaccine 24, 4130–4137. https://doi.org/10.1016/j.vaccine.2006.02.045

Van Der Velden, V.H.J.J., 1998. Glucocorticoids: Mechanisms of action and anti-inflammatory potential in asthma. Mediators Inflamm. 7, 229–237. https://doi.org/10.1080/09629359890910

Venkayya, R., Lam, M., Willkom, M., Grünig, G., Corry, D.B., Erle, D.J., 2002. The Th2 Lymphocyte Products IL-4 and IL-13 Rapidly Induce Airway Hyperresponsiveness Through Direct Effects on Resident Airway Cells, Am. J. Respir. Cell Mol. Biol.

Vidarsson, G., Dekkers, G., Rispens, T., 2014. IgG Subclasses and Allotypes: From Structure to Effector Functions. Front. Immunol. 5. https://doi.org/10.3389/fimmu.2014.00520

Vijgen, L., Keyaerts, E., Moës, E., Thoelen, I., Wollants, E., Lemey, P., Vandamme, A.-M., Van Ranst, M., 2005. Complete Genomic Sequence of Human Coronavirus OC43: Molecular Clock Analysis Suggests a Relatively Recent Zoonotic Coronavirus Transmission Event. J. Virol. 79, 1595–1604. https://doi.org/10.1128/jvi.79.3.1595-1604.2005

Waldmeier, L., Hellmann, I., Gutknecht, C.K., Wolter, F.I., Cook, S.C., Reddy, S.T., Grawunder, U., Beerli, R.R., 2016. Transpo-mAb display: Transposition-mediated B cell display and functional screening of full-length IgG antibody libraries. mAbs 8, 726–740. https://doi.org/10.1080/19420862.2016.1160990

Waldo, G.S., Standish, B.M., Berendzen, J., Terwilliger, T.C., 1999. Rapid protein-folding assay using green fluorescent protein, NATURE BIOTECHNOLOGY.

Walker, A., Pottinger, G., Scott, A., Hopkins, C., 2020. Anosmia and loss of smell in the era of covid-19. The BMJ 370. https://doi.org/10.1136/bmj.m2808

Wang, M., Wei, L., Xiang, H., Ren, B., Liu, X., Jiang, L., Yang, N., Shi, J., 2022. A megadiverse naïve library derived from numerous camelids for efficient and rapid development of VHH antibodies. Anal. Biochem. 657. https://doi.org/10.1016/j.ab.2022.114871

Wang, Y., Wrennall, J.A., Cai, Z., Li, H., Sheppard, D.N., 2014. Understanding how cystic fibrosis mutations disrupt CFTR function: From single molecules to animal models. Int. J. Biochem. Cell Biol. 52, 47–57. https://doi.org/10.1016/j.biocel.2014.04.001

Ward, E.S., Güssow, D., Griffiths, A.D., Jones, P.T., Winter, G., 1989. Binding activities of a repertoire of single immunoglobulin variable domains secreted from Escherichia coli. Nature 341, 544–546. https://doi.org/10.1038/341544a0

WHO COVID-19 dashboard [WWW Document], 2025. . WHO Data. URL https://data.who.int/dashboards/covid19/cases (accessed 7.8.25).

Wilson, R.K., 1993. High-throughput purification of M13 templates for DNA sequencing. BioTechniques 15, 414–20, 422.

Winter, G., Griffiths, A.D., Hawkins, R.E., Hoogenboom, H.R., 1994. Making Antibodies by Phage Display Technology. Annu. Rev. Immunol. 12, 433–455. https://doi.org/10.1146/annurev.iy.12.040194.002245

Woehlk, C., Ramu, S., Sverrild, A., Nieto-Fontarigo, J.J., Vázquez-Mera, S., Cerps, S., Pulga, A., Andreasson, L.M., Eriksen, L.L., Dyhre-Petersen, N., Menzel, M., Klein, D.K., Hansen, S., Uller, L., Porsbjerg, C., 2023. Allergen Immunotherapy Enhances Airway Epithelial Antiviral Immunity in Patients with Allergic Asthma (VITAL Study): A Double-Blind Randomized Controlled Trial. Am. J. Respir. Crit. Care Med. 207, 1161–1170. https://doi.org/10.1164/rccm.202209-1708oc

Wong, J.P., Yang, H., Blasetti, K.L., Schnell, G., Conley, J., Schofield, L.N., 2003. Liposome delivery of ciprofloxacin against intracellular Francisella tularensis infection. J. Controlled Release 92, 265–273. https://doi.org/10.1016/S0168-3659(03)00358-4

Woo, P.C.Y., Lau, S.K.P., Chu, C., Chan, K., Tsoi, H., Huang, Y., Wong, B.H.L., Poon, R.W.S., Cai, J.J., Luk, W., Poon, L.L.M., Wong, S.S.Y., Guan, Y., Peiris, J.S.M., Yuen, K., 2005. Characterization and Complete Genome Sequence of a Novel Coronavirus, Coronavirus HKU1, from Patients with Pneumonia. J. Virol. 79, 884–895. https://doi.org/10.1128/jvi.79.2.884-895.2005

World Development Report 2022: Finance for an Equitable Recovery, 2022. . The World Bank. https://doi.org/10.1596/978-1-4648-1730-4

World Health Organisation, 2020a. Chronic obstructive pulmonary disease (COPD).

World Health Organisation, 2020b. Asthma.

Wu, F., Zhao, S., Yu, B., Chen, Y.M., Wang, W., Song, Z.G., Hu, Y., Tao, Z.W., Tian, J.H., Pei, Y.Y., Yuan, M.L., Zhang, Y.L., Dai, F.H., Liu, Y., Wang, Q.M., Zheng, J.J., Xu, L., Holmes, E.C., Zhang, Y.Z., 2020. A new coronavirus associated with human respiratory disease in China. Nature 579, 265–269. https://doi.org/10.1038/s41586-020-2008-3

Wu, T., Huang, H., Sheng, Y., Shi, H., Min, Y., Liu, Y., 2018. Transglutaminase mediated PEGylation of nanobodies for targeted nano-drug delivery. J. Mater. Chem. B 6, 1011–1017. https://doi.org/10.1039/c7tb03132g

Wu, T., Wrennall, J.A., Dang, H., Baines, D.L., Tarran, R., 2023. Passaging Primary Human Bronchial Epithelia Reduces CFTR-Mediated Fluid Transport and Alters mRNA Expression. Cells 12. https://doi.org/10.3390/cells12070997

Xu, R.-H., He, J.-F., Evans, M.R., Peng, G.-W., Field, H.E., Yu, D.-W., Lee, C.-K., Luo, H.-M., Lin, W.-S., Lin, P., Li, L.-H., Liang, W.-J., Lin, J.-Y., Schnur, A., 2004.

Epidemiologic clues to SARS origin in China. Emerg. Infect. Dis. 10, 1030–7. https://doi.org/10.3201/eid1006.030852

Yaghi, A., Dolovich, M., 2016. Airway Epithelial Cell Cilia and Obstructive Lung Disease. Cells 5, 40. https://doi.org/10.3390/cells5040040

Yan, J., Li, G., Hu, Y., Ou, W., Wan, Y., 2014. Construction of a synthetic phage-displayed Nanobody library with CDR3 regions randomized by trinucleotide cassettes for diagnostic applications. J. Transl. Med. 12. https://doi.org/10.1186/s12967-014-0343-6

You, Y., Yang, X., Hung, D., Yang, Q., Wu, T., Deng, M., 2024. Asymptomatic COVID-19 infection: diagnosis, transmission, population characteristics. BMJ Support. Palliat. Care 14, E220–E227. https://doi.org/10.1136/bmjspcare-2020-002813

Young, C.L., Britton, Z.T., Robinson, A.S., 2012. Recombinant protein expression and purification: A comprehensive review of affinity tags and microbial applications. Biotechnol. J. 7, 620–634. https://doi.org/10.1002/biot.201100155

Zadeh, A.S., Grässer, A., Dinter, H., Hermes, M., Schindowski, K., 2019. Efficient Construction and Effective Screening of Synthetic Domain Antibody Libraries. Methods Protoc. 2, 17–17. https://doi.org/10.3390/mps2010017

Zaki, A.M., van Boheemen, S., Bestebroer, T.M., Osterhaus, A.D.M.E., Fouchier, R.A.M., 2012. Isolation of a Novel Coronavirus from a Man with Pneumonia in Saudi Arabia. N. Engl. J. Med. 367, 1814–1820. https://doi.org/10.1056/nejmoa1211721

Zhang, C., Pasquier, L.D., Hsu, E., Du Pasquier, L., Hsu, E., Pasquier, L.D., Hsu, E., Du Pasquier, L., Hsu, E., 2013. Shark IgW C Region Diversification through RNA Processing and Isotype Switching. J. Immunol. 191, 3410–3418. https://doi.org/10.4049/jimmunol.1301257

Zhang, N., Tang, W., Torres, L., Wang, X., Ajaj, Y., Zhu, L., Luan, Y., Zhou, H., Wang, Y., Zhang, D., Kurbatov, V., Khan, S.A., Kumar, P., Hidalgo, A., Wu, D., Lu, J., 2024. Cell surface RNAs control neutrophil recruitment. Cell 187, 846-860.e17. https://doi.org/10.1016/j.cell.2023.12.033

Zhao, H., Cui, K., MUSCHENBORN, A., WONG, S.T.C., 2008. Progress of engineered antibody-targeted molecular imaging for solid tumors (review). Mol. Med. Rep. 1, 131–134. https://doi.org/10.3892/mmr.1.1.131

Zhu, N., Zhang, D., Wang, W., Li, X., Yang, B., Song, J., Zhao, X., Huang, B., Shi, W., Lu, R., Niu, P., Zhan, F., Ma, X., Wang, D., Xu, W., Wu, G., Gao, G.F., Tan, W., 2020. A Novel Coronavirus from Patients with Pneumonia in China, 2019. N. Engl. J. Med. 382, 727–733. https://doi.org/10.1056/nejmoa2001017

Zielonka, S., Empting, M., Grzeschik, J., Könning, D., Barelle, C.J., Kolmar, H., 2015. Structural insights and biomedical potential of IgNAR scaffolds from sharks. mAbs 7, 15–25. https://doi.org/10.4161/19420862.2015.989032

Zipfel, P.F., Skerka, C., 2022. From magic bullets to modern therapeutics: Paul Ehrlich, the German immunobiologist and physician coined the term ‘complement.’ Mol. Immunol. 150, 90–98. https://doi.org/10.1016/j.molimm.2022.08.002

Appendix 1 Maps of Plasmids

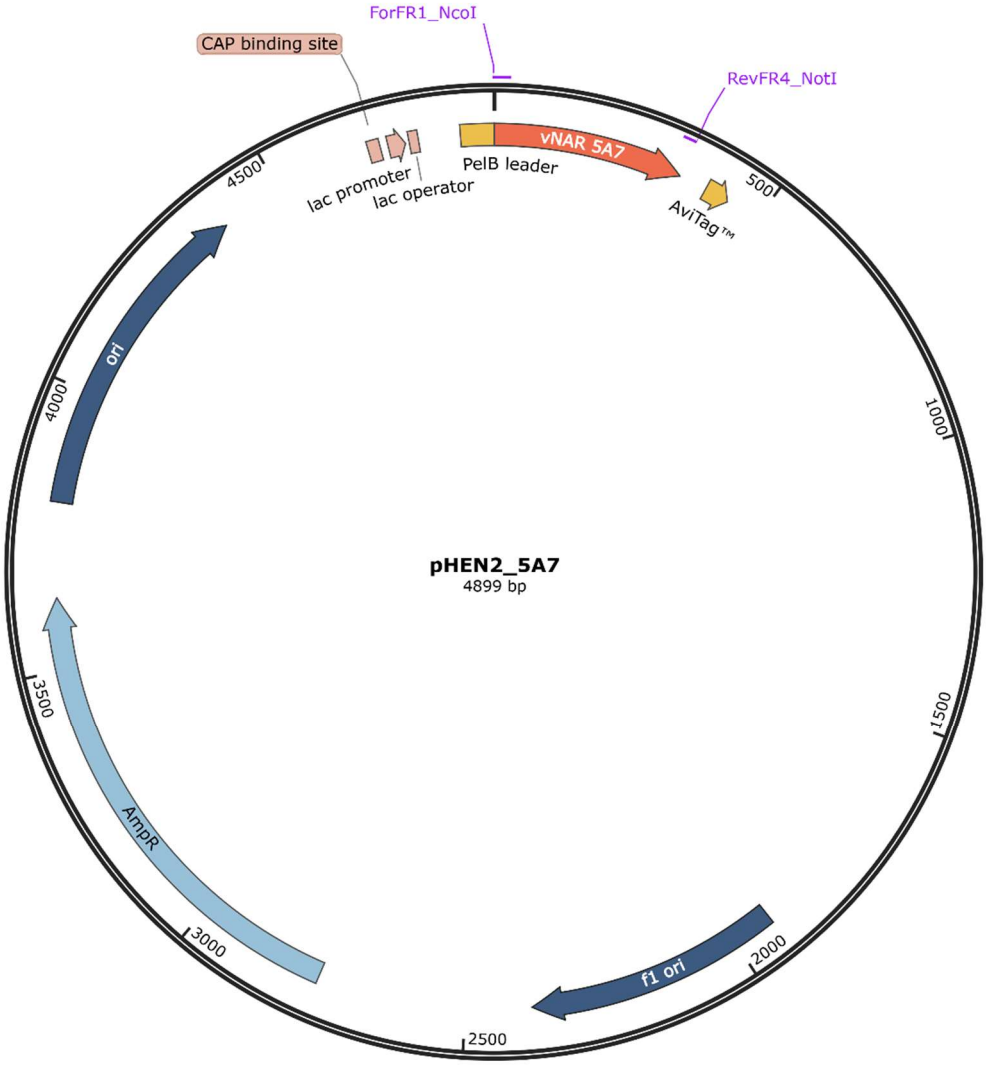


Figure A. 1 Representative plasmid map pHEN2_5A7 obtained from Dooley, Flajnik and Porter (2003).

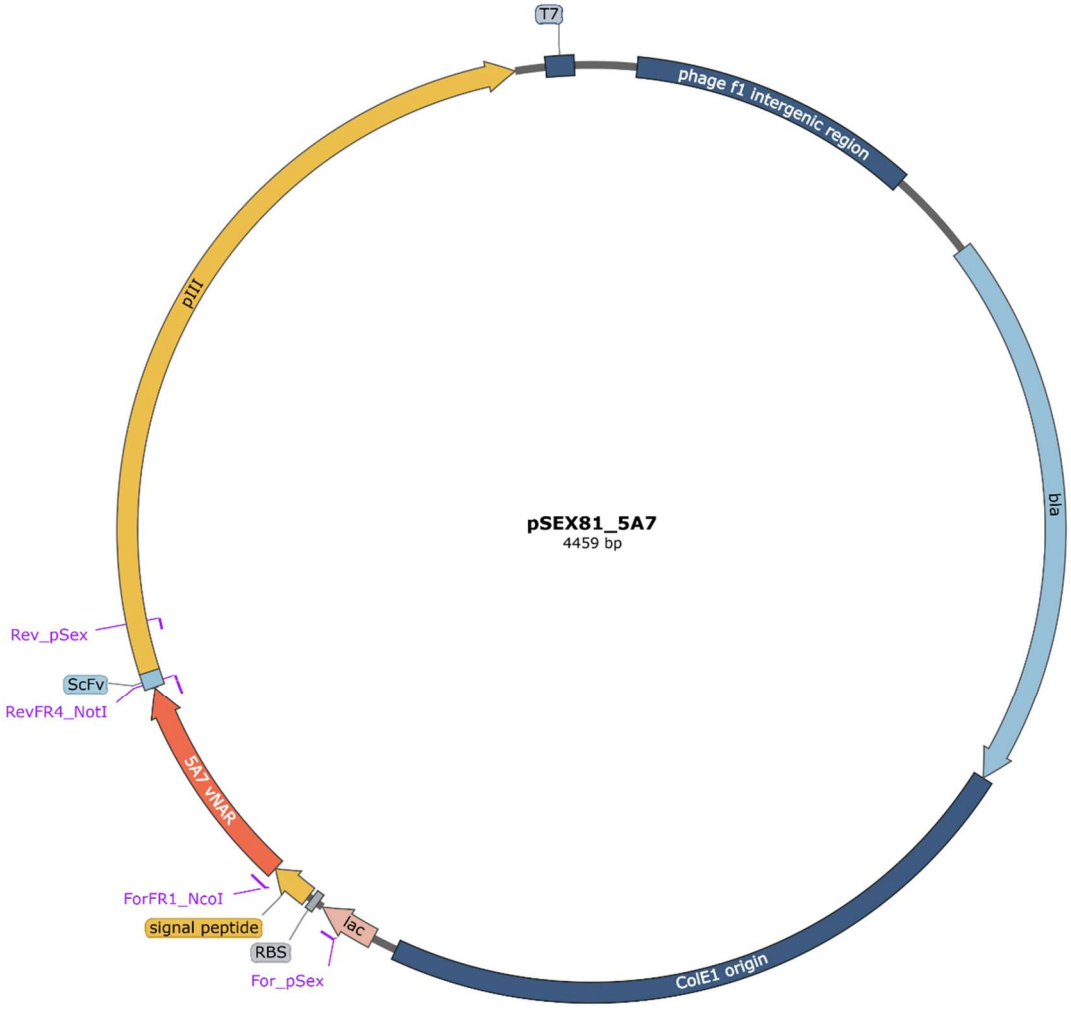


Figure A. 2 Representative map of the pSEX81_5A7 phagemid used for the packaging of 5A7 and other vNARs by M13KO7 phages.

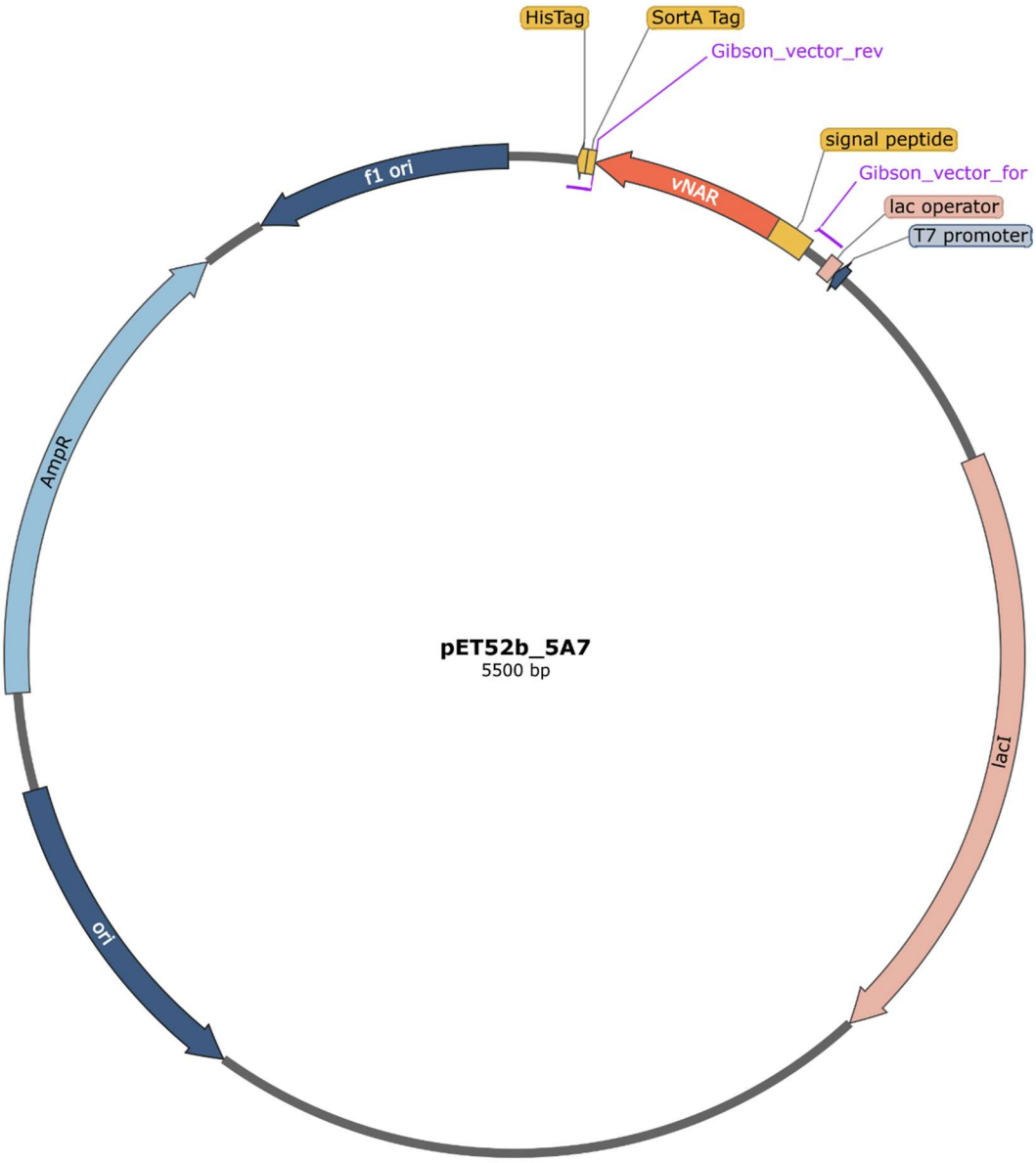


Figure A. 3 Representative map of the pET52b_5A7 plasmid constructed by Gibson assembly for the expression and purification of vNAR 5A7 in E. coli.

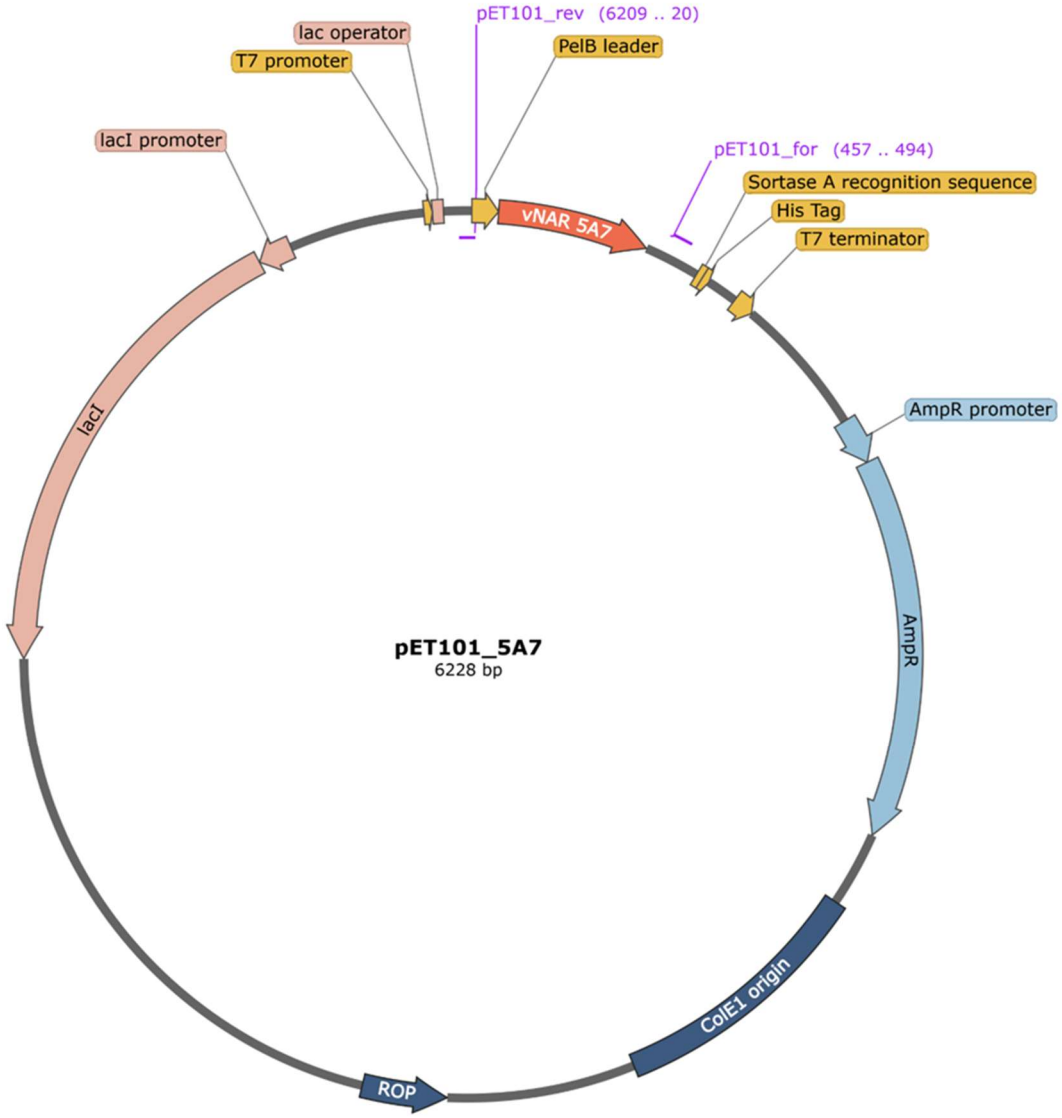
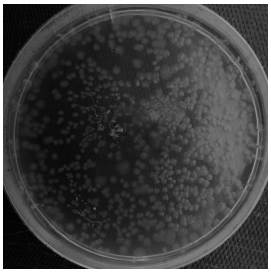


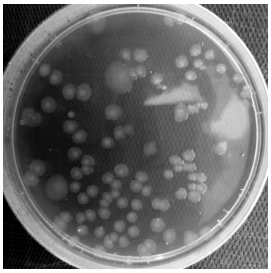
Figure A. 4 Representative map of the pET101_5A7 plasmid constructed by Gibson assembly for the expression and purification of vNAR 5A7 in E. coli.

Appendix 2 Agar Plates

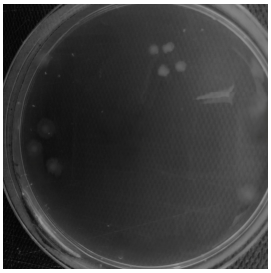
First Library Construction



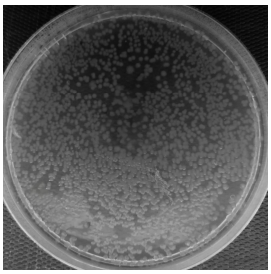
Library 10^{-2}



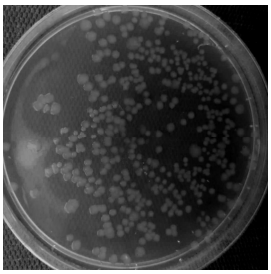
Library 10^{-3}



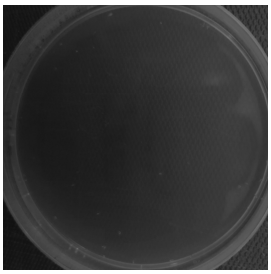
Library 10^{-4}



Library positive control 10^{-1}



Library positive control 10^{-2}

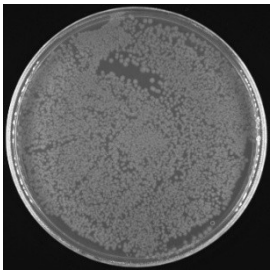


Library Negative control

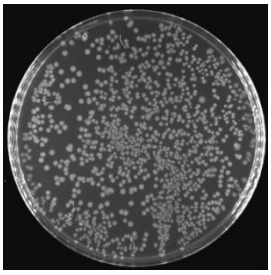
Figure A. 5 Pictures of agar plates inoculated with various dilutions of nanobody library 1 to determine the transformation titre.

Phage solutions at various concentrations were used to infect TG1 cells and plated on 2X TY-GA plates. pSEX81 plasmid transformed into TG1 cells was used as a positive control, and 50 µL of TG1 cells were plated as a negative control.

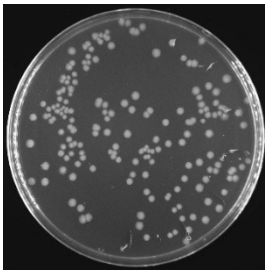
Second Library Construction



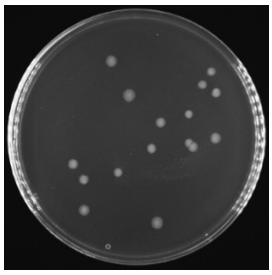
Library 10^{-2}



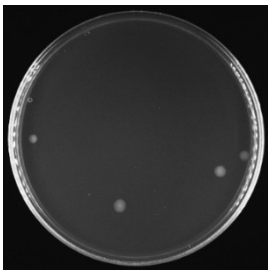
Library 10^{-3}



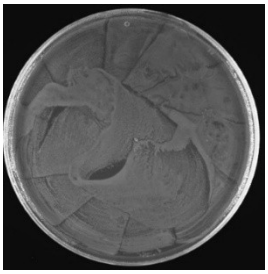
Library 10^{-4}



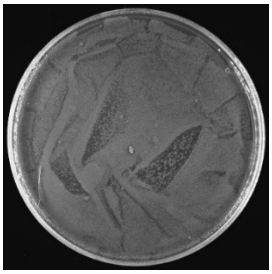
Library 10^{-5}



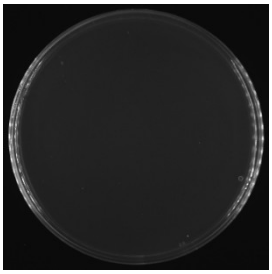
Library 10^{-6}



Library positive control undiluted



Library positive control 10^{-1}

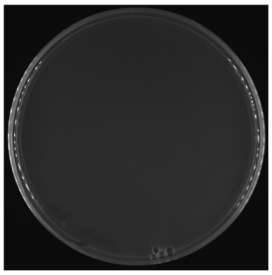


Library Negative control

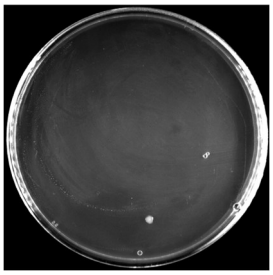
Figure A. 6 Pictures of agar plates inoculated with various dilutions of nanobody library 2 to determine the transformation titre.

Phage solutions at various concentrations were used to infect TG1 cells and plated on 2X TY-GA plates. pSEX81 plasmid transformed into TG1 cells was used as a positive control, and 50 µL of TG1 cells were plated as a negative control.

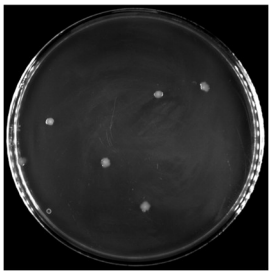
Biopanning Rounds



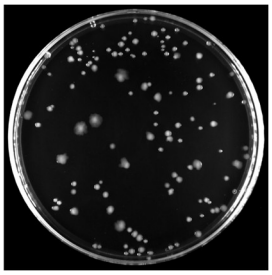
T1 undiluted



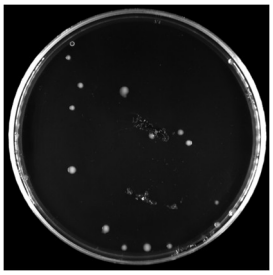
T2 undiluted



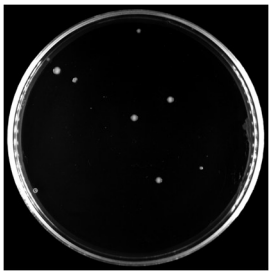
T3 undiluted



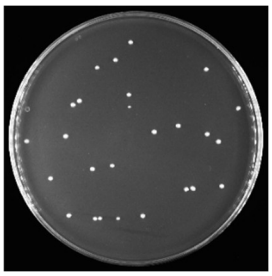
T4R1 undiluted



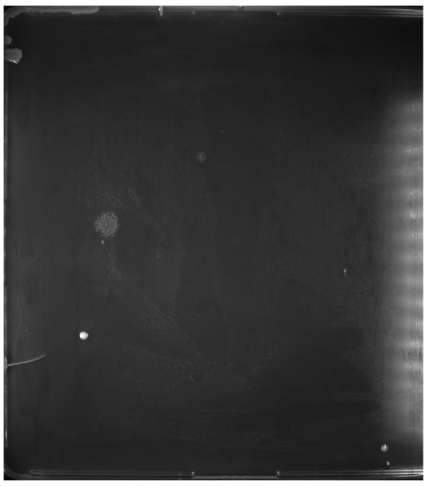
T4R1 10^{-1}



T4R1 10^{-2}



T4R2 undiluted



T4R3 undiluted

Figure A. 7 Pictures of agar plates inoculated with various dilutions of nanobody library 2 to determine the transformation titre.

Phage solutions at various concentrations were used to infect TG1 cells and plated on 2X TY-GA plates. pSEX81 plasmid transformed into TG1 cells was used as a positive control, and 50 µL of TG1 cells were plated as a negative control.

Appendix 3 Flow Cytometry Complementary Data

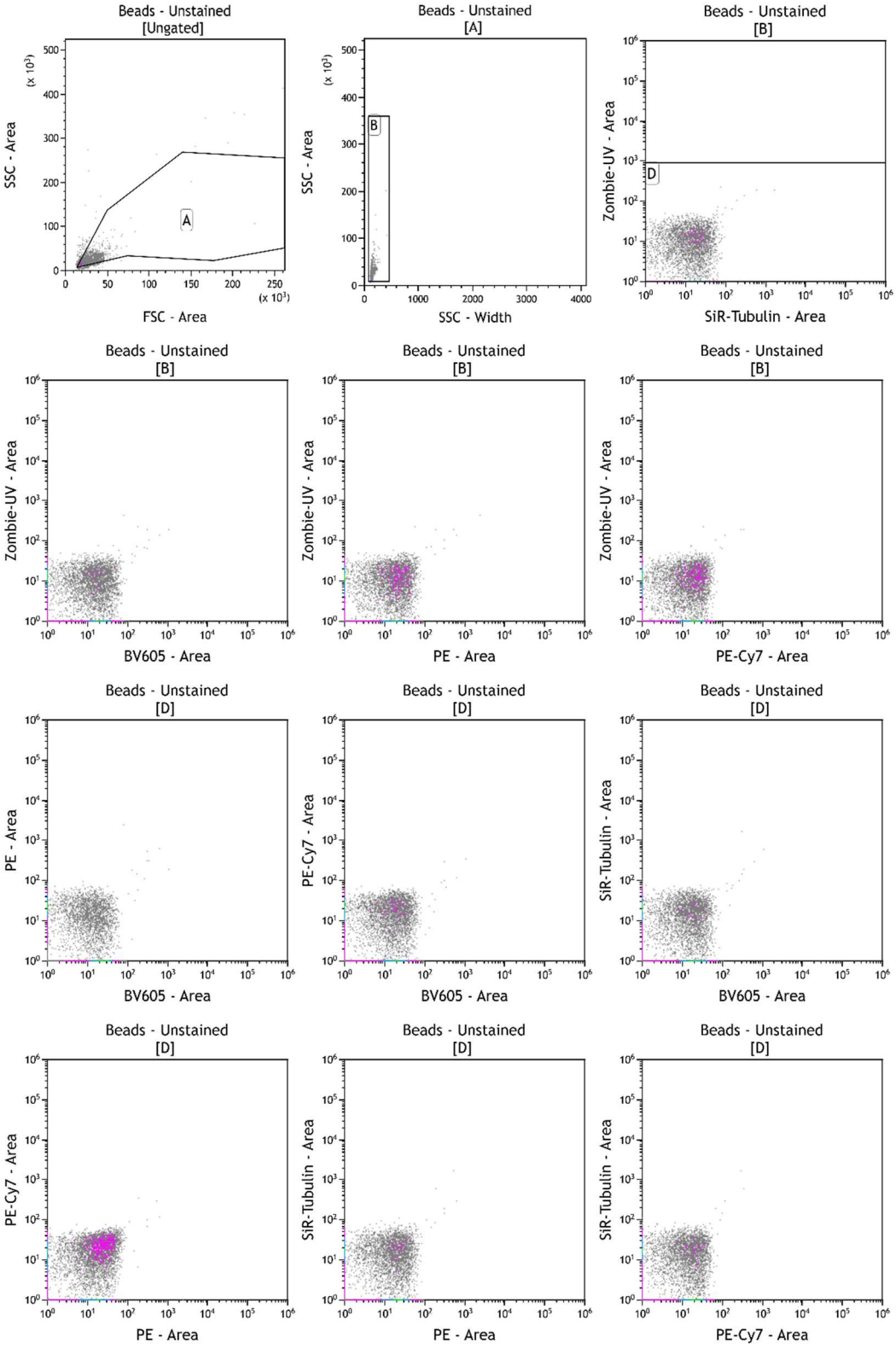
Single Colour Controls

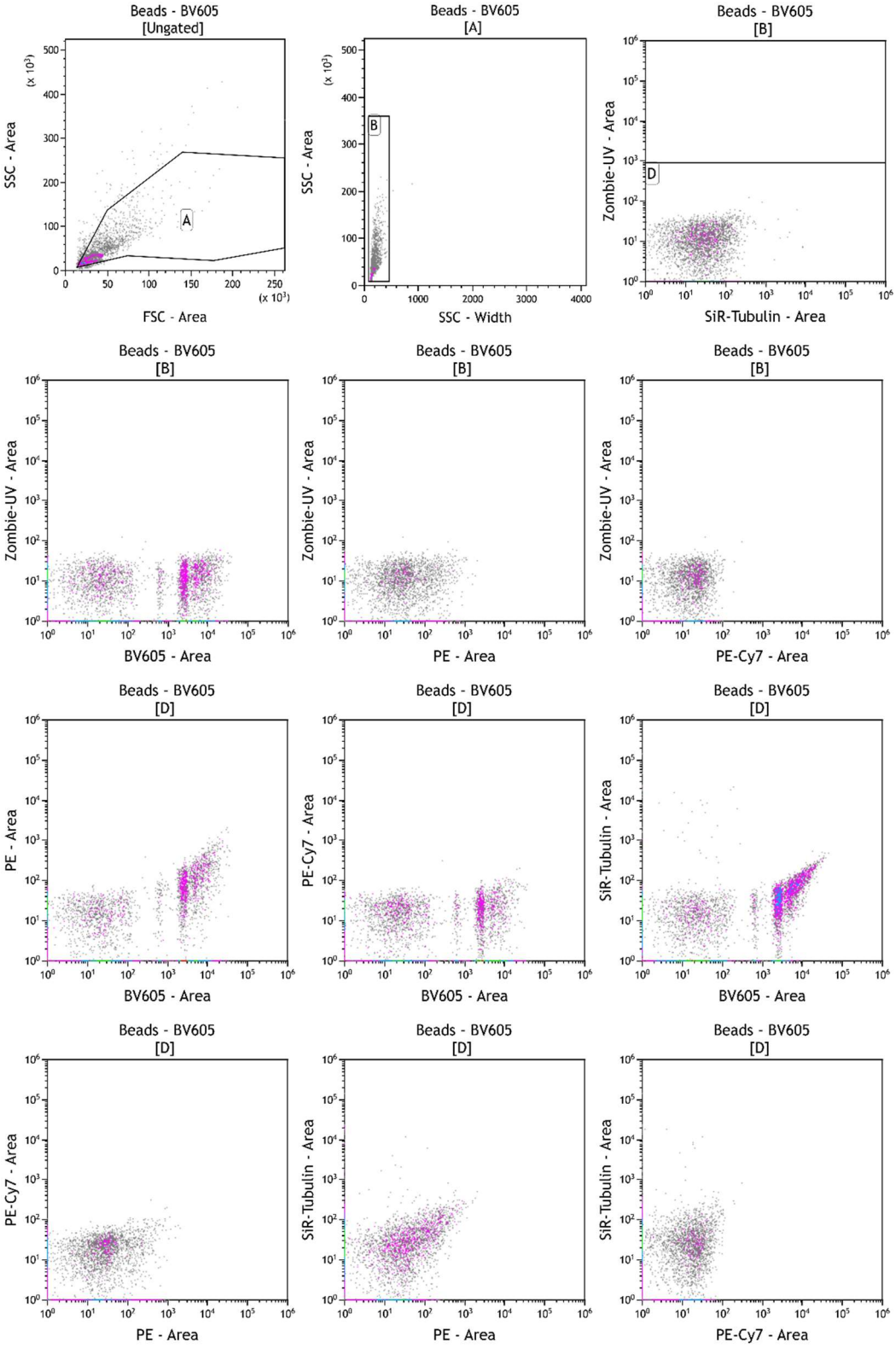
Beads were stained with each colour of the panel to measure channel spillage. The appropriate compensation was then determined by flow cytometry technician Nicola Croxall and can be seen in the table below.

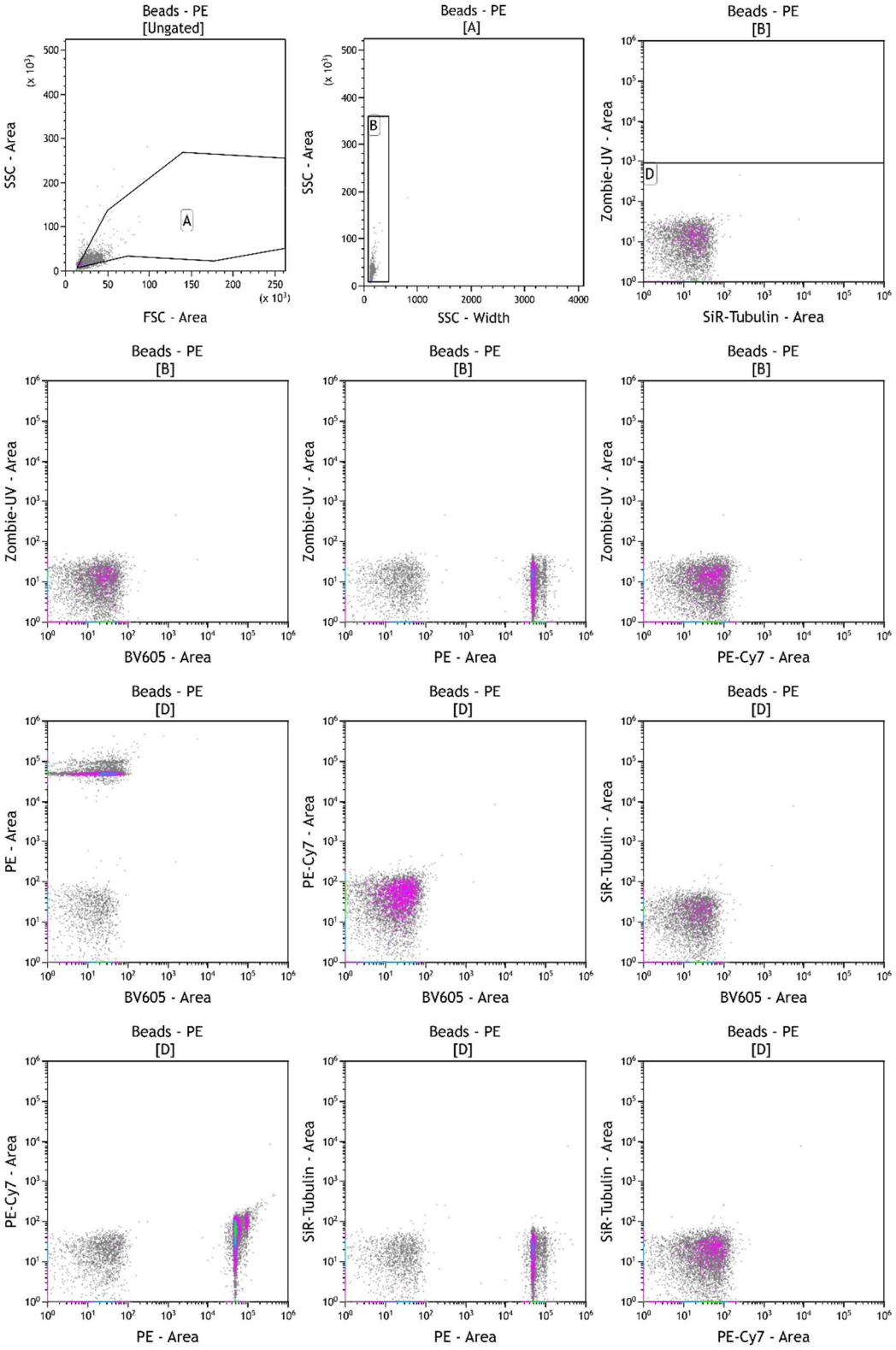
Table A. 1 Compensation data extrapolated from beads single colour controls on the Sony ID7000C Spectral Cell Analyser. This compensation profile was used for all subsequent experiments run on this equipment.

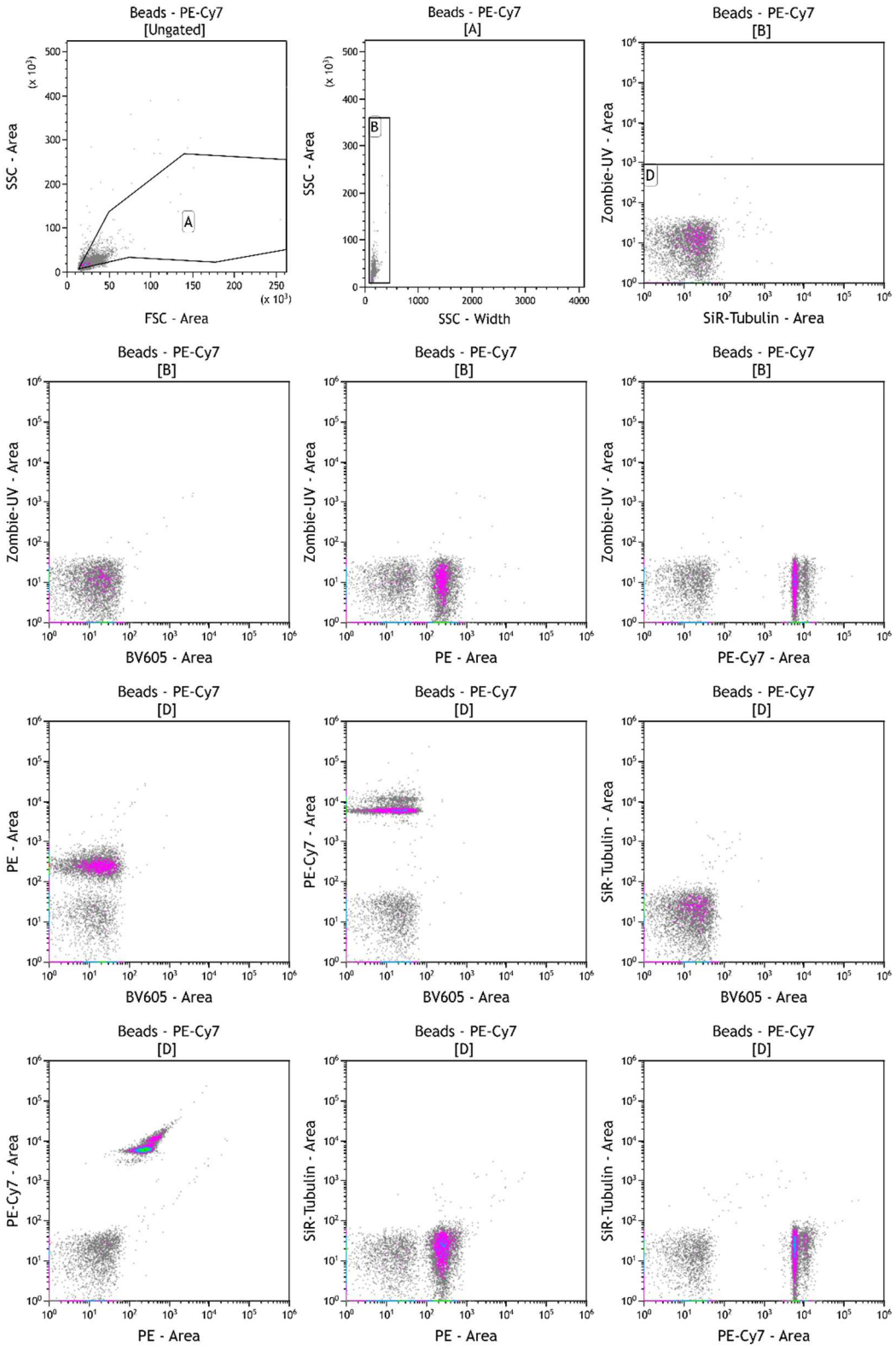
	Zombie-UV	BV605	PE	PE-Cy7	SiR-Tubulin
Zombie-UV		0.00	0.00	0.00	0.30
BV605	8.88		0.50	0.00	0.40
PE	1.40	57.91		6.47	0.80
PE-Cy7	0.20	5.91	0.59		0.49
SiR-Tubulin	49.75	0.00	0.00	0.00	

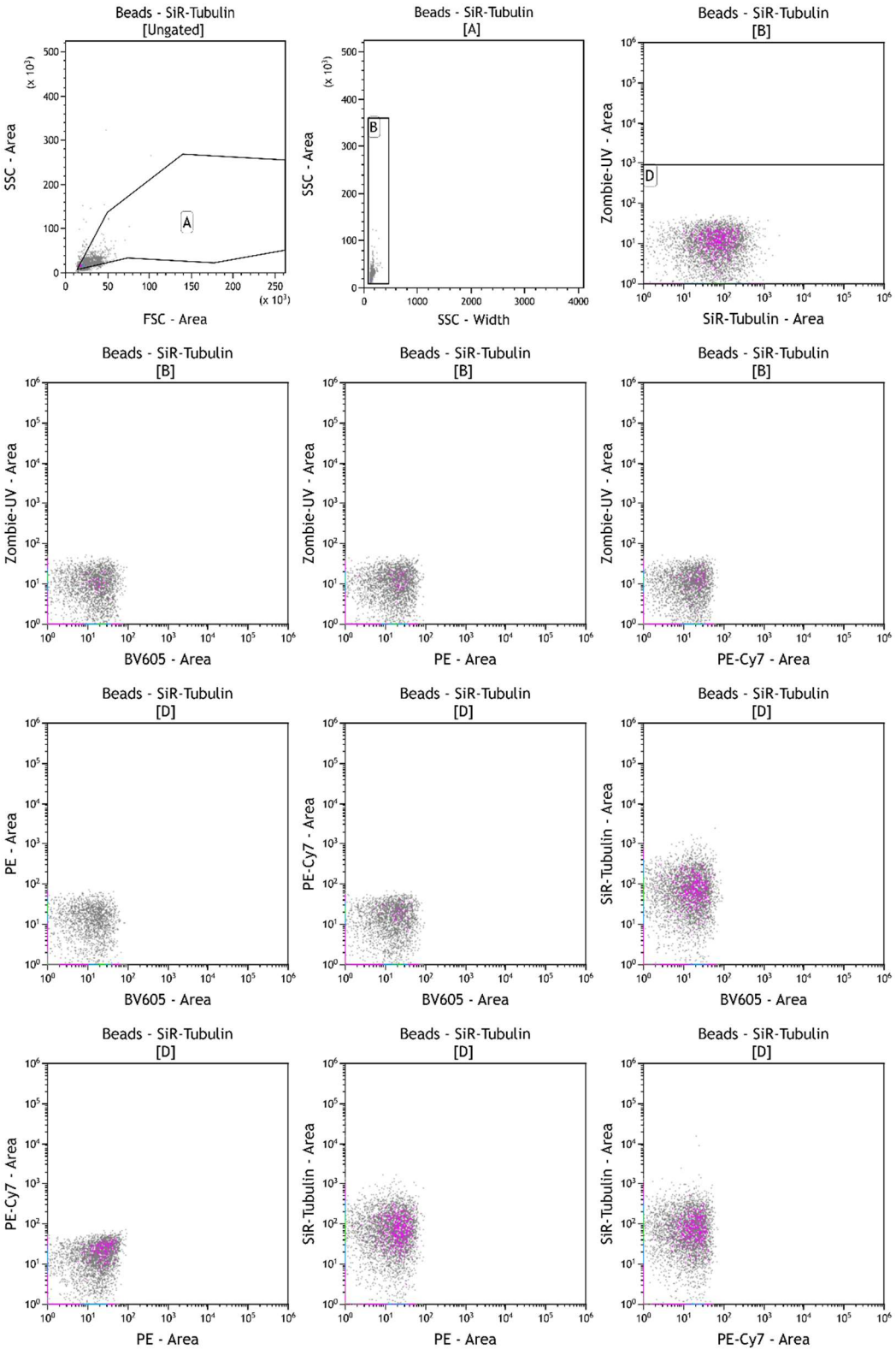
Below are all graphs collected from the beads single colour control experiments. All beads were first gated for debris and artefacts (gate A), then for possible doublets or clumped beads (gate B). Finally, beads were gated for Zombie-UV positivity to eliminate any potential contamination.


Beads - Unstained
[Ungated]
SSC - Area
FSC - Area
A
Beads - Unstained
[A]
SSC - Area
SSC - Width
B
Beads - Unstained
[B]
Zombie-UV - Area
SiR-Tubulin - Area
D
Beads - Unstained
[B]
Zombie-UV - Area
BV605 - Area
Beads - Unstained
[B]
Zombie-UV - Area
PE - Area
Beads - Unstained
[B]
Zombie-UV - Area
PE-Cy7 - Area
Beads - Unstained
[D]
PE - Area
BV605 - Area
Beads - Unstained
[D]
PE-Cy7 - Area
BV605 - Area
Beads - Unstained
[D]
SiR-Tubulin - Area
BV605 - Area
Beads - Unstained
[D]
PE-Cy7 - Area
PE - Area
Beads - Unstained
[D]
SiR-Tubulin - Area
PE - Area
Beads - Unstained
[D]
SiR-Tubulin - Area
PE-Cy7 - Area


Beads - BV605
[Ungated]
SSC - Area
FSC - Area
A
Beads - BV605
[A]
SSC - Area
SSC - Width
B
Beads - BV605
[B]
Zombie-UV - Area
SiR-Tubulin - Area
D
Beads - BV605
[B]
Zombie-UV - Area
BV605 - Area
Beads - BV605
[B]
Zombie-UV - Area
PE - Area
Beads - BV605
[B]
Zombie-UV - Area
PE-Cy7 - Area
Beads - BV605
[D]
PE - Area
BV605 - Area
Beads - BV605
[D]
PE-Cy7 - Area
BV605 - Area
Beads - BV605
[D]
SiR-Tubulin - Area
BV605 - Area
Beads - BV605
[D]
PE-Cy7 - Area
PE - Area
Beads - BV605
[D]
SiR-Tubulin - Area
PE - Area
Beads - BV605
[D]
SiR-Tubulin - Area
PE-Cy7 - Area


Beads - PE
[Ungated]
SSC - Area
FSC - Area
A
Beads - PE
[A]
SSC - Area
SSC - Width
B
Beads - PE
[B]
Zombie-UV - Area
SiR-Tubulin - Area
D
Beads - PE
[B]
Zombie-UV - Area
BV605 - Area
Beads - PE
[B]
Zombie-UV - Area
PE - Area
Beads - PE
[B]
Zombie-UV - Area
PE-Cy7 - Area
Beads - PE
[D]
PE - Area
BV605 - Area
Beads - PE
[D]
PE-Cy7 - Area
BV605 - Area
Beads - PE
[D]
SiR-Tubulin - Area
BV605 - Area
Beads - PE
[D]
PE-Cy7 - Area
PE - Area
Beads - PE
[D]
SiR-Tubulin - Area
PE - Area
Beads - PE
[D]
SiR-Tubulin - Area
PE-Cy7 - Area


Beads - PE-Cy7
[Ungated]
SSC - Area
FSC - Area
A
Beads - PE-Cy7
[A]
SSC - Area
SSC - Width
B
Beads - PE-Cy7
[B]
Zombie-UV - Area
SiR-Tubulin - Area
D
Beads - PE-Cy7
[B]
Zombie-UV - Area
BV605 - Area
Beads - PE-Cy7
[B]
Zombie-UV - Area
PE - Area
Beads - PE-Cy7
[B]
Zombie-UV - Area
PE-Cy7 - Area
Beads - PE-Cy7
[D]
PE - Area
BV605 - Area
Beads - PE-Cy7
[D]
PE-Cy7 - Area
BV605 - Area
Beads - PE-Cy7
[D]
SiR-Tubulin - Area
BV605 - Area
Beads - PE-Cy7
[D]
PE-Cy7 - Area
PE - Area
Beads - PE-Cy7
[D]
SiR-Tubulin - Area
PE - Area
Beads - PE-Cy7
[D]
SiR-Tubulin - Area
PE-Cy7 - Area


Beads - SiR-Tubulin
[Ungated]
SSC - Area
FSC - Area
A
Beads - SiR-Tubulin
[A]
SSC - Area
SSC - Width
B
Beads - SiR-Tubulin
[B]
Zombie-UV - Area
SiR-Tubulin - Area
D
Beads - SiR-Tubulin
[B]
Zombie-UV - Area
BV605 - Area
Beads - SiR-Tubulin
[B]
Zombie-UV - Area
PE - Area
Beads - SiR-Tubulin
[B]
Zombie-UV - Area
PE-Cy7 - Area
Beads - SiR-Tubulin
[D]
PE - Area
BV605 - Area
Beads - SiR-Tubulin
[D]
PE-Cy7 - Area
BV605 - Area
Beads - SiR-Tubulin
[D]
SiR-Tubulin - Area
BV605 - Area
Beads - SiR-Tubulin
[D]
PE-Cy7 - Area
PE - Area
Beads - SiR-Tubulin
[D]
SiR-Tubulin - Area
PE - Area
Beads - SiR-Tubulin
[D]
SiR-Tubulin - Area
PE-Cy7 - Area

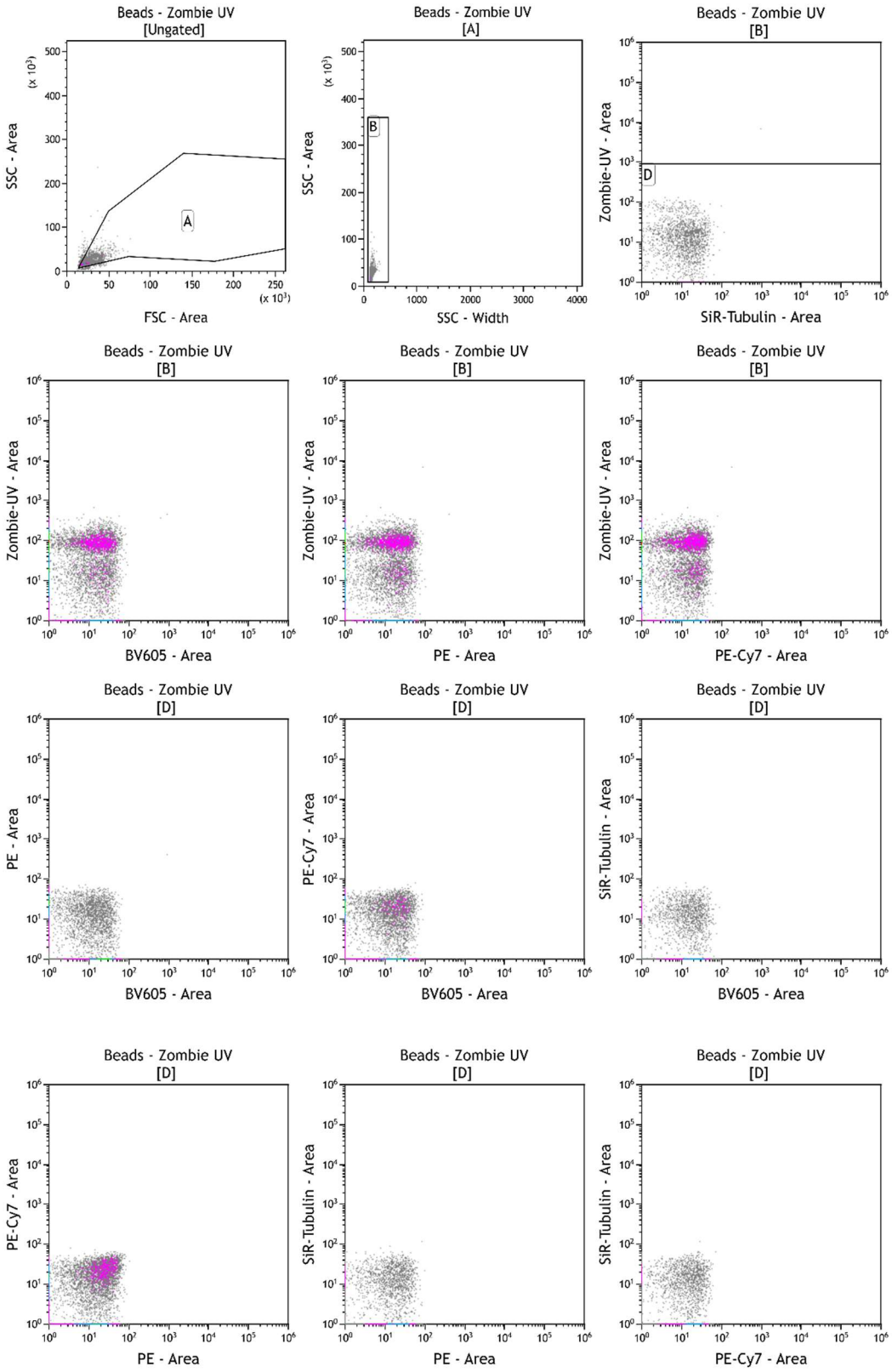
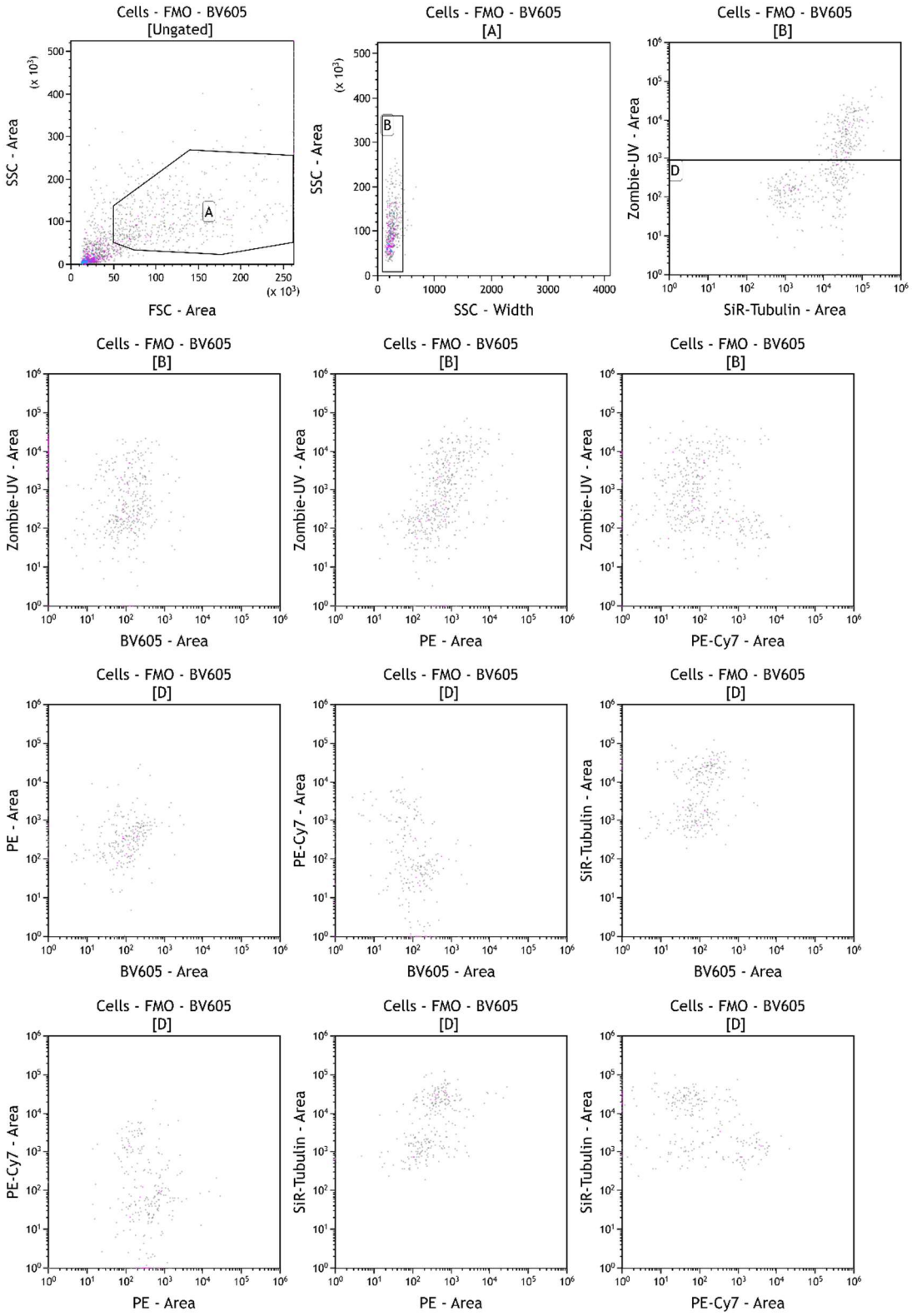
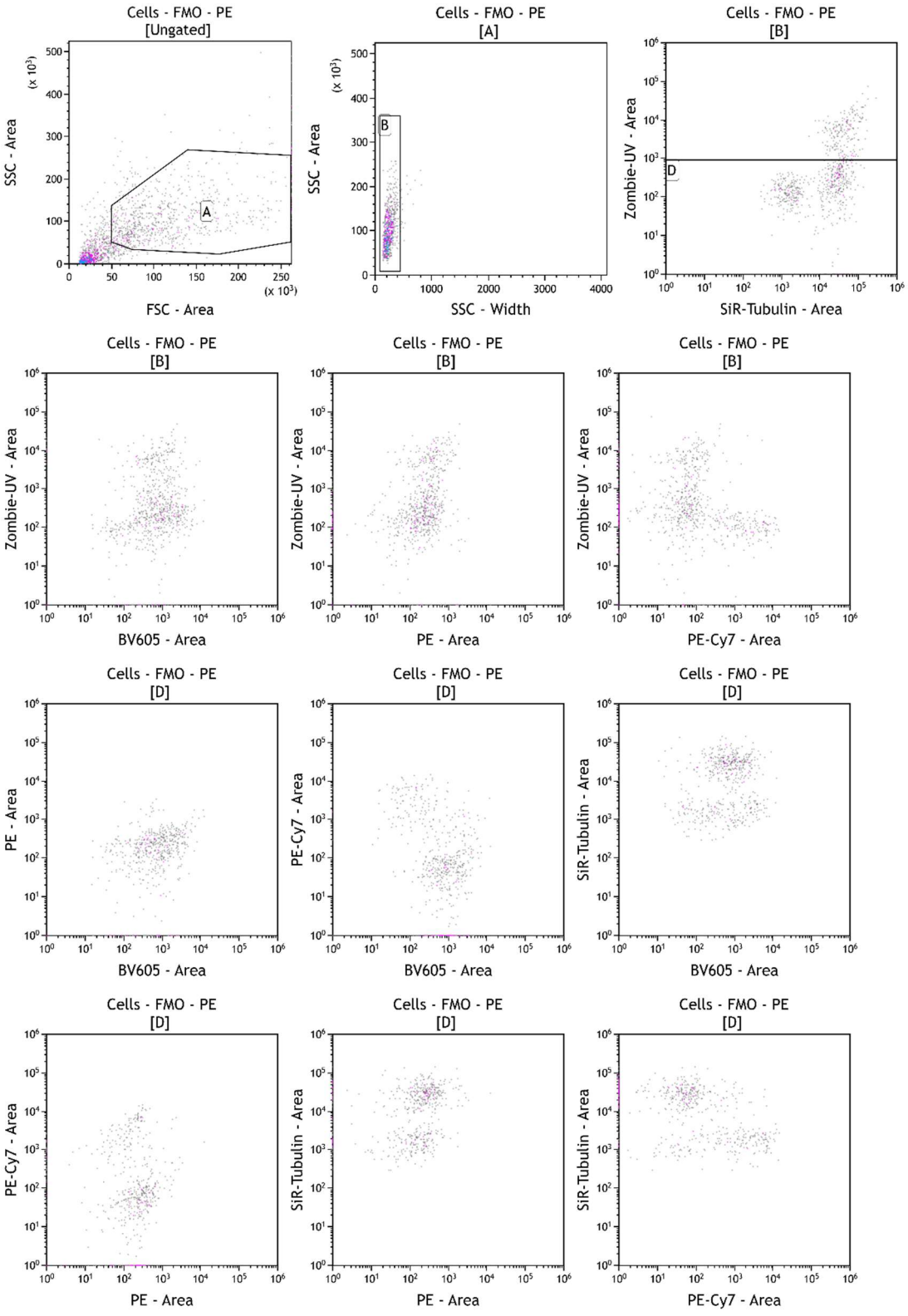
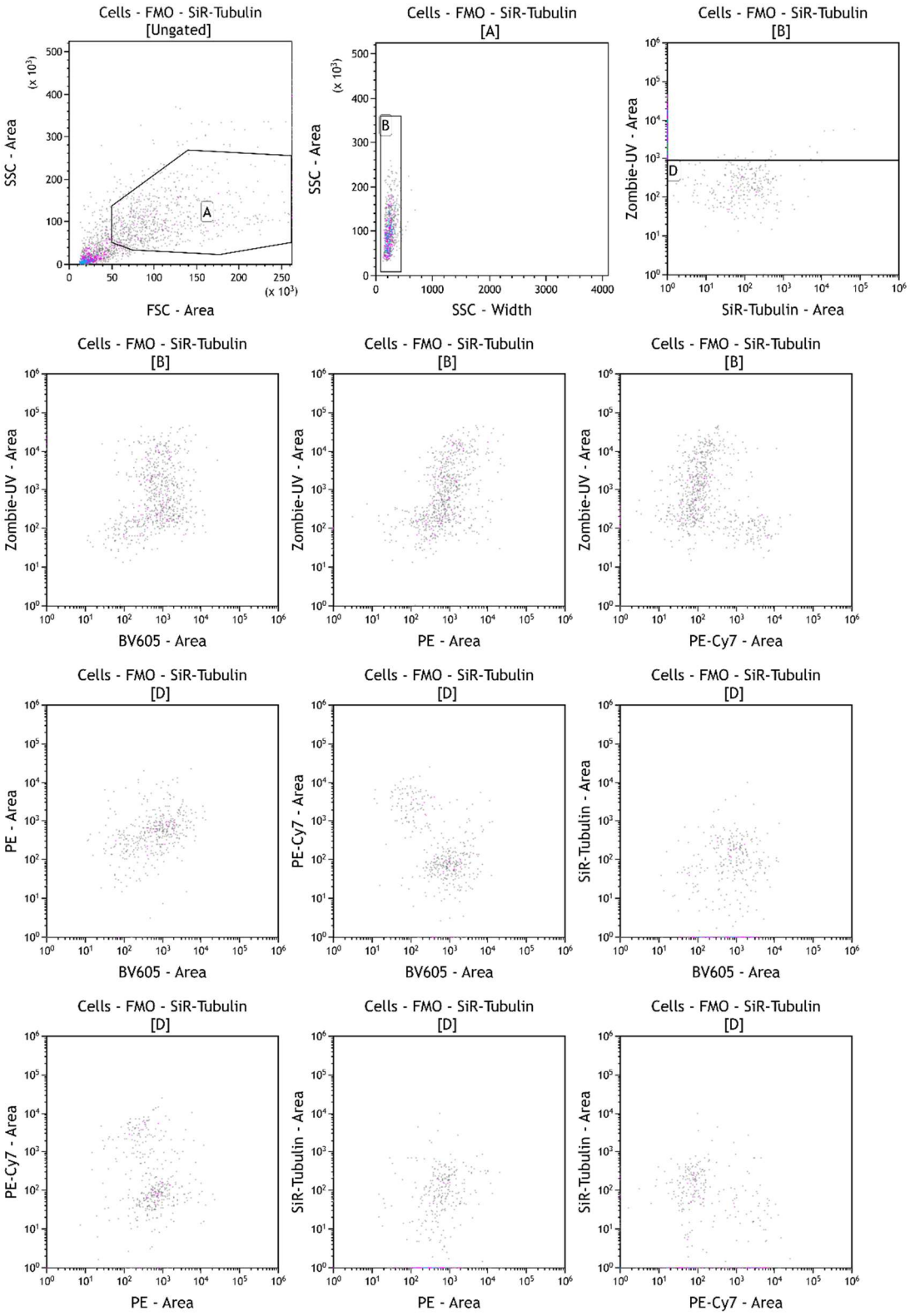


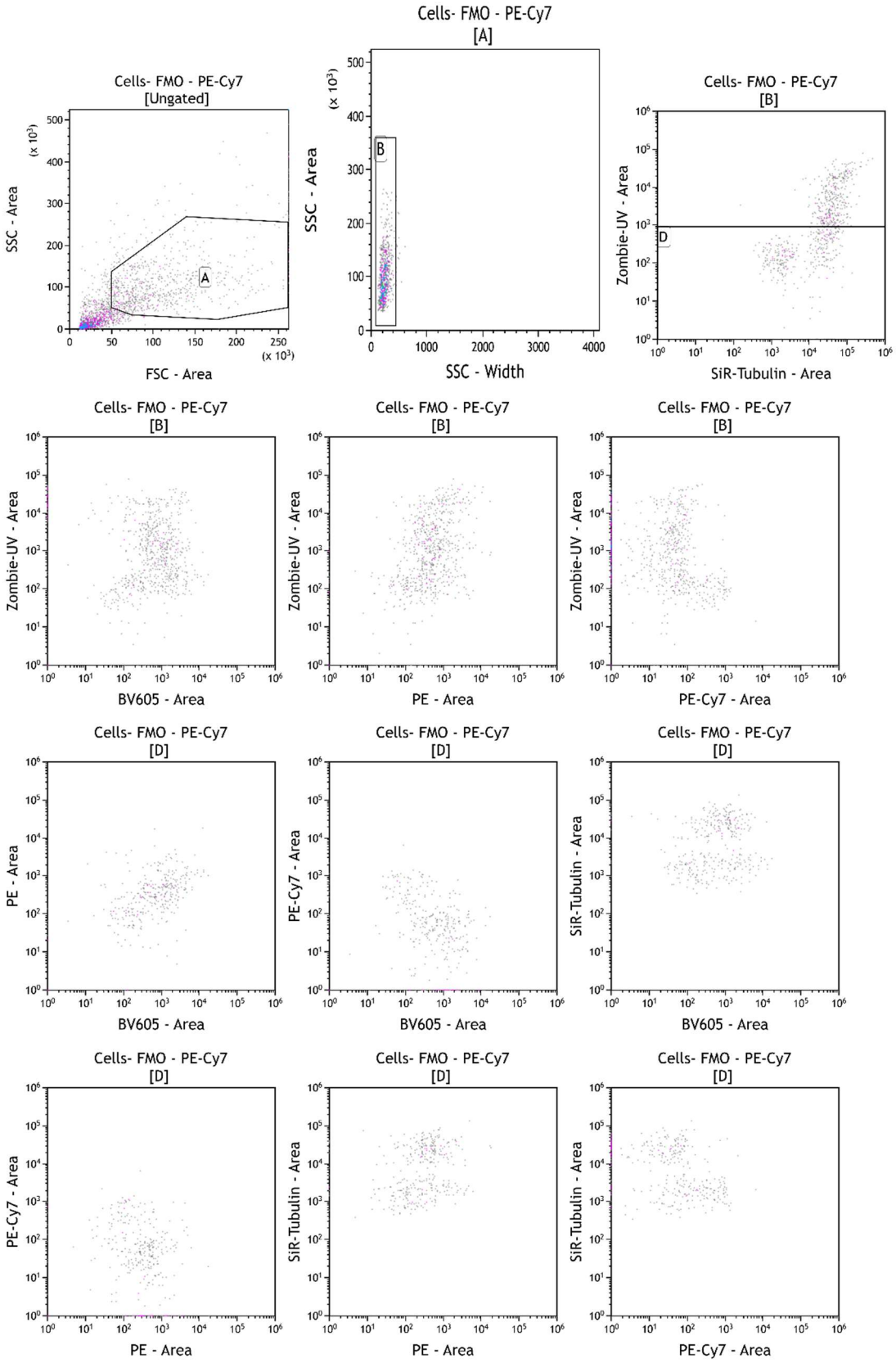
Figure A. 8 Flow cytometry graphs of single colour controls obtained by staining compensation beads with each fluorescent marker.

Fluorescence Minus One (FMO) Controls




Cells - FMO - PE
[Ungated]
SSC - Area
FSC - Area
A
Cells - FMO - PE
[A]
SSC - Area
SSC - Width
B
Cells - FMO - PE
[B]
Zombie-UV - Area
SiR-Tubulin - Area
D
Cells - FMO - PE
[B]
Zombie-UV - Area
BV605 - Area
Cells - FMO - PE
[B]
Zombie-UV - Area
PE - Area
Cells - FMO - PE
[B]
Zombie-UV - Area
PE-Cy7 - Area
Cells - FMO - PE
[D]
PE - Area
BV605 - Area
Cells - FMO - PE
[D]
PE-Cy7 - Area
BV605 - Area
Cells - FMO - PE
[D]
SiR-Tubulin - Area
BV605 - Area
Cells - FMO - PE
[D]
PE-Cy7 - Area
PE - Area
Cells - FMO - PE
[D]
SiR-Tubulin - Area
PE - Area
Cells - FMO - PE
[D]
SiR-Tubulin - Area
PE-Cy7 - Area


Cells - FMO - SiR-Tubulin
[Ungated]
SSC - Area
FSC - Area
A
Cells - FMO - SiR-Tubulin
[A]
SSC - Area
SSC - Width
B
Cells - FMO - SiR-Tubulin
[B]
Zombie-UV - Area
SiR-Tubulin - Area
D
Cells - FMO - SiR-Tubulin
[B]
Zombie-UV - Area
BV605 - Area
Cells - FMO - SiR-Tubulin
[B]
Zombie-UV - Area
PE - Area
Cells - FMO - SiR-Tubulin
[B]
Zombie-UV - Area
PE-Cy7 - Area
Cells - FMO - SiR-Tubulin
[D]
PE - Area
BV605 - Area
Cells - FMO - SiR-Tubulin
[D]
PE-Cy7 - Area
BV605 - Area
Cells - FMO - SiR-Tubulin
[D]
SiR-Tubulin - Area
BV605 - Area
Cells - FMO - SiR-Tubulin
[D]
PE-Cy7 - Area
PE - Area
Cells - FMO - SiR-Tubulin
[D]
SiR-Tubulin - Area
PE - Area
Cells - FMO - SiR-Tubulin
[D]
SiR-Tubulin - Area
PE-Cy7 - Area


Cells- FMO - PE-Cy7
[Ungated]
SSC - Area
FSC - Area
A
Cells- FMO - PE-Cy7
[A]
SSC - Area
SSC - Width
B
Cells- FMO - PE-Cy7
[B]
Zombie-UV - Area
SiR-Tubulin - Area
D
Cells- FMO - PE-Cy7
[B]
Zombie-UV - Area
BV605 - Area
Cells- FMO - PE-Cy7
[B]
Zombie-UV - Area
PE - Area
Cells- FMO - PE-Cy7
[B]
Zombie-UV - Area
PE-Cy7 - Area
Cells- FMO - PE-Cy7
[D]
PE - Area
BV605 - Area
Cells- FMO - PE-Cy7
[D]
PE-Cy7 - Area
BV605 - Area
Cells- FMO - PE-Cy7
[D]
SiR-Tubulin - Area
BV605 - Area
Cells- FMO - PE-Cy7
[D]
PE-Cy7 - Area
PE - Area
Cells- FMO - PE-Cy7
[D]
SiR-Tubulin - Area
PE - Area
Cells- FMO - PE-Cy7
[D]
SiR-Tubulin - Area
PE-Cy7 - Area

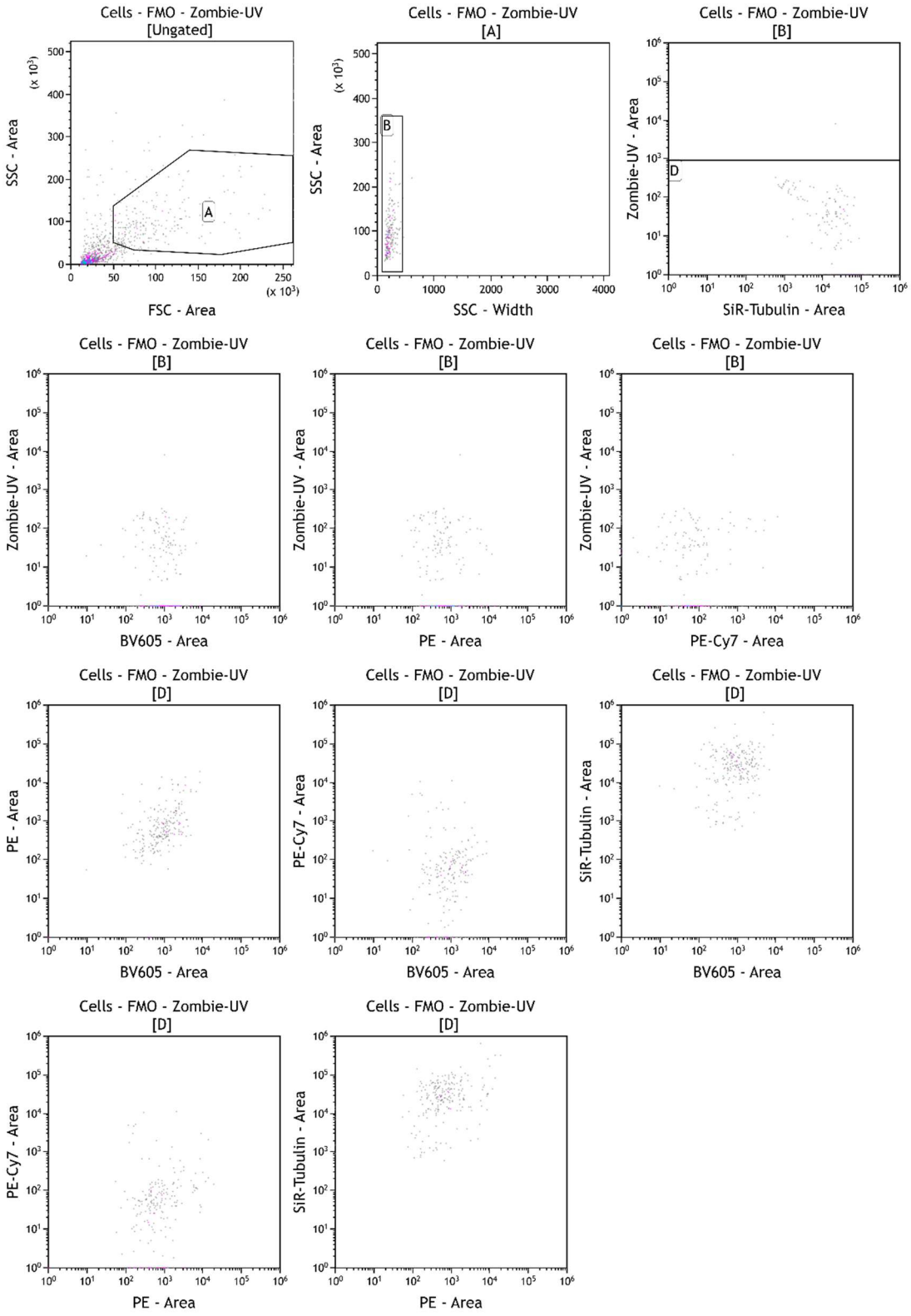


Figure A. 9 Flow cytometry graphs of FMO controls obtained by staining cells with all fluorescent markers but one.

Second Repeat

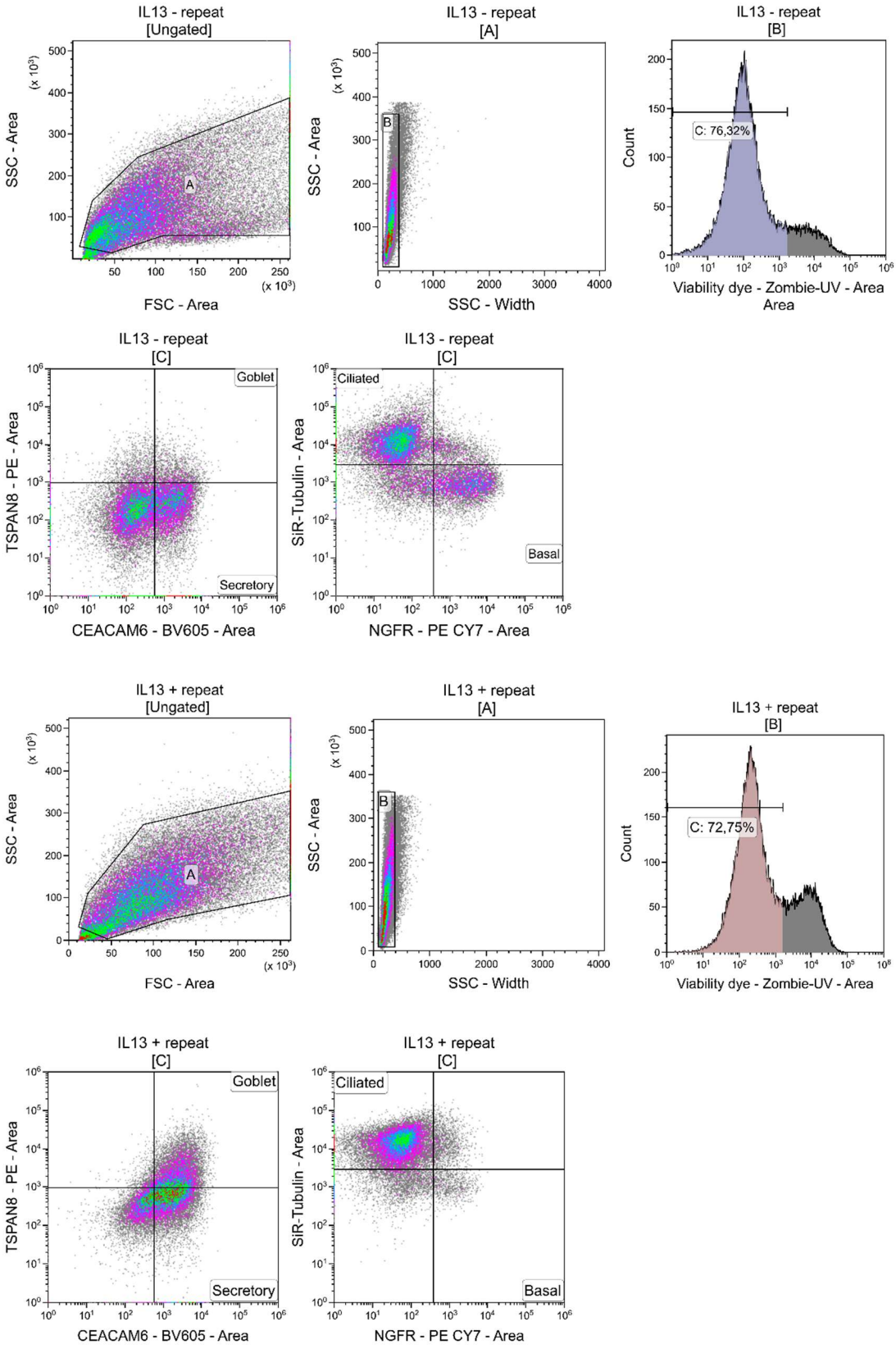
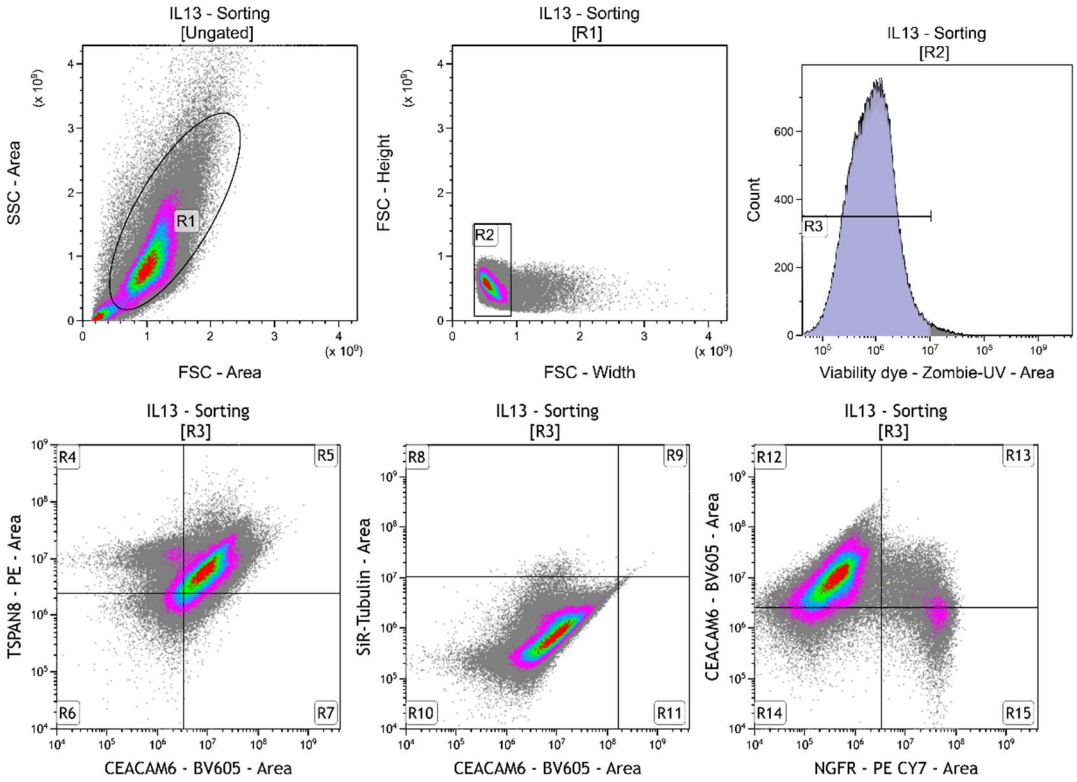


Figure A. 10 Flow cytometry gating strategy and analysis of IL-13+ and IL-13- cell populations stained with a multicolour panel for cell type identification. Second repeat.

Initial gate (A) based on forward scatter (FSC) and side scatter (SSC) to exclude debris, allowing for selection of intact cells. SSC width vs. SSC height gate (B) to remove doublets or clumped cells, isolating single cells. Final gate (C) using a viability dye to distinguish live cells from dead or apoptotic ones, refining the population for accurate analysis.

Cell Sorting (Third Repeat)



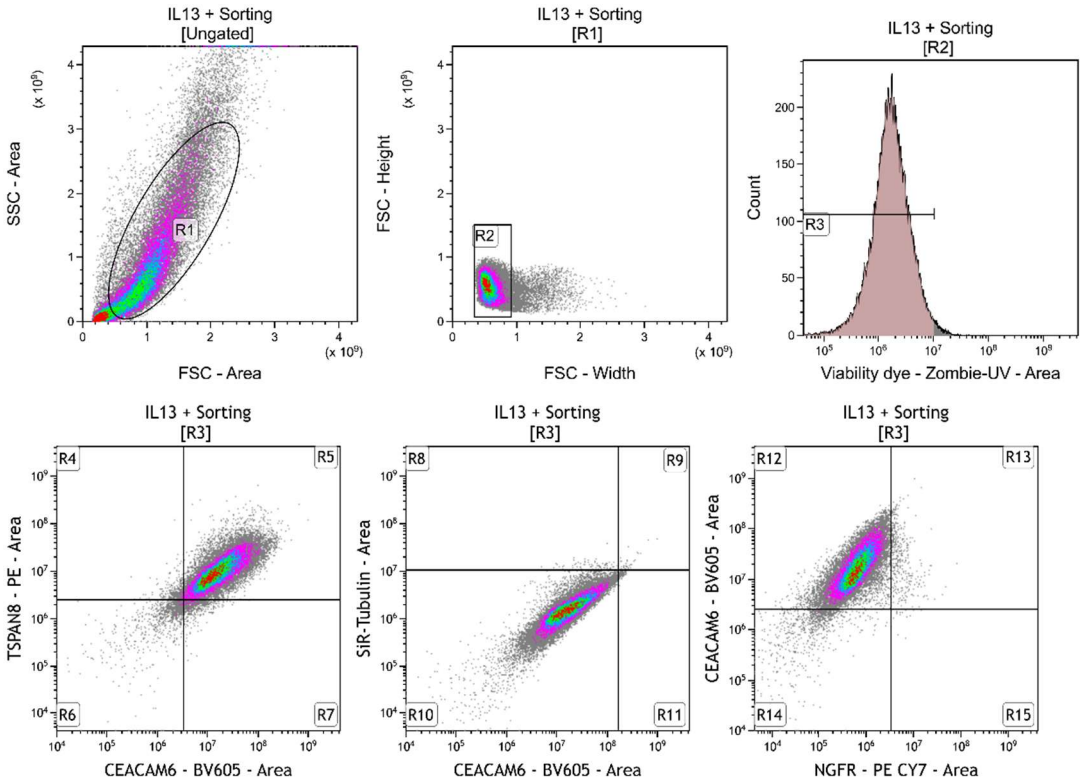


Figure A. 11 cytometry gating strategy and sorting of IL-13+ and IL-13- cell populations stained with a multicolour panel for cell type identification.

Initial gate (R1) based on forward scatter (FSC) and side scatter (SSC) to exclude debris, allowing for selection of intact cells. FSC width vs. FSC height gate (R2) to remove doublets or clumped cells, isolating single cells. Final gate (R3) using a viability dye to distinguish live cells from dead or apoptotic ones, refining the population for accurate analysis.

Appendix 4 PIPS Reflective Statement

Note To Examiners

This statement is included as an appendix to the thesis in order that the thesis accurately captures the PhD training experienced by the candidate as a BBSRC Doctoral Training Partnership student.

The Professional Internship for PhD Students is a compulsory three-month placement, which must be undertaken by DTP students. It is usually centred on a specific project and must not be related to the PhD project. This reflective statement is designed to capture the skills development that has taken place during the student's placement and the impact on their career plans it has had.

Statement

My placement was completed at a contract research organisation (CRO) – Sygnature Discovery, where I contributed to the development of an HTRF (Homogeneous Time Resolved Fluorescence) assay for the *in vitro* detection of protein degradation by proteolysis targeting chimera (PROTACs).

The project focused on developing an assay to evaluate the binding capacity of PROTACs developed by Signature Discovery chemistry department. Careful optimisation of cell culture and assay conditions were necessary to ensure the highest signal to background ratio. HTRF methodology was selected for its ease of use and reliability. Several compounds were tested, and binding curves were generated for each compound. The results of this assay were presented in a poster as part of the launch of the CHARMD platform at the American Association for Cancer Research Annual Meeting 2023 (see reference below). The CHARMD platform focuses on the high-throughput integrated platform for the development bioavailable hetero-bifunctional degraders for challenging oncology targets.

Poster reference: Roland Hjerpe, Louise Birch, Alex Brien, Lola Cusin, Lorna Duffy, Benoit Gourdet, Rachel Lawrence, Philip MacFaul, Hannah Mortlock, Hannah Neal, Christopher Pearce, Erica Pitti, Gonzalo Robles, Edith Rodrigues, Catriona Scott, Rajesh Singh, Stuart Thomson, Yujia Zhang, Allan Jordan. The Sygnature CHARMD platform – combinatorial high-throughput assembly and review of molecular degraders [abstract]. In: Proceedings of the American Association for Cancer Research Annual Meeting 2023; Part 1 (Regular and Invited Abstracts); 2023 Apr 14–19; Orlando, FL. Philadelphia (PA): AACR; Cancer Res 2023;83 (7_Suppl): Abstract nr 3111. Available at https://info.sygnaturediscovery.com/charmed-from-sygnature-discovery

Parallelly to this experimental work, I gained valuable insights into the operations of a CRO, particularly in supporting biotech and pharmaceutical companies by delivering essential research services on a contract basis, especially when considering the processes and regulatory considerations involved in translational research. I had the opportunity to collaborate closely with the chemistry department, providing me with a new understanding on how chemical approaches and methodologies can complement biological research. I developed my communication skills by learning to communicate complex biological concepts effectively to a different scientific audience. I also developed key skills in project management within a commercial research environment and was able to observe best practices in managing complex research projects and delivering high-quality results within strict timelines and regulatory frameworks

Overall, this placement has been instrumental in shaping my career aspirations, solidifying my interest in pursuing a career in the biotechnology and pharmaceutical industry, and providing me with a comprehensive understanding of the industry's structure and the role of CROs within it.